Cape Peninsula
University of Technology

FUEL CELL POWER CONDITIONING MULTIPHASE CONVERTER FOR 1400 V_{DC} MEGAWATTS STACKS

by

BEN HAMAD KHLID

Thesis submitted in fulfilment of the requirements for the degree

Doctor of Engineering in Electrical Engineering

in the Faculty of Engineering

at the Cape Peninsula University of Technology

Supervisor: Prof Mohamed Tariq Khan

Bellville
November 2019

DECLARATION

I, Ben Hamad Khlid, declare that the contents of this dissertation/thesis represent my own unaided work, and that the dissertation/thesis has not previously been submitted for academic examination towards any qualification. Furthermore, it represents my own opinions and not necessarily those of the Cape Peninsula University of Technology.

Signed **Date**

ABSTRACT

Energy systems based on fossil fuel have demonstrated their abilities to permit economic development. However, with the fast exhaustion of this energy source, the expansion of the world energy demand and concerns over global warming, new energy systems dependent on renewable and other sustainable energy are gaining more interests. It is a fact that future development in the energy sector is founded on the utilisation of renewable and sustainable energy sources. These energy sources can enable the world to meet the double targets of diminishing greenhouse gas emissions and ensuring reliable and cost-effective energy supply. Fuel cells are one of the advanced clean energy technologies to substitute power generation systems based on fossil fuel. They are viewed as reliable and efficient technologies to operate either tied or non-tied to the grid to power applications ranging from domestic, commercial to industrial. Multiple fuel cell stacks can be associated in series and parallel to obtain a fuel cell system with high power up to megawatts. The connection of megawatts fuel cell systems to a utility grid requires that the power condition unit serving as the interface between the fuel cell plant and the grid operates accordingly. Different power conditioning unit topologies can be adopted, this study considers a multilevel inverter.

Multilevel inverters are getting more popularity and attractiveness as compared to conventional inverters in high voltage and high-power applications. These inverters are suitable for harmonic mitigation in high-power applications whereby switching devices are unable to function at high switching frequencies. For a given application, the choice of appropriate multilevel topology and its control scheme are not defined and depend on various engineering compromises, however, the most developed multilevel inverter topologies include the Diode Clamped, the Flying Capacitor and the Cascade Full Bridge inverters. On the other hand, a multilevel inverter can be either a three or a five, or a nine level, however, this research focuses on the three-level diode clamped inverters.

The aim of this thesis is to model and control a three-level diode clamped inverter for the grid connection of a megawatt fuel cell stack. Besides the grid, the system consists of a 1.54 MW operating at 1400 V DC proton exchange membrane fuel cell stack, a 1.26 MW three-level diode clamped inverter with a nominal voltage of 600 V and an LCL filter which is designed to reduce harmonics and meet the standards such as IEEE 519 and IEC 61000-3-6. The inverter control scheme comprises voltage and current regulators to provide a good power factor and satisfy synchronisation requirements with the grid. The frequency and phase are synchronised with those of the grid through a

phase locked loop. The modelling and simulation are performed using Matlab/Simulink. The results show good performance of the developed system with a low total harmonic distortion of about 0.35% for the voltage and 0.19% for the current.

Keywords: Fuel cell, grid-connected multilevel inverter, grid synchronisation, passive filter, VSI control

ACKNOWLEDGEMENTS

Before anything else, I would like to thank ALLAH for giving me the knowledge, strength, ability and perseverance to complete this research successfully.

My deep thanks go to my supervisor, Professor MTE Kahn, for all the support, guidance and commitment throughout this research.

I would like as well to express my gratitude to Dr. Atanda K. Raji and all the members of the Centre for Distributed Power and Electronic Systems (CDPES) for their support and encouragement.

DEDICATION

To my parents, my wife and my sons, I dedicate my thesis

TABLE OF CONTENTS

TABLE OF FIGURES

TABLE OF TABLES

GLOSSARY

A	Fuel Cell Active Area
AFC	Alkaline Fuel Cell
B	Coefficient for Computing
C	Equivalent Capacitance
C_b	Base Capacitance
C_{cap}	Capital Cost
C_{dc}	Output Capacitor Filter
C_f	Filter Capacitance
C_{FC}	Input Capacitor Filter
C_{INT}	Initial Cost
$C_{o\&m}$	Costs Related to Operation and Maintenance
C_o	Concentration of Oxygen
C_p	Parasitic Capacitor
C_r	Resonant Capacitor of LLC Resonant DC to DC Converter
C_{sm}	Submodule Capacitor
DC	Direct Current
DMFC	Direct Methanol Fuel Cell
DTC	Direct Torque Control
$DSOGI$	Double Second Order Generalised Integrator
E_{Nernst}	Thermodynamic Potential (potential of the cell obtained in an open
E_{Yr}	Average Energy Production of A year in the Lifetime Cycle of the system
e^{ST_C}	Phase Lead Compensator
EMI	Electromagnetic Interference
$EPLL$	Enhanced Phase Locked Loop

f	Frequency
$\boldsymbol{F}$	Faraday Constant
$\mathbf{f_C}$	Crossover frequency
f_{crit}	critical frequency
$\boldsymbol{f_f}$	Fundamental Wave Frequency
$\boldsymbol{f_g}$	Grid Frequency
$\boldsymbol{f_{res}}$	Resonance Frequency
$\mathbf{f_S}$	Sampling frequency
f_{samp}	Sampling frequency
$\boldsymbol{f_{WS}}$	Switching Frequency
FB-ZVR	Full-Bridge Zero-Voltage Rectifier
FRT	Fault Ride Through
FC	Fuel Cells
GCL	closed-loop current control loop
$\boldsymbol{h}$	Harmonic Order
HAWTs	Horizontal Axis wind turbines
HERIC	Highly Efficient and Reliable Inverter Concept
$\boldsymbol{HHV}$	Higher Heating Value
HVDC	High Voltage Direct Current
Hz	Hertz
H2	Hydrogen
$\boldsymbol{I_{abc}}$	Three phase Grid Current
$\boldsymbol{I_c}$	Capacitor Current
i_{FC}	Fuel Cell Current
$\boldsymbol{I_g}$	Grid Current
$\boldsymbol{I_{dc}}$	Input Current
$\boldsymbol{I_i}$	Inverter Current

I_{max}	Peak Rated Output Current
i_P	Being The leakage Current
I_p	Grid Current
I_{rms}	Nominal Current
IM	Imaginary Part
J	Actual Current Density
J_{max}	Maximum Current Density
Ka	Desired Attenuation
K_{ir}	integral Gain
K_{Pr}	Proportional Gain
K_{P-dc}	PI Controller Proportional Gain
K_{rC}	Control Gain
K_{rh}	Control Gain
Kw	Kilowatt Power
K_1	Proportional Gain of the PI-Based Loop Filter
K_2	Integral Gain of the PI-Based Loop Filter
L	Arm Inductor
l	Thickness of membrane
L_{boost}	Boost Inductor
L_{dc}	DC Side Inductor
L_f	Output Filter Inductor
i_{FC}	Fuel Cell Current
L_g	Grid Side Inductor
L_i	Inverter Side Inductor
L_m	Resonant Parallel Inductor of LLC Resonant DC to DC Converter
L_r	Resonant Inductor of LLC Resonant DC to DC Converter
L_1	Resonant Inductor

L_2	Resonant Inductor
LCOE	Levelized Cost of Energy
3L	Three-level
m_a	Modulation Range
m_p	Corresponding Modulation Signal for the phase
MCFC	Molten Carbonate Fuel Cell
MMC	Modular Multilevel Converters
MPPT	Maximum Power Point Tracking
MW	Megawatt
NPC	Neutral-point-clamped
O_2	Oxygen
$\mathbf{P}$	Active Power
P_{ac}	Active Power at the grid Side
P_{air}	Absolute Supply Pressure of Air
P_{dc}	DC Power Routed to the Inverter
P_f	Power Factor
P_{FC}	Output power of the Fuel Cell Stack
P_{fuel}	Absolute Supply Pressure of Fuel
f_g	Grid Frequency
P_{H_2}	Pressures of Hydrogen
P_{ins}	Instantaneous Active Power
P_n	Rated Active Power
P_{O_2}	Pressures of Oxygen
PAFC	Phosphoric Acid Fuel Cell
PCC	Point of Common Coupling
PCU	Power Conditioning Unit
PEMFC	Proton Exchange Membrane Fuel Cell
PI	Controller

$\mathbf{PLL}$	Phase Locked Loop
PR	Proportional Resonant Controller and the repetitive Controller
PV	Photovoltaic
PWM	Pulse Width Modulation
Q	Reactive Power
$\boldsymbol{Q_{ins}}$	Instantaneous Reactive Power
$\boldsymbol{Q(s)}$	Low Pass Filter
$\boldsymbol{R}$	Universal Gas Constant
$\boldsymbol{R_a}$	Equivalent Resistance
$\boldsymbol{R_C}$	Membrane Contact Resistor
$\boldsymbol{R_d}$	Damping Resistance
$\boldsymbol{R_e}$	Real Part
$\mathbf{R_g = R_i}$	Inductors Resistances
$\boldsymbol{S_n}$	Rated Apparent Power
SM	Submodule
$\boldsymbol{SRF}$	Synchronous Rotating Reference Frame
$\boldsymbol{SPT}$	Standard Pressure and Temperature
SPWM	Sinusoidal Pulse Width Modulation
SOFC	Solid Oxide Fuel Fell
$\mathbf{SOGI}$	Second Order Generalised Integrator
$\boldsymbol{T}$	Fuel Cell Temperature
$\boldsymbol{T_C}$	Compensation Time
$\boldsymbol{T_{i-dc}}$	Integrator Time Constant
$\boldsymbol{T_{ref}}$	Reference Stack Temperature
$\mathbf{T_S}$	Switching Period
$\boldsymbol{T_{SW}}$	Switching Time
THD	Total Harmonic Distortion

TH-PWM	Third Harmonic Pulse Width Modulation
V	Voltage
$\boldsymbol{V_{abc}}$	Three-phase Grid Voltage
$\boldsymbol{V_{ac1,c2,c3}}$	Corresponding Microinverter Output Voltages
$\mathbf{V_{air}}$	Air Flow Rate
$\boldsymbol{V_{act}}$	Activation Voltage Drop
$\boldsymbol{V_{CMV}}$	Common-Mode Voltage
$\boldsymbol{V_{con}}$	Concentration voltage Drop
$\boldsymbol{V_{DC}}$	DC Link Voltage
$\boldsymbol{V_{FC}}$	Output Fuel Cell Voltage
$\boldsymbol{V_{fuel}}$	Fuel Flow Rate
$\boldsymbol{V_{g}}$	Grid Voltage
$\boldsymbol{V_{i}}$	Inverter Input Voltage
$\boldsymbol{V_{LL}}$	Line to Line RMS Voltage
$\boldsymbol{v_{m}}$	Phase Voltage Amplitude
$\boldsymbol{V_{mag}}$	Magnitude of the command Voltage
$\boldsymbol{v_{p}}$	Phase Voltage
$\boldsymbol{V_{offset}}$	Offset Voltage
$\boldsymbol{V_{ohmic}}$	Ohmic Voltage Drop
$\boldsymbol{v_{op}}$	Inverter Output Phase Voltage
V_{PH}	Phase Voltage
$\mathbf{V_{ref}}$	Command Voltage Vector
$\boldsymbol{V_{ref,max}}$	Largest Value Among the three-leg Command Voltages
$\boldsymbol{V_{ref,min}}$	Smallest Voltage Among the three-leg Command Voltages
$\boldsymbol{V_{S}}$	Stack Output Voltage
VAWTs	Vertical Axis wind turbines
$\mathbf{x\%}$	Percentage of Hydrogen in the fuel

$Y\%$	Percentage of hydrogen in the oxidant
$\boldsymbol{Z_b}$	Base Impedance
$\boldsymbol{\gamma}$	Second Order Generalised Integrator control gain
$\boldsymbol{\zeta}$	Curve Fitting Parameter
$\boldsymbol{\rho_m}$	Specific Resistivity of the Membrane
$\boldsymbol{\Psi}$	Electron Transfer Coefficient
$\boldsymbol{\mu_f}$	Fuel utilisation coefficient
τ	Time Constant
ζ	Damping Ratio
$\boldsymbol{\omega}$	Fundamental Frequency
$\boldsymbol{\omega_C}$	Crossover Frequency
$\boldsymbol{\omega_n}$	Undamped Natural Frequency
$\boldsymbol{\omega_{n-PLL}}$	natural frequency of Phase Locked Loop
$\boldsymbol{\xi_{PLL}}$	Damping Factor of Phase Locked Loop
$\boldsymbol{\theta}$	Voltage Phase
$\boldsymbol{\Delta G}$	The change in the free Gibbs Energy
$\boldsymbol{\Delta I}$	Inverter Side Current Ripple
$\boldsymbol{\Delta I_{Lmax}}$	Peak Rated Output Current Ripple
$\boldsymbol{\Delta S}$	The change of the entropy

CHAPTER ONE
INTRODUCTION

1.1 Introduction

Ever-growing world energy demand, increased awareness to safeguard the environment and fast exhaustion of fossil fuels are the essential drives that led to new energy systems dependent on renewable and other sustainable energy sources to gain more interests (Behrouzi et al., 2016). It is now a conviction that the upcoming energy industry needs to be established on renewable and sustainable energy sources. In this way, moving to sustainable energy sources can empower us to meet the double targets of diminishing greenhouse gas emissions, by that overcoming extreme weather conditions and ensuring reliable and cost-effective energy supply (Behrouzi et al., 2016).

Significant alternative energy resources accessible across the world include solar energy, wind energy, wood and biomass, and biogas production (Behrouzi et al., 2016). Solar power is a sort of energy with well prospect potential although currently it covers barely a lesser part of global energy needs (Kumar et al., 2019). It was reported in 2011 that, energy from solar constituted about 0.05% of the overall main energy supply, while the production of electricity was below 1% (Solangi et al., 2011). This is because solar power is still viewed as a costly type of renewable energy. However, in remote areas especially in Africa, technologies based on solar energy may represent currently best solutions for energy access (De Castro et al., 2013). Similarly, wind power is among the most developed of renewable energy technologies which has grown faster over the past decade (Rosales-Asensio et al., 2019). The technology has become the favourite option of energy for designers and public governments pursuing the diversification of energy, creating new industries (Lacal-arantegui, 2019), and providing new labour potentials (Mendecka & Lombardi, 2019). Currently, it is recorded that, the overall installed wind power exceeds largely 318.105 GW (Dai et al., 2015). In the same vein, biomass which refers to any organic matter that can be renewable and represents an important source of energy. It can be found with different characteristics, availability and energy content and are available in various types grouped in four following categories (Khiari et al., 2019):

- wastes such as domestic and certain types of low-quality bio-oil,
- processing residues such as sawmill dust,
- locally collected feedstock such as wood chips,
- internationally traded feedstock such as pellets, upgraded biogas and bio-oil.

Literature survey reveals that the use of biomass in some developing countries is gaining a dramatic interest; for instance, in Brazil, a higher portion of energy is produced using biomass and biofuels from sugar cane (Zwaan B, V et al., 2013). Similarly, in India, with approximately 66 % of the population living in rural areas (The World Bank, n.d.), it is evaluated that around 4.75 million households have their own bio-digesters (IRENA, 2015). In the same vein, African countries like Tanzania and Kenya are undertaking programmes in a domestic level for the implementations of bio-digesters and in the industrial level for the construction of power plants based on biogas (Owiro et al., 2015; Felix & Gheewala, 2011).

Along the same line, fuel cells are one of the advanced clean energy technologies and have demonstrated their ability to be a decent substitute to fossil fuel-based power systems (Hossain et al., 2017). They are viewed as reliable and one of the most efficient technologies as their efficiency ranges between 40 and 60% (Ramezanizadeh et al., 2019). A common fuel cell system utilises hydrogen to produce power with heat and pure water as the by-product (Luta & Raji, 2018). Various types of fuel cells can be found in the market, however, proton exchange membrane fuel cell (PEMFC) is the most appealing in view of its low operating temperature (Majlan et al., 2018), low noise, high efficiency and low pollution. PEMFC generates DC (direct current) power at a low-voltage level.

Generally, fuel cells, cannot accept current, hence, to block current flow back, a diode is often included in series with the fuel cell unit, whereas in applications, subject to an occurring of reverse current, a capacitor can be introduced to consume the current (Islam et al., 2015). However, a careful selection of this capacitor is required to ensure that it is not over stressed during the system operation.

Presently, no standard output voltage rating for fuel cells has been validated. Most fuel cell stacks generate an output voltage in the range from 24 to 150 VDC (Naik & Samuel, 2016). To acquire high-power fuel cell systems, PEMFCs are associated in series and parallel to form multi-stack fuel cell systems (Marx et al., 2014). Additionally, numerous applications whereby fuel cells can be included require the presence of a power conditioning unit (PCU) to achieve the following objectives (Yu et al., 2007):

i. control the fuel cell voltage
ii. convert the fuel cell output to a suitable magnitude and type
iii. provide a high-power factor (grid applications)
iv. ensure lesser to zero harmonics
v. function efficiently under all conditions and
vi. add little to the cost of the overall system.

PCUs are essentially based on DC to DC boost converters and inverters as depicted in Figure 1.1a. The unit role is to boost the fuel cell voltage and convert the DC voltage to AC (Lai & Ellis, 2017). In addition to boosting the voltage, it is expected from the boost converter to regulate the fuel cell voltage used as input to the inverter and to perform the electrical isolation task from low to high-voltage side (Obaid et al., 2018), while the inverter is required to convert the DC power to AC with appropriate harmonic rejection and depending on applications the inverter can either be single, dual, or three phases (Hassaine et al., 2014). Three-phase inverters are more suitable for large scale and grid-connected applications whereas single and dual-phase inverters are mostly utilised for domestic and residential applications (Yu et al., 2007). Besides the above-mentioned topology, another configuration shown in Figure 1.1b consists of neglecting the use of DC to DC converters and rather relying on a transformer at the output of the inverter to boost the voltage (Lai & Ellis, 2017).

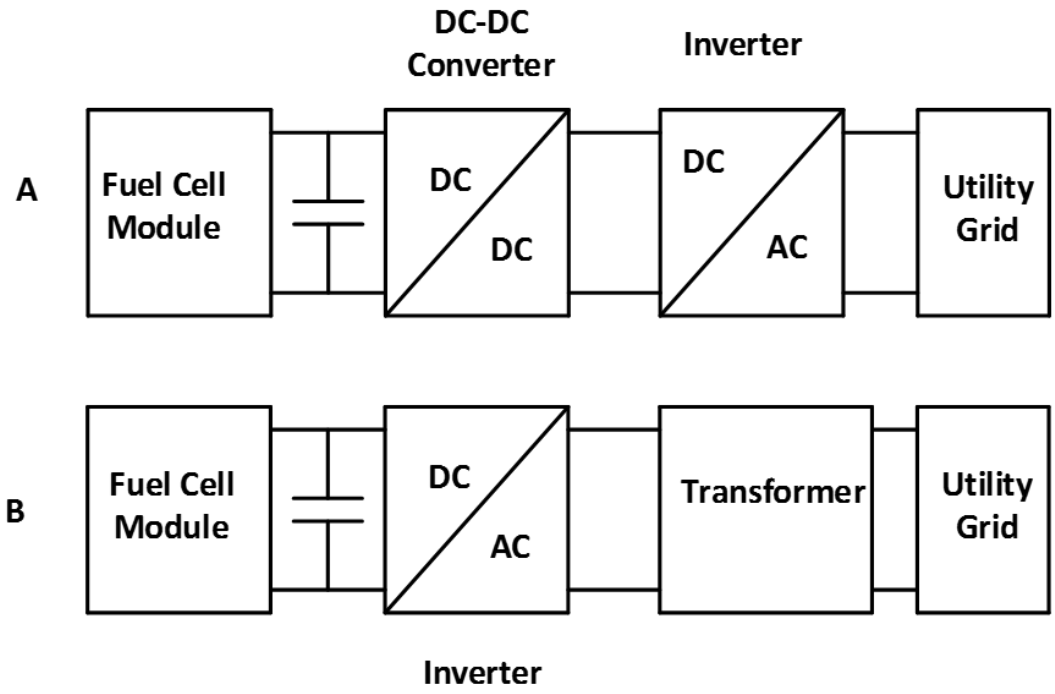

Figure 1. 1: (a) Double PCU; (b) Single stage PCU with transformer. (Lai & Ellis, 2017)

Several methods exist to connect fuel cell systems into an AC utility grid using PCU based on the above-mentioned topologies, the most popular configurations include (Mancilla-David et al., 2012a):

i. Centralised configuration,
ii. String configuration and
iii. Multi-string configuration.

In the first configuration (centralised configuration), a single PCU is used as an interface to multiple stacks, while in the string configuration, each string of fuel cell stacks is connected to the PCU and lastly, tin multi-string configuration, several strings are coupled with their own PCUs (Konara et al., 2016) . The topology adopted in this study is centralised configuration based on the single-stage PCU consisting only of an inverter without a DC to DC converter (Suryoatmojo et al., 2018) . Different types of inverter ranging from low to high level can be used in centralised configuration depending on the power requirement (Islam & Mekhilef, 2014) . For low power and low-voltage applications, the two-level inverter configuration is the most used topology whereas for high power and high-voltage applications, multi-level inverter configuration is more. Applications of multi-level inverters range from medium to high voltage and comprise power distribution, motor drives, etc. (Mancilla-David et al., 2012b) . For a given application, the choice of appropriate multi-level topology and its control scheme are not defined and depend on various engineering compromises (Marx et al., 2014), however, the most developed multi-level inverter topologies include the Diode Clamped, the Flying Capacitor and the Cascade Full Bridge inverters(Lai & Ellis, 2017).

Diode clamped multilevel inverter is the most accepted topology; the concept behind this inverter is to use diodes to limit the power devices voltage stress. The voltage at each capacitor and each switch is Vdc. An n-level inverter requires (n-1) voltage sources, 2(n-1) switching devices and (n-1) (n-2) diodes. By enlarging the number of voltage levels, the output voltage quality is improved, and the voltage waveform is nearly sinusoidal. The voltage across each capacitor is Vdc/2 and each device voltage stress will be limited to one capacitor voltage level Vdc/2 through clamping diodes. The three-level diode clamped inverter is one of the most available topologies in the market; it is widely used in industrial applications in the range of 2.3 to 6.6 KV (Yao et al., 2017).

A common inverter generates harmonics as its output voltage and current are not a pure sine wave. In general, harmonics are caused by nonlinear loads, drawing non-sinusoidal current from sinusoidal voltage sources. These loads include power electronics converters, motor drives and electric arc furnaces. Loads including

fluorescent lamps, computers, fax machines, photocopiers, laser printers, battery chargers, etc. are also sources of harmonics. These harmonics impact negatively on sensitive equipment above several kilowatts of the connected loads (Jeong et al., 2010). IEEE and IEC standards set the allowable harmonic distortion for both the current and the voltage in a power system based on the current level and the voltage level respectively. Conventional criteria used to reduce harmonics is the use of an input inductance while the output inductance of the power conversion devices serves as filters. However, due to the increase in the size of systems, realising practical filters becomes difficult due to high cost and poor system dynamic response. An LCL filter is connected after the inverter to eliminate harmonics resulting from the inverter switching. In comparison with other filters such as an L and LC filters, an LCL filter has the benefit of achieving better attenuation capacity for complex harmonics and has better dynamic characteristics (Bao et al., 2013; Dhar & Dash, 2016). However, an LCL filter can cause instability problems because of its zero impedance which may create resonance for some frequencies. To overcome this issue, various damping techniques such as incorporating a physical passive element in series with the filter capacitor (Hamoud et al., 2016) have been proposed. Among these damping techniques, the technique using a passive element is simple and reliable, however, the passive element causes power loss and weakens the effect of the LCL filter which can be overcome by using an active damping technique (Yao et al., 2017).

When operating in grid-connection mode, the inverter output voltage and frequency should be the same as those of the grid. Hence, the current injected into the grid should be balanced, sinusoidal, and have a total harmonic distortion lower than 5% (Sahoo & Subudhi, 2018). To achieve these requirements, the control of the inverter plays a vital role and in such a case, the objective of the control action is to properly feed the extracted power to the grid. To obtain higher performance several control strategies for grid-connected inverters have been proposed , such as selective harmonics elimination pulse-width modulation (SHE-PWM), pulse-width modulation (PWM) and optimised harmonics stepped pulse-width modulation (OHS-PWM) (Colak et al., 2011), however, this research focuses on the PWM control approach. The PWM control approach can be grouped into open loop and closed loop control systems; the open-loop PWM techniques are SPMW, space vector PWM, sigma–delta modulation, while closed loop control systems are current control methods. For grid-connected inverters, the closed-loop control consists of three major steps namely the outer loop control (Aly & Ramadan, 2019), inner loop control and synchronisation. The outer control loop can be a DC-link voltage control or a power control loop, which generates the inner current references, on the other, the inner current loop regulates the injected currents, while

the synchronisation is achieved through a phase locked loop (PLL) which uses the grid to provide the correct phase and frequency.

1.2 Statement of the Research Problem

The connection of megawatts fuel cell systems to a utility grid requires that the power condition unit serving as the interface between the fuel cell plant and the grid operates accordingly to comply with grid connection standards and codes.

1.3 Aim and objectives of the research

The aim of this research is to model and control a three-level diode clamped inverter for the grid connection of a megawatt fuel cell stack.

In order to achieve the above aim, the following shall be done:

i. a complete literature review of power conditioners, particularly for high megawatt power conditioning;
ii. classify power converter architectures, topologies, and component technology that may reduce cost;
iii. design an LCL filter to mitigate the effect of harmonics;
iv. develop a closed loop control system for the three-level inverter;
v. detailed simulation of the inverter model in MATLAB/Simulink to predict the model performance;
vi. performance evaluation of the inverter under different load conditions.

1.4 Outline of the thesis

Besides the introduction, the rest of the thesis is organised as follows:

Chapter 2: Literature review

This chapter deals with the literature survey on renewable and other alternative power technologies, as well as power electronics converters and their control for fuel cell applications.

Chapter 3: System description and components modelling

This chapter deals with the description of the megawatt fuel cell energy system and the modelling of components involved on it. The adopted configuration consists of components such as a 1.54 MW fuel cell stack, a three-level diode clamped inverter to convert the 1400 DC volts of the fuel cell into 600 AC volts between phases, and an

LCL filter to mitigate the effect of voltage and the current harmonics generated by the inverter. The megawatt fuel cell stack consists of several proton exchange membrane fuel cell (PEMFC) stacks connected in series and parallel. The system was developed based on the model of each component and the designed parameters of the fuel cell, inverter, LCL filter were also presented. The last section of this chapter is oriented to the modelling of the control system for the inverter to properly deliver the generated power from the megawatt fuel cell stack to the grid and local load.

Chapter 4: Simulation Results and Discussion

The megawatt fuel cell system was considered to operate in grid-tied mode, thereafter, a simulation was carried out to evaluate the operation of the system in off-grid mode. A total of twelve stacks were connected in parallel to obtain the megawatt fuel cell stack. The characteristics of each individual stack are given in the appendices. It was assumed that during the simulation, the hydrogen and oxygen composition, system temperature, hydrogen and oxygen pressure were kept constant, whereas the hydrogen and oxygen flow rate were depending on Equation 4.1 and Equation 4.2.

Conclusion

The final chapter concludes the thesis and identifies topics for further research.

1.5 Publications

The publications below have evolved from the doctoral research:

1.5.1 International Journals

Hamad, Khlid B & Kahn, M. TE. 2019. Modelling and control of a grid-tied power conditioning unit for a megawatt fuel cell system. *International Journal of Engineering & Technology*, 9(1): 149–163. https://www.sciencepubco.com/index.php/ijet/article/view/29997/16210.

1.5.2 Conference proceedings

Hamad, Khlid B. & Kahn, M.T. 2019. Modeling of a Solid Oxide Fuel Cell Microgrid System for Megawatt Load. In *Industrial and Commercial Use of Energy*. Cape Town: 198–203.

Ben Hamad, K., Taha, M.H., Almaktoof, A. & Kahn, M.T.E. 2019. Modelling and analysis of a grid-connected Megawatt Fuel Cell stack. In *2019 International Conference on the Domestic Use of Energy (DUE)*. Wellington: IEEE: 147–155. https://ieeexplore.ieee.org/document/8734449.

Hamad, K.B. & Kahn, M.T. 2018. A Pattern for LCL Filter Design for Renewable Power Converter. In *International Society for Engineering Rersearch and Development*. Cape

Town: ISERD: 5–10. http://www.worldresearchlibrary.org/up_proc/pdf/1498-15278546355-10.pdf.

CHAPTER TWO
LITERATURE REVIEW

2.1 Introduction

This chapter deals with the literature survey on alternative power technologies including solar power, wind turbine, geothermal power, hydropower, biomass power and fuel cell. A section dedicated to power quality requirements for the grid connection of these technologies is considered with focus on grid code modifications to allow these alternative energy systems to operate in smart manner when they are connected to the utility grid. Furthermore, a section dealing with power converters for alternative energy systems including the different topologies for various power rating is presented.

2.2 Alternative Energy Systems

Energy sources dependent on oil, natural gas and coal have demonstrated their capacities to permit economic development. However, with the fast exhaustion of fossil fuels, the expansion of the world energy demand and concerns over global warming, new energy systems based on renewable and other sustainable energy sources are gaining more interests. It is now a reality that future development in the energy sector is basically founded on the utilisation of renewable and sustainable energy technologies. In this way, moving to sustainable energy sources can empower us to meet the double targets of diminishing greenhouse gas emissions, by that overcoming extreme weather conditions and ensuring reliable and cost-effective energy supply.

2.2.1 Solar Power System

The generation of electricity using solar energy can be achieved in two different ways namely solar thermal and photovoltaic conversions. Solar thermal power consists of converting solar energy into heat to drive a steam turbine hence generate electricity, whereas photovoltaic conversion uses the photoelectric phenomena to convert sunlight into electricity (Maghami et al., 2016).

Solar thermal power systems, also referred to, as concentrated solar power, tracks the sun and directly concentrates the sunlight to produce heat that is transferred to water to produce steam, which is then used to produce power. Solar power systems can be classified in three types which are troughs that concentrate sunlight along the central axes of parabolic collectors, power towers with a field of concentrating mirrors surrounding a central receiver, and dish-engine systems that utilise reflecting dishes to concentrate sunlight on a heat driven engine put at the dish's point of convergence.

2.2.1.1 Trough systems

Trough systems (Figure 2.1) represent about 90 % of the world's capacitor of solar power. This technology utilises long trough arrangements of parabolic reflectors to centre and focus solar radiation on oil-filled glass cylinders put next to the trough's central line. The oil gets heated up to 400^{o}C by absorbing the solar radiation, and moves its heat to water, producing steam that goes through a common turbine generator. The troughs are gathered to generate enormous amount of heat or power.

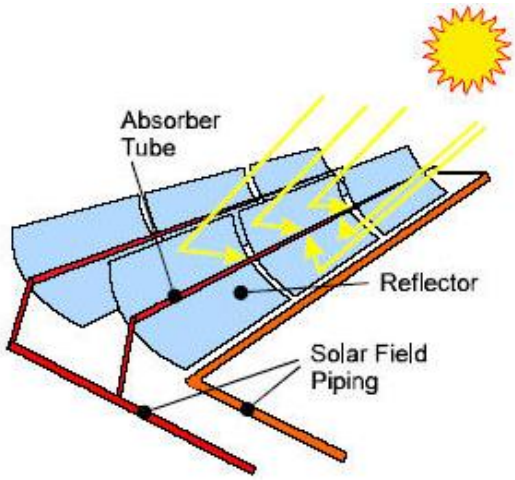

Figure 2.1: Through solar collector. (SolarPACES, 2018)

2.2.1.2 Power-towers

Power towers (Figure 2.2), also referred to as central receivers, consist of a fixed receiver mounted on a tall tower surrounded by large fields of mirrors known as heliostats. Each heliostat tracks the sun independently and concentrates sunlight on the receiver where it warms a liquid (water or air) to an extremely high temperature of around 650°C. The liquid is then left to expand through a turbine associated with an electric generator. It is believed the practical capacity of power towers can go up to 200 MW.

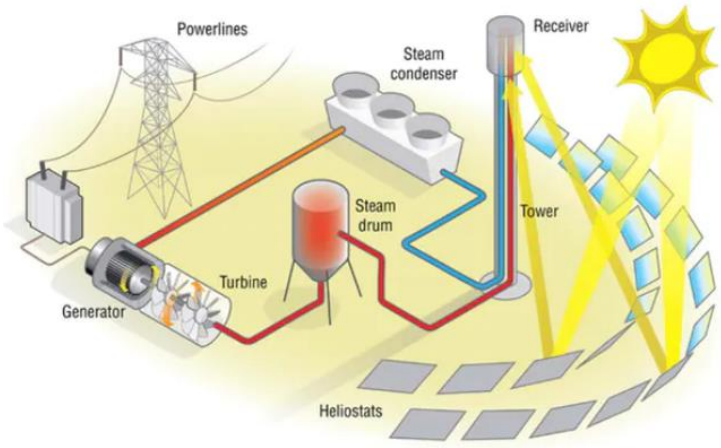

Figure 2. 2: Power tower plant. (Brown, 2019)

2.2.1.3 Dish engine technologies

A typical dish-engine system (Figure 2.3) utilises a dish parabolic reflector in a form of a set of smaller mirrors to centre the solar radiation to go to a collector fixed over the dish at its convergence point. Two pivot tracking systems are utilised to increase the amount of solar energy captured, and regularly a Stirling motor is mounted on the collector. Such configurations are not yet into the market; however, it has been tested for capacities ranging from 5 to 50 kW. Generally, dish-engine systems and power towers have higher concentration ratios of solar radiation compared to troughs, and hence, lower costs for heat to electricity conversion and higher efficiencies can be achieved. Furthermore, all three systems can be associated to operate as a hybrid system.

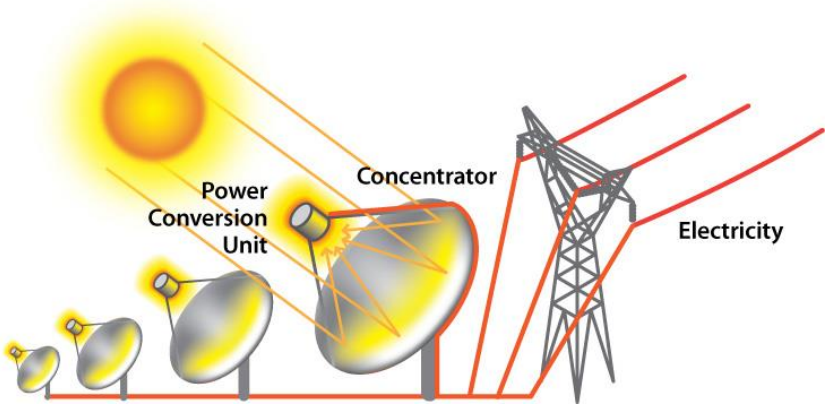

Figure 2.3: Dish-engine system. (Energy.gov, 2019)

2.2.1.4 Photovoltaics

Photovoltaic is the direct conversion of sunlight to electricity. It is considered as the most promising of the renewable electric technologies and attractive option to traditional sources of electricity due to several bases including it:

i. is pollution and noise free, versatile and modular;
ii. does not involve motion of its parts;
iii. has a high reliability and with very low maintenance requirements and
iv. can be incorporated into a variety of building products and can be installed almost anywhere.

A photovoltaic cell (solar cell) is the basic element of a photovoltaic conversion system, it includes layers of semiconductor materials having different electronic properties. However, silicon solar cells are the most utilised.

Depending on applications, photovoltaic systems are built through the series and parallel connection of individual modules to deliver the expected voltage and current. In the same vein, a single module is built from series and parallel connection individual solar cells. These modules can be found for a power rating in the range from few watts to 250 watts.

In addition to the modules, an entire PV system consists of other components known as balance-of-system. As shown in Figure 2.4, this “balance-of-system” consists of a frame to support the modules and properly orient them to the sun, a DC to AC converter, an energy storage device (battery bank), a charge regulator to hinder overcharging of batteries by the PV array and excessive discharge by the electrical load and wiring and safety elements. A typical photovoltaic system can function either tied or non-tied to the utility grid.

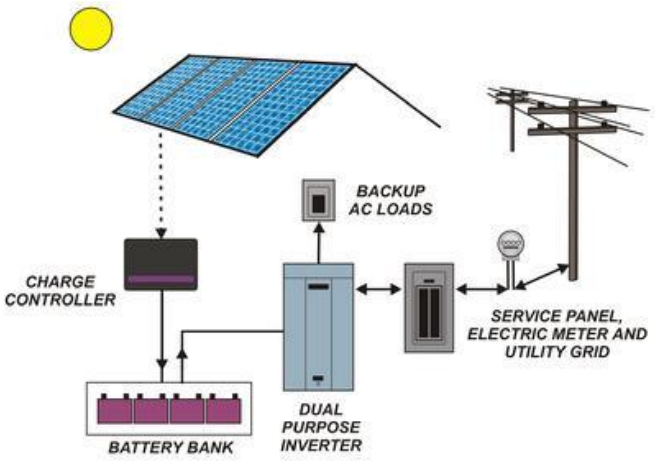

Figure 2.4: Photovoltaic system.

2.2.2 Wind turbine

There are two main types of wind turbines available into the market namely the horizontal axis and vertical axis (Figure 2.5) (Camm et al., 2009). Among the installed wind turbines in the world, 97 % are HAWTs, although no clear indication showed that HAWTs are superior to VAWTs (Drewry & Georgiou, 2007).

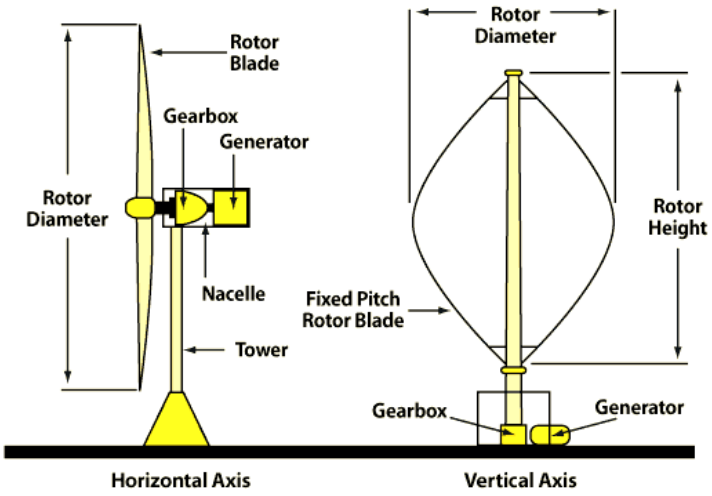

Figure 2.5: Horizontal and Vertical Axis wind turbines.

2.2.2.1 Horizontal-Axis Wind Turbines (HAWTs)

Several configurations of HAWTs can be found based on orientation of the rotors (upwind or downwind), their flexibility (rigid or teetered) and the number of blades (two or three). An upwind HAWT rotates upwind of the tower and yaw mechanism is required to change the position of the rotor in case the wind direction changes. On the other hand, in a downwind HAWT, the wind flowing toward a rotor is obstructed by the turbine

tower over part of the rotor area. It aligns itself with the prevailing wind passively, eliminating the need for yaw drive components.

In general, a rigid hub turbine generally has two or three blades coupled to the hub. A teetered rotor, however, comprises two blades attached to the hub, which forms a pivot with the main shaft of the turbine. At the point when the wind speed over the main shaft is higher than that beneath the main shaft, the rotor moves slightly downwind above the top half of the rotational cycle to decrease the loads on the blades. Two-blade rotors commonly utilise teetering pivots, and three-blade rotors are mounted on rigid hubs.

2.2.2.2 Vertical-Axis Wind Turbines (VAWTs)

In a vertical-axis wind turbine (VAWT), the axis of rotation is perpendicular to the ground and component including the generator and gearbox are closer to the ground. Furthermore, the turbine is independent upon its position relative to the direction of wind. The rotates about an axis perpendicular to the wind. The major disadvantage of VAWTs is their short lifetime.

2.2.3 Geothermal Power

Geothermal energy represents energy in form of heat that originates within the earth. The temperature at the centre of our planet is around 4,200°C, and heat flows outward to the cooler surface, where it can be manifested as volcanoes, geysers, and hot springs, or be used to heat buildings, generate electricity, or perform other useful functions.

Generally, geothermal sources are classified into hydrothermal reservoirs, geo-pressurised zones, hot dry rock, normal geothermal gradient, and magma (Zhu et al., 2015), however, hydrothermal reservoirs (Figure 2.6) are the main geothermal sources that have been utilised for commercial energy production. They originate from groundwater seeping down along faults in the Earth’s crust and become warmed through contact with hot rocks underneath. Sometimes this boiling water gathers in an interconnected system of fractures and becomes a hydrothermal reservoir. The water might stay underground or might rise by convection through cracks to the surface, producing geysers and hot springs.

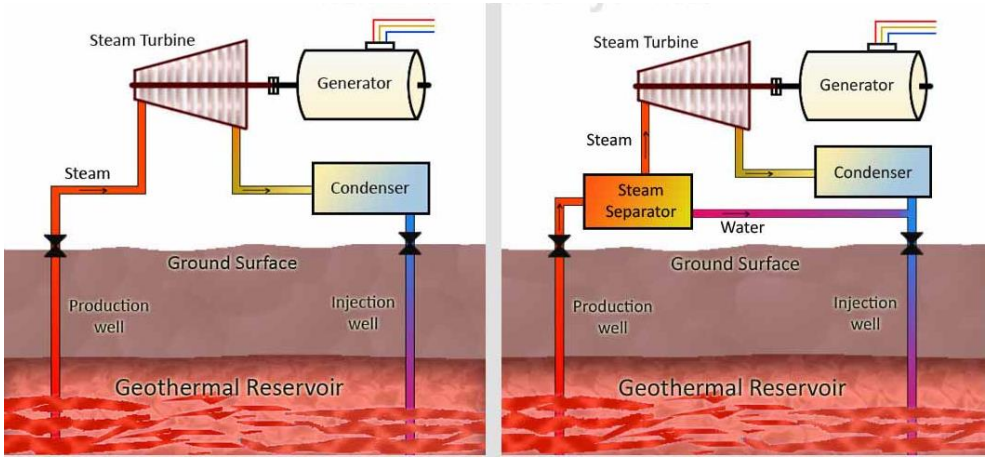

Figure 2.6: Layout of geothermal reservoir power plant. (Daware, 2015)

To generate electric power through geothermal process, deep holes are drilled to reach the geothermal reservoir, and while the heated water in high-pressure goes to the surface of the earth, some become steam due to the decrease of pressure. The amount of dry steam produced depends of the heat received from the original source. The technology to generate power from dry steam is similar to power plants that utilise fossil fuels to generate steam, however, the pressure and temperature of the geothermal vapour are much lower. Since geothermal vapour temperature is lower than fossil-fuel steam, the conversion efficiency of thermal energy to electricity is below than that of a fossil fuel plant.

2.2.4 Hydropower

Hydropower (Figure 2.7) is to the process of generating electricity from the water flowing into the river or the oceans. The goal of hydropower generation is to produce clean energy (Basar et al., 2011). A typical hydropower plant consists essentially of a generator, a turbine, a penstock and a wicket gate. Generally, two types of turbines are used: a pulse turbine, for example a Pelton Wheel turbine, and a reaction turbine such as the Francis and Kaplan turbine. The generator and turbine are usually connected directly by a vertical shaft.

The existence of a high head produces a fast flow of water through the penstock and reaches the turbine (Naghizadeh et al., 2012). The flow of water in the turbine is controlled by the wicket gate which may be adjusted with the opening of the pivot around the periphery of the turbine to control the amount of water flowing into the turbine. Servo actuators controlled by the regulator help to adjust these gates. Water drives the turbogenerator and the rotating generator produces electricity. At the initial stage, water stored with a clear hydraulic head has potential energy, while crossing the

penstock, it gradually loses potential energy and gains kinetic energy before reaching the turbine.

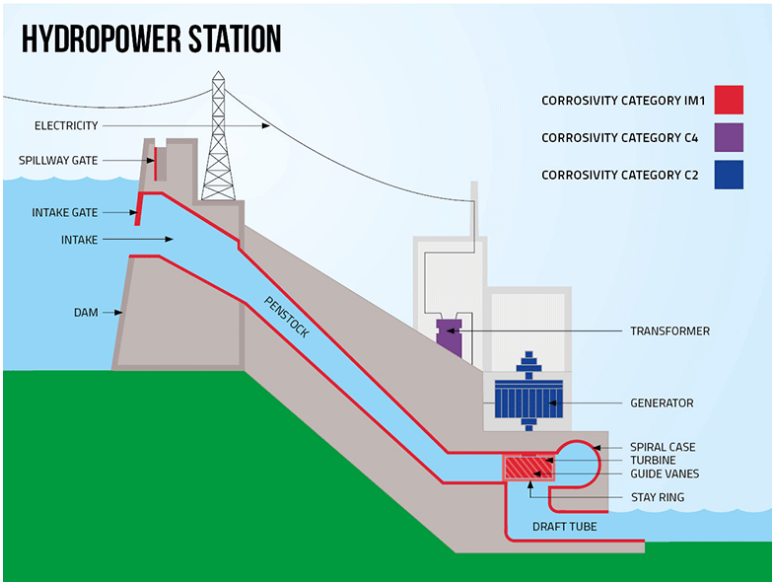

Figure 2. 7: Hydropower plant. (Teknos, 2018)

2.2.5 Biomass Energy

Biomass power consists of using biomass to produce biogas; the produced biogas is then used as fuel into a biomass generator (Das & Das, 2009). Biomass includes both energy crops and wastes, such as forest residues (cotton stalks, paddy straw, rice bales, sawdust) and a range of other agricultural and industrial products. Hence, the sources of biogas and the methods used for their production are not exhaustive. However, electricity production is by using direct combustion, gasification, pyrolysis, and digester gas.

Biogas consists primarily of methane (CH_4) and carbon dioxide. It is a by-product from anaerobic bacteria breaking down organic matter. Huge amounts of biogas can be obtained from areas such as livestock waste lagoons, sewage treatment plants, and landfills. Since biogas is primarily methane, it is like natural gas and can be used to generate electricity using stationary engine generators. The objectives of capturing biogas are often to keep these greenhouse gases from being released into the atmosphere, to control the odour, and to produce fertiliser, while energy production is often secondary.

2.2.6 Fuel cell

A fuel cell converts a fuel's chemical energy directly into electricity without involving any mechanical motion. This generation of electricity is accompanied by the release of water and heat. Similar to batteries, the cell generates a DC electric output and like heat engines, the fuel delivery system ensures that fuel cells are rapidly refuelled to operate for long periods. Cells need to be stacked to form a fuel cell stack, hence produce a useful output. Besides the stack, other important ancillary parts are required to allow proper operation of the stack.

2.2.6.1 Fuel cell stack

As it is the case for a typical battery, in a fuel cell, energy from chemical reaction is converted directly into electric power. This chemical energy is not held in the electrolyte, but continuously provided from a separate source of hydrogen. Generally, a fuel cell transforms hydrogen in the form of gas and oxygen into electricity, water and some heat through the stages below:

- The anode consists of a material that readily strips electrons from the hydrogen molecules and frees them to move through a load in the direction of the cathode in the form of direct electric current, and the protons (hydrogen ions) move through the electrolyte in the direction of the cathode.
- At the cathode side, oxygen is ionised by electrons that are incoming and combined with protons to form water

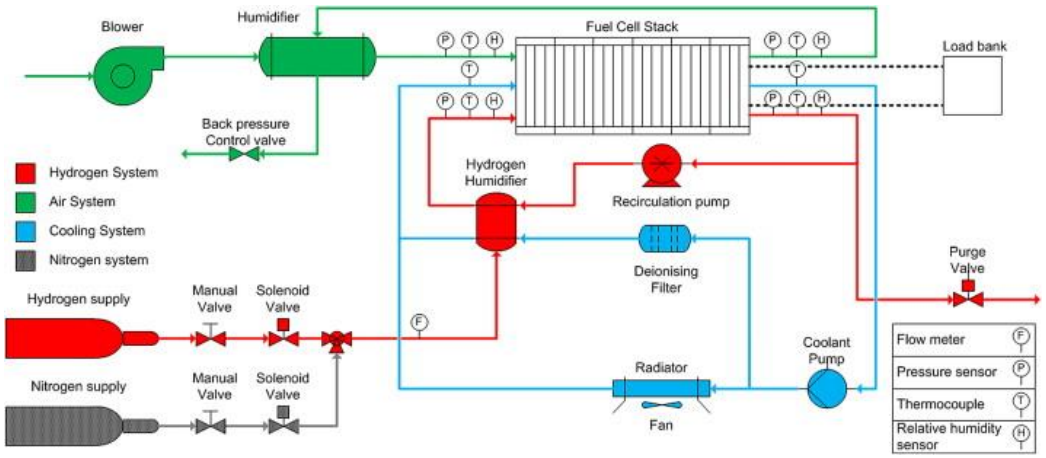

Figure 2. 8: Layout of a fuel cell unit including the ancillary. (Wu et al., 2014)

A typical voltage output from one cell is around 0.4 to 0.8 V, hence, many cells must be associated in series to obtain a practical voltage. A bipolar plate serves as the connecting cell function while also distributing reactants and producing gases to increase power output.

The fuel cell stack voltage changes with load condition; when the current is low, the cathode's activation overvoltage slows the reaction, and this reduces the voltage, whereas at high currents, there is a limitation on how rapidly the different fluids can enter and leave the cell, and this restrains the current that can be generated. In the majority of operating range, however, it is the ohmic polarisation, caused by various electrical resistances that leads cell behaviour. Due to these losses, fuel cells produce important heat, and this limits the maximum power available as it is very difficult to provide enough cooling. This self-heating, however, helps to heat the system from cold start.

Even when operating on pure hydrogen, a complete fuel cell system is complex as a fuel cell stack cannot generate power without functioning air, fuel, thermal, and electrical systems. The basic elements of a typical fuel cell are shown in Figure 2.8.

2.2.6.2 Air subsystem

The reaction kinetics on the cathode side are moderate since oxygen's separation and subsequent multi-electron ionisation is a complex sequence of events than at the anode. To overcome this activation barrier, it is important to increase the oxygen pressure. This is achieved by compressing the approaching air up to 2 to 3 atmospheres. Alternatively, the fuel cell stack can be worked at ambient pressure. Even though this simplifies the system significantly and improves overall efficiency, it reduces stack power and increase thermal management challenges.

2.2.6.3 Fuel subsystem

Hydrogen is not presently distributed like conventional fuels. Even though many ways exist to store it, none of those ways is cost-effective because of hydrogen low energy density. Very high pressures are required to store viable amounts as gas, and such tanks are heavy and costly. In liquid form, hydrogen is more energy-dense and might be favoured for transportation, yet it requires storage at temperatures around –253°C and this makes handling and venting issues. Furthermore, hydrogen is generally made by steam changing natural gas, and liquefying needs intensive energy that 50 % of the energy contained in the natural gas is lost when it is changed over into liquid hydrogen. A third way is to assimilate hydrogen into composites that "trap" it securely and at low pressure. Unfortunately, metal hydrides are highly expensive and heavy.

Since it is so hard to economically store and transport hydrogen, there is interest in producing hydrogen on request by passing conventional fuels into catalysis processes; such a methodology is referred to as fuel processing. The issue for fuel cell applications is to obtain hydrogen-rich from available, relatively impure, fossil fuels without polluting the different catalysts used in the fuel processor and fuel cell stack.

Based on the type of fuel cell stack and its operating temperature, there can be four consecutive stages engaged in fuel processing:

i. treatment of fuel with a chemical before use (for instance vaporisation and desulphurisation);
ii. reforming of fuel (transformation into hydrogen-rich feed, also referred to either as syngas or synthesis gas);
iii. water-gas move for transforming nearly all the carbon monoxide by-product into carbonic acid; and
iv. preferential oxidation for conclusive expulsion of the rest of carbon monoxide.

The majority of the separation between different fuel processor procedures happens in stage two. One transforming technique utilises steam from the reaction in the fuel cell stack to obtain hydrogen from the reform of fuel. This procedure steam reforming absorbs energy, based on the type of fuel high temperatures might be required, and as the catalysts that allow the reaction are selective, various fuels might not be utilised in the identical catalytic reactor. However, a main benefit is that the resulting hydrogen is rich. This operation is advantageous for unmoving applications, whereby an individual fuel and steady-state mode are common.

As opposed to steam reforming, in the partial oxidation (POX) air is utilised rather than steam and burns the fuel in limited quantities of air with the goal of producing relatively combusted products, which include hydrogen. Partial oxidation has the potential to respond faster than a steam reformer and produces heat. Furthermore, as the complete fuels burn, partial oxidation does not require a catalyst, even though improved designs sometimes utilise flames at low temperatures to assist in relaxing materials demands and improving emissions and efficiency. However, the concentration of hydrogen is significantly lower (around 40%) as none originates from steam while there is around 80% nitrogen diluent in the air.

Autothermal reforming (ATR) integrates steam reforming and partial oxidation. Because the heat liberated from POX is absorbed by steam reforming, the reactor might be adiabatic (or autothermal).

2.2.6.4 Thermal subsystem

Cooling relies on the fuel cell operating temperature and on the fuel cell's external environment. For low temperature fuel cells, cooling imposes an important energy debit as pumps must force coolant out to a heat exchanger, from which heat must be dismissed to the air. Operating the fuel cell at maximum efficiency reduces heat loads, but also decreases power output, driving an increase in fuel cell stack size and cost. However, for high-temperature fuel cells, waste heat can be used by expanding the off gases through a turbine to produce extra power; such cogeneration efficiencies can reach 80%. In certain applications, even the remaining 20 percent can offer some benefit by for instance warming a building. Heat rejection is just a single aspect of thermal management. Thermal integration is fundamental for improving fuel cell system efficiency, cost, volume and weight.

Depending on the fuel cell, other critical tasks are water recovery from fuel cell stack to fuel processor and freeze-thaw management.

2.2.6.5 Electrical subsystem

Electrical management or power conditioning of fuel cell output is often essential as the fuel cell voltage is always DC and may not be at an appropriate level. For stationary applications, an inverter is expected to change over the DC to AC, while in situations where DC voltage is acceptable, a DC to DC converter may be accepted to conform to the load voltage. In electric vehicles, for instance, a mix of DC to DC conversion followed by inversion might be important to interface the fuel cell stack to an AC motor.

2.2.6.6 Types of fuel cell

Five types of fuel cell can be distinguished depending on the electrolyte used, which can be either liquid (alkaline or acidic), polymer film, molten salt, or ceramic. As shown in Table 2.1, each type has advantages and disadvantages that make it appropriate for various applications.

Table 2. 1: Fuel cell technologies and features. (Albarbar & Alrweq, 2018)

Type	Working Temperature (ºC)	Advantages	Disadvantages	Applications
Alkaline	25 to 100	• developed technology • No valuable metals	• Use pure hydrogen	• Space
Proton Exchange Membrane	0 to 85	• Function at ambient temperature • High-power density	• Need for humidification • Sensitive to CO poisoning	• Distributed power • Transportation
Phosphoric Acid	170 to 220	• Mature • Reformate intolerant	• Cannot start from ambient temperature • Bulky	• Heavy-duty transportation
Molten Carbonate	650	• Some fuel flexibility • High-grade waste heat	• Fragile electrolyte matrix • Electrode sintering	• Utilities • Distributed power
Solid Oxide	800 to 1000	• Maximum fuel flexibility • Highest cogeneration efficiency	• Exotic materials • Sealing and cracking issues	• Utilities • Distributed power

Alkaline Fuel Cell (AFC)

Alkaline fuel cells (AFC) (Figure 2.9) are amongst the first practical fuel cell, especially for space applications for on-board electricity and potable water for the crew. The AFC has some attractive characteristics, such as moderately high efficiency because of low internal resistance and high electrochemical activity, quick start-ups, few precious metal requirements and low corrosion. However, the AFC's corrosive environment requires that it utilises some exotic materials, and the alkaline (potassium hydroxide solution) concentration must be firmly controlled as it has poor tolerance to deviations. Fundamentally, the alkali is promptly killed by acidic gases, so both the approaching fuel and air need carbon dioxide clean-up. This restraints AFC application to those in which pure hydrogen is utilised as the fuel, since a fuel processor produces substantial amounts of carbon dioxide. The small amount of carbon dioxide in air (˜0.03%) can be taken care of using an alkaline trap upstream of the fuel cell and, subsequently, is not as much of an issue

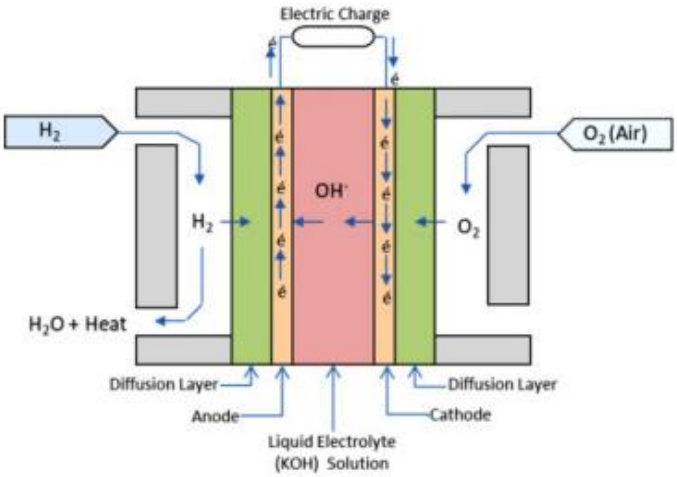

Figure 2. 9: Alkaline Fuel Cell. (Abderezzak, 2018)

.

Phosphoric Acid Fuel Cell (PAFC)

Although Phosphoric Acid Fuel Cell (PAFC) (Figure 2.10) accepts carbon dioxide, the requirement for water to be available to support proton movement augments the system complexity. It is presently a developed technology, designed broadly for unmoving power applications, and units with power of around 200 kW are in the market and have shown 40,000 hours of operation. Unlike the AFC, the PAFC provide reliable operation with system efficiency of 40 % to 50 % even when functioning on low quality fuels. This fuel flexibility is empowered by higher operating temperature of about 200°C against 100°C for the AFC as this increases electro-catalyst resilience to impurities. However, the PAFC still has a large weight and does not have a fast start-up since it requires heating up to 100°C prior to deliver a current. The PAFC is, however, appropriate for fixed power generation.

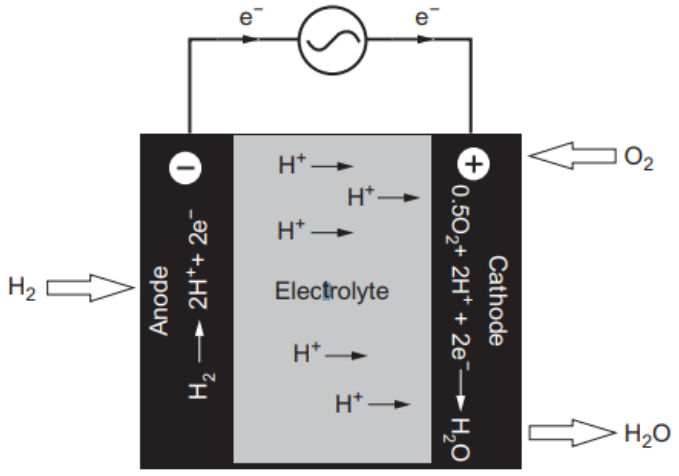

Figure 2. 10: Schematic of PAFC. (Barbir et al., 2016)

Molten carbonate Fuel Cell (MCFC)

Molten Carbonate Fuel Cell (MCFC) (Figure 2.11) functions at 650°C and utilises an electrolyte produced using lithium carbonate and molten potassium salts. Operation at high-temperature is perfect for unmoving applications since the heat by-product can be used for combined heat and power systems; it also permits fossil fuels to be reformed directly, and this decreases the size and complexity of the system. However, the MCFC experiences cathode corrosion and sealing issues initiated by the high-temperature its molten electrolyte. Similarly, thermal cycling is constrained since once the electrolyte becomes solid; it is likely to create cracks at the time of reheating. Further existing issues are anode sintering and elution of the oxidised nickel cathode into the electrolyte.

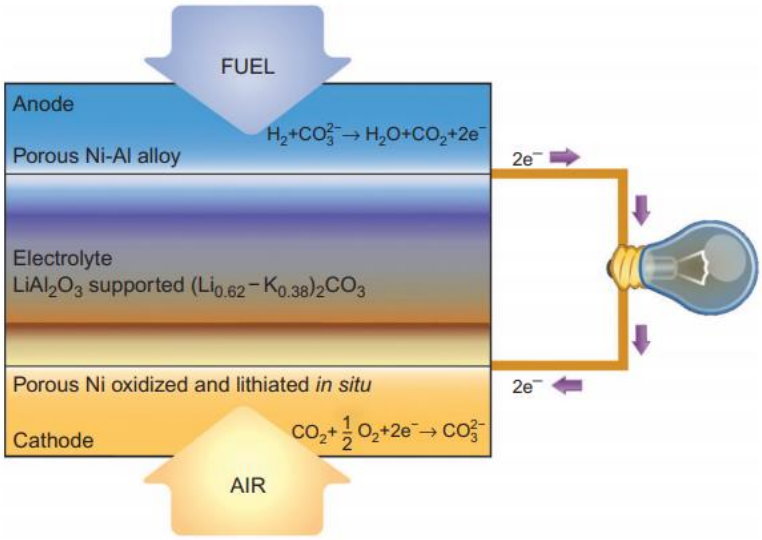

Figure 2. 11: Schematic of MCFC. (Barbir et al., 2016)

Solid Oxide Fuel Cell (SOFC)

In Solid Oxide Fuel Cell (SOFC) (Figure 2.12), the electrolyte is a solid oxide ceramic. So as to prepare strong solid oxide ions, the cell must operate at temperatures as high as 1,000°C. This guarantees fast diffusion of gases into the permeable electrodes and subsequent electrode reaction and suppresses the need for external reforming. Therefore, besides hydrogen and carbon monoxide fuels, the solid oxide fuel cell can also reform methane directly. Subsequently, this fuel cell has attractive specific power, and cogeneration efficiencies greater than 80 % might be feasible. Furthermore, the SOFC can be air-cooled, simplifying the cooling system, although the need to preheat air requires extra heat exchangers.

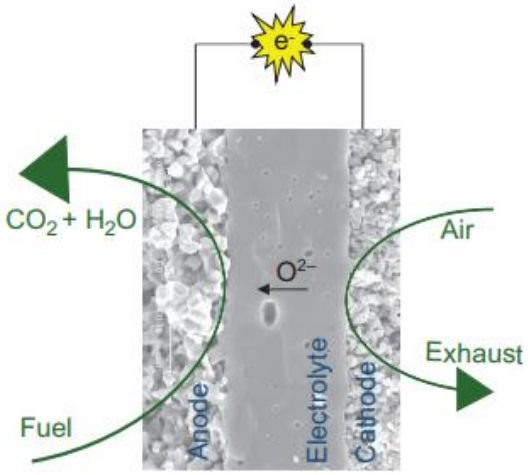

Figure 2. 12: Schematic of SOFC. (Barbir et al., 2016)

Elegant based on its conception, the SOFC, however, has essentially costly materials, for instance an electrolyte fabricated from zirconium dioxide stabilised with yttrium oxide, a strontium-doped lanthanum manganite cathode, and a nickel-doped stabilised zirconia anode. Furthermore, no cheap techniques for the fabrication of the unit exist.

Proton exchange Membrane Fuel Cell (PEMFC)

Proton exchange membrane fuel cells (PEMFC) (Figure 2.13) are the most promising fuel cell for transportation purposes. Unlike the PAFC, it has much greater power density; a typical PEMFC stacks can generate about 1 kW per litre. Potentially, it is more affordable and, since it utilises a thin solid polymer electrolyte sheet, it has few corrosions and sealing problems, furthermore, no issues related to electrolyte dilution because of water by-product. Because it can function at ambient temperature, the PEMFC can start up fast. However, it has two main drawbacks which are:

i. low efficiency and
ii. more strict purity demands.

The low efficiency results from the complication during the recovery of heat by-products, while the catalysed electrode's resilience to impurities decreases considerably because of the temperature drop. For instance, while a PAFC functioning at 200°C can accept 1 % of carbon monoxide, the PEMFC, functioning at 80°C can only accept ˜0.01 %.

The membrane of a PEMFC demands constant humidification to keep a pressure of about 0.5 bars, as failure to achieve that can result to a huge rise in resistance. Operating at temperatures higher than 100°C would significantly reduce the system

design, yet available membranes are not able to last long when operating at higher temperatures and require further improvement. This type of fuel cell can operate using fuels others than hydrogen. For instance, in the direct methanol fuel cell (DMFC), a dilute methanol solution of 3 % is supplied into the anode, and a multistep procedure induces the liberation of protons and electrons while water and carbon dioxide are released. Since fuel processor is not needed, the unit is conceptually very attractive. Nevertheless, the multistep procedure is not faster than the simpler hydrogen reaction, and this makes the direct methanol fuel cell stack to deliver less power and to require more catalyst.

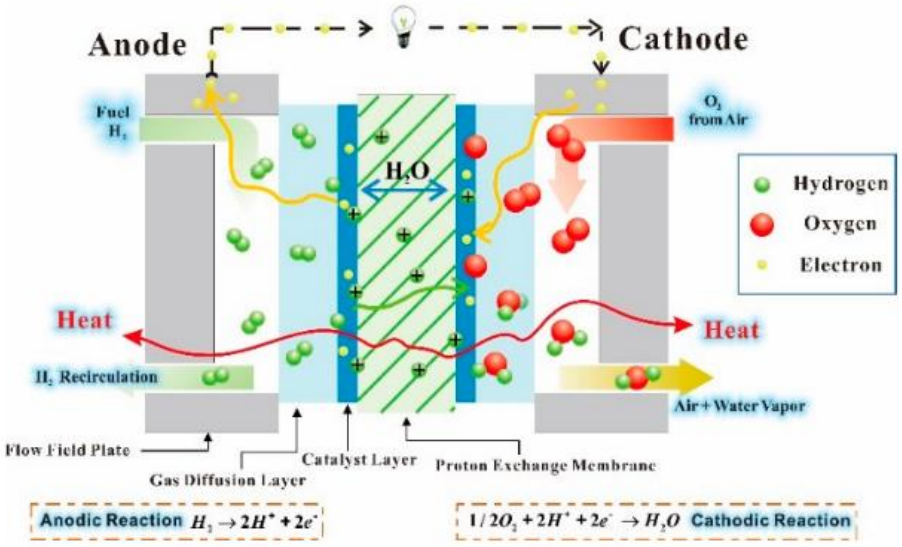

Figure 2. 13: Layout of proton Exchange Membrane Fuel cell. (Yuan et al., 2019)

2.3 Power Quality Requirement for Grid-Connected Alternative Energy Systems

Generally, the design, control and operation of a grid-connected alternative energy system depend on the grid connection requirement. These requirements are referred to as grid codes and need to be complied with during the commissioning stage. The most basic of these requirements that have been the centre of interest is the power quality in the rated operating conditions as shown in Figure 2.14. Most grid codes require a Total Harmonics Distortion (THD) level of less than 5%, additionally, singular harmonics of frequencies up until 2 kHz are the most involved (Blaabjerg et al., 2006), as depicted in Figure 2.15. Being the centre of the power transformation, the controllability of the power converters must be kept up, to obtain significant efficiency.

In accordance to the present grid codes, the grid-connected alternative energy systems are obliged to stop supplying nearby loads in response to grid disturbances (voltage sags through islanding detection). It is requested in the IEEE standard 929-2000 that

alternative energy systems should be turned off within 120 cycles in case the grid voltage is within 0.5 to 0.88 p.u. Generally, those grid codes are set to guarantee the protection of the network maintenance personnel, to ensure the security of the equipment that is connected to the grid, and maintain the safety of the public, based on low penetration level of these alternative energy systems (Blaabjerg et al., 2006). These requirements are different from disengaging traditional power plants or enormous wind turbines, where the impact from a low-level penetration of alternative energy systems on the grid is not important. However, for a large-scale entry of grid-connected alternative energy systems in the distributed grid, the disengagement in reaction to the grid disturbances may lead to severe consequences including (Ben Hamad et al., 2019) :

i. voltage flicker;
ii. power outage and
iii. system instability.

These disturbances refer to two aspects such as the intermittency of renewable sources and the highly aggregated alternative energy systems that participate to a large quantity of power as a sudden shut down of such a power generation can defy the stability (Aguilar, M, D et al., 2016; Alatrash et al., 2012).

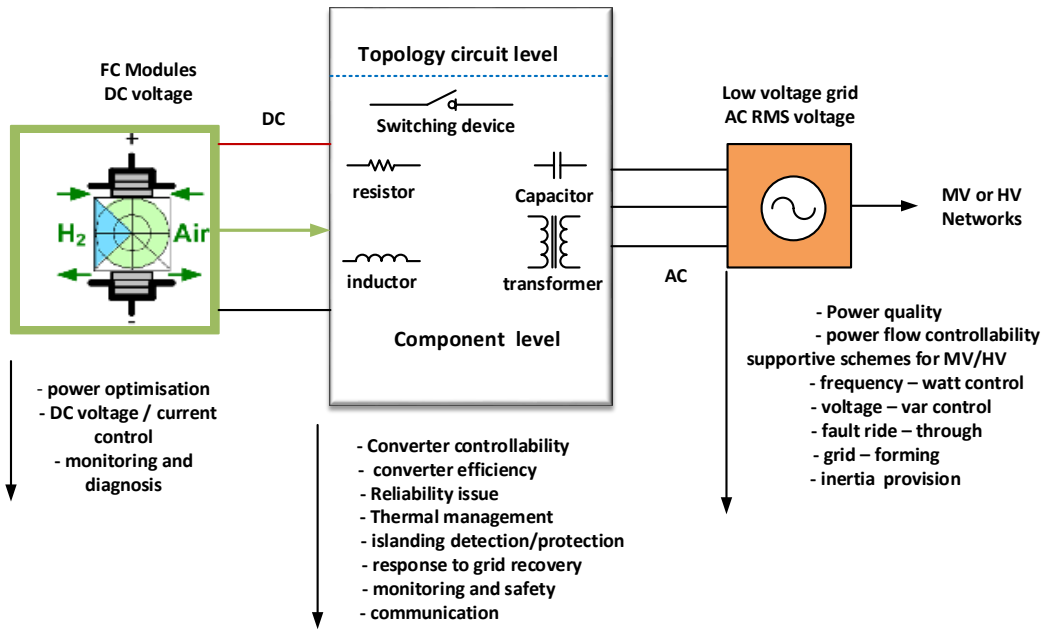

Figure 2. 14: Grid-connected fuel cell conversion systems. (Ben Hamad et al., 2019)

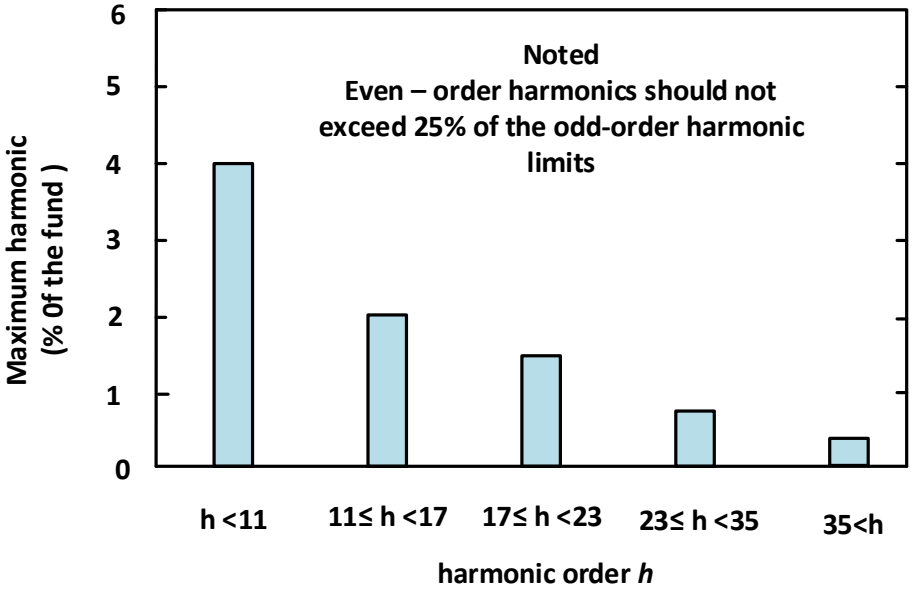

Figure 2. 15: Power quality requirements for grid-tied alternative energy systems based on IEEE 1547 and IEC 61727 standards. (Blaabjerg et al., 2006)

Considering these issues, the current active grid requirements necessitate revision based on a set of standardised alternative energy systems characteristics and advanced demands for an adequate grid integration. Several researches have demonstrated the potential of alternative energy systems to have an active role in the regulation of distributed grids similar as conventional power plants perform nowadays. Furthermore, alternative energy units can also be utilised to contribute to auxiliary services to reduce problems associated with power converters (Yang et al., 2015).

On top of the elementary energy conversion, a typical alternative energy system operating in the context of a smart energy system should have the following characteristics:

i. Fault-ride-through ability;
ii. Grid-support ability;
iii. Flexible power controllability and
iv. Intelligent delivery of auxiliary services.

To allow those characteristics, the present grid standards or requirements for alternative energy systems need to be re-examined and improved consequently, and similarly, the control of the power converters needs to be developed based on the considerations below (Yang et al., 2015) :

i. Flexible power controllability,
ii. Control of reactive power,

iii. Frequency regulation,
iv. Harmonic compensation,
v. Dynamic grid support,
vi. Improved reliability and efficiency

2.3.1 Flexible power controllability of alternative energy systems

As a result of the reverse power flow toward upstream voltage levels (Braun et al., 2011) and the power difference between the alternative energy system and load requirements, a voltage increase on distributed feeders can occur as one of the main problems caused by highly aggregated presence of alternative energy systems. A possible solution is to directly reduce the active power when the grid voltage gets its limit (Braun et al., 2011). Overloading has been recognised as another antagonistic effect of large-scale adoption of alternative energy systems when the peak power production period occurs (Yang, Blaabjerg, et al., 2016).

Therefore, the demand of flexible active power control for these energy systems is enabled, where the alternative energy systems should be able to function with a power generation which is controllable, based on a flexible power command. Therefore, a remote active power control function for low-voltage alternative energy systems is added and will be additionally reinforced in the future grid codes. Figure 2.16 presents the current active power control limitations for grid-connected alternative energy systems. Additionally, the flexible power reduction control can also be looked at as an advanced derating operation for inverters, which may enhance system reliability and hence minimise cost of energy during the lifetime (Yang, Sangwongwanich, et al., 2016). The active power command can also be developed based on the grid voltage level to hinder tripping caused by overcurrent. Some European countries have been introducing the absolute power control in wind turbine systems and alternative energy systems with the power rating above 11 kW. The use of such a function in alternative energy systems demonstrates a lot of potential to improve the whole grid performance, especially in extending their lifetime.

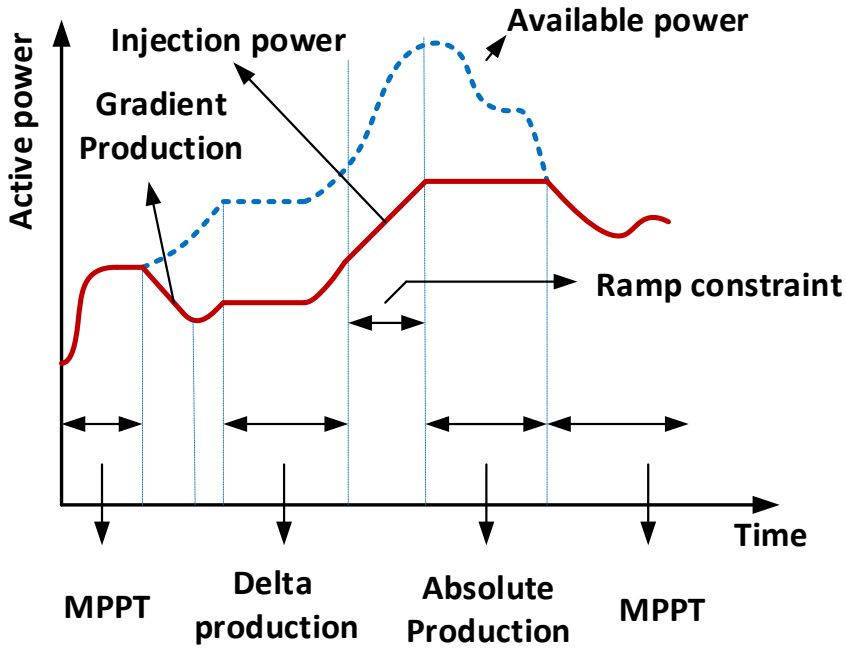

Figure 2. 16: Various active power regulation functions for grid-tied alternative energy systems. (Yang, Blaabjerg, et al., 2016)

2.3.2 Reactive power control

In the event of more inductive feeders, the grid-connected alternative energy systems can modify the exchange of reactive power with the grid to improve the voltage profile of the feeder. It is practical, as these alternative energy systems are usually planned with good margins and function under partial loading conditions. There are many possibilities for the control of reactive power, especially during night times. However, it should be adopted that the reactive power capability of the inverter is constrained by its pre-designed apparent power given as:

$$|Q_{ins}| \leq \sqrt{S_n^2 - P_{ins}^2} \tag{2.1}$$

where $\boldsymbol{Q_{ins}}$ is the instantaneous reactive power to be exchanged, $\boldsymbol{P_{ins}}$ is the instantaneous active power injected to the grid by the inverter, and $\boldsymbol{S_n}$ is the rated apparent power of the inverter.

Based on Equation 2.1, a power derating operation of the alternative energy systems allows more reactive power support.

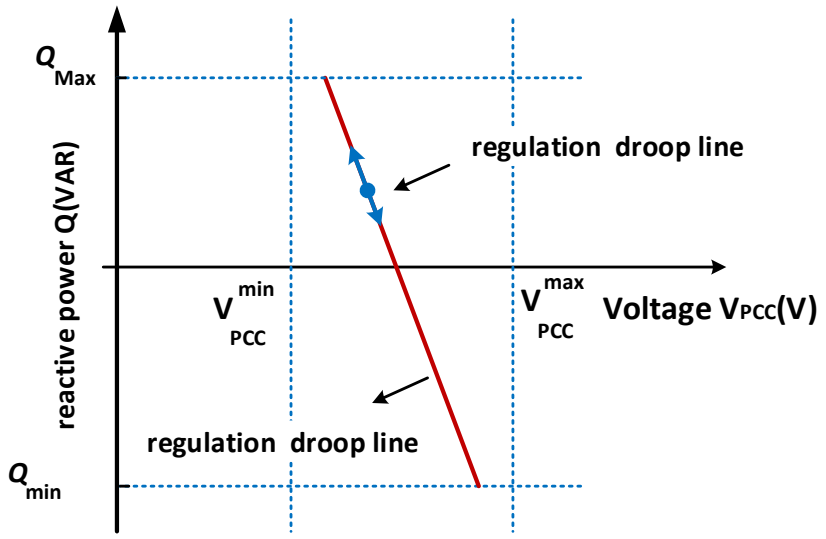

Figure 2. 17: Voltage-var droop control characteristics. (Braun et al., 2011)

Some grid codes for an extremely high-level of penetration of alternative energy systems exist to trigger reactive power control for the grid support (Tafti et al., 2015), especially for the medium or high voltage distributed networks. Considering a country like Germany, all alternative energy units coupled to low or medium voltage are required to support the grid by providing reactive power (Braun et al., 2011), while simultaneously, meeting the lowest power factor. Presently, comparable codes are being improved in case of low-voltage alternative energy systems to enhance more capacity, as they can contribute in the management of reactive power and voltage regulation (Yang, Blaabjerg, et al., 2016).

For low-power units, the voltage support is performed at the substation level or incorporated in developed inverters. In case the exchange of reactive power between the inverter and the grid is regulated, the voltage profile can be ameliorated. Three control strategies can be distinguished namely:

i. independent Q control, in which the reactive power control does not depend on the active power regulation at the Point of Common Coupling;
ii. power factor control, where the reactive power is regulated based on the active power to obtain a steady power factor and
iii. voltage control, in which the grid reference voltage at the Point of Common Coupling is regulated by modifying the exchange of reactive power.

Figure 2.17 shows the voltage control function of alternative energy systems, in which the regulation of the voltage is performed via the droop control of reactive power

exchange. Additionally, the distribution of reactive power can be optimised and coordinated to enhance the voltage profile.

2.3.3 Frequency regulation

A high penetration of fluctuating alternative energy sources can negatively impact on the grid stability. Whenever the grid frequency changes, inverters must react to the disturbance by disengaging and stopping active power supply. However, the shutdown of a large-scale penetration of these energy units can represent a danger of important power blackouts and the whole grid stability. Hence, the frequency-watt control is initiated to hinder such instability problems, where it is needed that alternative energy units change automatically the active power generation and assist in the control of network frequency.

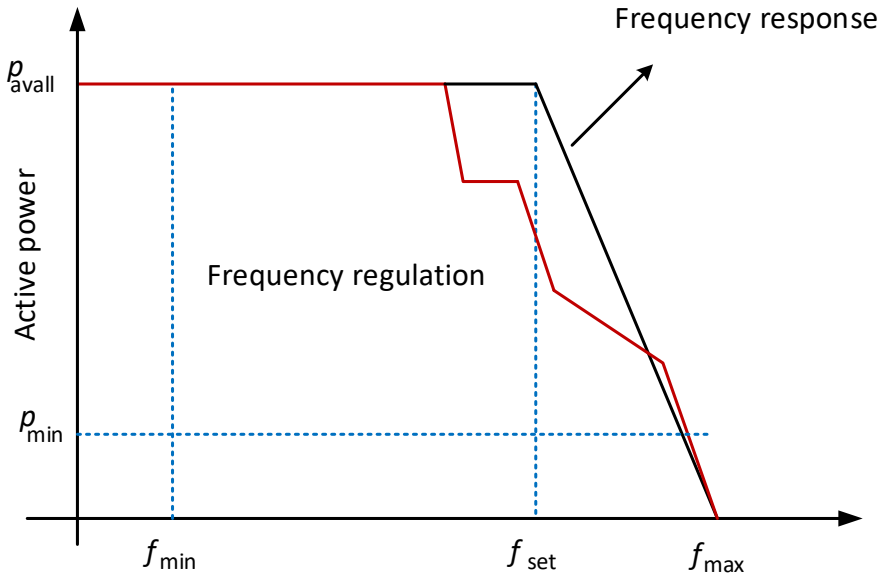

Figure 2. 18: Frequency response versus frequency regulation characteristics. (Wu et al., 2018)

Figure 2.18 display frequency response and frequency control characteristics, demonstrating that the frequency regulation is performed via the frequency and active power droop relation.

2.3.4 Harmonic compensation

Because of the nonlinear loads such as diode rectifier feeding motor drives, etc. the voltage quality at the Point of Common Coupling is deteriorated. To enhance this, the harmonic filter must to be added, resulting to an increase of expenses. At the point when DC to AC converters are connected to the Point of Common Coupling, harmonics

can be corrected by empowering the alternative energy units as power filters. This can be accomplished in a local area, in which the inverter is used to correct the voltage harmonics resulting from the connection of nonlinear loads (Figure 2.19). The principle is to supply the nonlinear currents by the DC to AC converter, and hence, the grid current becomes sinusoidal with low harmonics (Li & He, 2014). Nevertheless, the challenging problem is how to quantify and isolate the harmonic components of the nonlinear loads and then to realise an accurate compensation. However, several developed solutions to enable the power filtering by inverters have been proposed in the literature (Tuyen & Fujita, 2015). Generally, they can function in the current controlled or the voltage-controlled modes.

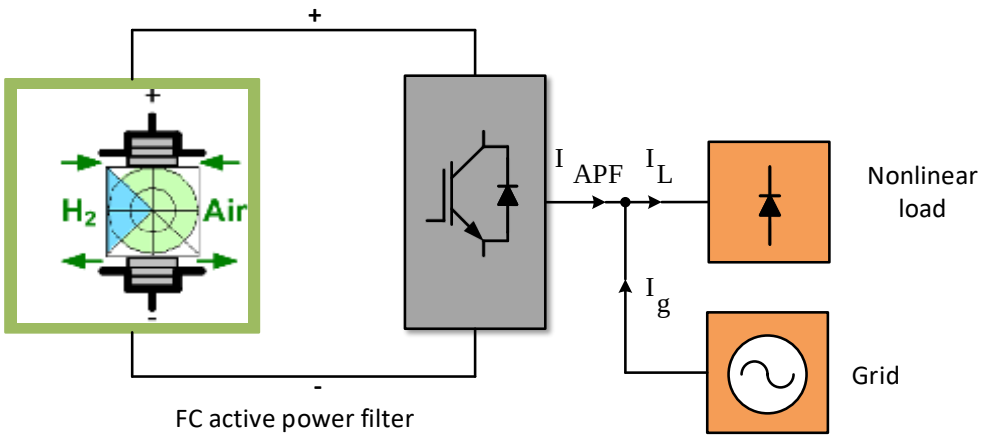

Figure 2. 19: Fuel cell inverter as an active power filter. (Tuyen & Fujita, 2015)

2.3.5 Dynamic grid support of grid-tied alternative energy systems

As shown in Figure 2.20, the dynamic grid-support ability is centred on the fault ride through (FRT) for alternative energy systems and reactive current injection during fault transients (Braun et al., 2011). The objectives of this function are to:

- protect the DC to AC converter from overcurrent power down and
- assist in the grid-voltage restoration.

The fault ride through demands were initially introduced in the generation units of medium and high-power capacities coupled to medium or high-voltage grids. As alternative energy systems level of penetration is increasing, a move of those demands toward smart alternative energy systems has been recognised (Kobayashi, 2012; Aoki, 2009; Braun et al., 2011). Without suitable power transmission, the power unit may be heated up in case the system enters fault ride through mode. Consequently, the excess

power needs to be transmitted in the event of voltage faults even though the use of energy storage is still limited. However, the active power transmission can be accomplished via:

a) changing the Maximum Power Point Tracking control;
b) utilising a DC chopper like in wind turbines and
c) managing the power exchange between alternative units and energy storage devices.

However, the improvement of the fault ride through performance can be accomplished using advanced grid fault monitoring, synchronisation, and control techniques.

Furthermore, as depicted in Figure 2.20, for a fault ride through operation, reactive currents are needed to support the restoration of the grid when a fault occurs. Operating in a smart way, in the case of voltage faults, the alternative energy system must comply with two demands:

(i) stay tied to the grid during the transient like wind turbines and
(ii) deliver reactive currents to support the voltage restoration, especially in the case of a high penetration level.

Nevertheless, the implementation of the fault ride through is opposed to the anti-islanding demands (Yang, Blaabjerg, et al., 2016). This demonstrates that the anti-islanding requirement should be reviewed to include the FRT ability. In addition, in the event that the grid voltage is equal to zero, as shown in Figure 2.20A, the alternative energy units must remain connected.

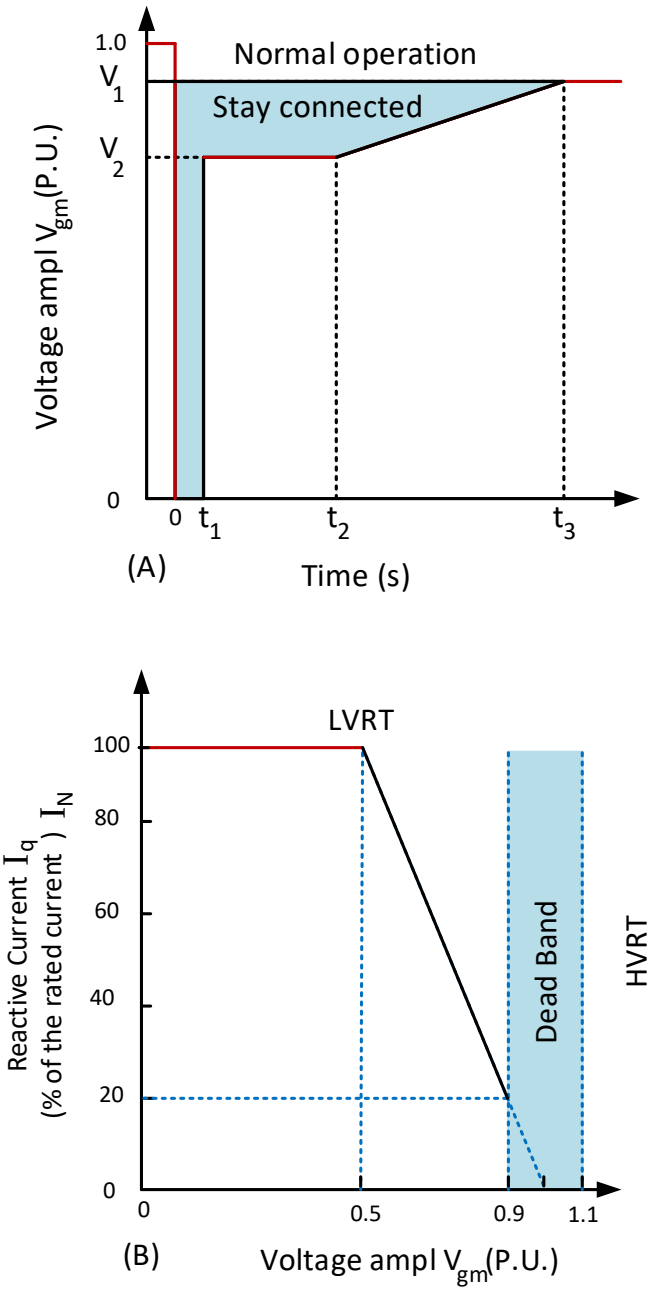

Figure 2. 20: Fault-ride-through requirements for smart alternative energy units. (Yang, Blaabjerg, et al., 2016)

2.3.6 Reliability and efficiency control

There is always a need to further decrease the cost of energy, especially in the case of smart alternative energy systems in order to increase their competence among different renewable sources. The Levelized Cost of Energy (LCOE) is given as (Yang, Sangwongwanich, et al., 2016):

$$LCOE = \frac{C_{int}+C_{cap}+C_{o\&m}}{E_{Yr}} \quad (2.2)$$

where C_{int} is the initial cost of developments, C_{cap} is the capital cost, $C_{o\&m}$ is the costs of operation and maintenance, and E_{Yr} gives the average energy produced per annum in the lifetime cycle of the system.

Based on Equation 2.2, two approaches can be considered to reduce the LCOE which are maintaining a high reliability as it contributes to a low cost for operation and maintenance and improving the efficiency of energy conversion. A high reliability of the system is important for its annual energy production. This can be achieved through topological innovations and advanced control strategies.

By developing innovative power converters with emerging power devices, both the efficiency and reliability can be improved. However, the control for reliability and efficiency is relatively not direct, which requires more essays. Figure 2.21 displays a concept of the control for reliability and efficiency where an observer-based model is used to predict or estimate the reliability and efficiency, and thereafter, the corresponding system control commands will be modified to achieve the targets. The alternative energy systems must operate in diverse modes and switch from one to another smoothly. The reliability and efficiency performances in this case may be affected because of the redistributed loss distribution.

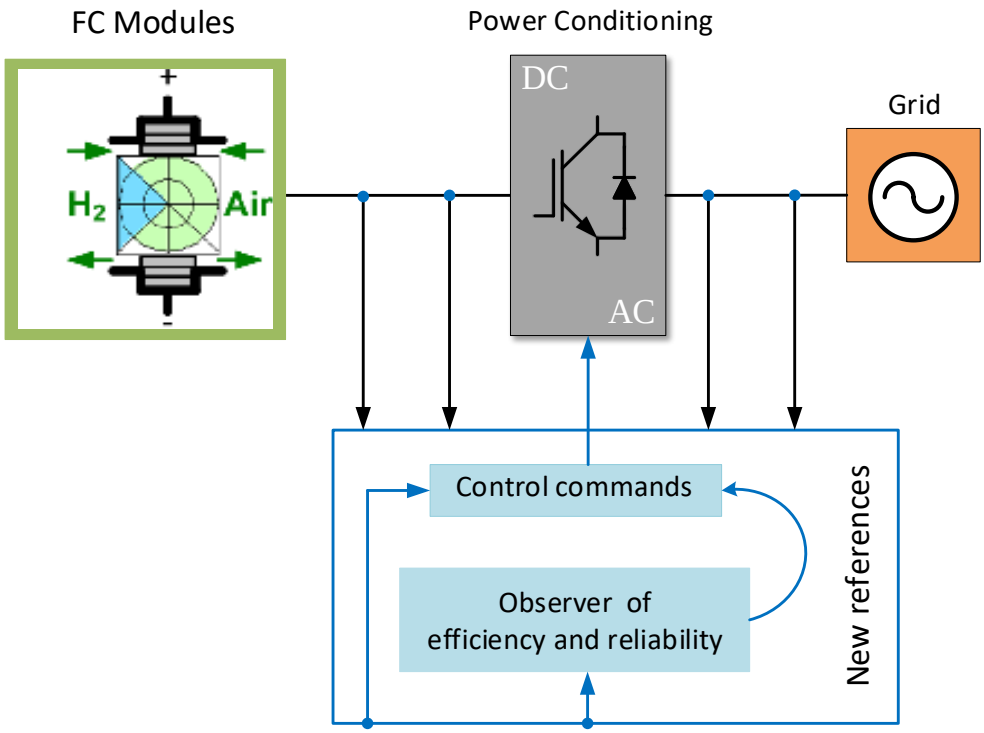

Figure 2. 21: Reliability and efficiency control for smart alternative energy units. (Yang, Sangwongwanich, et al., 2016)

2.4 Power Converter Technologies for Alternative Energy Systems

As the power per alternative energy generating units is relatively low while the resulting cost of energy is still at high levels, there is a need to improve the efficiency. Additionally, as shown in Figure 2.22, the power converters for alternative energy sources are power dependent, where the efficiency gets up to 98.8 %. Three possible power conversion to process the energy generated from alternative energy sources namely, the modular converter, string inverter, and central inverter technologies can be distinguished (Crosson et al., 2011; Rslan et al., 2010; Gaiceanu, 2007). The share of the market of central inverters and string inverters are almost similar, because of the strong demand in electricity generation and the fast decrease in the module price, on the other hand, the module converters are advancing (Rslan et al., 2010).

Central inverters are commonly used in large-scale commercial and utility scale using DC alternative energy systems with the power rating higher than 100 kW, and string inverters are typical for applications with the power below 100 kW. In case of very low-power applications, power optimisers and microinverters are favourite based on efficiency and power optimisation. However, as the amplitude and frequency of the voltage or current of these alternative energy generators is often not compatible with the load, the power electronic converters must be used. Hence, to ensure a secure, reliable, and efficient energy conversion from alternative energy sources, the design, control, and operation of the power electronic converters need to be carefully examined. The efficiency and reliability are two of the most important focus based on the cost of energy.

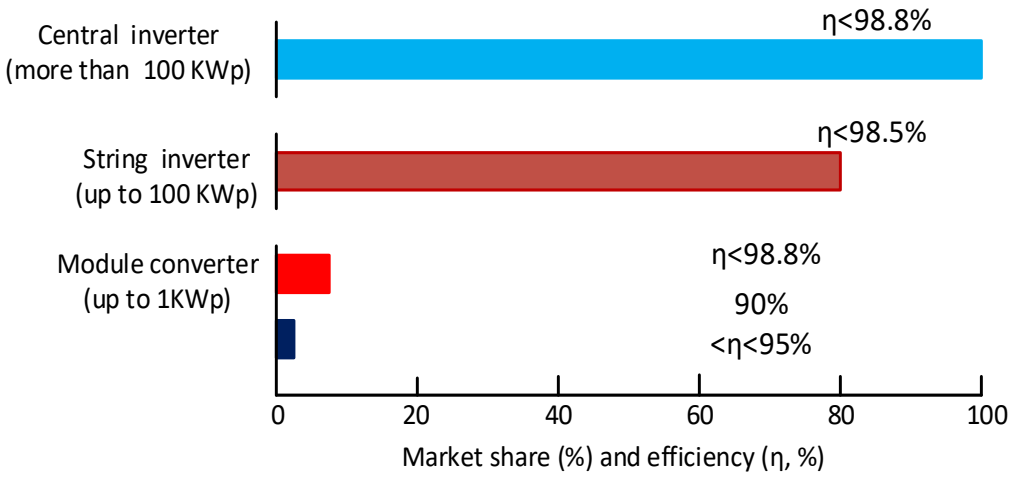

Figure 2. 22: Market share of converters in 2016 and their corresponding efficiencies.
(Chakraborty et al., 2019; Yang & Blaabjerg, 2015)

2.4.1 Modular converters for alternative energy systems

Two sorts of power converters functioning at the modular level exist namely the power optimiser and the microinverter. The first type is meant to optimise the energy collected from a single alternative energy module (photovoltaic and fuel cell), and it is generally a DC to DC converter. The load connected to it can be either a DC load, or an inverter tied to an off-grid AC load or an AC grid (Figure 2.23). Because the voltage of an individual alternative energy module is relatively low, for grid-tied use, power optimisers are usually associated in series for the collection of DC power, and the DC power is then converted and supplied to the grid. Moreover, the cascaded arrangement allows the integration of these units in DC nano or microgrids. The power optimisers provide an important benefit compared to other technologies which is the high efficiency, and the Maximum Power Point Tracker is realised in a distributed way on each module.

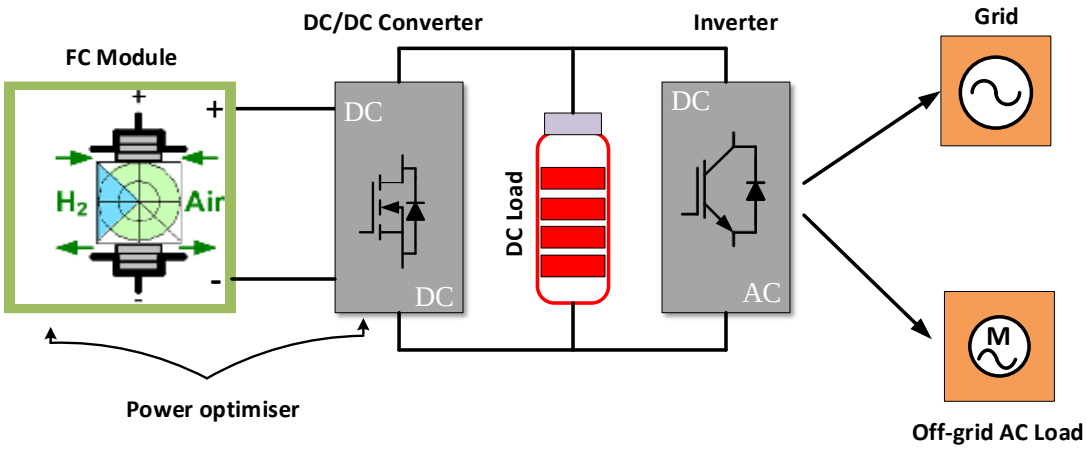

Figure 2. 23: Configuration of a power optimiser for a DC load and a grid-tied inverter. (Ben Hamad et al., 2019)

Figure 2.24 illustrates one potential configuration of power optimisers for grid-tied alternative energy units such as fuel cells. The power optimisers can be assembled and afterward associated in parallel at the DC link to improve the total power. Differential power-processing technology can also be considered.

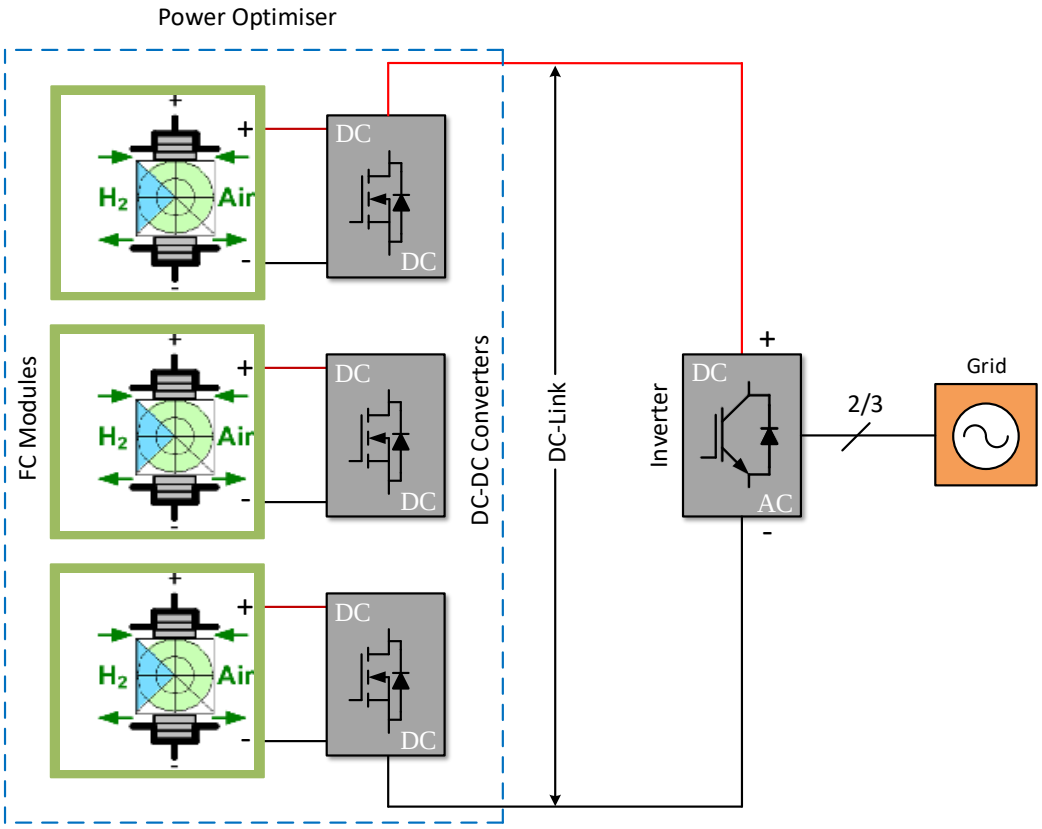

Figure 2. 24: Grid-tied power optimisers. (Ben Hamad et al., 2019)

For the DC to DC converters, typical topologies are the buck, boost, buck boost, and Cuk converters (Kazimierczuk, 2016). Since the design, control, and analysis of those converters are very well presented in the literature, only the boost converter is shown in Figure 2.25.

To reduce the number of parallel power optimisers and the resulting system cost and complexity, a large voltage conversion ratio is important, even though the efficiency might be compromised. Therefore, some topologies have been assessed to provide a high-voltage gain (Chu et al., 2017). The flyback converter shown in Figure 2.26 is amongst the most accepted topologies. The operational principle of the flyback converter is the same as that of the buck boost converter. However, the voltage gain does not only dependent on the duty cycle but also on the turn ratio of the transformer. Additionally, to increase the power processing ability, the interleaved topology can be used for both the boost based and the flyback based optimisers.

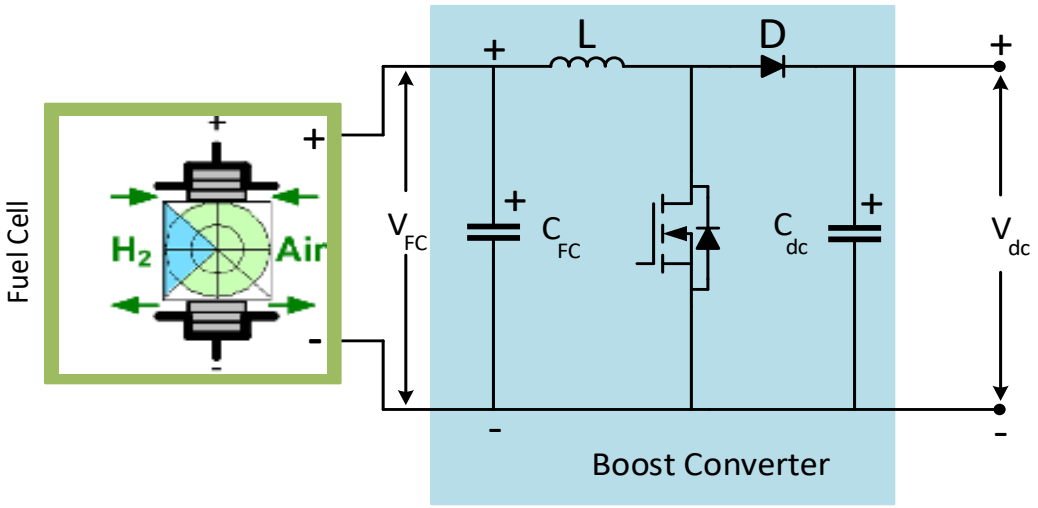

Figure 2. 25: Power optimiser using a DC to DC boost converter. (Lai & Ellis, 2017)

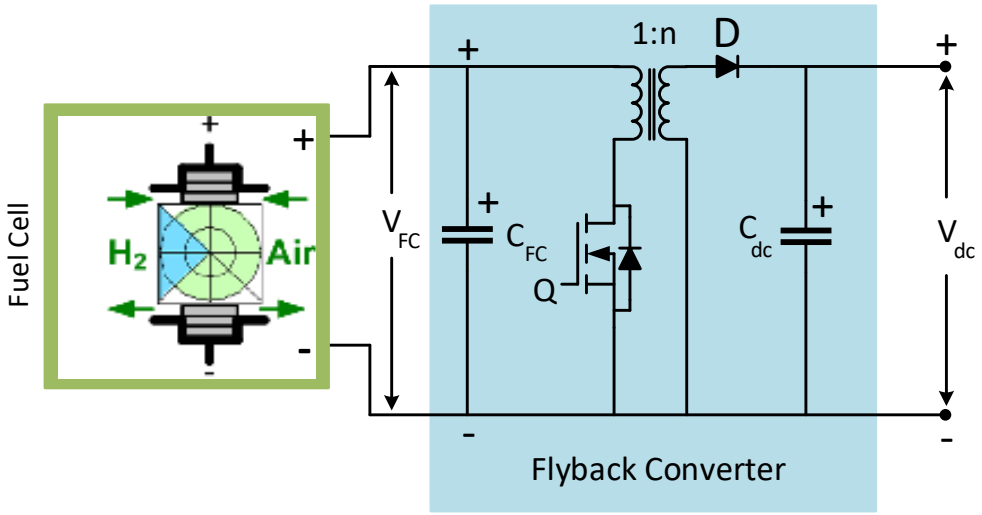

Figure 2. 26: Power optimiser using a flyback-converter. (Chakraborty et al., 2019; Yang & Blaabjerg, 2015)

Besides the above-mentioned DC to DC converters, switched-inductor and switched-capacitor converters, impedance-source networks, and full-bridge (or half-bridge) converters with high-frequency transformers can also be used in the power optimisers (Yu et al., 2012).

In case a power optimiser is coupled to an inverter, it creates a two-stage microinverter (Figure 2.27); the DC to DC converter assists in the tracking of Maximum Power Point, while the inverter controls of the DC-link voltage and grid current. A capacitor is usually used at the DC link for power balancing between the DC and the AC parts. The control of two-stage microinverter is more direct.

In overall, the efficiency of two-stage microinverter can be deteriorated and in case a high-frequency transformer is used, the whole conversion efficiency might get much lower. Figure 2.29 illustrates microinverter topologies with high-frequency transformers, in which the inverters can be either a traditional single phase, or three-phase full-bridge configurations. Furthermore, as shown in Figure 2.28, DC to DC converters with high step-up gains may be utilised as the front side in microinverter use.

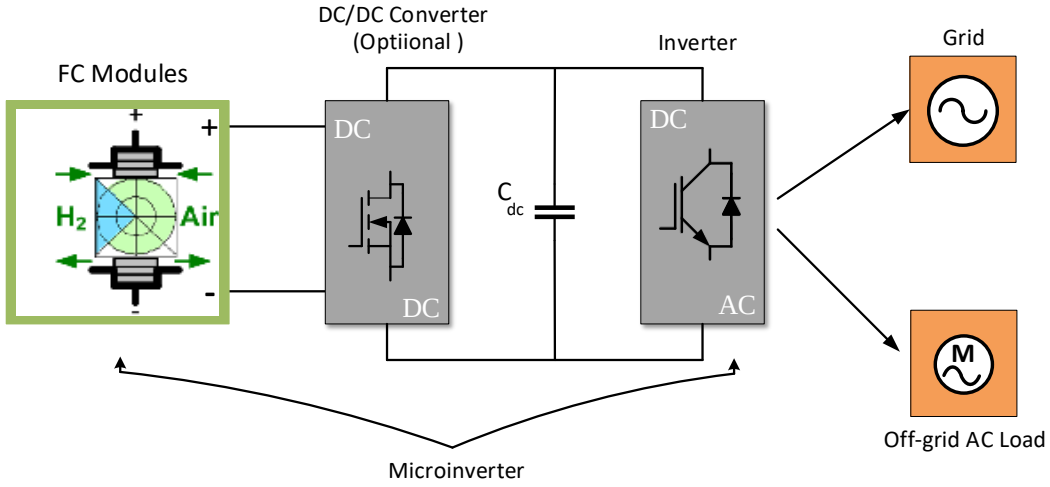

Figure 2. 27: Structure of a two-stage microinverter.

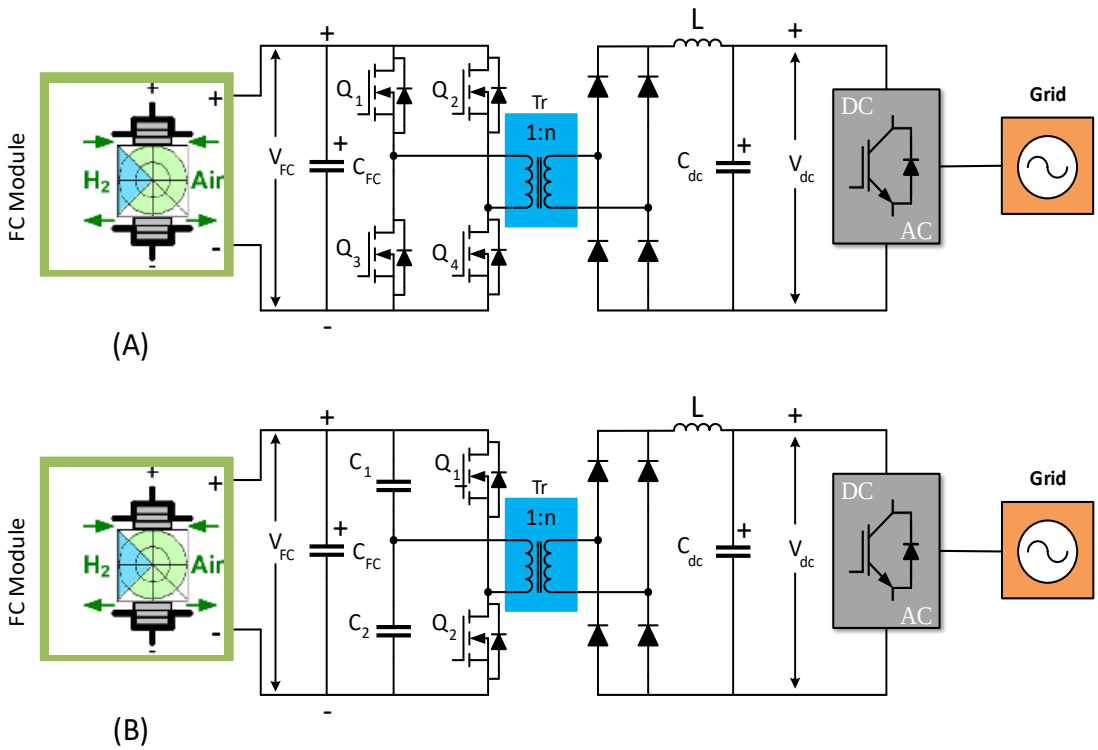

Figure 2. 28: Microinverters (A) with a full-bridge inverter and (B) with a half-bridge inverter.
(Chakraborty et al., 2019; Yang & Blaabjerg, 2015)

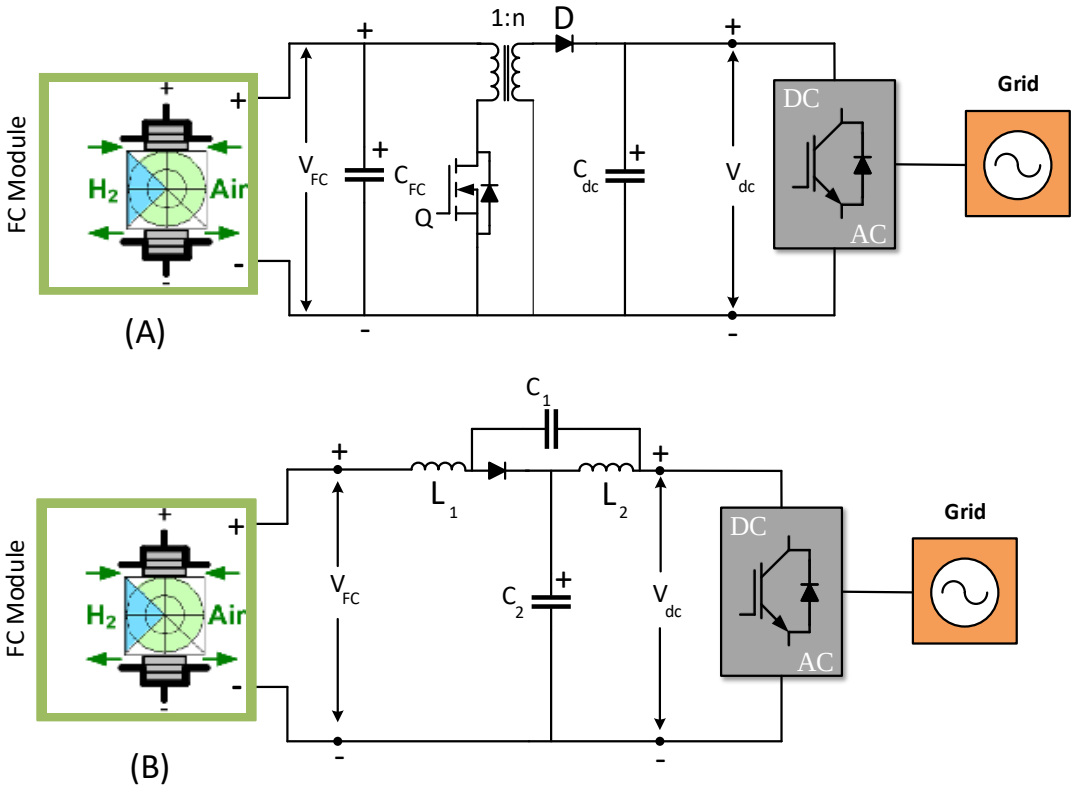

Figure 2. 29: Microinverters using (A) flyback and (B) quasi-Z-source. (Wang, 2004; Prasad et al., 2008)

To diminish the size of the whole unit, two inductors as shown in Figure 2.29(B) can be combined. To further improve the efficiency and decrease the volume, single-stage microinverters are used.

Figure 2.30 displays three power converters integrating the DC to DC and DC to AC phases (Wang, 2004; Prasad et al., 2008). The universal microinverter can function in boost, buck, or buck-boost mode, with a varying input voltage in a large range. However, other two buck-boost microinverters are more attractive.

To deal with a higher power, several AC outputs can be associated in parallel (Jafarian et al., 2018). As shown in Figure 2.31 illustrates an AC stacked microinverter, which allows completely decentralised operation and a weak demand voltage conversion ratio.

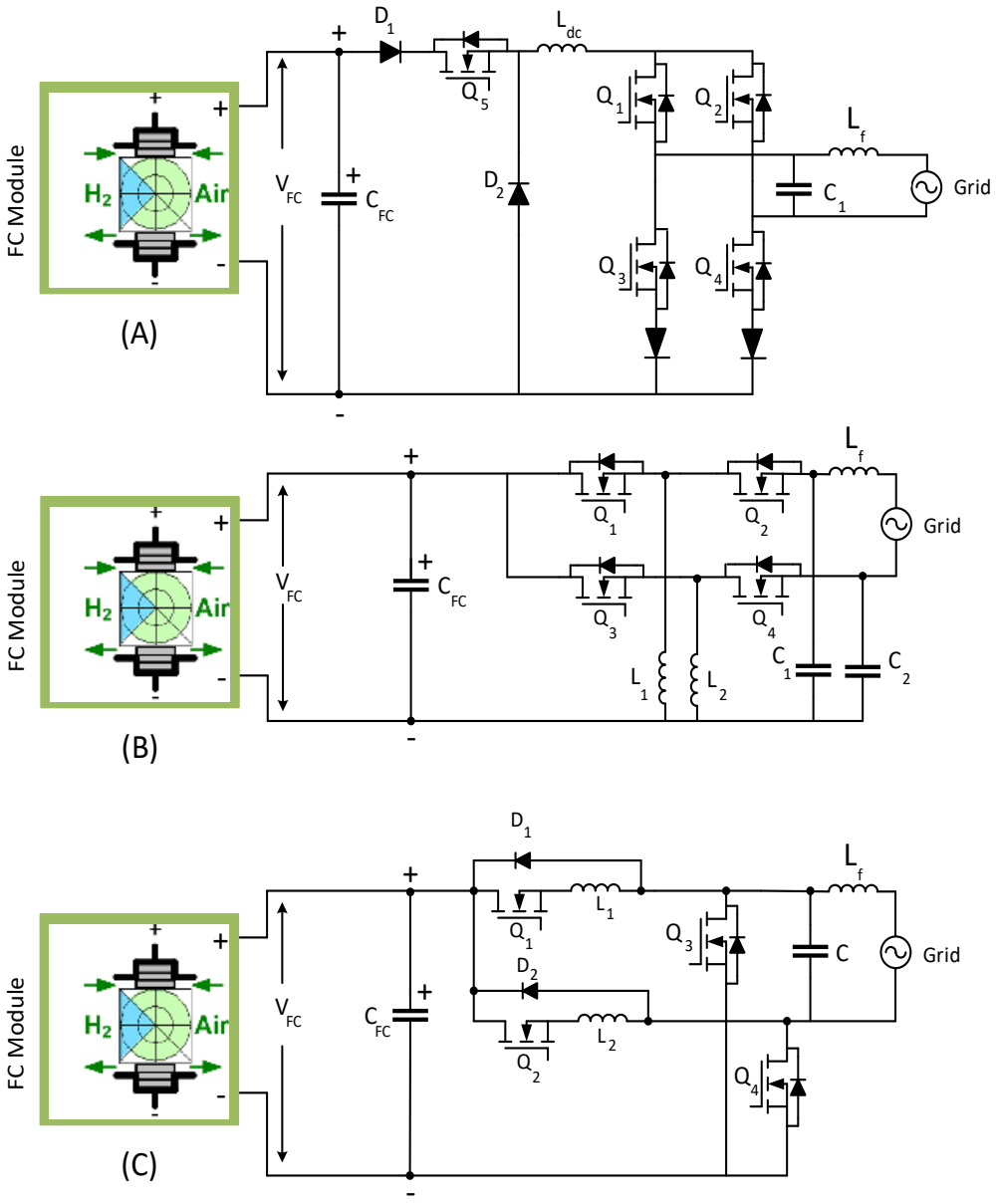

Figure 2. 30: Grid-tied single-stage microinverter: (A) universal microinverter (Prasad et al., 2008)**, (B) differential buck boost** (Viuquezl et al., 1999)**, and (C) buck boost.** (Wang, 2004)

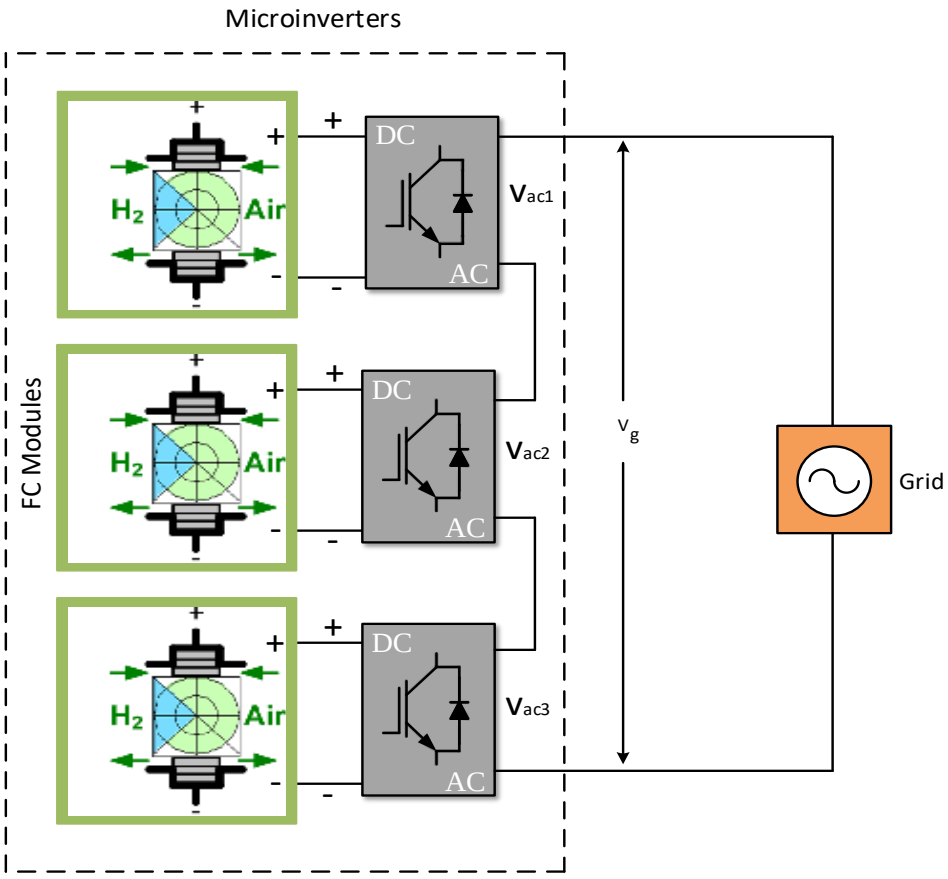

Figure 2. 31: Alternative energy system with AC-stacked microinverters. (Yang & Blaabjerg, 2015)

2.4.2 String inverter topologies

The power converter used to connect to the grid alternative energy sources associated as strings is referred to a string inverter. Two types of string inverters exist namely single-stage converters and two-stage converters. They are often classified into galvanic isolated and transformerless inverters. Both types target higher efficiency and power density. However, they may involve a complex control system as the inverter need to perform the MPPT and power feed in simultaneously and, on the other hand, transformerless inverter is required to eliminate the leakage currents. Furthermore, most string inverters are connected to single-phase feeders with the power ratings below 10 kW.

2.4.2.1 Single stage inverters

The most utilised string inverter is the full bridge single phase topology because it is simpler regarding the control and does not involve many switching devices. Figure 2.32 shows a typical layout of the full-bridge single-phase inverter system including an LCL filter.

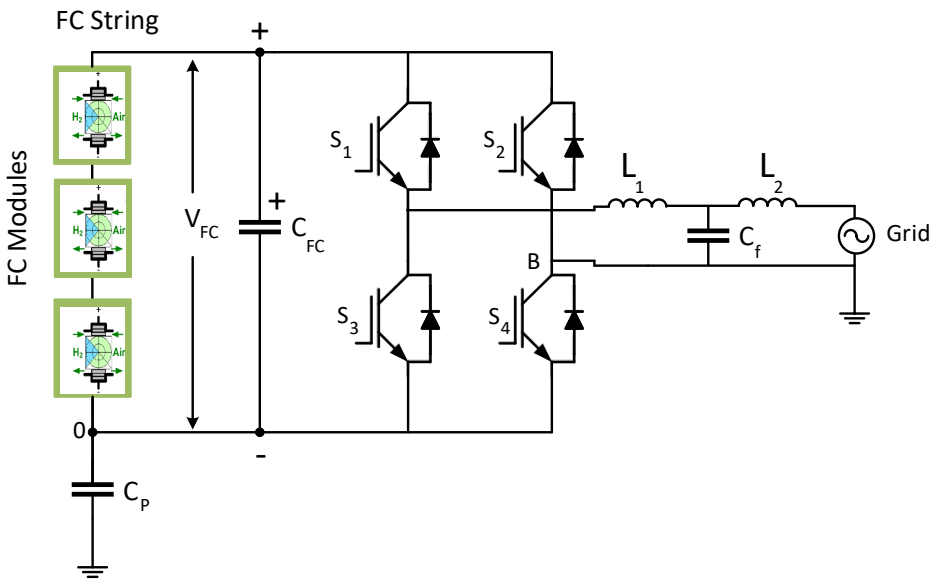

Figure 2.32: Single-phase full bridge transformerless inverter feeding power to the grid. (Yang & Blaabjerg, 2015)

Due to the elimination of the isolation transformer, leakage currents can occur, hence, causing protection problems. Leakage current depends on the common mode voltage and is expressed as (Chakraborty et al., 2019; Yang & Blaabjerg, 2015):

$$i_{P= C_P \frac{dv_{CMV}}{dt}} \tag{2.3}$$

where $\boldsymbol{i_P}$ is the leakage current, $\boldsymbol{C_P}$ represents the parasitic capacitor and $\boldsymbol{V_{CMV}}$ refers to the common-mode voltage.

To minimise leakage currents, the common-mode voltage needs to be kept steady. This may be achieved through a proper design of the modulation strategy and/or the addition of supplementary power units. For modulation strategies, a bipolar modulation scheme may provoke a stable common-mode voltage and needs more actions for filtering harmonics resulting from the switching frequency. Hence, the full-bridge inverter is unfeasible for transformerless applications in practice. As a result, transformerless inverters become more popular in string inverter use.

The majority of transformerless string inverters available in the market derive from the full-bridge inverter by including a bypass path at the DC or the AC sides, as it can be seen in Figure 2.32. This is beneficial to isolate the string from the grid when there are zero-voltage modes or clamping neutral with the DC-link midpoint to attenuate or suppress the leakage.

Two topologies of transformerless inverters with extra power devices at the DC side are depicted in Figure 2.33, specifically H5 inverters and H6 inverters (Hu et al., 2014). The isolation can be achieved by the addition of an AC path, as illustrated in Figure 2.34, which includes the highly efficient and reliable inverter concept (HERIC) topology (Frappé et al., 2010) and the full-bridge zero-voltage rectifier (FB-ZVR)-based inverter (Kerekes et al., 2011).

The HERIC topology utilises two additional switches with antiparallel diodes to short-circuit the grid and then realise zero-voltage states. On the other hand, the FB-ZVR uses a rectifier to replace one of the two devices for zero voltage states. These transformerless inverters can achieve efficiencies of more than 95%. However, their main drawback is their inability to inject no reactive power (Freddy et al., 2017). When used in smart alternative energy systems, the modulation schemes may require a modification to enable the reactive power capability (Frappé et al., 2010).

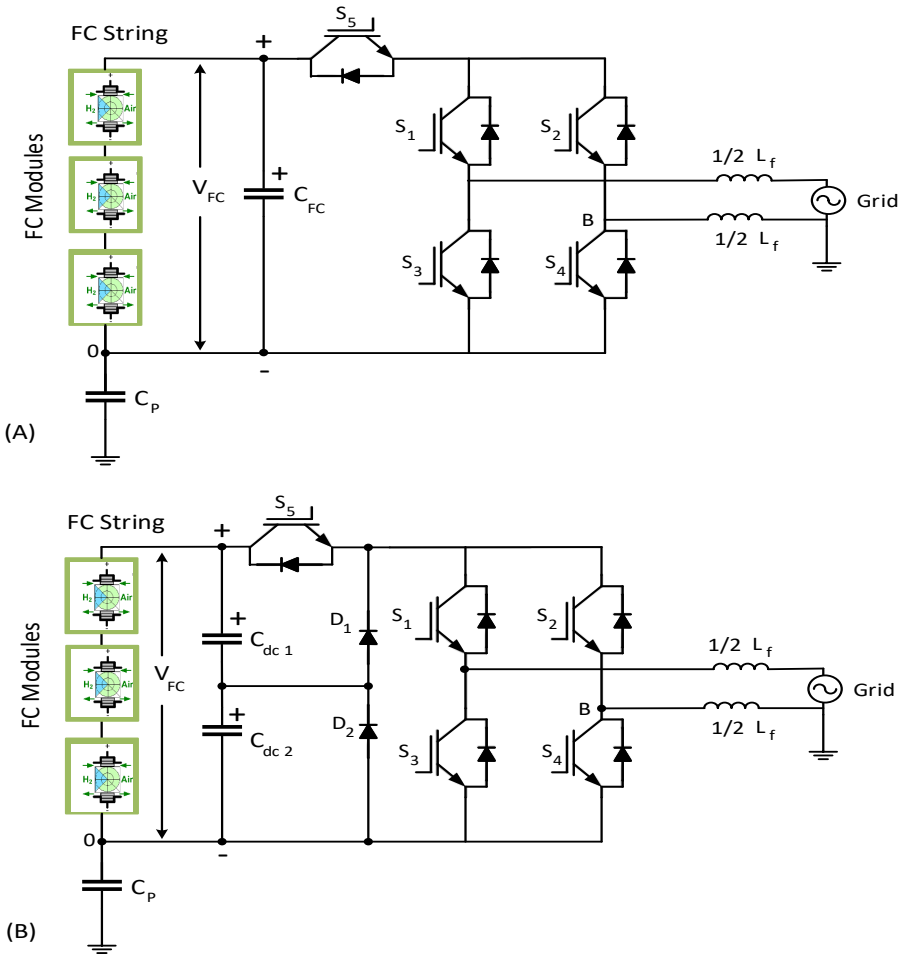

Figure 2. 33: Grid-tied full-bridge string inverters with extra power units at the DC: (A) H5 string (Wang et al., 2012; Dai et al., 2018) **and (B) H6 string.** (Sanjeevarayudu et al., 2017; Zhang et al., 2014)

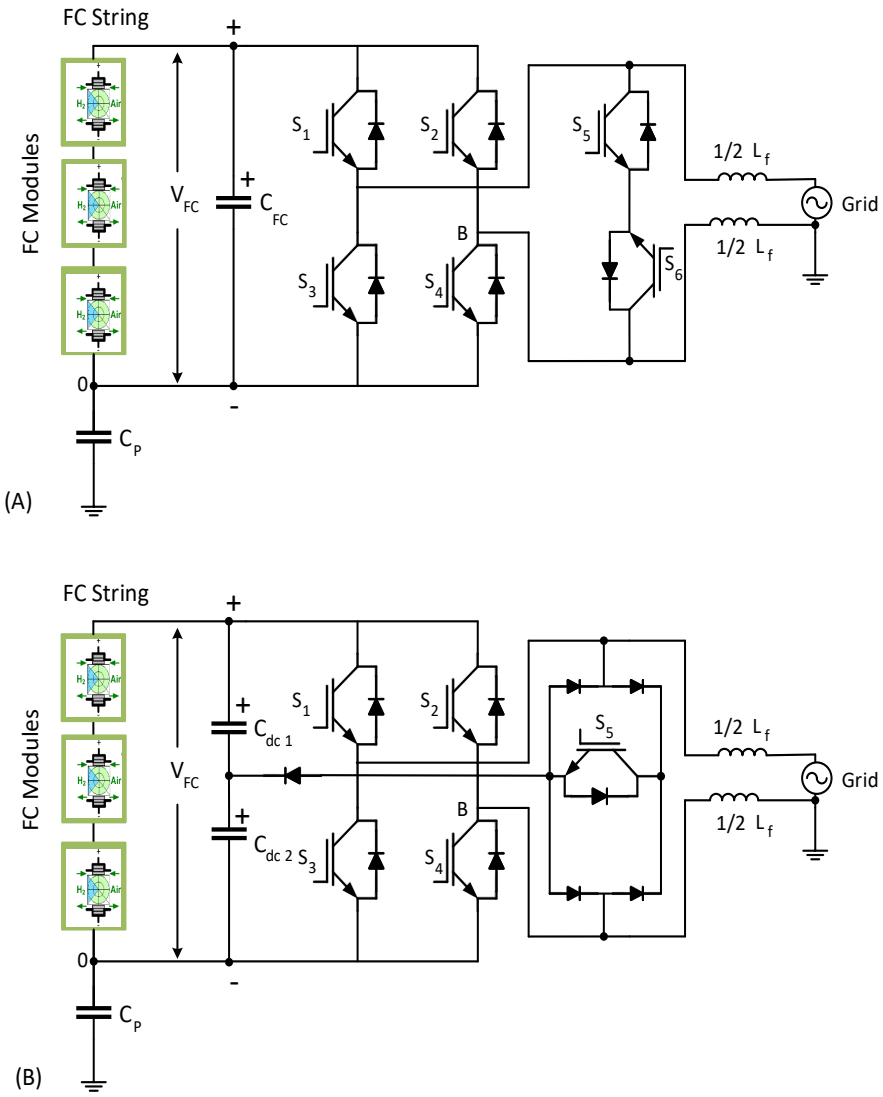

Figure 2. 34: grid-tied full-bridge string inverters with extra power units at the AC side: (A) (HERIC) (Manias, 2016) **and (B) (FB-ZVR).** (Kerekes et al., 2011)

Besides the above-mentioned inverters, multilevel neutral-point-clamped (NPC) converters can also be used as transformerless inverters, in such a case, the modulation scheme needs to be specially designed. For single-phase systems, the I-type and T-type three-level (3L) NPC converters are the two preferred topologies in alternative energy systems. The typical schematics of these two inverters are depicted in Figure 2.35; due to the clamping, zero-voltage states can be easily achieved in operation, and hence, the isolation is realised for transformerless usages. However, the main drawback for the I-type 3L-NPC inverter is the power loss balancing, and the leakage current may be observed in both NPC inverters in case there is any inductance in the neutral connection.

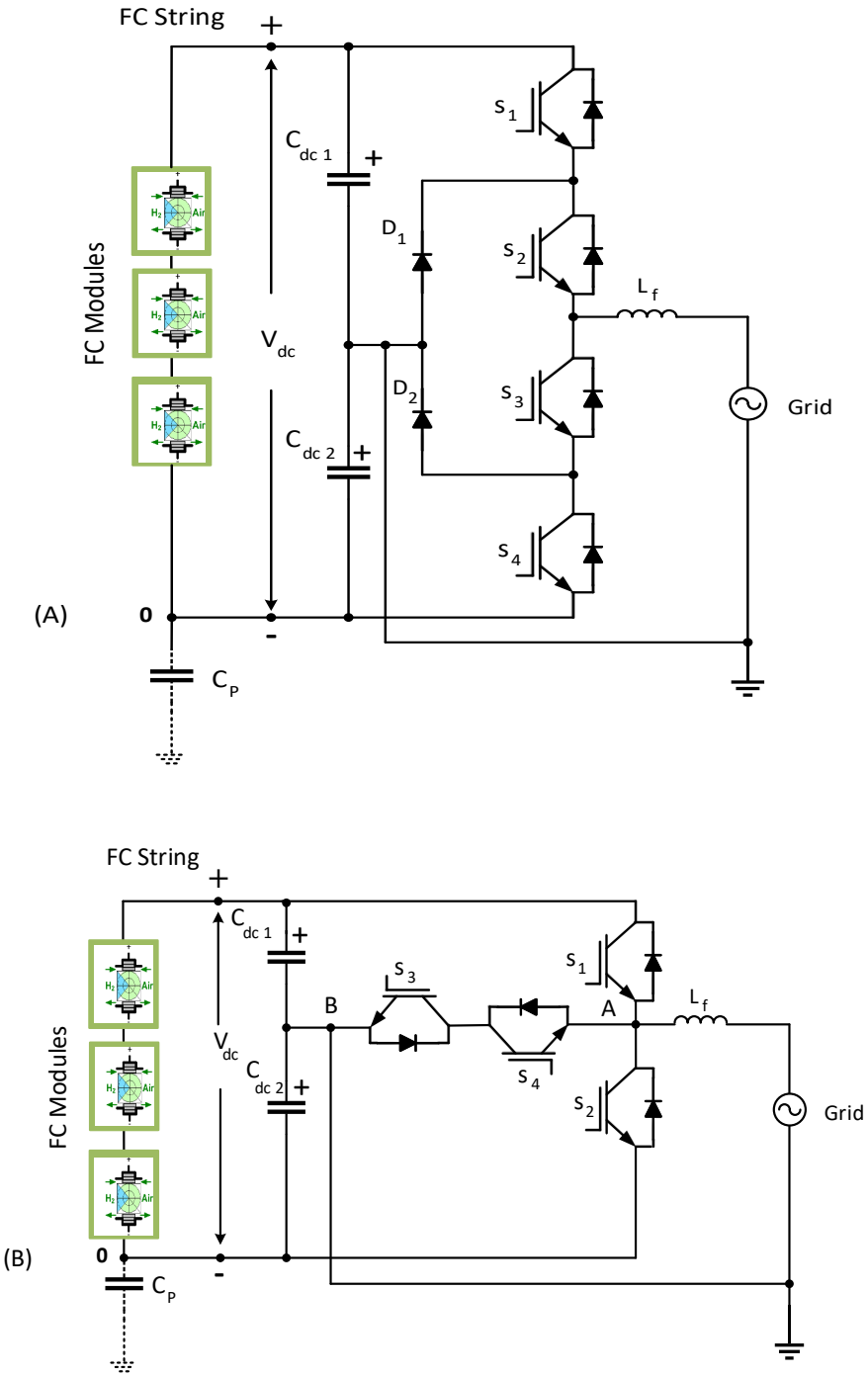

Figure 2. 35: Grid-tied transformerless inverters using the three-level neutral point clamped topology: (A) I-type NPC and (B) T-type NPC. (Lee & Lee, 2017)

2.4.2.2 Double stage inverters

Figure 2.36 shows a typical double-stage single phase string inverter with a DC to DC boost converter. Various boost converter topologies exist for the double-stage inverters, such as the time-sharing and the soft-switched boost converters (Maswood & Tafti, 2019; Gonzalez et al., 2013), and a DC to DC converter with parallel inputs and series outputs shown in Figure 2.37. In addition, for rated power above 10 kW, the

single-phase inverters based on the impedance-source networks shown in Figure 2.38 and the LLC converters in Figure 2.39 can also be used as the front-end stage for double stage inverters, while for higher power ratings, three-phase two-level and multilevel inverters are used. (Ragab et al., 2017; Chen & Liu, 2017). Moreover, the string inverters can be associated in series or parallel to process more power.

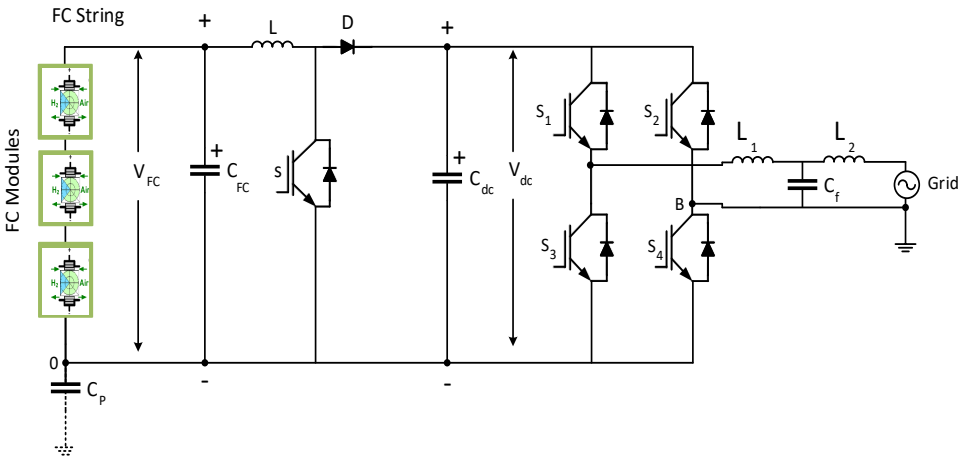

Figure 2. 36: Grid-tied single-phase double-stage transformerless inverter. (Yang & Blaabjerg, 2015)

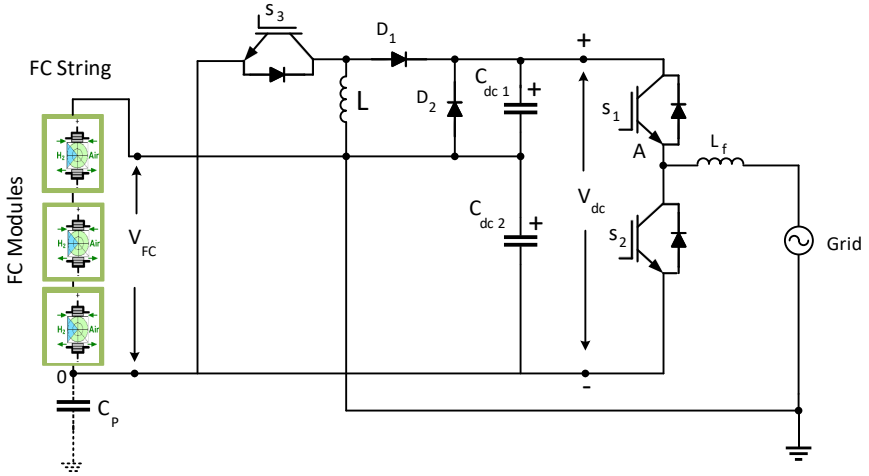

Figure 2. 37: Grid-tied single-phase double-stage transformerless inverter including a parallel-input series output DC to DC converter. (Jiang et al., 2016; Chakraborty et al., 2019; Yang & Blaabjerg, 2015)**.**

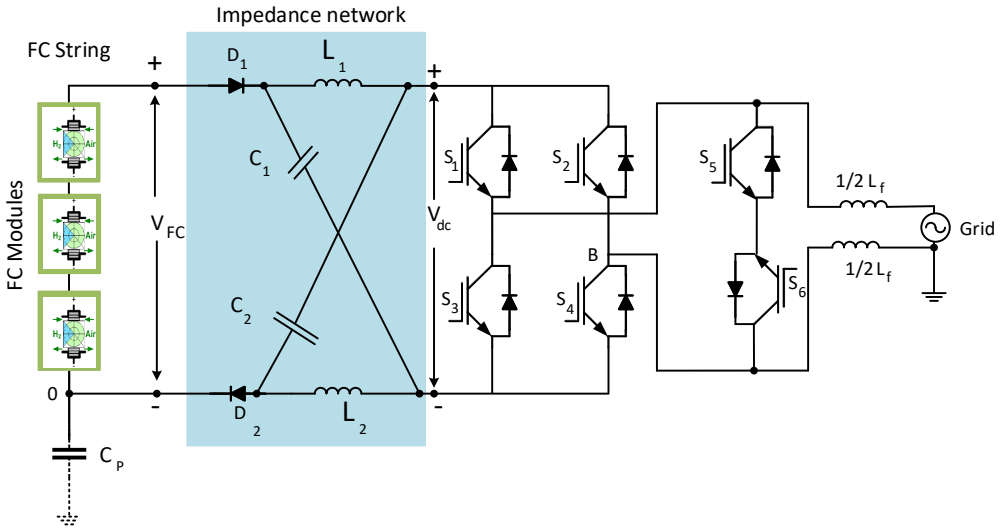

Figure 2. 38: Grid-tied impedance-source single-phase double-stage transformerless inverter. (Yang & Blaabjerg, 2015)**.**

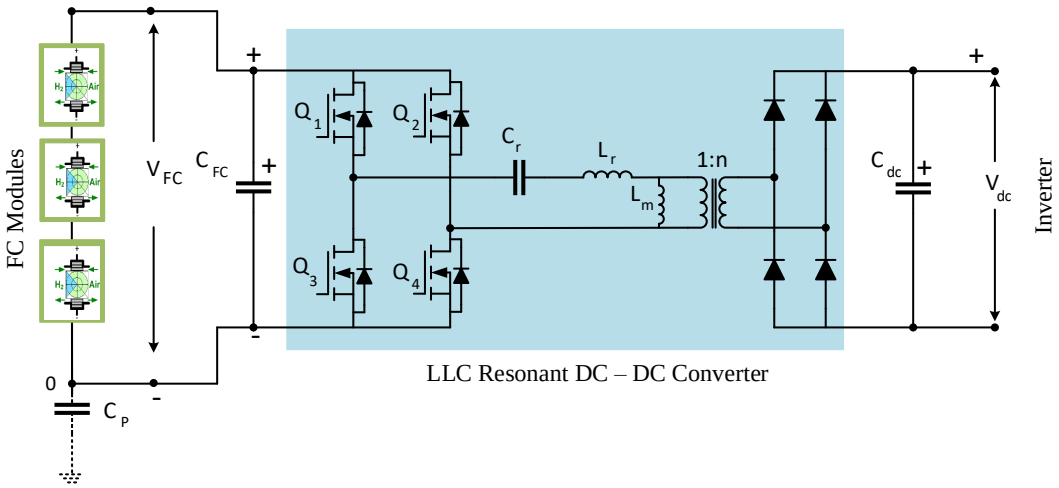

Figure 2. 39: Resonant DC to DC converter. (Ragab et al., 2017; Chen & Liu, 2017)

In case DC to DC converters are used for multiple alternative energy systems (photovoltaic, fuel cell, etc.) in string configuration, the energy collection may be maximised at the string level, thereafter, the power can be gathered at the DC output (Figure 2.40).

If faulty conditions occur in some strings, the series connection in Figure 2.40(A) may not supply power, whereas the parallel connection (Figure 2.40(B)) may still supply power to the grid when disconnecting the faulty strings. In both topologies, energy storage units can be coupled to the DC-link.

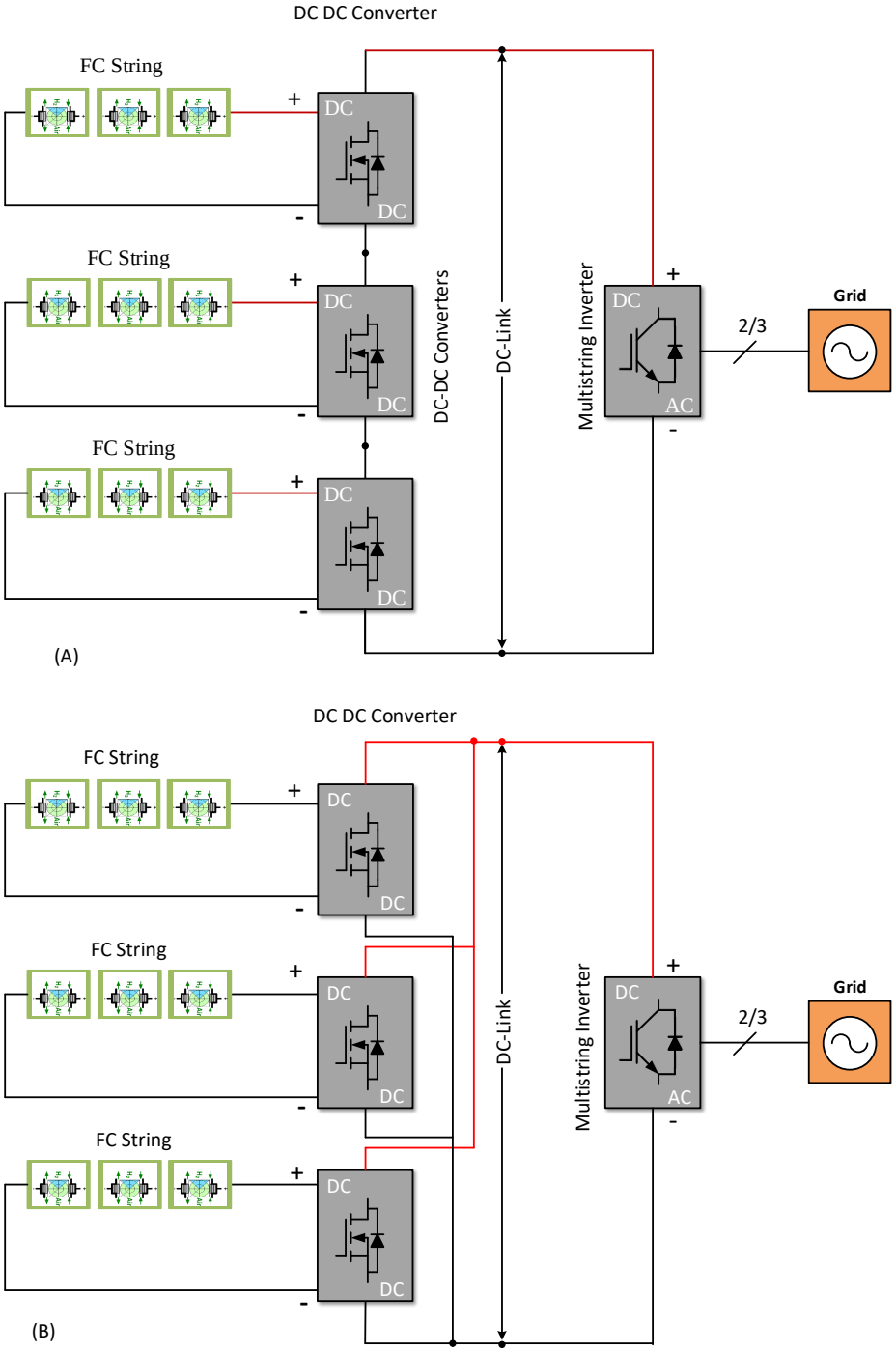

Figure 2. 40: Multistring grid-connected three-phase inverter using: (A) series and (B) parallel connection. (Ben Hamad et al., 2019)

2.4.3 Centralised inverters

Power rating of centralised inverters is quite high, and for the efficiency improvement and cost effectiveness, only single stage topology is considered. The typical three-phase centralised inverter is shown in Figure 2.41 whereby it is coupled to a grid via an LCL filter and a transformer. The configuration is the most fundamental with just six switching devices, and a DC input voltage comes from an alternative energy string with

voltage levels up to 1500 V. In addition, the power can be increased when several strings are connected in parallel to form an array of alternative energy sources. For large utility scale, multiple centralised inverters can be utilised.

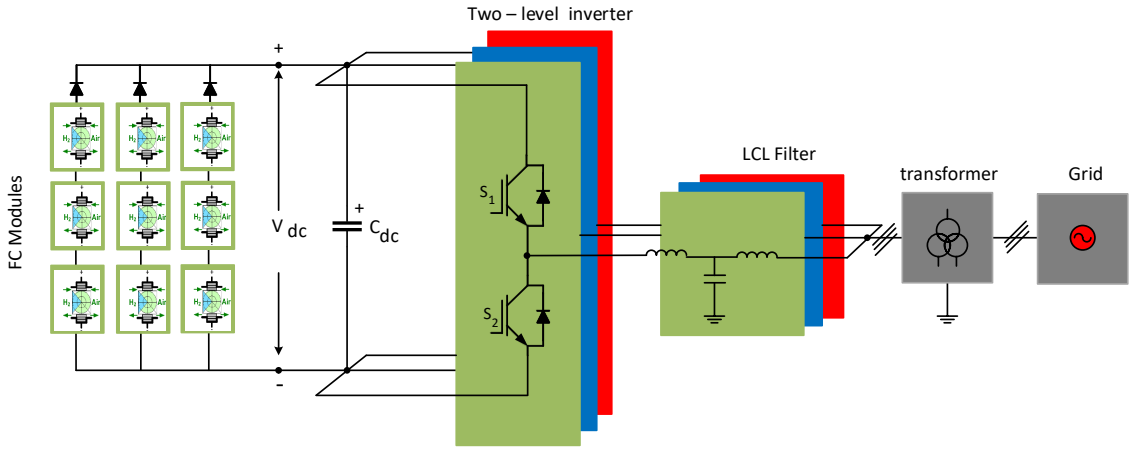

Figure 2. 41: Grid-connected two-level centralised inverter. (Gonzalez et al., 2013)

As the power increases, the two-level inverter topology (Figure 2.41) might become an unreliable option because of high-voltage stresses on the power devices, in addition to high-power losses. In such a case, multilevel inverter topologies are more suitable options. Among the multilevel converter configurations, the three-level neutral point clamped (NPC) inverters shown in Figure 2.42 are the most attractive ones. Because of the increased output voltage level, the filtering is simpler compared to the traditional two-level full-bridge inverter. In addition, the voltage stress is also lower as compared to two-level topologies.

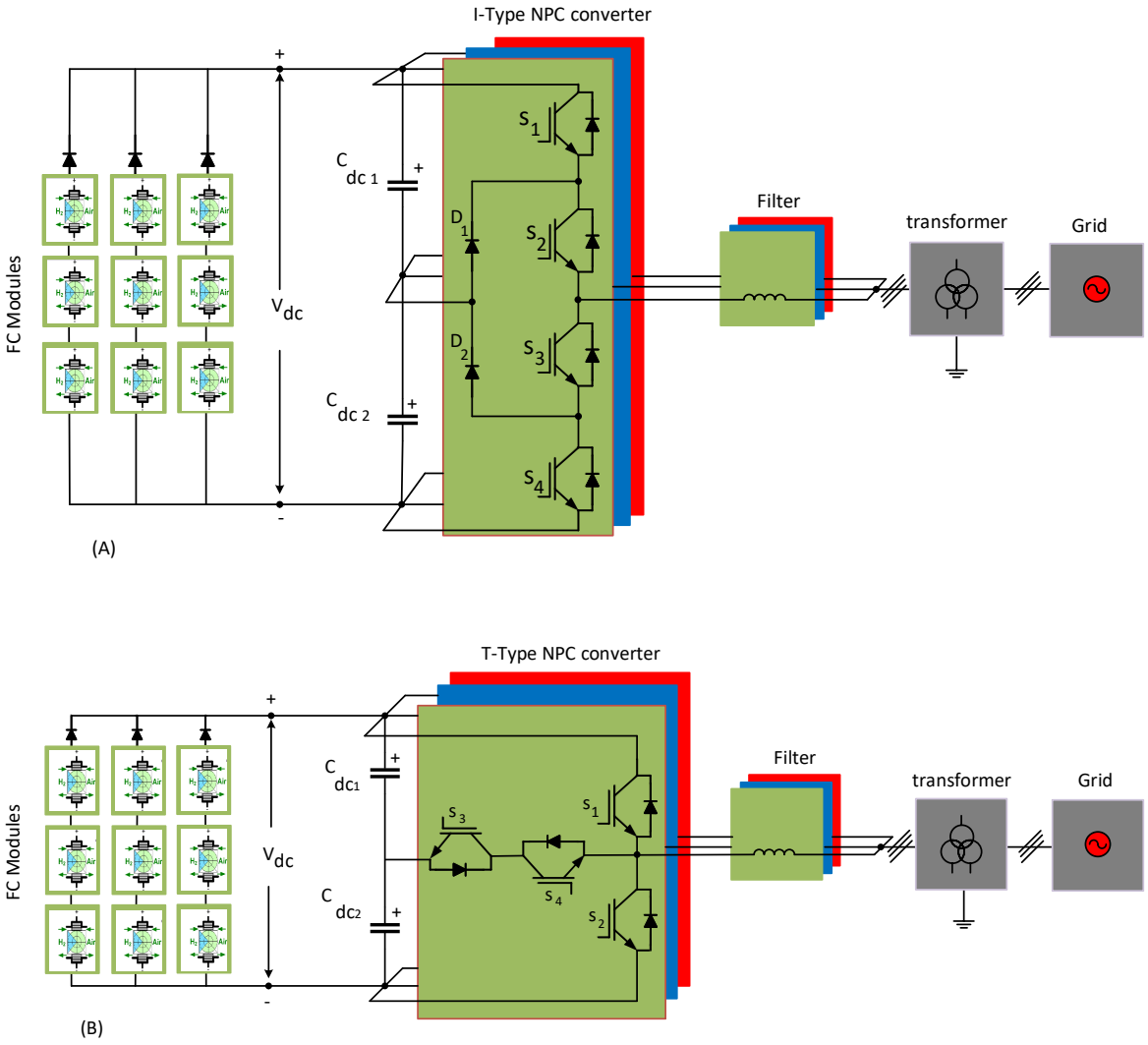

Figure 2. 42: Grid tied three-level neutral point clamped centralised inverter: (A) I-type NPC and (B) T-type NPC. (Aly & Ramadan, 2019)

2.4.4 High power and voltage converters

Alternative energy systems with rated power reaching megawatts or even higher, the redesign of power converters is required considering efficiencies and voltage stresses. Regarding the voltage stresses, multilevel inverters with levels higher than three can be developed.

There is a tendency to use modular multilevel converters or cascaded converters in large alternative energy system plants. Figure 2.43 shows a schematic of a modular multilevel converter consisting of a series of submodules (SMs) with the output voltage depending on the number of SMs. A variety of submodules topologies can be used (Yang et al., 2019) , including the half-bridge converter which is the most utilised in the real world. By increasing the number of SMs, the inverter is more flexible in respect to

fault-tolerant control, however, it also improves the dynamic interactions among the units and the control complexity.

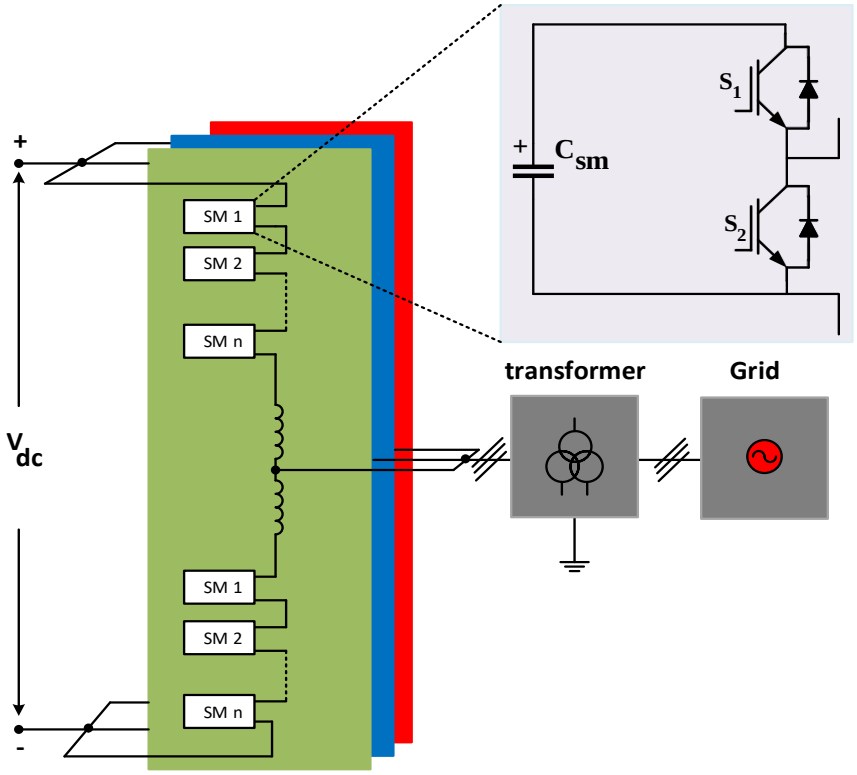

Figure 2. 43: Grid-tied multilevel inverter with half-bridge. (Nademi et al., 2016)

2.5 Summary

This chapter dealt with the literature survey on alternative power technologies including solar power, wind turbine, geothermal power, hydropower, biomass power and fuel cell. A section dedicated to power quality requirements for the grid connection of these technologies was also considered with focus on grid code modifications to allow the alternative energy systems to operate in smart manner when connected to the utility grid. Furthermore, a section dealing with power converters for the grid connection of alternative energy systems and their different topologies for various power rating was presented.

CHAPTER THREE
SYSTEM DESCRIPTION AND COMPONENTS MODELLING

3.1 Introduction

This chapter deals with the description of the megawatt fuel cell energy system and the modelling of components involved on it. The adopted configuration consists of components such as a 1.54 MW fuel cell stack, a three-level diode clamped inverter to convert the 1400 DC volts of the fuel cell into 600 AC volts between phases, and an LCL filter to mitigate the effect of voltage and the current harmonics generated by the inverter.

The megawatt fuel cell stack consists of several proton exchange membrane fuel cell (PEMFC) stacks connected in series and parallel. The system was developed based on the model of each component and the designed parameters of the fuel cell, inverter, LCL filter are also presented.

The last section of this chapter is oriented to the modelling of the control system for the inverter to properly deliver the generated power from the megawatt fuel cell stack to the grid and local load. Under nominal grid operation, the control of the feed-in current is important. This control was realised using a dual-loop control. The current control was realised in different reference frames including the dq frame which allowed the use of PI controllers. Moreover, the harmonic compensation and the synchronisation were also considered.

3.2 System Description

In general, PEMFC produces DC (direct current) power at a low-voltage level. To acquire high-power fuel cell systems, PEMFCs were associated in series and parallel to form multi-stacks fuel cell systems. For grid tied operation mode, a power converter was required to condition the generated DC voltage and converts it to AC power with synchronised frequency and phases. This power converter also permitted the control of power quality and power supply. A power converter can be either a DC to DC converter or an inverter or both depending on the load. A common power converter needs to comply with the following specifications (Lee & Lee, 2017):

i. high gain;
ii. small current ripple and
iii. high efficiency and low costs.

Several ways exist to connect fuel cell systems into an AC utility grid using power converters, the most popular configurations are (Mancilla-David et al., 2012a):

i. centralised configuration;
ii. string configuration and
iii. multistring configuration.

Centralised and string configurations (Figure 3.1A and 3.1B) can provide the similar output power without a converter to boost the output voltage of the fuel cell. However, their principal issue is the low output voltage in case it is fully loaded and high voltage when there is no-load (Hassaine et al., 2014). A solution to overcome this issue is to connect a DC to DC voltage regulator before the inverter (Fig. 1C) to keep the voltage constant at the DC link, thereby suppressing the dependence of the inverter input voltage on the load current. In such a case, a DC to DC boost converter can be associated to each fuel cell and the steady DC outputs of these converters can be connected in parallel. Despite its high capital cost, this configuration includes benefits such as:

i. each fuel cell can be controlled independently with the DC to DC converter;
ii. the stack can be disconnected from the system for maintenance or replaced while the remainder of the system is kept operating;
iii. the system's reliability can be improved alongside with fault-tolerant operations by including redundant fuel cell stacks with DC to DC converters and
iv. each subsystem can be designed independently and combined as required.

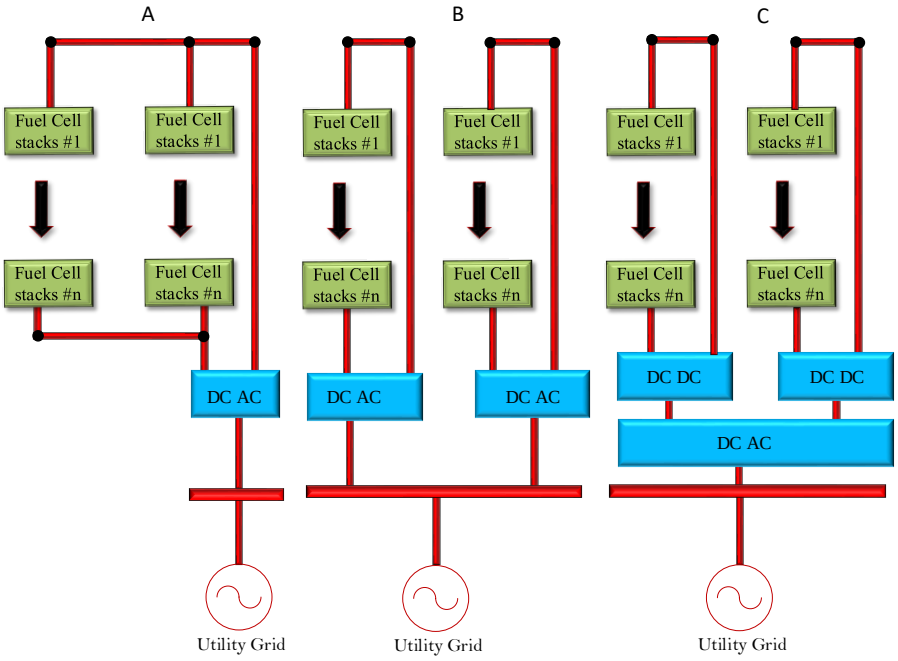

Figure 3. 1: Topologies for fuel cell grid connection: (A) Centralised configuration, (B) String configuration and (C) multi-string configuration. (Mancilla-David et al., 2012a)

The topology adopted in this study is the centralised configuration, whereby the megawatt fuel cell stack is connected to the utility grid directly through the inverter without the use of DC/DC converters. As depicted in Figure 3.2, besides the megawatt PEMFC stack, the system includes a three-level neutral point clamped inverter and a power filter unit connecting the system to the utility grid. The megawatt stack is realised through series and parallel connection of individual PEMFC stacks. Each PEMFC stack generates 126 kW at 1400 Vdc. The overall power of the megawatt multi-stack fuel cell is 1.54 MW. A three-level neutral point clamped inverter converts the 1400 DC voltage of the fuel cell to AC to supply a local load and feed any excess into the utility grid depending on the generation conditions. To mitigate the effects of harmonic voltage and current, an LCL filter is interfaced between the inverter, the local load and the grid.

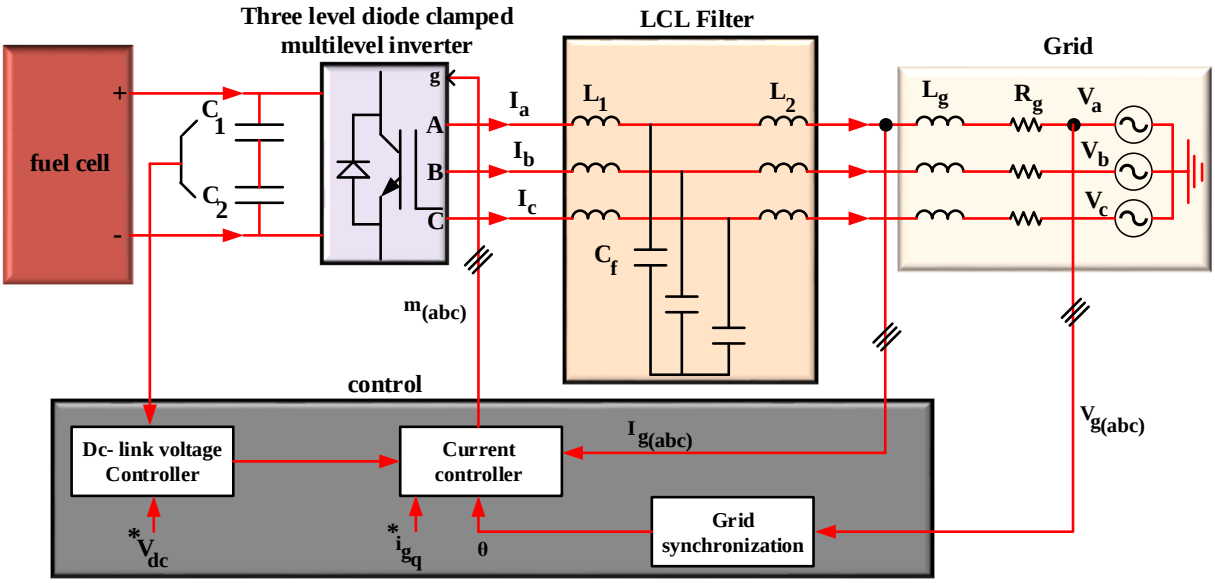

Figure 3. 2: Schematic of a grid-connected megawatt fuel cell.

3.3 System Modelling

3.3.1 Modelling the Fuel cell

The output voltage of a cell can be defined using the following expression (Dicks, L & Rand, J, A, 2018; Mann et al., 2000; Ioannis et al., 2010):

$$V_{FC} = E_{Nernst} - V_{act} - V_{ohm} - V_{Con} \quad (3.1)$$

In Equation 3.1, E_{Nernst} represents the thermodynamic potential of the cell or the cell reversible voltage, V_{act} is the voltage drop resulting from the activation of the anode and cathode, V_{ohmic} is the ohmic voltage drop and V_{con} is the voltage drop from the reduction in concentration of the reactants gases or, alternatively, from the transport of mass of oxygen and hydrogen.

There is another voltage drop (J_n) related to the internal currents and/or the fuel crossover (Dicks, L & Rand, J, A, 2018). The model considers that voltage drop using a fixed current density even at no-load operation.

The first term of Equation 3.1 represents the FC open circuit voltage, while the three last terms are the reduction in this voltage to supply V_{FC} which is the useful voltage across the cell electrodes, for a certain operating current. Each one of the terms of Equation 3.1 is discussed and modelled separately in subsections below.

3.3.1.1 Cell reversible voltage

The reversible voltage of the cell (E_{Nernst}) refers to the potential of the cell in an open circuit thermodynamic balance. In this model, E_{Nernst} is determined starting from a modified version of the equation of Nernst, with an extra term to consider changes in the temperature regarding the standard reference temperature 25ºC. This is given by Equation 3.2 (Albarbar & Alrweq, 2018):

$$E_{Nernst} = \frac{\Delta G}{2*F} + \frac{\Delta S}{2*F} * \left(T - T_{ref}\right) + \frac{R*T}{2*F} * \left[\ln\left(P_{H_2}\right) + \frac{1}{2}\ln\left(P_{O_2}\right)\right] \quad (3.2)$$

where ΔG represents the change in the free Gibbs energy (J/mol), ΔS is the change of the entropy (J/mol), F is the constant of Faraday (96.487º C), R is the universal constant of the gases (8.314 $J/K.mol$), T is the cell operating temperature (K), T_{ref} the reference temperature, P_{H_2} is the partial pressures of hydrogen (atm) and P_{O_2} that of the oxygen (atm).

Using the values for ΔG , ΔS and T_{ref} corresponding to the standard pressure and temperature, Equation 3.2 can be written as (National Energy Technology Laboratory, 2005; Albarbar & Alrweq, 2018; Dicks, L & Rand, J, A, 2018):

$$E_{Nernst} = 1.229 - 0.85 * 10^{-3}(T - 298.15) + 4.3085 * 10^{-5} * T * [ln(P_{H_2}) + \frac{1}{2} ln(P_{O_2})] \quad (3.3)$$

3.3.1.2 Activation voltage drop

The activation voltage drop, including the anode and cathode, can be expressed by (Novak et al., 2015):

$$V_{act} = -[\zeta_1 + \zeta_2 * T + \zeta_3 * T * \ln(C_{O2}) + \zeta_4 * T * \ln(i_{FC})] \quad (3.4)$$

where i_{FC} is the cell operating current (A), $\zeta_1, \zeta_2, \zeta_3$ and ζ_4 are the parametric coefficients for each cell model, whose values are given by theoretical equations with kinetic, thermodynamic and electrochemical foundations. C_{O_2} is the concentration of oxygen in the catalytic interface of the cathode (mol/cm^3), given by (Jia, Yang, et al., 2009; Lee & Cho, 2009; Ioannis et al., 2010; Mann et al., 2000):

$$C_{O_2} = \frac{P_{O_2}}{5.08 * 10^6 * \exp(-498/T)} \quad (3.5)$$

3.3.1.3 Ohmic voltage drop

The ohmic voltage drop occurs from the resistance to the electrons transfer through the collecting plates and carbon electrodes, and the resistance to the protons transfer through the solid membrane. A general expression for resistance is defined to include all the important parameters of the membrane and the equivalent resistance of the membrane is given by (Gao et al., 2012):

$$R_m = \frac{\rho_m l}{A} \quad (3.6)$$

where ρ_m represents the specific resistivity of the membrane for the electron flow ($\Omega . cm$), A is the cell active area (cm^2) and l is the thickness of the membrane (cm).

This study considers the membranes of the type $Nafion^{®}$ used mostly in PEMFC. The following product designations denote the thickness of the membranes based on nafion (Corrêa et al., 2004):

i. Nafion 117:7 mil ($l = 178 \mu m$)
ii. Nafion 115:5 mil ($l = 127 \mu m$)
iii. Nafion 112:2 mil ($l = 51\ \mu m$)

The equation for the resistivity of the membranes based on nafion is expressed as (Saeed & Warkozek, 2015; Seyezhai & Mathur, 2011; Gao et al., 2012):

$$\rho_m = \frac{181.6\left[1+0.03\left(\frac{i_{FC}}{A}\right)+0.062\left(\frac{T}{303}\right)^2\left(\frac{i_{FC}}{A}\right)^{2.5}\right]}{\left(\left[\Psi-0.634-3\left(\frac{i_{FC}}{A}\right)\right]exp\left(\frac{4.18*(T-303)}{T}\right)\right)} \quad (3.7)$$

Ψ is a modifiable parameter with a possible maximum value of 23 influenced by the preparation procedure of the membrane. It may have a value order of 14 under the ideal condition of 100% of relative humidity.

Using the value of Equation 3.7 for the membrane resistance, the ohmic voltage drop can be determined by the following expression (Ali & Salman, 2006):

$$V_{ohm} = i_{FC}.(R_m + R_c) \quad (3.8)$$

where R_C expresses the resistance to the transfer of protons through the membrane often considered as constant.

3.3.1.4 Concentration voltage drop

The concentrations of hydrogen and oxygen are affected by the mass transport which causes a decrease of the partial pressures of these gases. Reduction in the pressures of oxygen and hydrogen is a function of the electrical current and the physical characteristics of the system. In order to determine an equation for this voltage drop, a maximum current density, J_{max} is defined, under which the fuel is being utilised at the exact rate of the maximum supply speed. The current density cannot exceed this limit as the fuel cannot be supplied at a larger rate. Common values for J_{max} range from 500 to 1500 mA/cm^2. Hence, the voltage drop resulting from the mass transport can be expressed as (Yongli, 2013):

$$V_{conc} = -B.\ln\left(1-\frac{J}{J_{max}}\right) \quad (3.9)$$

where $B(V)$ expresses a parametric coefficient depending on the cell and its operation state, while J represents the actual current density of the cell (A/cm^2).

3.3.1.5 Cell dynamics

A phenomenon known as "charge double layer" occurring in a fuel cell is extremely important to understand the cell dynamics, if two oppositely charged materials are in contact, charges accumulation occurs on their surfaces or a load transfer from one to others. The charge layer on the interface electrode/electrolyte behaves as a storage of

electrical charges and energy since it acts as an electrical capacitor. In case the voltage changes, there will be some time for the charge to vanish (if the voltage increases) or to increase (if the voltage decreases). Such a delay affects the activation and concentration potentials. It is important to point out that the ohmic over-potential is not affected, since it is linearly related to the cell current through the Ohm's Law. Thus, a change in the current causes an immediate change in the ohmic voltage drop. In this way, it can be considered that a first order delay exists in the activation and concentration voltages. The time constant, τ(s), associated with this delay is the product (Jia, Li, et al., 2009):

$$\tau = C.R_a \tag{3.10}$$

where C represents the equivalent capacitance (F) of the system and R_a is the equivalent resistance (Ω). The value of the capacitance is only few Farads, whereas the resistance R_a is determined from the cell output current and the calculated activation and concentration voltages. R_a is given as (Jia, Li, et al., 2009; Saeed & Warkozek, 2015; Gao et al., 2012):

$$R_a = \frac{V_{act}+V_{Con}}{i_{FC}} \quad . \tag{3.11}$$

3.3.1.6 Power generation

A typical PEMFC stack is depicted in Figure 3.3; V_S represents the stack output voltage obtained from the multiplication of the FC voltage and the number of cells. The electrical output of energy of the cell is connected to a load. There is no restriction related to the load type, since the power supplied by the stack is enough to feed it. For example, in systems used to inject energy into the grid, the load can represent a boost DC to DC converter, followed by a DC to AC converter, linked to the grid through a transformer. In isolated systems it can represent a pure resistive load (heating) or a resistive-inductive load (motor), for example. In any case, the density of the current of the cell, J (A/cm2), is defined by the following expression (Jia, Li, et al., 2009):

$$J = \frac{I_{FC}}{A} \tag{3.12}$$

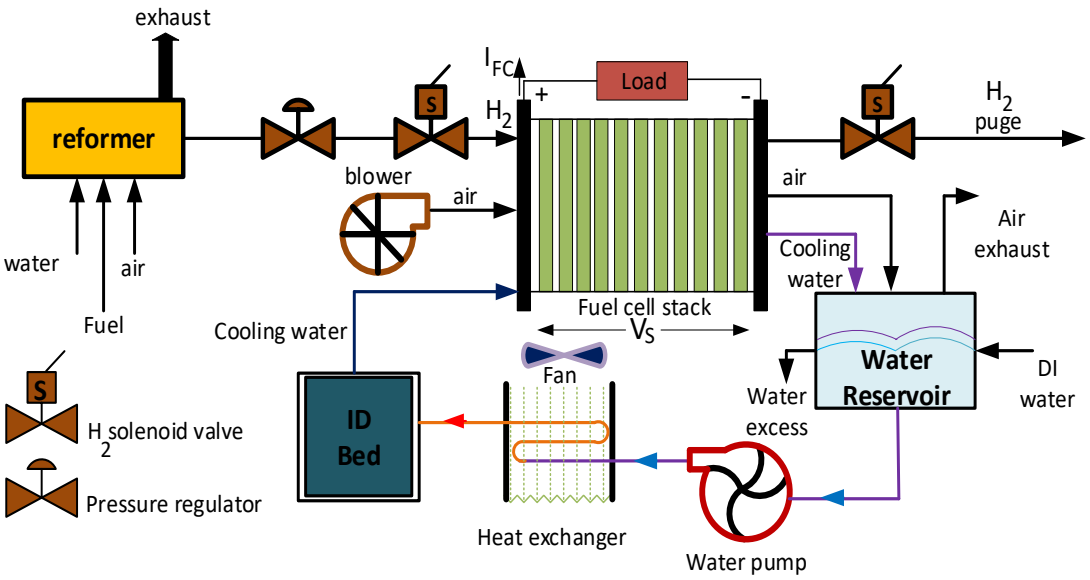

Figure 3. 3: PEMFC stacks schematic. (Murugesan & Senniappan, 2013)

The electric power provided by the stack to the load is given by Equation 3.13 as follows (Albarbar & Alrweq, 2018; Dicks, L & Rand, J, A, 2018):

$$P_{FC} = V_{FC} * i_{FC} \tag{3.13}$$

where V_{FC} and P_{FC} denote the output voltage of the stack under nominal operating condition and the output power respectively.

The FC efficiency can be determined by Equation 3.14 as follows (Albarbar & Alrweq, 2018; Dicks, L & Rand, J, A, 2018):

$$\eta = \mu_f * \frac{V_{FC}}{1.48} \tag{3.14}$$

where μ_f is the fuel utilisation coefficient, generally in the range of 95%, and 1.48 V represents the maximum voltage that can be obtained using the higher heating value (HHV) for the hydrogen enthalpy. Fuel utilisation is assumed to be constant, which is valid where the fuel cell has a hydrogen flow rate control. In this case, the hydrogen is supplied according to the load current.

3.3.1.7 Designed parameters of the megawatt fuel cell stack

The parameters, physical meaning with units and value used in the modelling of a PEMFC stack are given in Table 3.1 (Frappé et al., 2010), while Table 3.2 shows the

general characteristics of the obtained Megawatt fuel cell stack. The Polarisation curves and the stack efficiency are shown in the Appendices from A.1 to A.6.

Table 3. 1: Single PEMFC parameters. (Murugesan & Senniappan, 2013)

Parameter	PEMFC stack	
	Physical meaning and units	Value
T	Stack temperature ^{o}K	338
A	Activation area cm^2	50.6
l	Membrane thickness μm	178 (Nation 117)
P_{H2}	Hydrogen pressure atm (0.1 MPa)	1 atm
P_{O2}	Oxygen pressure atm (0.1 MPa)	1 atm
R_C	Membrane contact resistor Ω	0.0003
B	Coefficient for computing V_{con}	0.016
ζ_1	Curve fitting parameter	-0.948
ζ_2	Curve fitting parameter	0.00312
ζ_3	Curve fitting parameter	$7.6x10^{-5}$
ζ_4	Curve fitting parameter	$-1.93x10^{-4}$
Ψ	Membrane moisture content	23
I_L	Current density driven from PEMFC mA/cm^2	1500
C_{O_2}	O_2 concentration at the cathode /(mole/cm3)	-

Table 3. 2: Megawatt PEMFC parameters

Parameter	Megawatt PEMFC stack	
	Value	Unit
Stack nominal power	126000	W
Stack maximum power	134400	W
Fuel cell resistance	8.2936	Ohms (Ω)
Nerst voltage of a stack E_n	1.1039	V
Nominal utilisation: Hydrogen (H_2) Oxygen (O_2)	 98.47 99.99	 % %
Nominal consumption: Fuel Air	 1259 2985	 Slpm Slpm
Exchange current (i_o)	12.8226	A
Exchange coefficient (alpha)	-0.38762	-
Fuel cell signal variation parameters: Fuel cell composition (x_H2) Oxygen composition (y_O2)	 99.56 21	 % %
Fuel flow rate at nominal hydrogen utilisation: Nominal Maximum	 1056 1970	 lpm lpm
Air flow rate at nominal hydrogen utilisation: Nominal Maximum	 3700 6907	 lpm lpm
System temperature (T)	338	Kelvin
Fuel supply pressure (P_{fuel})	10.5	bar
Air supply pressure (P_{air})	1	bar
Number of cells	2000	-
Nominal stack efficiency	55	%
Number of stacks	12	
Megawatt fuel cell voltage at 0A	2000	V
Megawatt fuel cell voltage at 1 A	1800	V
Megawatt stack nominal power	1.4	MW
Megawatt stack nominal current	1100	A
Megawatt fuel cell nominal operating point of the current	90	A
Megawatt fuel cell nominal operating point of the voltage	1400	V
Megawatt fuel cell maximum operating point of the current	168	A
Megawatt fuel cell Maximum operating point of the voltage	800	V

3.3.2 Modelling the Three-level diode clamped inverter

A typical three-level diode clamped inverter is composed of twelve switches and six clamping diodes (Figure 3.5). The DC link consists of two capacitors, and the neutral point refers to the point between the upper and lower capacitors. Six diodes called clamping diodes couple the output of each inverter leg to the neutral point. The topology is based on a series connection of four switches in the individual legs. Compared to the two-level inverter, the rated voltage of the switch can be reduced to half, allowing the topology to be appropriate for large power applications.

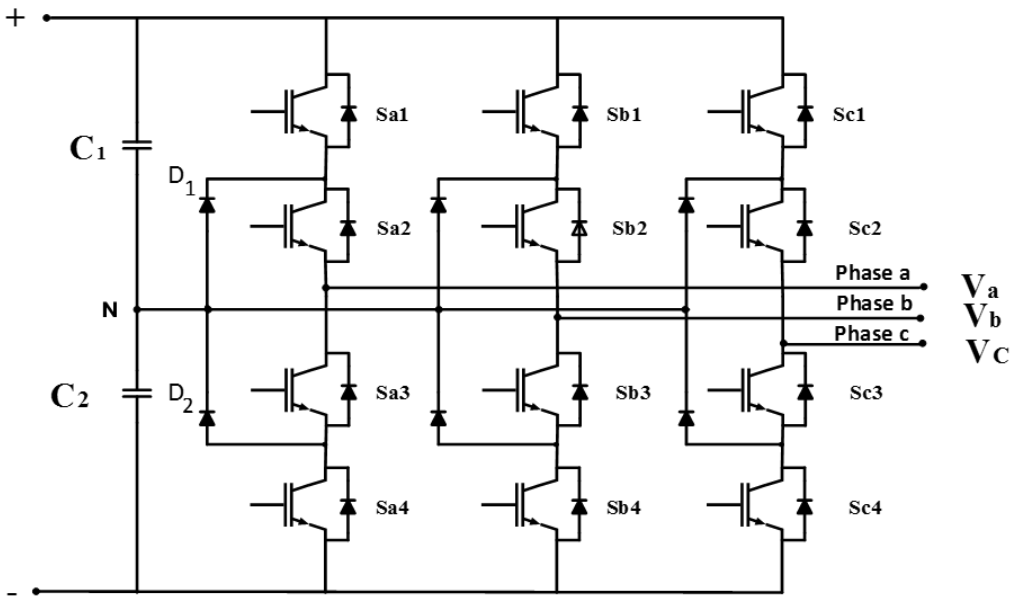

Figure 3. 4: Three-level diode clamped inverter topology (Chaturvedi et al., 2005)

3.3.2.1 Input – output characteristics

The input-output characteristics of a typical three-level inverter can be obtained by comparison with the input-output characteristics of a two-level inverter. As depicted in Figure 3.5(a), the input voltage of the two-level inverter is referred to the DC voltage (V_{dc}), and the output voltage (V_{xz}) has a value of $V_{dc}/2$ or $-V_{dc}/2$ depending on the switching state. On the other hand, the input voltage of the three-level inverter is the same DC voltage (V_{dc}) as the two-level inverter. Since the three-level inverter has a switching state connected to the neutral point, an output voltage of $V_{dc}/2$, 0 or $-V_{dc}/2$ can be produced as shown in Figure 3.5(b).

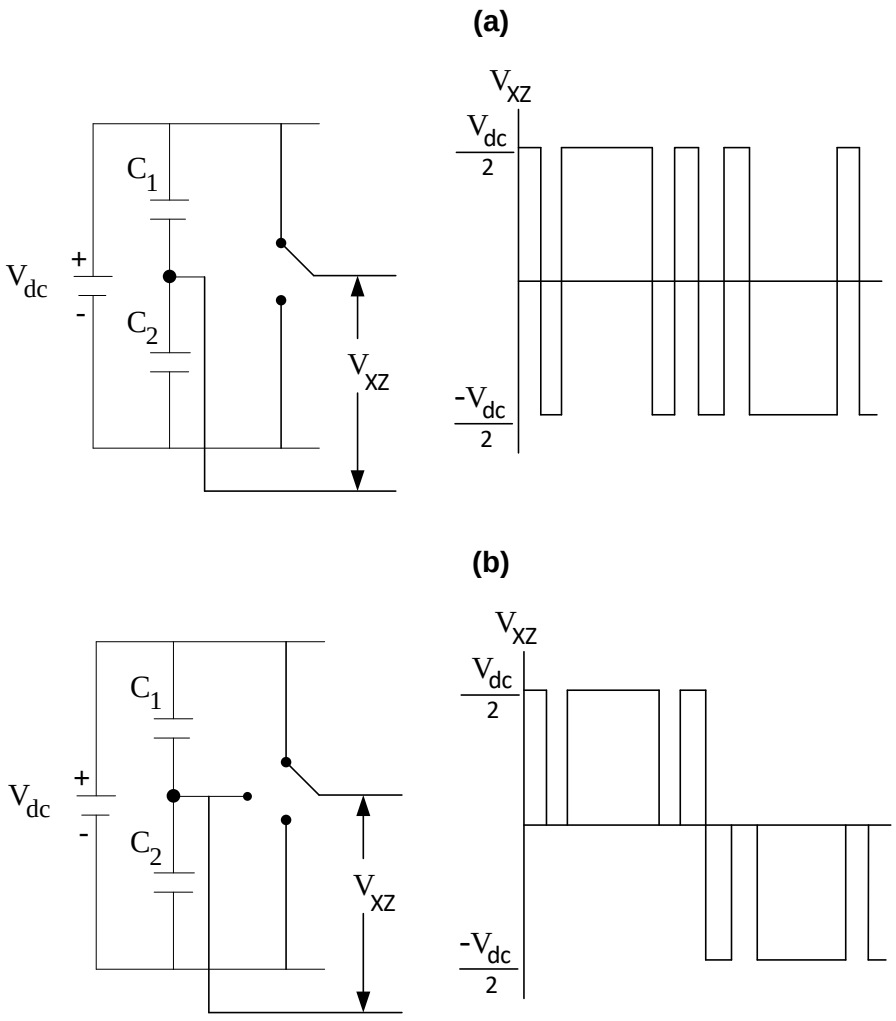

Figure 3. 5: (a) Two-level inverter and (b) Three-level inverter. (Wu & Narimani, 2017)

In the three-level diode clamped inverter, the output voltage is obtained by the on-off operation of individual switches (Figure 3.6). If the first switch (S_{X1}) and the second switch (S_{X2}) are on and the third switch (S_{X3}) and the fourth switch (S_{X4}) are off, the output is linked to the top of the DC side, and the resulting output voltage is $V_{dc}/2$. On the contrary, if the first switch (S_{X1}) and the second switch (S_{X2}) are turned off and the third switch (S_{X3}) and the fourth switch (S_{X4}) are turned on, the output voltage has a value of $-V_{dc}/2$. Lastly, if the first switch (S_{X1}) and the fourth switch (S_{X4}) are turned off and the second switch (S_{X2}) and the third switch (S_{X3}) are turned on, the output voltage is zero. Table 3.3 shows the switching operation of a diode clamped three-level inverter.

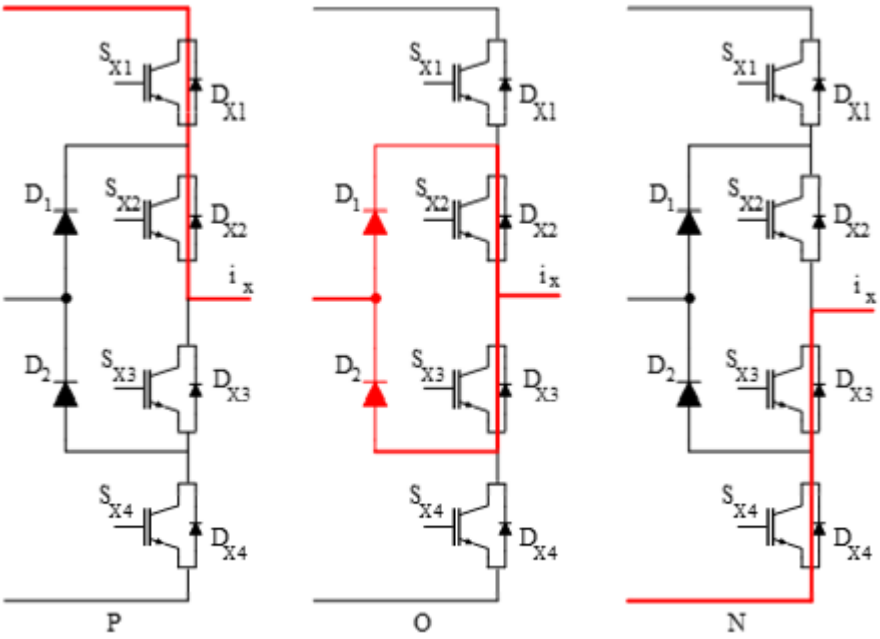

Figure 3. 6: ON/OFF states of switches (Lee & Lee, 2017)

Table 3. 3: ON/OFF operational characteristics of each switch.

Switching state	Switching device states				Output voltage $V_{XZ}(X = a, b, c)$
	S_{X1}	S_{X2}	S_{X3}	S_{X4}	
P	ON	ON	OFF	OFF	$V_{dc}/2$
O	OFF	ON	ON	OFF	0
N	OFF	OFF	ON	ON	$-V_{dc}/2$

3.3.2.3 Three-Level inverter voltage

The switching state of each leg can be expressed as P, N and O. Hence, it is possible to represent the three-leg output voltage utilising the switching states of the three legs. In total, there are 27 switching states that can be represented by the three-leg output voltage, and these 27 switching states can be expressed as vectors as shown in Figure 3.7, while the switching states and voltage vectors are shown in Table 3.4. A vector diagram of the three-level inverter consists of a large vector, a medium vector, a small vector, and a zero vector and small vectors have two types, P-type and N-type.

Table 3. 4: Switching device states and voltage vectors.

Space vector		Switching state		Types of vector	Magnitude
V_0		[POO][OOO][NNN]		Zero vector	0
		P-type	N-type	Small vector	$\frac{1}{3}V_{dc}$
V_1	V_{1P}	[POO]	–		
	V_{1N}	–	[ONN]		
V_2	V_{2P}	[PPO]	–		
	V_{2N}	–	[OON]		
V_3	V_{3P}	[OPO]	–		
	V_{3N}	–	[NON]		
V_4	V_{4P}	[OPP]	–		
	V_{4N}	–	[NOO]		
V_5	V_{5P}	[OOP]	–		
	V_{5N}	–	[NNO]		
V_6	V_{6P}	[POP]	–		
	V_{6N}	–	[ONO]		
V_7		[PON]		Medium vector	$\frac{\sqrt{3}}{3}V_{dc}$
V_8		[OPN]			
V_9		[NPO]			
V_{10}		[NOP]			
V_{11}		[ONP]			
V_{12}		[PNO]			
V_{13}		[PNN]		Large vector	$\frac{2}{3}V_{dc}$
V_{14}		[PPN]			
V_{15}		[NPN]			
V_{16}		[NPP]			
V_{17}		[NNP]			
V_{18}		[PNP]			

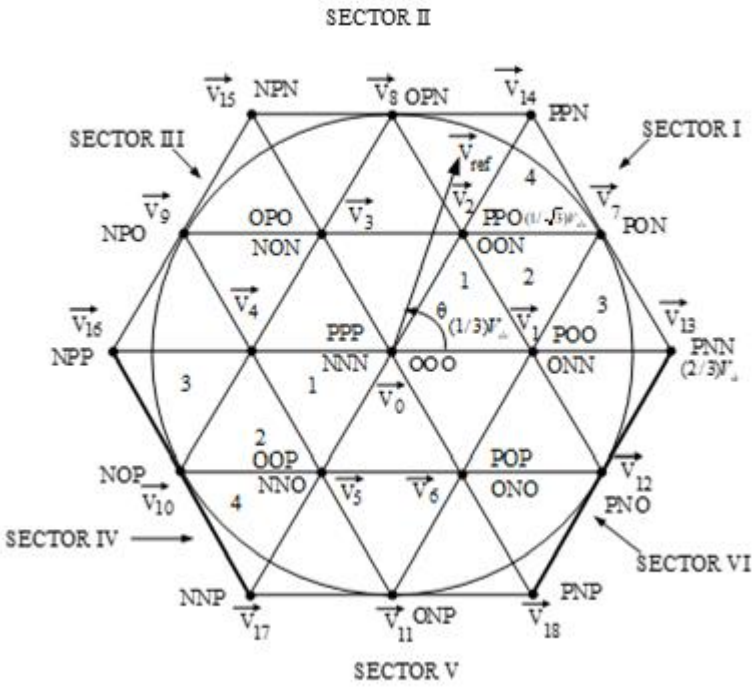

Figure 3. 7: Three-level inverter voltage vectors. (Wu & Narimani, 2017)

3.3.2.4 Space Vector PWM (SVPWM)

As shown in Figure 3.8, the diagram representing the voltage vector of a three-level inverter is distributed into six sectors which are referred to as Sectors I to VI. Each sector can be subdivided into four parts known as areas one to four.

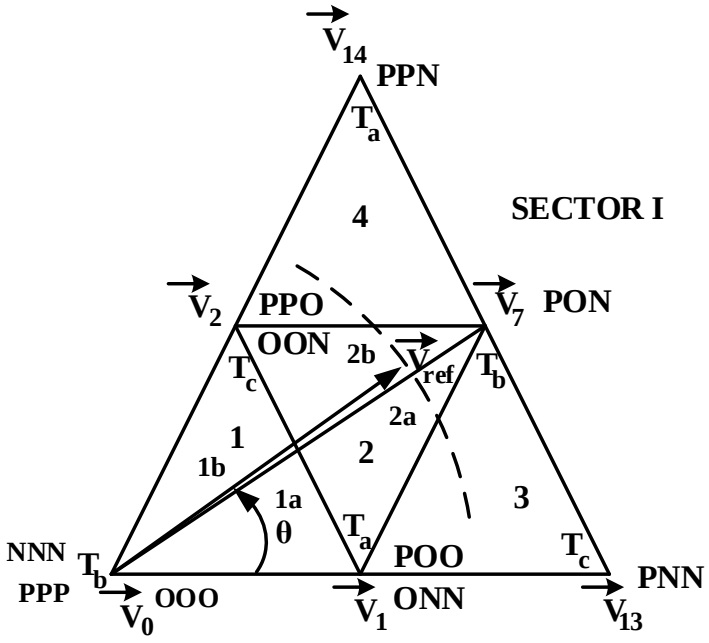

Figure 3. 8: Command voltage vectors in Sector 1.

In the space vector PWM technique, the control voltage vector is obtained by the output voltage of the three-level inverter using steps below:

i. determination of the Sector and area of the command voltage vector;
ii. determination of the actual vector for producing the control voltage vector and
iii. calculate the time of the selected actual vectors, however, prior to the calculation, the control voltage vector is obtained based on the amplitude ($\mathrm{V_{ref}}$) and phase (θ) as expressed in Equation 3.15:

$$\vec{V}_{ref} = V_{ref} e^{j\theta} \tag{3.15}$$

Equation 3.16 is established when the amplitude and phase of the chosen voltage vectors $\mathrm{V_1}$, $\mathrm{V_2}$, and $\mathrm{V_7}$ are utilised.

$$\begin{aligned} \overrightarrow{V_1} &= \frac{1}{3} V_{dc} \\ \overrightarrow{V_2} &= \frac{1}{3} V_{dc} e^{j\pi/3} \quad , \\ \overrightarrow{V_7} &= \frac{\sqrt{3}}{3} V_{dc} e^{j\pi/6} \end{aligned} \tag{3.16}$$

The time of the chosen valid vectors was determined in such a way that the average output voltage throughout a switching period ($\mathrm{T_S}$) turns into the control voltage vector ($\mathrm{V^*}$). Hence, Equations 3.17-3.18 need to be fulfilled:

$$\overrightarrow{V_{ref}} T_s = \overrightarrow{V_1} T_1 + \overrightarrow{V_2} T_2 + \overrightarrow{V_7} T_7 \tag{3.17}$$

$$T_s = T_1 + T_2 + T_7 \tag{3.18}$$

where T_1 , T_2 , and T_7 represents the switching time of the chosen voltage vector V_1, V_2 and V_7 respectively.

By substituting Equation 3.15 and Equation 3.16 into Equation 3.17, Equation 3.19 is obtained as follows:

$$V_{ref} e^{j\theta} T_s = \frac{1}{3} V_{dc} T_1 + \frac{\sqrt{3}}{3} V_{dc} e^{j\pi/6} T_2 + \frac{1}{3} V_{dc} e^{j\pi/3} T_7 \tag{3.19}$$

Equation 3.19 can be expressed in complex form as the real part (R_e) and imaginary part (IM) as follows:

$$V_{ref}(cos\theta + sin\theta)T_s = \frac{1}{3}V_{dc}T_1 + \frac{\sqrt{3}}{3}V_{dc}(cos\frac{\pi}{6} + sin\frac{\pi}{6})T_2 + \frac{1}{3}V_{dc}(cos\frac{\pi}{3} + sin\frac{\pi}{3})T_7 \quad (3.20)$$

$$Re: T_1 + \frac{3}{2}T_2 + \frac{1}{2}T_7 = 3\frac{V_{ref}}{V_{dc}}(cos\theta)T_s$$

$$Im: \tfrac{3}{2}T_2 + \tfrac{\sqrt{3}}{2}T_7 = 3\tfrac{V_{ref}}{V_{dc}}(sin\theta)T_s \quad (3.21)$$

When Equation 3.21 is substituted into Equation 3.20, the actual switching time of the V_1, V_2, and V_7 voltage vectors in Sector I area 2 are expressed in Equation 3.22 as:

$$T_1 = T_S[1 - \tfrac{2V_{ref}}{V_{dc}}\sin\theta]$$

$$T_2 = T_S[\tfrac{2V_{ref}}{V_{dc}}sin\left(\tfrac{\pi}{3} + \theta\right) - 1] \quad (3.22)$$

$$T_7 = T_S[1 - \tfrac{2V_{ref}}{V_{dc}}sin\left(\tfrac{\pi}{3} - \theta\right)]$$

The chosen valid vectors in Sector **I**-area 2 are produced for the calculated effective switching time. In Sector **I** , the effective vectors and effective switching time depending on the area are determined using equations as shown in Table 3.5.

Table 3. 5: Chosen valid vector and actual switching time in sector I.

Area	T_x		T_x		T_x	
1	V_1	$T_S[\frac{2V_{ref}}{V_{dc}}sin\left(\frac{\pi}{3} - \theta\right)]$	V_0	$T_S[1 - \frac{2V_{ref}}{V_{dc}}sin\left(\frac{\pi}{3} + \theta\right)]$	V_2	$T_S[\frac{2V_{ref}}{V_{dc}}sin\theta]$
2	V_1	$T_S[1 - \frac{2V_{ref}}{V_{dc}}\sin\theta]$	V_7	$T_S[\frac{2V_{ref}}{V_{dc}}sin\left(\frac{\pi}{3} + \theta\right) - 1]$	V_2	$T_S\left[1 - \frac{2V_{ref}}{V_{dc}}sin\left(\frac{\pi}{3} - \theta\right)\right]$
3	V_1	$T_S[2 - \frac{2V_{ref}}{V_{dc}}\sin(\frac{\pi}{3} + \theta)]$	V_7	$T_S[\frac{2V_{ref}}{V_{dc}}sin\theta]$	V_{13}	$T_S[\frac{2V_{ref}}{V_{dc}}sin\left(\frac{\pi}{3} - \theta\right) - 1]$
4	V_{14}	$T_S[\frac{2V_{ref}}{V_{dc}}sin\theta - 1]$	V_7	$T_S[\frac{2V_{ref}}{V_{dc}}sin\left(\frac{\pi}{3} - \theta\right)]$	V_2	$T_S[2 - \frac{2V_{ref}}{V_{dc}}\sin(\frac{\pi}{3} + \theta)]$

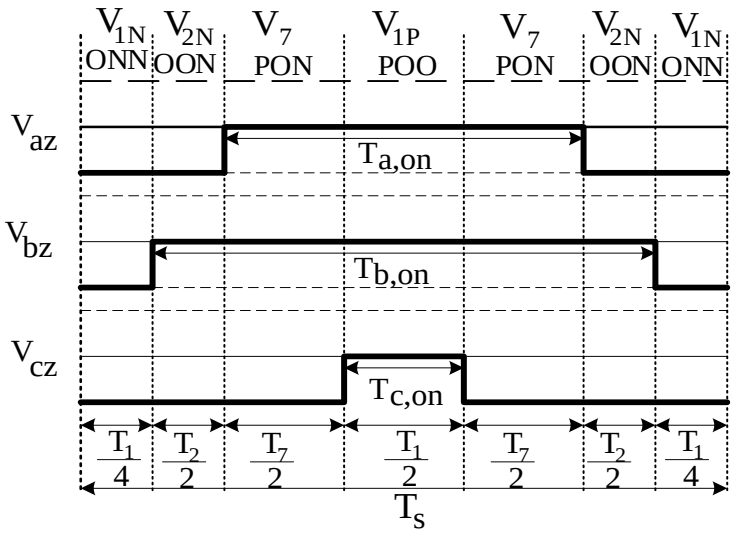

Figure 3. 9: Switching succession in Sector I area 2a. (Pereira & Martins, 2009)

1. Determination of the output order of the chosen valid vectors; two aspects must be considered in the output order of the chosen valid vectors. For the first, one switching needs to be performed during a switching period T_S to obtain a stable switching frequency, while for the second, since N-type and P-type can be chosen as small vectors, the N-type and P type small vectors need to be disposed evenly. Figure 3.9 depicts the correct vector and its actual switching time in Sector I-area 2a. The output order of the valid vectors is V_{1N} , V_{2N}, V_7, V_{1P}, V_7, V_{2N} and V_{1N} , and the small vector is separated into P-type and N-type. Each leg output state turns with the output order of the actual vectors based on the time, and individual four phases switches on and off based on the output state. Since the actual switching time is determined so as the average output voltage during (T_S) is equal to the control voltage vector (V^*), the output order of the valid vectors must not to be taken into account. However, a stable switching frequency permits an easy implementation and simplifies the selection of frequency of the attenuation target in the filter design. Moreover, positioning the P-type and N-type small vectors evenly assists in maintaining the neutral-point voltage at equilibrium.

3.3.2.5 Carrier-Based PWM

Space vector PWM technique performs different control objectives by modifying the voltage vector selection technique. DTC (Direct Torque Control) (Lee et al., 2005) can also be considered as a type of space voltage PWM technique. Nevertheless, the space vector PWM technique involves complex equations and processes prior to the generation of the output voltage. A probable solution is to utilise a carrier-based PWM method, where the switching state of each individual switch is obtained through comparison of the triangular carrier and the control voltage as shown in Figure 3.11, and different control objectives may be performed based on how the control voltage is

changed. The control voltage for the carrier-based PWM technique in the three-level inverter may be produced by using Sinusoidal PWM (SPWM), PWM techniques based on the offset voltage, and Third Harmonic Injection PWM (TH-PWM).

Three-leg control voltages ($V_{a,ref}$, $V_{b,ref}$, and $V_{c,ref}$) are expressed as follows (Lee & Lee, 2017):

$$V_{a,ref} = V_{mag}\cos(2\pi f_f t)$$

$$V_{b,ref} = V_{mag}\,cos(2\pi f_f t - 2\pi/3) \quad (3.23)$$

$$V_{b,ref} = V_{mag}\,cos(2\pi f_f t + 2\pi/3)$$

where V_{mag} is the amplitude of the control voltage and f_f is the fundamental signal frequency.

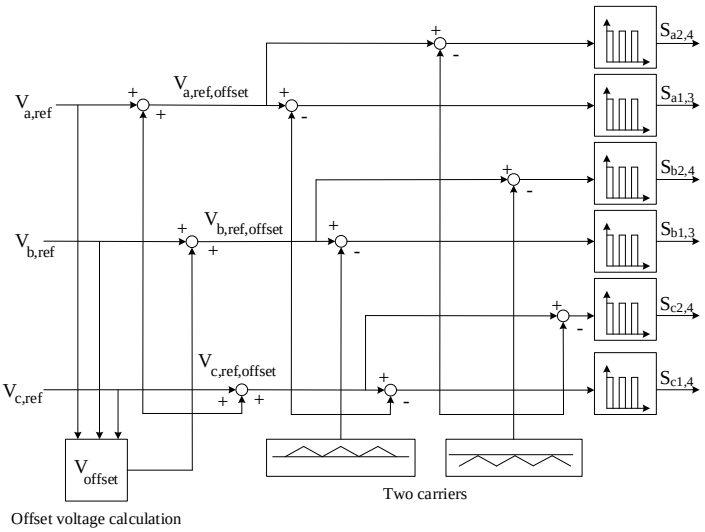

Figure 3. 10: Carrier-based PWM technique based on the offset voltage.

The offset voltage (V_{offset}) is utilised to enhance the voltage modulation range and is given as:

$$V_{offset} = \frac{V_{ref,max}+V_{ref,min}}{2} \quad (3.24)$$

where $V_{ref,max}$ and $V_{ref,min}$ are the largest value of the three-leg control voltages and the smallest voltage of the three-leg control voltages respectively.

The offset voltage (V_{offset}) given in Equation 3.24 is added to the three-leg control voltage in Equation 3.25.

$$V_{a,ref,offset} = V_{a,ref} + V_{offset}$$
$$V_{b,ref,offset} = V_{b,ref} + V_{offset} \quad (3.25)$$
$$V_{c,ref,offset} = V_{c,ref} + V_{offset}$$

The technique of producing the control voltage in the PWM technique based on the offset voltage is similar to the two-level inverter. However, contrary to two-level inverter where the control voltage is compared to a carrier, in a three-level inverter, two carriers are compared with the control voltage to generate an output voltage. The on-off functioning of the four switches in one leg is obtained through comparison of the control voltage with two carriers positioned in parallel (Figure 3.11a) and is expressed as the:

- above carrier signals identify the complementary switch states of S_{X1} and S_{X2}

  Carrier $<$ control voltage: S_{X1} (ON), S_{X3} (OFF)
  Carrier $>$ control voltage: S_{X1} (OFF), S_{X3} (ON)

- following carrier signals identify the complementary switch states of S_{X2} and S_{X4}

  Carrier $<$ control voltage: S_{X2} (ON), S_{X4} (OFF)
  Carrier $>$ control voltage: S_{X2} (OFF), S_{X4} (ON)

When an offset voltage PWM technique is being utilised in a practical system, a carrier function produced by a Micro Controller Unit (MCU) is utilised. However, this carrier function is not realised in parallel with a single triangular function. To solve this problem, two control voltages are produced (Figure 3.11b), so as only a carrier is utilised. One of the two control voltages is compared to the carrier for the complementary on-off operations of S_{X1} and S_{X3} and the other control voltage is compared with the carrier for the complementary on-off operations of S_{X2} and S_{X4} .

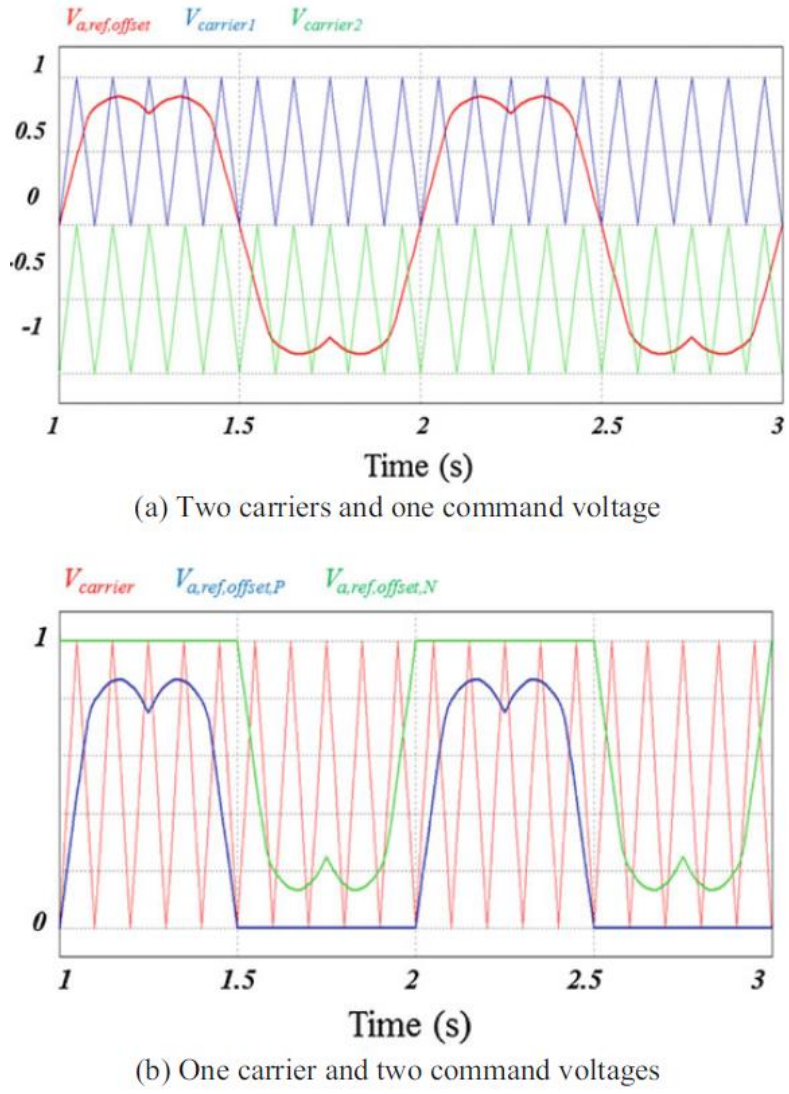

Figure 3. 11: PWM technique using carrier signals in three-level inverter: (a) one control voltage and two carriers, (b) Two control voltages and one carrier. (Lee & Lee, 2017)

3.3.2.6 Fluctuation of Neutral Point Voltage

The three-level inverter has two DC capacitors, the input and output characteristics consider that half of the total DC capacitor voltage is applied to each of the DC capacitors (neutral-point voltage equilibrium state). Neutral-point voltage refers to the difference between two DC capacitor voltages. The PWM methods of a three-level inverter require the consideration of the change in the neutral-point voltage, and each switching state creates different changes in the neutral-point voltage as shown in Figure 3.12.

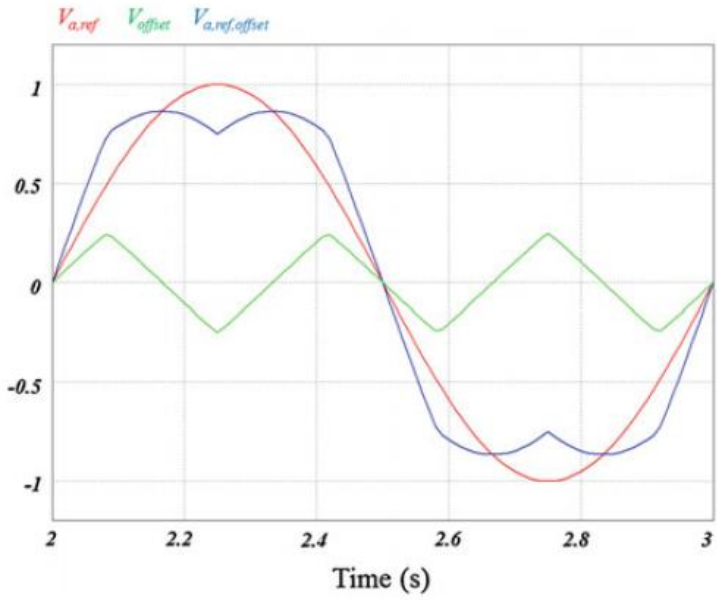

Figure 3. 12: Comparison of SPWM and PWM technique control voltages based on offset voltage. (Lee & Lee, 2017)

The voltage vector promptly influencing the neutral-point voltage is a small vector. During the three-level inverter operation, the small vector of P-type decreases both the topmost and bottom capacitor voltages. Similarly, the N-type small vector increases both the topmost and bottom capacitor voltages. The medium vector is not immediately connected to the modification in the neutral-point voltage. However, it implicitly impacts the modification in the neutral-point voltage based on the output current state. Moreover, the large vector does not impact the modification of the neutral-point voltage by producing similar voltage change in the two DC capacitor voltages.

Additionally, the zero vector has no modification on the neutral-point voltage. In case of a three-level rectifier, the modification in the two DC capacitor voltages as a result of small and medium vectors is contrary to the three-level inverter. Although neutral-point voltage equilibrium is taken into account in the PWM technique of the three-level converter, the unbalance of the neutral voltage can result from divers causes including the disparities in the capacitance of DC short capacitors produced during the manufacturing stage, the features of individual switching devices, and disparities of switching on-off points.

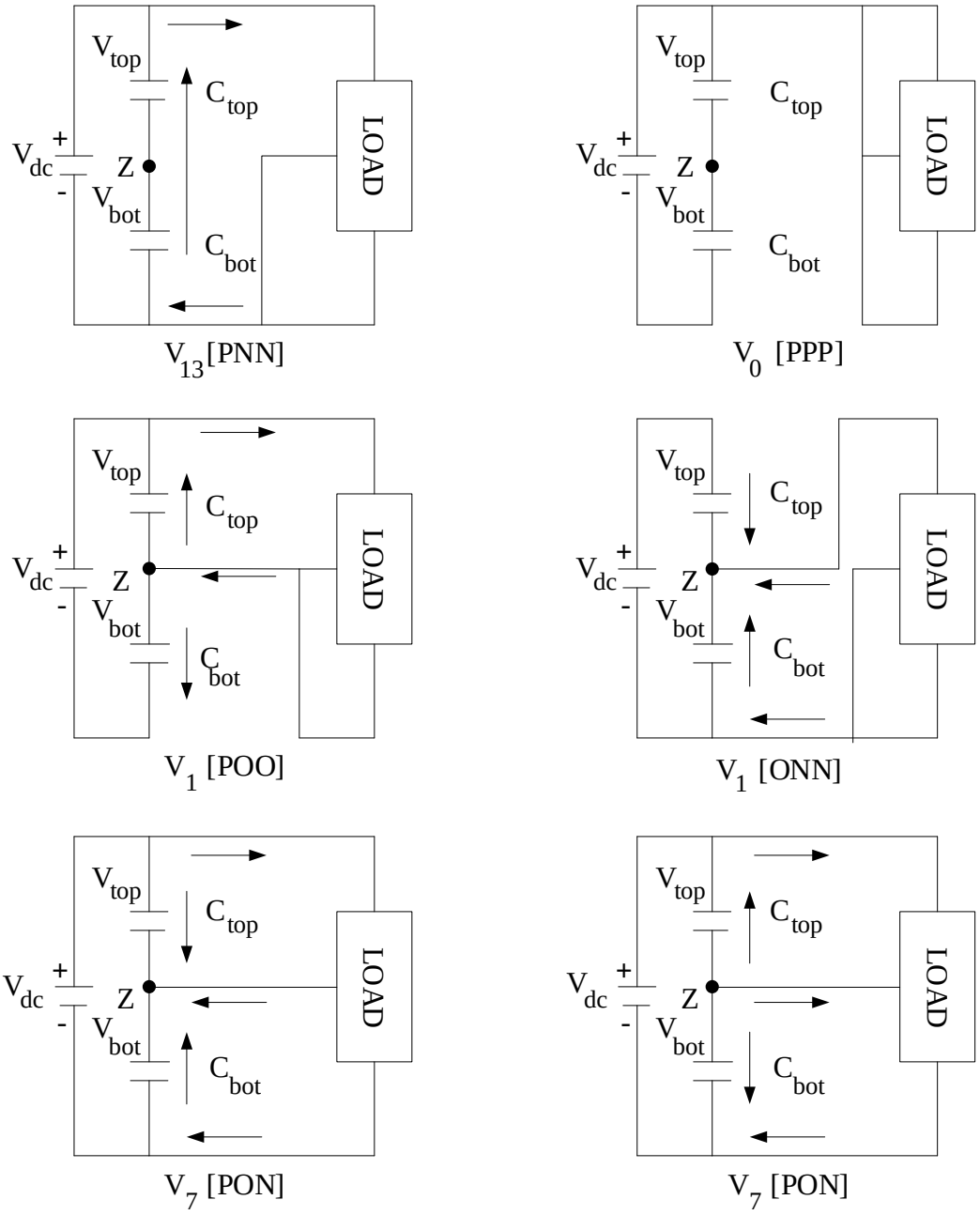

Figure 3. 13: Modification of the neutral point voltage based on three-level inverter voltage vector type. (Lee & Lee, 2017)

3.3.2.7 Design parameters of the inverter

The parameters used in the design of the inverter are given in Table 3.6; the DC input power to the inverter is 1.2 MW, while the voltage at the DC link side is 1400 V. On the hand, the expected phase to phase voltage of the inverter is 600 V, with a phase RMS current of 2000 A.

Table 3. 6: Parameters design of the inverter.

Output DC power of Fuel cell P_{DC}	1.54 MW
DC-Link Voltage V_{DC}	1400 V
Output power of the Inverter V_{DC}	1.2 MW
Phase to phase inverter voltage before filter	1400 V
Phase to ground inverter voltage before filter	930 V
Phase to phase inverter voltage V_{LL} after filter	600 V
Phase to ground inverter voltage V_{PH} after filter	347 V
Inverter current I_{rms} after filter	1200 A
Power factor P_f	0.85
Peak to peak current I_{max}	1630.22 A
PWM carrier frequency I_{max}	2000 Hz
Grid frequency f_g	50 Hz
Modulation range m_a	0.7
Attenuation factor K_a	20%
Grid acceptable maximal power factor variation X	5%
Inverter configuration 3φ	Three-phase

3.3.3 Modelling the Filter

A typical inverter is a source of harmonics as in general its output is not a pure sine wave. Standards including IEEE 519 and IEC 61000-3-6 define the allowable harmonic distortion for the current and voltage of a power system as a function of the current and voltage level respectively. In Table 3.7, the allowable total harmonic distortion of the voltage is defined based on voltage levels, while the current total demand distortion limit is expressed as a function of the ratio of the short-circuit current to the rated load current and the voltage level (Table 3.8). The total harmonic distortion is defined in IEEE 519-2014 as the ratio of the root mean square of the harmonic content, considering harmonic components up to the 50th order and specifically excluding inter harmonics, expressed as a percent of the fundamental.

Table 3. 7: Voltage THD limits based on IEEE 519-2014. (Sahoo & Subudhi, 2018)

Bus Voltage V at PCC	Individual harmonic (%)	Total harmonic distortion
V≤1.0 kV	5.0	8.0
1 kV<V≤68 kV	3.0	5.0
69 kV<V≤161 KV	1.5	2.5
161 kV<V	1.0	1.5[a]

On the other hand, the total demand distortion is defined as the ratio of the root mean square of the harmonic content, considering harmonic components up to the 50th order and specifically excluding inter harmonics (Table 3.9).

Table 3. 8: Current distortion limits according to IEEE 519-2014. (Sahoo & Subudhi, 2018)

Voltage	$I_{sc}/I(load)$	TDD (%)	< 11	$11 \leq h < 17$	$17 \leq h < 35$	$35 \leq h < 50$
$< 69\,\mathrm{kV}$	< 20	5	4	2	1.5	0.6
	$20 - 50$	8	7	3.5	2.5	1
	$50 - 100$	12	10	4.5	4	1.5
	$100 - 1000$	15	12	5.5	5	2
	> 1000	20	15	7	6	2.5
$69 - 161\,\mathrm{kV}$	< 20	2.5	2	1	0.75	0.3
	$20 - 50$	4	3.5	1.75	1.25	0.5
	$50 - 100$	6	5	2.25	2	0.75
	$100 - 1000$	7.5	6	2.75	2.5	1
	> 1000	10	7.5	3.5	3	1.25
$> 161\,\mathrm{kV}$	< 25	1.5	1	0.5	0.38	0.1
	$25 - 50$	2.5	2	1	0.75	0.3
	≥ 50	3.75	3	1.5	1.15	0.45

Table 3. 9: IEC 61000-3-6 voltage harmonic limits. (Sahoo & Subudhi, 2018)

Odd harmonics non-multiple			Odd harmonics non-multiple of three (%)			Even harmonics (%)		
h	MV	HV-EHV	H	MV	HV-EHV	H	MV	HV-EHV
5	5	2	3	4	2	2	1.8	1.4
7	4	2	9	1.2	1	4	1	0.8
11	3	1.5	15	0.3	0.3	6	0.5	0.4
13	2.5	1.5	21	0.2	0.2	8	0.5	0.4
$17 \leq h < 35$	$1.9\frac{17}{h}$ -0.2	$1.2\frac{17}{h}$	$21 \leq h < 45$	0.2	0.2	$10 \leq h < 50$	$0.25\frac{10}{h}$ +0.2	$0.19\frac{10}{h}$ +0.16

3.3.3.1 LCL Filter

The main function of the LCL filter is to reduce high – order harmonics on the output side of the inverter. However, poor design may cause an increase in distortion. Figure 3.14 depicts a typical layout of an LCL filter, where L_i is the inverter side inductor, L_g is the grid – side inductor, R_i and R_g are inductors series resistance, C_f is the filter capacitance, R_d is the damping resistance, V_i is the inverter input voltage , V_g is the output voltage of the system (grid voltage), I_i is the inverter output current, I_g is the grid current and I_c is the capacitor current.

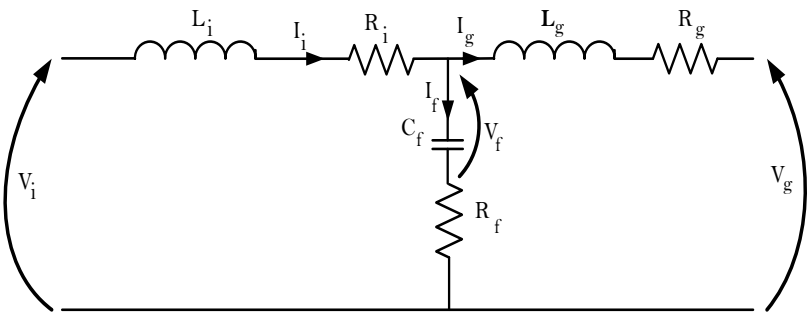

Figure 3. 14: LCL filter layout

The filter transfer function can be expressed as (Azani et al., 2016):

$$\boldsymbol{H_{LCL}} = \frac{\boldsymbol{I_g}}{\boldsymbol{V_i}}, \tag{3.26}$$

and, the grid voltage is considered as an ideal voltage source able to dump all the harmonic frequencies. For $V_g = 0$, the transfer function will be (Azani et al., 2016):

$$\boldsymbol{H_{LCL}} = \frac{\mathbf{1}}{\boldsymbol{L_i L_g C_f S^3 + (L_i + L_g) S}} \tag{3.27}$$

With dumping resistance, the transfer function can be, furthermore, expressed as (Azani et al., 2016):

$$\boldsymbol{Hd_{LCL}} = \frac{\boldsymbol{C_f R_d S + 1}}{\boldsymbol{L_i C_f S^3 + C_f (L_i + L_g) R_d S^2 + (L_i + L_g) S}} \tag{3.28}$$

The proposed design refers to the method adopted by (Reznik et al., 2014). Various characteristics need to be considered in the design of an LCL filter namely current ripples, switching ripple attenuation and filter size. The reactive power demands may provoke a resonance of the capacitor that interacts with the grid. Thus, passive or active damping need to be considered through the use of a resistor in series with the capacitor (Bouchafaa et al., 2010; Liu et al., 2016). In this research, the passive damping option has been adopted.

The parameters below are required when designing the filter:

i. V_{LL}, Phase to phase voltage (inverter output)
ii. P_n, Nominal power
iii. V_{DC}, DC-link voltage
iv. V_g, Grid voltage
v. f_{SW}, Switching frequency
vi. f_{res}, Resonance frequency

The base impedance (Z_b) and base capacitance (C_b) are given by Equation 3.29 and Equation 3.30 respectively (Novak et al., 2015):

$$Z_b = \frac{U_n^2}{P_n} \tag{3.29}$$

$$C_b = \frac{1}{W_g Z_b} \tag{3.30}$$

The filter capacitance (C_f) serving as a sink for high frequency harmonics is obtained by setting a percentage of not more than 5% of the base capacitance (C_b). The filter capacitance is given as:

$$C_f = X.C_b \tag{3.31}$$

The inverter maximum current ripple is given by Equation 3.32 (Reznik et al., 2014):

$$\Delta I_{Lmax} = \frac{2V_{DC}}{3L_i}(1-m)mT_{SW} \tag{3.32}$$

In which, L_i denotes the inductor at the inverter side, $T_{SW} = \frac{1}{f_{SW}}$ period, and (m) the inverter modulation; usually between 0 and1. In this study, m is considered equal to 0.77. In Equation 3.35, if m=0.77, ΔI_{Lmax} will become:

$$\Delta I_{Lmax} = \frac{0.49*V_{DC}}{3L_i f_{SW}} \tag{3.33}$$

Inverter side current ripple (ΔI) percentage must be between 10 and 25% (Yao et al., 2017) of the maximum rated output current (I_{max}), thus, ΔI_{Lmax} can be expressed as (Buau et al., 2018):

$$\Delta I_{Lmax} = (1\% - 5\%) * I_{max} \tag{3.34}$$

In this study the percentage is considered as 1% so that $\Delta I_{Lmax} = 0.01 I_{max}$.

where

$$I_{max} = \frac{P_n\sqrt{2}}{3V_{ph}} \tag{3.35}$$

From Equation 3.32, L_i can be expressed as:

$$L_i = \frac{0.49V_{DC}}{3\Delta I_{Lmax} * f_{SW}} \tag{3.36}$$

The LCL filter must mitigate the current ripple to 20%, resulting in a ripple current of about 5 % of the output current (Reznik et al., 2014). Equation 3.37 relates the harmonic current produced by the inverter as a function of grid harmonic current as:

$$\frac{I_g(h)}{I_i(h)} = \frac{1}{\left|1+r\left[1-L_i C_b \omega_{SW}^2 X\right]\right|} K_a \tag{3.37}$$

In which, K_a is the expected attenuation and r refers to the ratio to the inductance at the inverter side to that of the grid side. This ratio can be expressed as:

$$L_i = rL_g \tag{3.38}$$

The grid inductance is given by Equation 3.39 as follows:

$$L_g = \frac{\sqrt{\frac{1}{K_a^2}}+1}{C_f \omega_{SW}^2} \tag{3.39}$$

The resonant frequency $\boldsymbol{\omega_{res}}$ and the damping ratio (ζ) of the LCL filter are given as (Kantar et al., 2014):

$$\omega_{res} = \sqrt{\frac{L_i+L_g}{L_i L_g C_f}} \tag{3.40}$$

$$\zeta = \frac{C_f \omega_{res} R_d}{2} \tag{3.41}$$

The resonant frequency for the LCL filter is determined as:

$$f_{res} = \frac{1}{2\pi}\sqrt{\frac{L_i+L_g}{L_i L_g C_f}} \tag{3.42}$$

The resonance frequency f_{res} is chosen not to be closer to zero as unstable region operation may occur near zero, hence, the key point is in determining the proportion of f_{res} to sampling frequency f_{samp}. The critical frequency f_{crit} of the filter is expressed in Equation 3.43 as follows (Zhong & Hornik, 2013):

$$f_{crit} = \frac{\pi}{3} f_{samp} \frac{1}{2\pi} = \frac{f_{samp}}{6} \tag{3.43}$$

The value of the critical frequency is always 16.7 % of the sampling frequency (Zhong & Hornik, 2013), thus, choice of the resonance frequency depends on Equation 3.44 given as follows:

$$\frac{f_{res}}{f_{samp}} = 0.10 \sim 0.12 \tag{3.44}$$

This frequency is always set to satisfy Equation 3.45 given as (Mahlooji et al., 2018):

$$10f_g < f_{res} < 0.5f_{SW} \tag{3.45}$$

In case Equation 3.45 is not satisfied, parameters must be recalculated, and the damping resistor is expressed as (Mahlooji et al., 2018):

$$R_d = \frac{1}{3\omega_{res}C_f} \tag{3.46}$$

3.3.3.2 Designed LCL Filter parameters

Table 3.10 provides the designed parameters of the LCL filter using the algorithm depicted in Figure 3.15

Table 3. 10: Designed LCL filter parameter values.

Filter		
Inverter Side inductor	L_i	$0.9\ \mathrm{mH}$
Grid side inductor	L_g	$0.072\ \mathrm{mH}$
Capacitor filter	C_f	$531\mu F$
Damping Resistor	R_f	$0.118\ \Omega$
Resonant frequency	f_{res}	$845\ \mathrm{Hz}$
Inductors resistances	$R_i = R_g$	0.00761Ω
Sampling frequency	f_S	10000 Hz
Crossover frequency	f_C	254 Hz

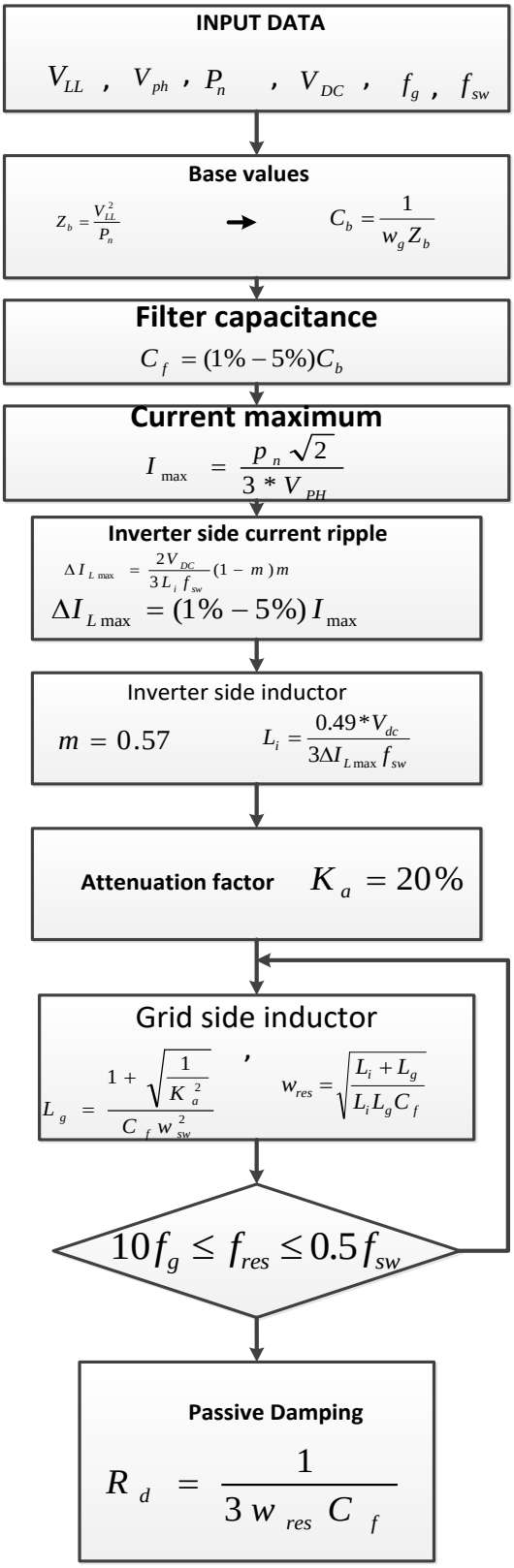

Figure 3. 15: LCL filter design flowchart. (Benzazah et al., 2015)

3.3.4 Modelling the Inverter Control

The primary function of an inverter control consists of properly supplying the extracted power either to a load connected at the output on the inverter, or to the grid if the inverter is grid-tied. This function is realised by using a dual-loop control of the current whereby the outer control loop might be a DC-link voltage control or a power control loop producing the inner current references (Figure 3.16).

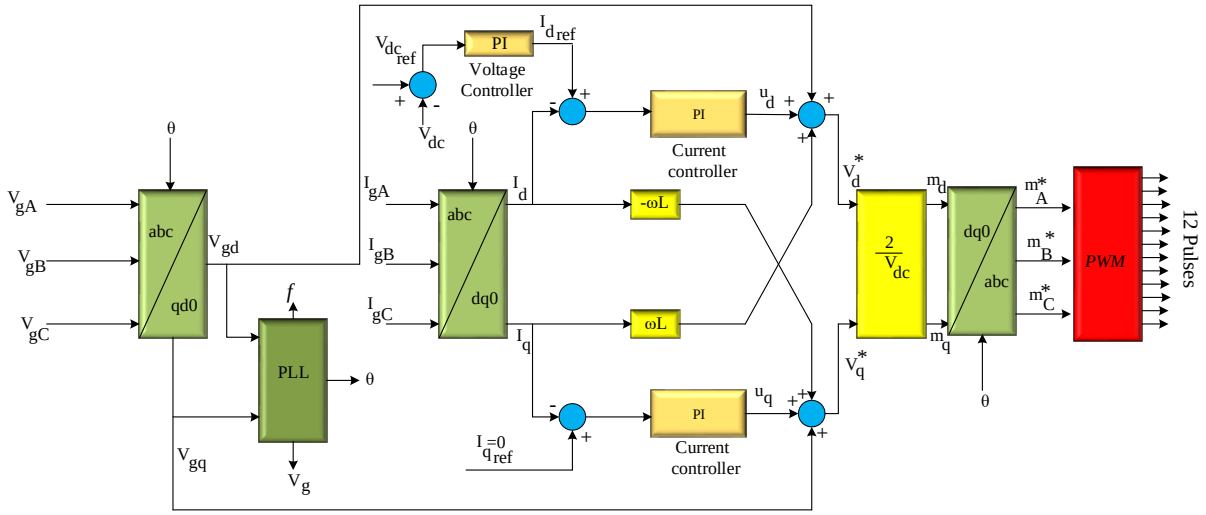

Figure 3. 16: Schematic diagram of the inverter control. (Esmaeilian et al., 2014)

The inner control loop could be developed in various reference frames; hence, the transformations of the reference frame are primarily presented.

3.3.4.1 Reference frame transformations

In a three-phase two-level inverter, there are two sets of AC variables namely the voltage V_{abc} and the current I_{abc}. If the system is balanced, the three-phase variables with a phase difference of 120 degrees can be expressed by a two phase in quadrature system as follows(Zou et al., 2018; Dhar & Dash, 2016):

$$[x_\alpha \quad x_\beta]^T = C[x_a \quad x_b \quad x_c]^T \tag{3.47}$$

where x represents the voltage or current of the system, a, b and c are the phase variables in the abc-reference frame, α and β are the variables in the stationary $\alpha\beta$ reference frame and C is the Clarke transformation matrix defined as (Tarasantisuk et al., 2016):

$$C = \frac{2}{3}\begin{bmatrix} 1 & \frac{1}{2} & -\frac{1}{2} \\ 0 & \frac{\sqrt{3}}{2} & -\frac{\sqrt{3}}{2} \end{bmatrix} \tag{3.48}$$

Hence, by using the Clarke transformation, the AC variables are transformed into two perpendicular AC variables, which decrease the complexity when designing the controller. However, in case of PI controllers, zero-tracking errors cannot be ensured. Consequently, the AC variables in the stationary $\alpha\beta$ reference frame are linked to the synchronous rotating dq reference frame, in which the resultant dq variables are DC values. The resulting transformation is the Park transformation given as (Vu et al., 2012):

$$[x_d \quad x_q]^T = \mathrm{P}[x_\alpha \quad x_\beta]^T \tag{3.49}$$

The indexes d and q are the transformed variable in the d and q axis respectively, and P represents the Park transformation matrix of the system voltage phase θ as (Spanias & Lestas, 2019):

$$P = \begin{bmatrix} \cos\theta & \sin\theta \\ -\sin\theta & \cos\theta \end{bmatrix} \tag{3.50}$$

where $\theta = \omega t$ and ω is the system angular frequency.

Therefore, Park transformation permits the PI controllers use when the phase information is required as shown in Figure 3.17.

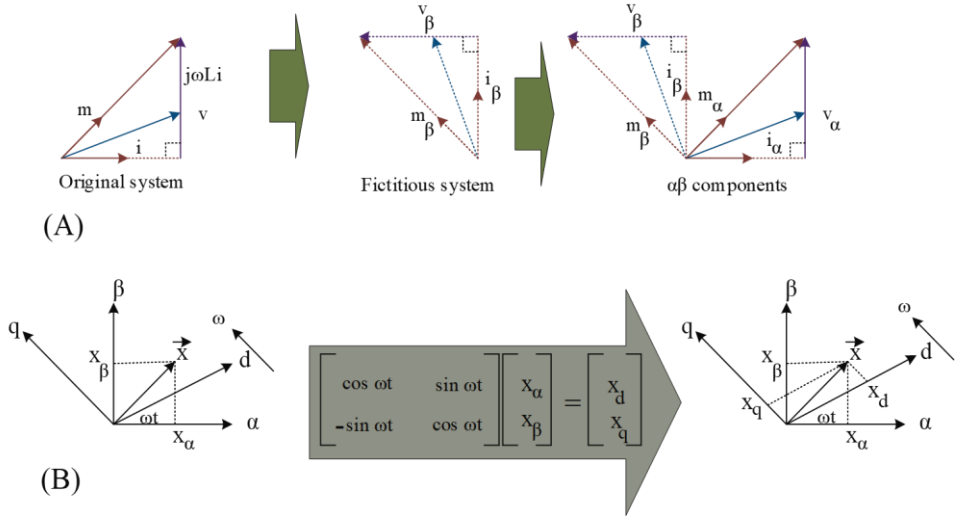

Figure 3. 17: Single-phase systems Park transformation (A) perpendicular system generation and (B) Park transformation. (Teodorescu et al., 2011)

3.3.4.2 Outer control loop

For grid connection of voltage source inverters, a capacitive DC link is required to balance the DC input power and the AC output power. The larger the power injected to the grid, the higher the current will be. Hence, one alternative to control the active power of the inverter is through the control of the DC-link voltage across the capacitor (Blaabjerg et al., 2006), as depicted in Figure 3.18. The DC-link voltage is kept constant in grid-connected alternative energy systems, especially, in case of double-stage configurations where the DC-link voltage is controlled at a desired level. To guarantee an appropriate power injection to the grid, the DC-link voltage must be at least higher than the grid peak voltage. However, the controllability of the active power through the DC-link voltage control can be detailed based on the power balance.

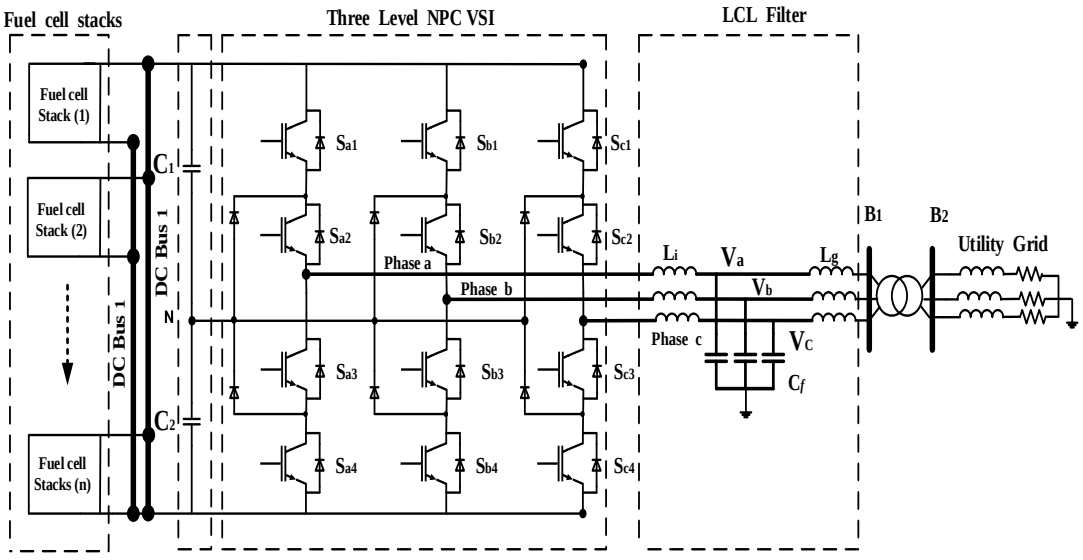

Figure 3. 18: Three-phase three-level diode clamped inverter schematic. (Ben Hamad et al., 2019)

By considering the inverter power losses as negligible, the DC power and the active power were made similar. Therefore, the relation below can be written (Roy & Mahmud, 2017):

$$\begin{cases} P_{dc} = v_{dc} i_{dc} - v_{dc} C_{dc} \frac{dv_{dc}}{dt} \\ P_{ac} = \frac{3}{2}(v_d i_d + v_q i_q) \end{cases} \qquad (3.51)$$

$$v_{dc} i_{dc} - v_{dc} C_{dc} \frac{dv_{dc}}{dt} = \frac{3}{2}(v_d i_d + v_q i_q)$$

In which v_{dc}, I_{dc} and P_{dc} are the DC link voltage, inverter input current and power respectively, P_{ac} is the grid active power, and v_{dq} and I_{dq} are the dq variables of the voltage and current of the grid.

Whenever the d-axis of the synchronous rotating frame lines up with the grid voltage, the q-axis voltage is equal zero, ($v_q = 0$) hence, the d-axis voltage is equal to the phase voltage magnitude ($v_d = v_m$ where v_m denotes the phase voltage magnitude).

For the linearisation of the model in Equation 3.52, the small-signal analysis is used, leading to (Al-Shetwi et al., 2018):

$$v_{dc}(S) = G_{P-dc}(S)I_d(s) = \frac{3}{2}\frac{V_m}{I_{dc}-SC_{dc}V_{dc}}.I_d(S) \tag{3.52}$$

where V_{dc} is the average DC-link voltage, I_{dc} the input current, and $G_{P-dc}(S)$ is the DC-link voltage.

Therefore, a PI controller may be used to control the DC-link voltage for the generation of the d-axis current reference given in Equation 3.53 (Vukosavic, 2018):

$$I_d^* = G_{PI-dc}(s)(V_{dc}^* - V_{dc}) \tag{3.53}$$

where $G_{PI-dc}(S)$ represents the PI controller of the DC-link voltage control loop.

Figure 3.19 depicts the outer control loop, where $G_{CL-d}(S)$ is the closed loop current control for the d-axis current. Nevertheless, the system model has the input current, making the design difficult. To decouple this when $v_d = v_m$, $v_q = 0$, and small DC-link voltage changes, the model in Equation 3.52 is given (Chen et al., 2014):

$$C_{dc}\frac{dv_{dc}}{dt} = -\frac{3}{2}\frac{V_m}{v_{dc}}i_d + i_{dc} \tag{3.54}$$

hence, the DC-link voltage is (Al-Shetwi et al., 2018):

$$v_{dc}(s) = -\frac{3}{2}\frac{V_m}{V_{dc}C_{dc}s}i_d(s) + \frac{1}{C_{dc}s}i_{dc}(s) \tag{3.55}$$

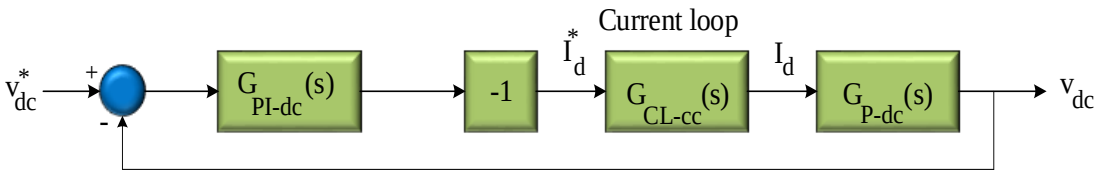

Figure 3. 19: Outer control loop. (Teodorescu et al., 2011)

Consequently, the DC-link plant may be represented as depicted in Figure 3.20. A PI controller given in Equation 3.56 is adopted (Hani et al., 2017):

$$G_{PI-dc}(s) = K_P - dc(\,1 + \frac{1}{T_{i-dc}s}\,) \tag{3.56}$$

where K_{P-dc} is the proportional gain and T_{i-dc}, the integrator time constant of the PI controller.

The closed-loop current control can be given by (Kun-qi et al., 2017):

$$G_{CL-CC}(S) = \frac{1}{1+3T_s s} \tag{3.57}$$

where T_s is the control system sampling period.

The open-loop control of the DC-link voltage can be expressed as:

$$G_{OL-dc}(s) = \frac{3V_m}{2V_{dc}} \frac{1}{C_{dc}s} \frac{K_{P-dc}(1+T_{i-dc}s)}{T_{i-dc}s} \frac{1}{1+3T_s s} \tag{3.58}$$

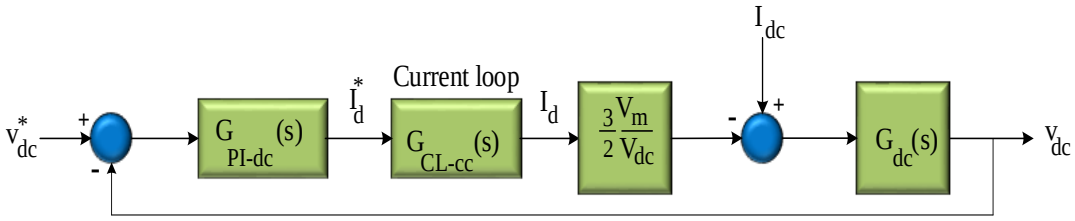

Figure 3. 20: DC-link voltage loop control based on current balancing. (Ouchen et al., 2016)

Based on a method referred to as symmetrical optimum, the phase crossover frequency $\boldsymbol{\omega_C}$ is given as (Ouchen et al., 2016):

$$\omega_C = \frac{1}{\sqrt{3T_s T_{i-dc}}} \tag{3.59}$$

Hence, the parameters of the outer loop control are expressed as:

$$\begin{cases} K_{P-dc} = 0.12\frac{C_{dc}}{T_s} \\ T_{i-dc} = 17T_s \end{cases} \tag{3.60}$$

Equation 3.61 gives the instantaneous active and reactive power (Roy & Mahmud, 2017):

$$\begin{cases} P = \frac{3}{2}(V_d i_d + V_q i_q) \\ Q = \frac{3}{2}(V_q i_d - V_d i_q) \end{cases} \tag{3.61}$$

If $V_q = 0$, Equation 3.61 becomes:

$$\begin{cases} P = \frac{3}{2}V_d i_d \\ Q = -\frac{3}{2}V_d i_q \end{cases} \tag{3.62}$$

Therefore, the dq0 currents may be controlled by regulating the active and reactive power as:

$$\begin{bmatrix} i_d^* \\ i_q^* \end{bmatrix} = \begin{bmatrix} G_{PI-P}(s)(P^* - P) \\ G_{PI-Q}(s)(Q^* - Q) \end{bmatrix} \tag{3.63}$$

In which P is the active power, Q the reactive power, $G_{PI-P}(s)$ and $G_{PI-Q}(s)$ are the corresponding PI controller of active and reactive power and "*" represents the reference values.

Figure 3.20 displays the outer power control loop utilised to produce the current references, in which a power calculation unit is needed.

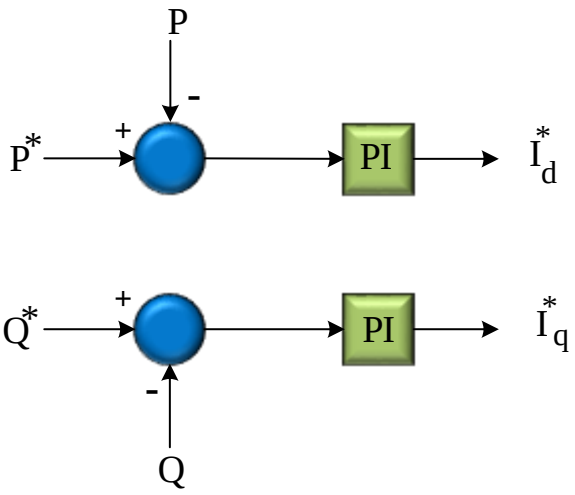

Figure 3. 21: Outer power control loop. (Firdaus et al., 2017)

3.3.4.3 Inner current control loop

For the three-phase inverter shown in Figure 3.17, the AC side of the inverter can be expressed as (Keawthai & Po-ngam, 2015):

$$L\frac{di_p}{dt} + Ri_p = v_{op} - v_p \tag{3.64}$$

where p=a, b and c, represent the corresponding phase; $\boldsymbol{v_{op}}$ is the inverter output phase voltage; $\boldsymbol{v_p}$ is the phase voltage; and $\boldsymbol{i_p}$ is the grid current.

When considering the inverter output voltage and the modulation signal, Equation 3.65 can be given as (Keawthai & Po-ngam, 2015):

$$L\frac{di_p}{dt} + Ri_p = m_p v_{dc} - v_p \tag{3.65}$$

where $\boldsymbol{m_p}$ is the modulation signal for the phase p.

Applying the Clarke transformation to Equation 3.65, the inverter AC side can be expressed in the stationary reference frame as (Buau et al., 2018):

$$\begin{cases} L\frac{di_\alpha}{dt} + Ri_\alpha = m_\alpha v_{dc} - v_\alpha \\ L\frac{di_\beta}{dt} + Ri_\beta = m_\beta v_{dc} - v_\beta \end{cases} \tag{3.66}$$

While in the s-domain Equation 3.66 can be written as (Chatterjee & Mohanty, 2018) :

$$(Ls + R)i_{\alpha\beta}(s) = V_{dc}m_{\alpha\beta}(s) - v_{\alpha\beta}(s) \tag{3.67}$$

where $i_{\alpha\beta} = [i_\alpha \quad i_\beta]^T$, $m_{\alpha\beta} = [m_\alpha \quad m_\beta]^T$, and $v_{\alpha\beta} = [v_\alpha \quad v_\beta]^T$.

To properly control the output voltage, the injected grid current ought to be regulated. Thus, the control signals is given as (Chatterjee & Mohanty, 2018):

$$m_{\alpha\beta} = \frac{1}{v_{dc}} G_{CC-\alpha\beta}(s)\left(i^*_{\alpha\beta} - i_{\alpha\beta}\right) \tag{3.68}$$

where $G_{CC-\alpha\beta}(s)$ is the current controller.

Figure 3.22 depicts the closed-loop current control in the dq0 reference frame. It can be noted that the periodic signal controllers should be utilised (Firdaus et al., 2017) .

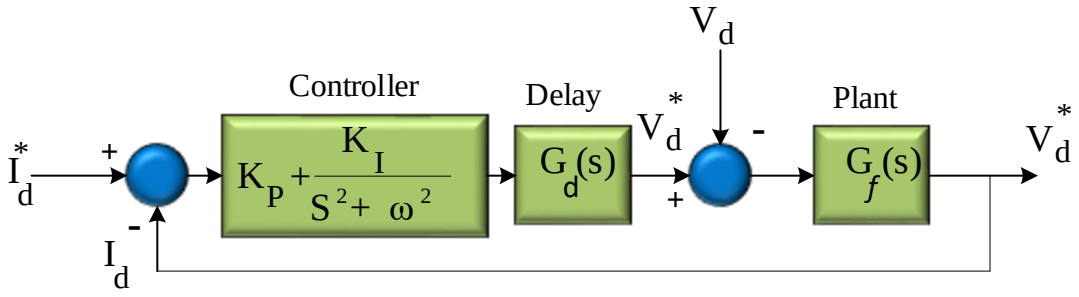

Figure 3. 22: Closed-loop current control in the dq0 reference frame. (Liu et al., 2019)

Using the Park transformation in Equation 3.67, the inverter system can be expressed by Equation 3.69:

$$\begin{cases} L\frac{di_d}{dt} + Ri_d - \omega L i_q = m_d v_{dc} - v_d \\ L\frac{di_q}{dt} + Ri_q - \omega L i_d = m_q v_{dc} - v_q \end{cases} \tag{3.69}$$

In which the indexes dq represents the variable in the dq0 reference frame.

The output voltage references are changed by the addition of a decoupling element and a feed-forward voltage as given by (Patel & Pandya, 2018):

$$\begin{cases} m_d^* = m_d + \frac{\omega L}{V_{dc}} i_q - \frac{1}{v_{dc}} v_d \\ m_q^* = m_q + \frac{\omega L}{V_{dc}} i_d - \frac{1}{v_{dc}} v_q \end{cases} \tag{3.70}$$

Using Equation 3.69 into Equation 3.70, the current control loop model is expressed as (Jian et al., 2014):

$$\begin{cases} m_d^* = \frac{2}{V_{dc}}(u_d + L\omega I_q + V_{gd}) \\ m_q^* = \frac{2}{V_{dc}}(u_q - L\omega I_d + V_{gq}) \end{cases} \quad (3.71)$$

where u_d and u_q are the output signals of the current errors, V_{gd} and V_{gq} are disturbance inputs.

In the s-domain, Equation 3.71 is expressed as (Wang et al., 2017; Erfanmanesh & Dehghani, 2013):

$$m_{dq}^*(s) = \frac{1}{v_{dc}}(Ls + R)i_{dq}(s) \quad (3.72)$$

Hence, the outputs of the inner current loop in $dq0$ reference frame are decoupled (Figure 3.23). In addition, as expressed in Equation 3.73, the dynamics of the $dq0$ currents are similar. Therefore, the closed current control in dq0 reference frame is expressed as (Arancibia et al., 2013):

$$m_{dq}^* = \frac{1}{v_{dc}} G_{CC-dq}(s)(i_{dq}^* - i_{dq}^*) \quad (3.73)$$

where $G_{CC-dq}(s)$ is the PI current controller in dq0 reference frame.

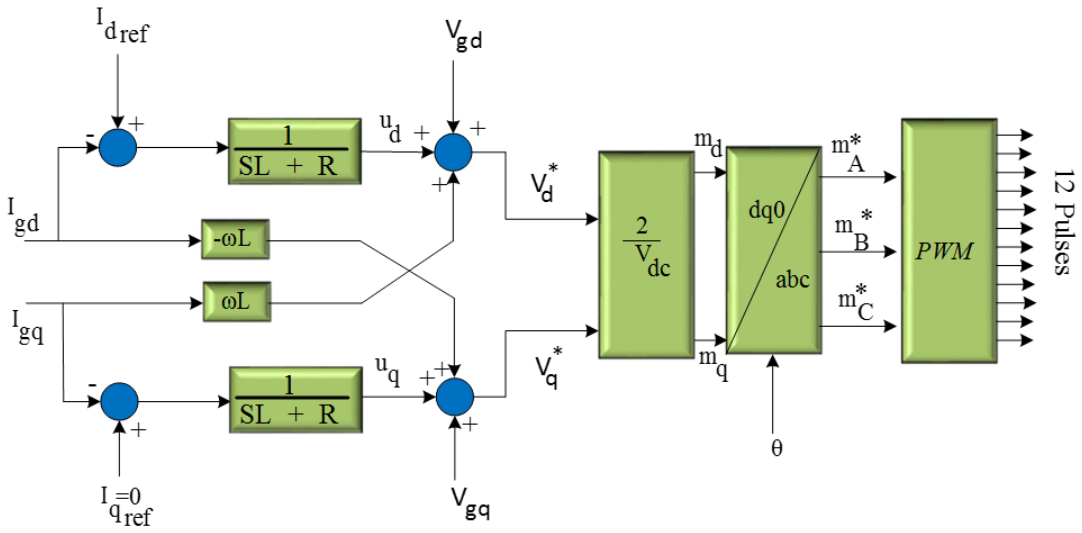

Figure 3. 23: Schematic diagram of inner current control loop. (Al-Shetwi et al., 2019)

The PI current controller is given as:

$$G_{CC-dq}(s) = K_{P-CC}(1 + \frac{1}{T_{i-cc}s}) \tag{3.74}$$

in which feed-forward voltage and cross-coupling are negligible, k_{P-cc} is the proportional gain and T_{i-cc} is the integrator time constant of the PI controller.

The delay time that includes the PWM and computing time in the control system is given as (Zhou et al., 2017):

$$G_d(s) = \frac{1}{1+1.5T_sS} \tag{3.75}$$

Figure 3.23 shows the closed-loop current control system for the inverter in the dq reference frame, where the cross-coupling term and the feed-forward voltage term are not shown.

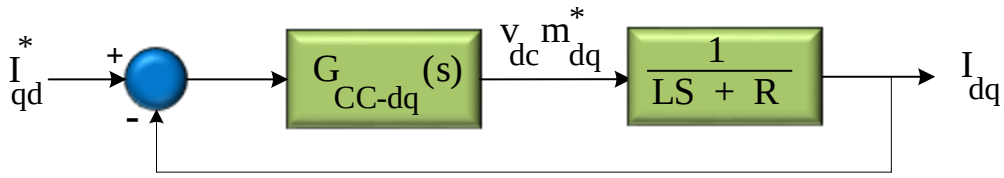

Figure 3. 24: $dq0$ reference frame current closed-loop control. (Vu et al., 2012)

The complete current open-loop control is given as (Merai et al., 2018; Sen et al., 2014; Bayoumi, 2015; Behera & Thakur, 2016; Zhang et al., 2017; Jian et al., 2014; Tarasantisuk et al., 2016):

$$G_{OL-CC}(s) = \frac{K_{P-CC}(1+T_{i-cc}s)}{T_{i-cc}s}\frac{1}{(1+1.5T_sS)}\frac{T_f}{L(1+T_fs)} \tag{3.76}$$

where $T_f = L/R$ is the plant time constant.

If the PI controller time constant is designed as the system time constant $T_{i-cc} = T_f$, the model can be simplified as (Merai et al., 2018):

$$G_{OL-cc}(s) = \frac{K_{P-CC}}{\frac{3}{2}TL_sS^2+L_S} \tag{3.77}$$

The closed-loop current control is expressed as (Teodorescu et al., 2011):

$$G_{CL-CC}(s) = \frac{G_{OL-cc}(s)}{1 + G_{OL-cc}(s)} = \frac{\frac{K_{P-CC}}{3T_sL}}{S^2 + \frac{2}{3T_s}s + \frac{2K_{P-CC}}{3T_sL}} \quad (3.78)$$

Furthermore, Equation 3.78 is expressed as a second-order system where (Merai et al., 2018):

$$\begin{cases} \omega_n^2 = \frac{2K_{P-CC}}{3T_sL} \\ 2\zeta\omega_n = \frac{2}{3T_s} \end{cases} \quad (3.79)$$

in which ω_n and ζ are the undamped natural frequency and damping ratio respectively.

Practically, $\zeta = 0.707$ representing an optimal damped system with an overshoot of approximately 5%. Hence, the proportional and integrator time constant are expressed as (İnci, 2019):

$$\begin{cases} K_{P-cc} = \frac{L}{3T_s} \\ T_{i-CC} = \frac{L}{R} \end{cases} \quad (3.80)$$

Using the designed parameters in Equation 3.80, the closed-loop current control may be estimated by a first-order system given by (Merai et al., 2018):

$$G_{CL-CC}(s) \approx \frac{1}{1+3T_sS} = \frac{1}{1+\tau s} \quad (3.81)$$

where $\boldsymbol{\tau}$ is the estimated time constant of the closed-loop current control.

In addition, the bandwidth of the current control loop can be determined from Equation 3.82 as (Luna et al., 2015):

$$f_{b-cc} = \frac{1}{2\pi\tau} \approx \frac{f_s}{20} \quad (3.82)$$

where $f_s = 1/T_s$ being the sampling frequency.

Therefore, the bandwidth of the current control loop is closed to $\mathbf{1/20}$ of the sampling frequency (Firdaus et al., 2017).

More controllers for grid-tied inverters are based on periodic controllers using "**PID** " technique (Zhou et al., 2017), as shown in Figure 3.24. The feedback loop is meant to maintain the complete control loop stability and dynamics and the periodic controllers performs zero error tracking.

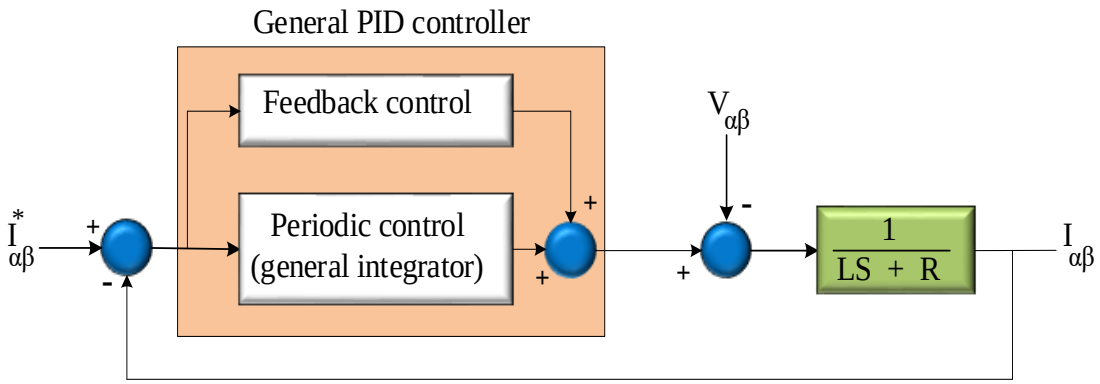

Figure 3. 25: αβ-reference frame PID control approach for the grid current (Yang et al., 2019) **.**

3.3.4.4 Harmonic compensation

Practically, the grid voltage contains harmonics, especially in case of a weak grid, besides harmonics due to the non-linearity in the system. This leads to making more efforts for harmonic mitigation in grid-connected alternative energy systems. On the other hand, it is required by the grid codes that the connecting units should not produce important harmonics, as they may result to system resonances, cause efficiency to drop, and make other equipment malfunction. Fortunately, harmonics can be compensated in the current control loop (Bayoumi, 2015).

Indeed, the current control can be realised in different reference frames. This is also in application to the harmonic compensation as it can be done in the stationary αβ-reference frame or synchronous dq-reference frame. Figure 3.26 shows the harmonic compensation scheme in multiple synchronous reference frames to compensate the 5^{th} and 7^{th} order harmonics, using multiple Park and inverse Park transformations. For the compensation of higher-order harmonics, the implementation complexity will increase significantly (Blaabjerg et al., 2006).

The harmonic controllers utilised in Figure 3.26 are integral controllers given as (Sen et al., 2014) :

$$\begin{cases} G_5(s) = K_{i5}.\frac{1}{s} \\ G_7(s) = K_{i7}.\frac{1}{s} \end{cases} \tag{3.83}$$

where K_{i5} and K_{i7} is the corresponding control gain.

The integral controllers can achieve infinite gains for DC signals, and therefore, in a closed loop control system in Figure 3.26 the DC harmonics will be eliminated.

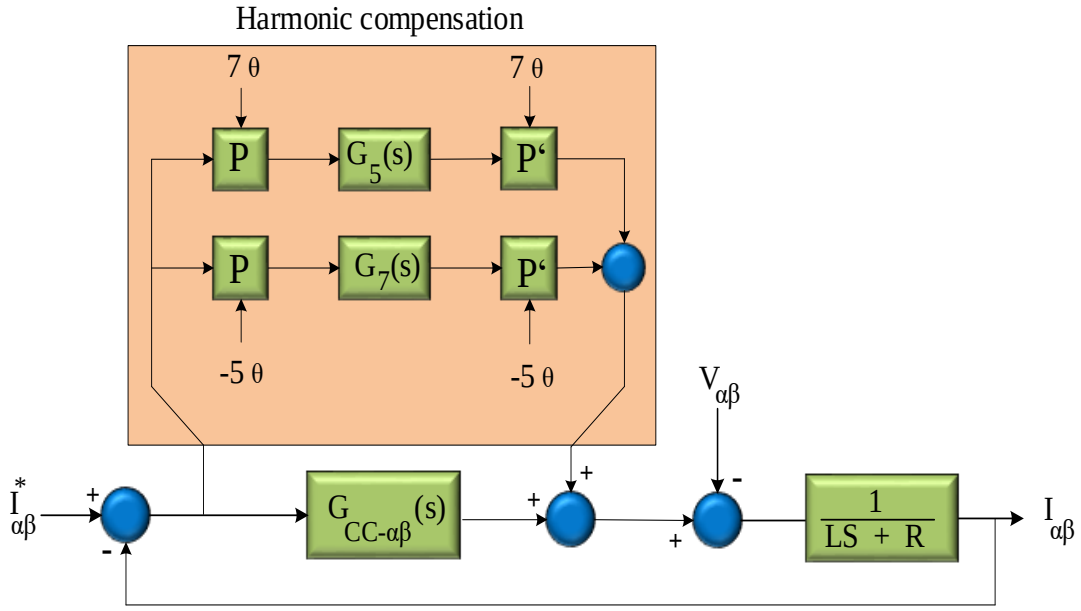

Figure 3. 26: αβ-reference frame current control loop with the harmonic compensator (Yang et al., 2019)

Possibly, using a generalised integrator, an infinite gain is achieved at the tuned frequency. Hence, harmonics can be compensated by connecting a series of generalised integrators in parallel to play the role of a resonant harmonic compensator (Figure 3.27.)

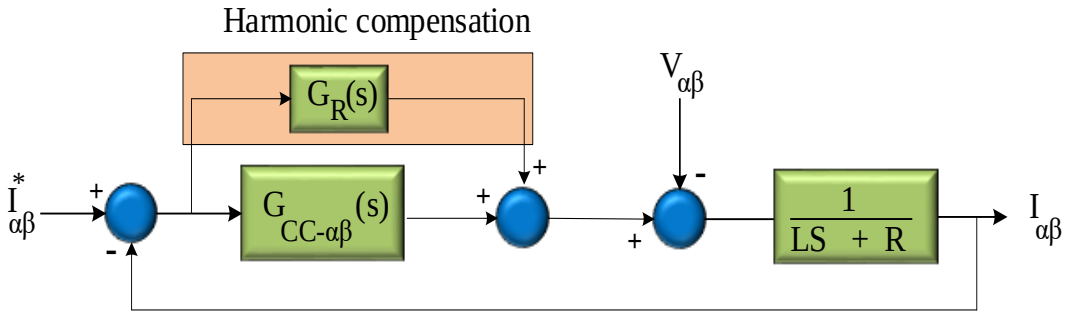

Figure 3. 27: αβ reference frame current control loop with resonant harmonic compensator.
(Mirhosseini, 2019)

Parallel resonant controllers for harmonic compensation is written as follows:

$$G_R(s) = \sum_h \frac{K_{rh}s}{s^2+(h\omega)^2} \tag{3.84}$$

where h, K_{rh} and ω are the harmonic order, control gain and fundamental frequency respectively.

As shown in Figure 3.27, harmonics having frequency equal to $h\omega$ are removed in a closed-loop control system.

The harmonic compensation through parallel resonant controllers represents an interesting answer for grid-tied alternative energy systems, in which low order harmonics are prevailing. Moreover, the ideal repetitive controller in Equation 3.90, with $K_{rc} = 1$, $Q(s) = 1$, and $e^{STc} = 1$, is enlarged as a total of an integral controller, a DC gain, and the infinite parallel resonant controllers (Zhou et al., 2017).

This compensator is given as (Zhou et al., 2017):

$$G_{RC}(s) = -\frac{1}{2} + \frac{1}{ST} + \frac{1}{T}\sum_h^{\infty} \frac{2s}{s^2+(h\omega)^2} \tag{3.85}$$

where T the fundamental period.

It is inherent to connect the repetitive controller in the current control loop for harmonic reduction (Figure 3.28).

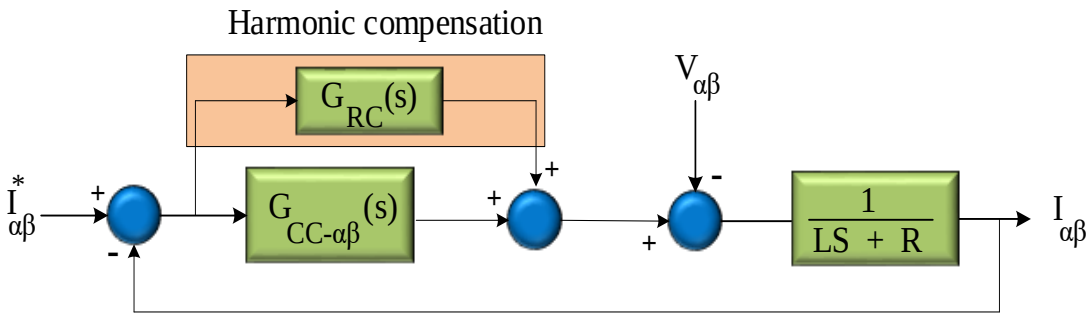

Figure 3. 28: αβ-reference frame current control loop with a plug-in repetitive controller. (Behera & Thakur, 2016)

3.3.4.5 Phase-Locked Loop synchronisation method

Various synchronisation methods exist; however, the most commonly used method uses the phase-locked loop (PLL) approach. The structure of a PLL system including a phase detector, loop filter, and voltage-controlled oscillator is shown in Figure 3.29.

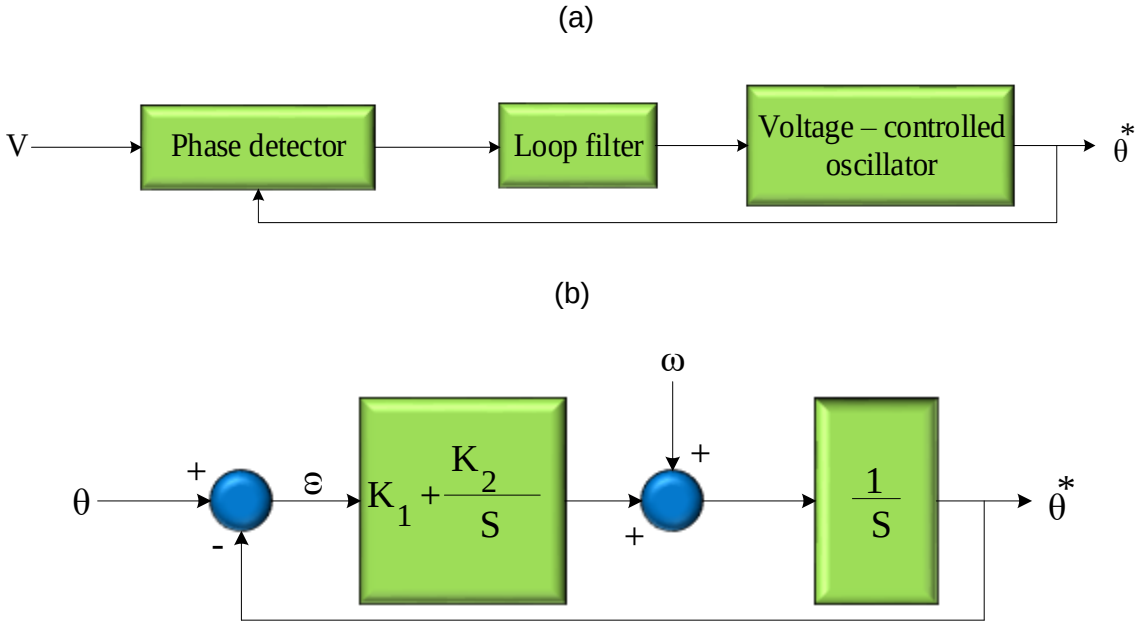

Figure 3. 29: PLL: (a) structure, and (b) small-signal model. (Behera & Thakur, 2016)

The closed-loop PLL system can be expressed as (Timbus et al., 2005):

$$G_{CL-PLL}(S) = \frac{\theta^*}{\theta} = \frac{K_1 s + K_2}{S^2 + K_1 s + K_2} \quad (3.86)$$

In which K_1 is the PI loop filter proportional and K_2 is its corresponding integral gain.

The natural frequency ω_{n-PLL} and damping ratio ξ_{PLL} are given as (Teodorescu et al., 2011):

$$\begin{cases} \omega_{n-PLL} = \sqrt{K_2} \\ \xi_{PLL} = \frac{K_1}{2\sqrt{K_2}} \end{cases} \tag{3.87}$$

In case of a three-phase balance grid, the synchronisation is trial to realise with the use of the $\alpha\beta$ and $dq0$ transformations, in which the q-axis voltage ($V_q = 0$) is considered as the loop filter input, and then the synchronisation performed.

Considering a three-phase voltage given as:

$$\begin{cases} V_a = V_m \cos\theta \\ V_b = V_m\, cos(\,\theta - 120^0) \\ V_b = V_m\, cos(\,\theta + 120^0) \end{cases} \tag{3.88}$$

In which V_m and θ are the voltage magnitude and the phase respectively.

Equation 3.89 is obtained by applying the Clarke transformation:

$$\begin{cases} V_\alpha = V_m\, cos\,\theta \\ V_\beta = V_m \sin\theta \end{cases} \tag{3.89}$$

In case the PLL traces the phase with neglected errors ($\theta = \theta^*$), and applying the Park transformation to Equation 3.89, Equation 3.90 is obtained as (Firdaus et al., 2017):

$$\begin{cases} V_d = V_\alpha\, cos\,\theta^* + V_\beta\, sin\,\theta^* \approx V_m \\ V_q = V_\alpha\, cos\,\theta^* + V_\beta\, sin\,\theta^* \approx V_m(\theta - \theta^*) \end{cases} \tag{3.90}$$

Hence, the phase error utilised in the closed-loop PLL is detected as (Behera & Thakur, 2016):

$$\varepsilon = \theta - \theta^* = \frac{V_d}{V_m} \tag{3.91}$$

Based on Equations 3.87 and 3.88, the parameters for the loop filter are separated by the voltage magnitude (V_m). The complete PLL is then built (Figure 3.29).

Because the phase error of PLL synchronisation is identified in the dq0 reference frame (SRF), the PLL in Figure 3.29 is referred to SRF-PLL units. This PLL operates well in case of a grid under ideal conditions (Ali et al., 2018). However, the grid voltage is not pure sine wave, and harmonics or unbalances can occur. In such a case, in steady state, the SRF-PLL unit is unable to trace the phase with zero errors. In such a case,

harmonic filters can be included, for instance, a periodic signal filter (Zhou et al., 2017), or for the unbalanced grid containing zero sequence, and positive and negative components, the positive sequence voltage needs to be retrieved and utilised for synchronisation.

The sequence voltage extraction is realised in a decoupled double synchronous reference frame or using a Double Second Order Generalised Integrator (DSOGI) (Zhou et al., 2017; Teodorescu et al., 2011; Espinoza et al., 2000; Luna et al., 2015; Ali et al., 2018). The structure of the DSOGI PLL system is shown in Figure 3.29. The second order generalised integrator is expressed as:

$$\begin{bmatrix} V^* \\ qV^* \end{bmatrix} = \begin{bmatrix} \frac{\gamma\omega^* s}{s^2+\gamma\omega^* s+(\omega^*)^2} \\ \frac{\gamma(\omega^*)^2}{s^2+\gamma\omega^* s+(\omega^*)^2} \end{bmatrix} \tag{3.92}$$

where γ is the second order generalised integrator control gain, V^* is the filtered voltage of the input voltage V , qV^* is the in-quadrature voltage, and γ is the second order generalised integrator control gain chosen as $\gamma = 1.414$.

3.3.4.6 Designed control parameters

The designed parameters of the inverter are depicted in Table 3.11; these parameters include the outer control parameters, the inner control loop parameters and the synchronisation designed parameters.

Table 3. 11: Inverter control designed parameters.

Outer control loop parameters

Parameter	Value
DC-link capacitor (C_{DC})	50000 µF
Controller Proportional gain (K_{pv})	133.5
Controller Integral gain (K_{iv})	303,409.1

Inner control loop parameters

Parameter	Value
Controller Proportional gain (K_{pc})	3.24
Controller Integral gain (K_{ic})	50.625

PLL based loop filter parameters

Parameter	Value
Controller Proportional gain (K_1)	9.7
Controller Integral gain (K_2)	22045.45

3.4 Summary

This chapter focused on the description of the megawatt fuel cell energy system and the modelling of components involved on it. The adopted configuration consists of components such as a 1.54 MW fuel cell stack, a three-level diode clamped inverter to convert the 1400 DC volts of the fuel cell into 600 AC volts between phases, and an LCL filter to reduce the effect of voltage and the current harmonics generated by the inverter. The megawatt fuel cell stack consists of several proton exchange membrane fuel cell (PEMFC) stacks connected in series and parallel.

The entire system model was developed based on the model of each component and the designed parameters of the fuel cell, inverter, LCL filter.

The last section of this chapter was oriented to the modelling of the control system for proper operation of the grid connected inverter. It was stated that under nominal grid operation, the control of the feed-in current is important. This control is realised through a dual-loop control. The control of the current can be realised in different reference frames including the dq frame which allow the use of PI controllers. Moreover, the harmonic compensation and the synchronisation were also considered.

CHAPTER FOUR
SIMULATION RESULTS AND DISCUSSION

4.1 Introduction

The megawatt fuel cell system depicted in Figure 3.2 was simulated using Matlab/Simulink software for a duration of 2.5 seconds to assess the performance of the designed system based on parameters provided in chapter three. The megawatt fuel cell system was considered to operate in grid-tied mode, thereafter, a simulation was carried out to evaluate the operation of the system in off-grid mode. A total of twelve stacks were connected in parallel to obtain the megawatt fuel cell stack. The characteristics of each individual stack are given in the appendices. It is assumed that during the simulation, the hydrogen and oxygen composition, system temperature, hydrogen and oxygen pressure are unchanged, whereas the hydrogen and oxygen flow rate are depended on Equation 4.1 and Equation 4.2 given as follows:

$$U_{fH_2} = \frac{60000\ R\ T i_{fc}}{Z\ F\ P_{fuel} V_{fuel} x\%} \tag{4.1}$$

$$U_{fO_2} = \frac{60000\ R\ T i_{fc}}{2\ Z\ F\ P_{air} V_{air} y\%} \tag{4.2}$$

where P_{fuel} and P_{air} are the absolute supply pressures of fuel and of air respectively, V_{fuel} and V_{air} are fuel flow rate and air flow rate respectively, $\mathrm{x}\%$ and $y\%$ are the percentage of hydrogen and oxygen respectively, Z is the number of moving electrons, R is the universal gas constant, i_{fc} is the current of the fuel cell and T is the temperature.

Hence, the efficiency of each stack and the resulting fuel cell system is 37 %. The parameters used in Equation 4.1 and Equation 4.2 are given in Table 4.1.

Table 4. 1: Fuel cell flow rate parameters.

Fuel cell stack flow rate parameters	
R	8.3145 J/mol ^{o}K
T	338 ^{o}K
i_{fc}	90 Amp
Z	2
F	96485 A s/mol
P_{fuel}	1.5 bar
V_{fuel}	99.56%
$x\%$	98.98%
P_{air}	1 bar
$y\%$	50%
V_{air}	21%

The results from the simulation are divided in two parts namely the DC and AC parts. The DC side comprises the voltage, current and power generated by the megawatt stack then fed to the DC link, while the AC side consists of the inverter, filter and the control.

4.2 DC side Results

Figure 4.1 displays the voltage, current, and power response of the megawatt stack; their steady state values are approximately 1400 V, 1100 A, and 1.546 MW for the voltage, current and power respectively. To reach these steady state values, the simulation of megawatt stack took about 0.5 seconds.

The DC link voltage had a rising time of about 5 milliseconds corresponding to the time needed for the voltage to rise from 0 to 100 % of its final value. Additionally, the overshoot and undershoot of the voltage at the beginning of the simulation were 115.864 % and 1.939 % respectively before getting to its stable value. Similarly, the DC current presented an overshoot and undershoot at the beginning of the simulation that were 1.970 % and 68.052 % respectively.

Regarding the power response, it had a rising time of about 22.437 milliseconds, while the overshoot and undershoot of the voltage at the beginning of the simulation were 11.741 % and 3.217 % respectively before getting to its stable value.

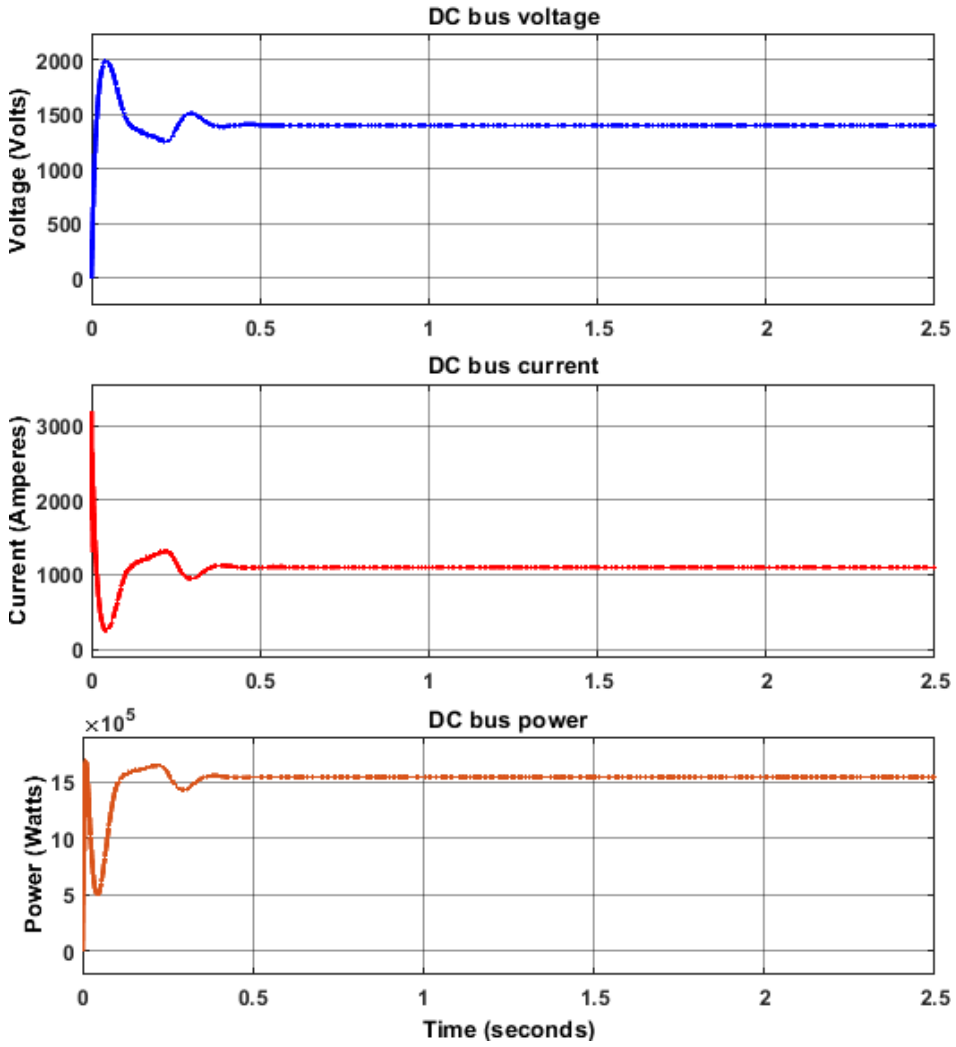

Figure 4. 1: DC bus voltage, current and power.

Figure 4.2 shows the voltage at each DC link capacitor; the 1400 V of the DC link voltage was shared between the two capacitors such that each had a voltage of 700 V. The rise time of the voltage at each capacitor was about 4.711 milliseconds corresponding to the time needed for the voltage to rise from 0 to 100 % of its final value. Additionally, the overshoot and undershoot of the voltage at the beginning of the simulation were 120.86 % and 1.989 % respectively.

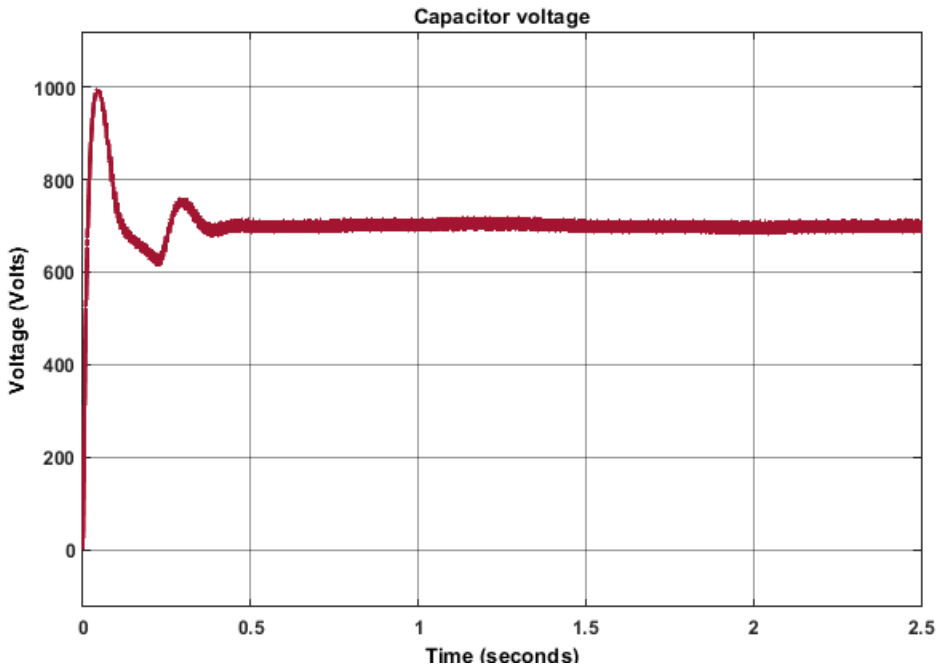

Figure 4. 2: Voltage at each capacitor.

4.3 Inverter and AC side results

The inverter was operated such that it provided a voltage that was suitable for the grid. At least a three-level inverter was used to ensure proper operation. This three-level inverter balanced its individual voltage level regardless of the inverter control and load characteristics. It converted the DC link voltage into an AC voltage. This AC voltage was a three-level signal with the line to line value swinging between $-V_{DC}$ link to $+V_{DC}$ link as depicted in Figure 4.3.

This AC voltage was obtained at the output of the inverter without a filtering device. Its peak to peak value is about 2800 V, hence, the maximum and minimum values were + 1400 V and -1400 V respectively (see Figure 4.3), while the RMS voltage was about 938 V. The signal shown is in the form of pulses with varying widths according to the amplitude of the reference sine wave. The fundamental frequency of this signal is equal to that of the grid frequency, which is 50 Hz. The resulting current waveforms can be seen in Appendix A.7.

The rise time of the phase to phase voltage was about 3.841 milliseconds, while the fall time was 3.971 milliseconds. Additionally, the overshoot and undershoot of the voltage at the beginning of the simulation were 0.49 % and 25.347 % respectively.

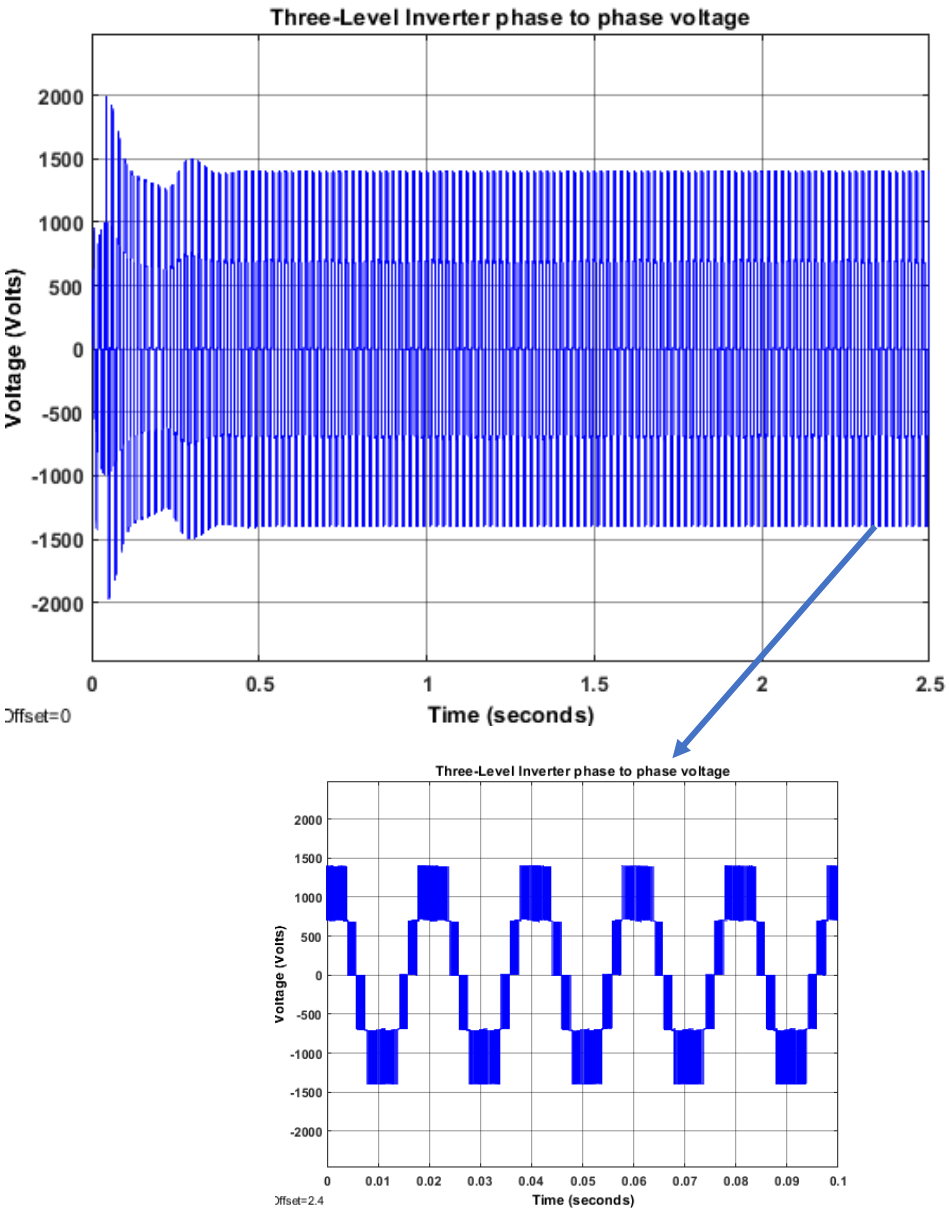

Figure 4. 3: Three-level inverter output voltage before filtering.

Similarly, the phase to ground voltage of the inverter before filtering was as depicted in Figure 4.4; Its peak to peak value was about 1876 V, hence, the maximum and minimum values were + 938 V and -938 V respectively (see Figure 4.4), while the RMS voltage was about 540 V. The rise time of the phase to ground voltage was about 2.11 milliseconds, while the fall time was 2.141 milliseconds. Additionally, the overshoot and undershoot of the voltage at the beginning of the simulation were 19.838 % and 39.003 % respectively.

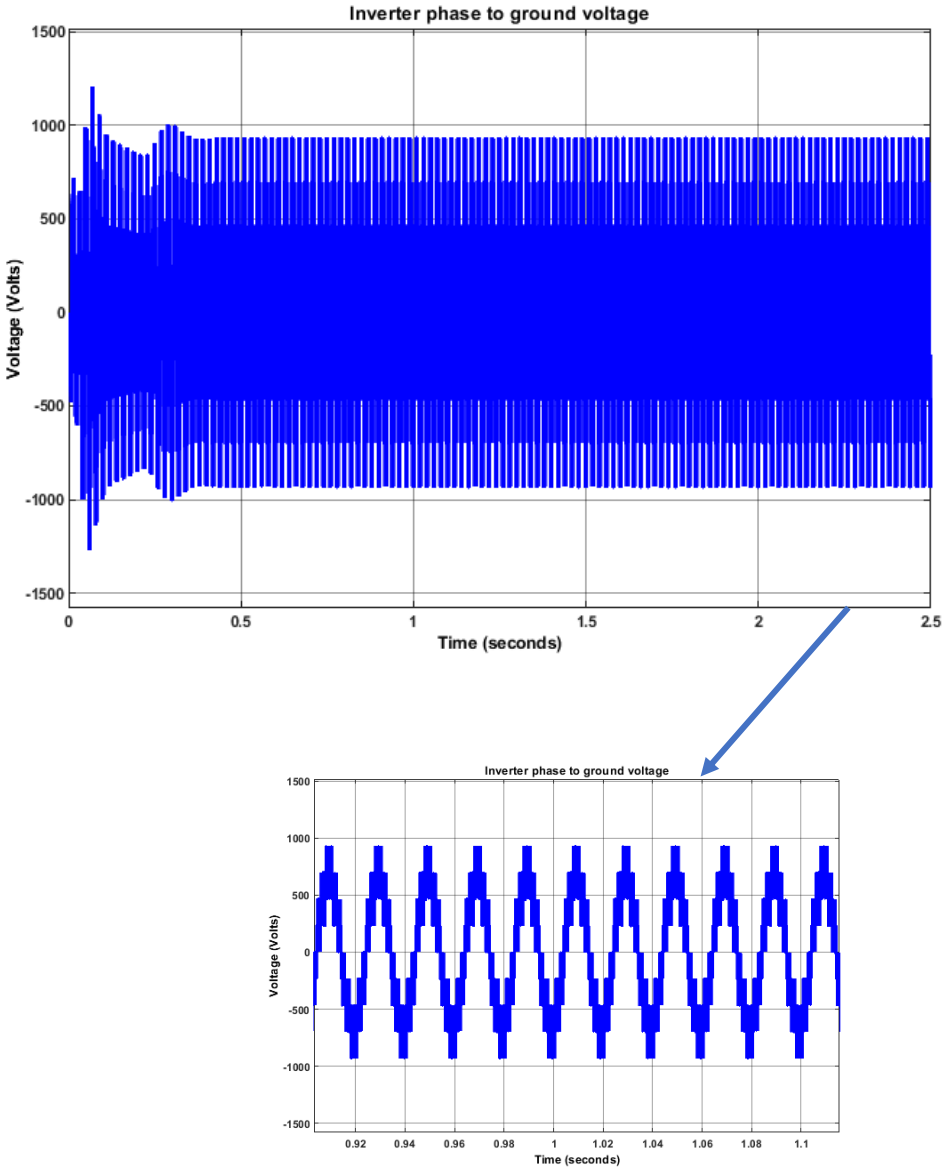

Figure 4. 4: Three-level inverter phase to ground voltage.

The phase to phase voltage of the three-level inverter shown in Figure 4.3 was subjected to harmonics caused by the switching of power electronics devices in the inverter. These harmonics negatively impacted on the system and, caused problems such as low efficiency, poor power factor, transient, etc. Standards such each IEEE 519 and IEC 61000-3-6 define the allowable harmonic distortion for both the current and the voltage in a typical power system based on the current level and the voltage level respectively.

In Table 3.7, the allowable voltage total harmonic distortion was defined in terms of voltage level, while the current total demand distortion limit was expressed as a function of the voltage level and the ratio of the short-circuit current to the rated load current (Table 3.8). IEEE 519-2014 defines the total harmonic distortion as the ratio of the root

mean square of the harmonic content, considering harmonic components up to the 50th order and specifically excluding inter harmonics, expressed as a percent of the fundamental.

On the other hand, the total demand distortion as the ratio of the root mean square of the harmonic content, considering harmonic components up to the 50th order and specifically excluding inter harmonics. Table 3.9 gives the IEC 61000-3-6 voltage harmonic limits.

The voltage total harmonic distortion was as depicted in Figure 4.5; its value is around 45.01% for frequencies up to 5 kHz when the fundamental is 50 Hz. This percentage is far above the limit as set by standards (Table 4.1, Table 4.2). With such a distortion, a load can be subjected to fast deterioration, furthermore, the lifespan of the fuel cell can also be shortened, hence, the filtering of the inverter voltage waveform was required.

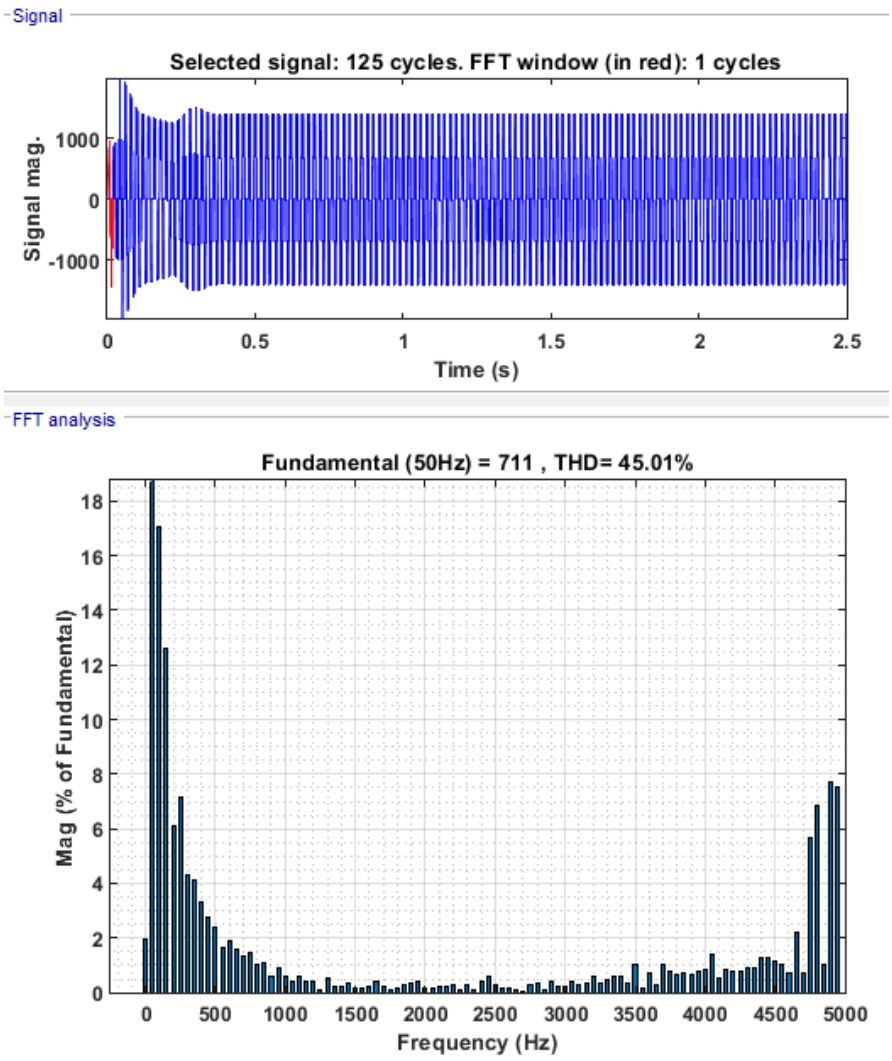

Figure 4. 5: Voltage harmonic distortion before filter.

The phase to phase voltages V_a, V_b, and V_c after the passage of voltage waveforms into the low-pass LCL filter are shown in Figure 4.6. As expected, the magnitudes of the phase voltages were about 600 V, while the magnitudes of the phase currents were around 1213 A. The rise time of the phase to phase voltage was about 5.853 milliseconds, while the fall time was 5.837 milliseconds. Additionally, the overshoot and undershoot of the voltage at the beginning of the simulation were 0.324 % and 1.985 % respectively.

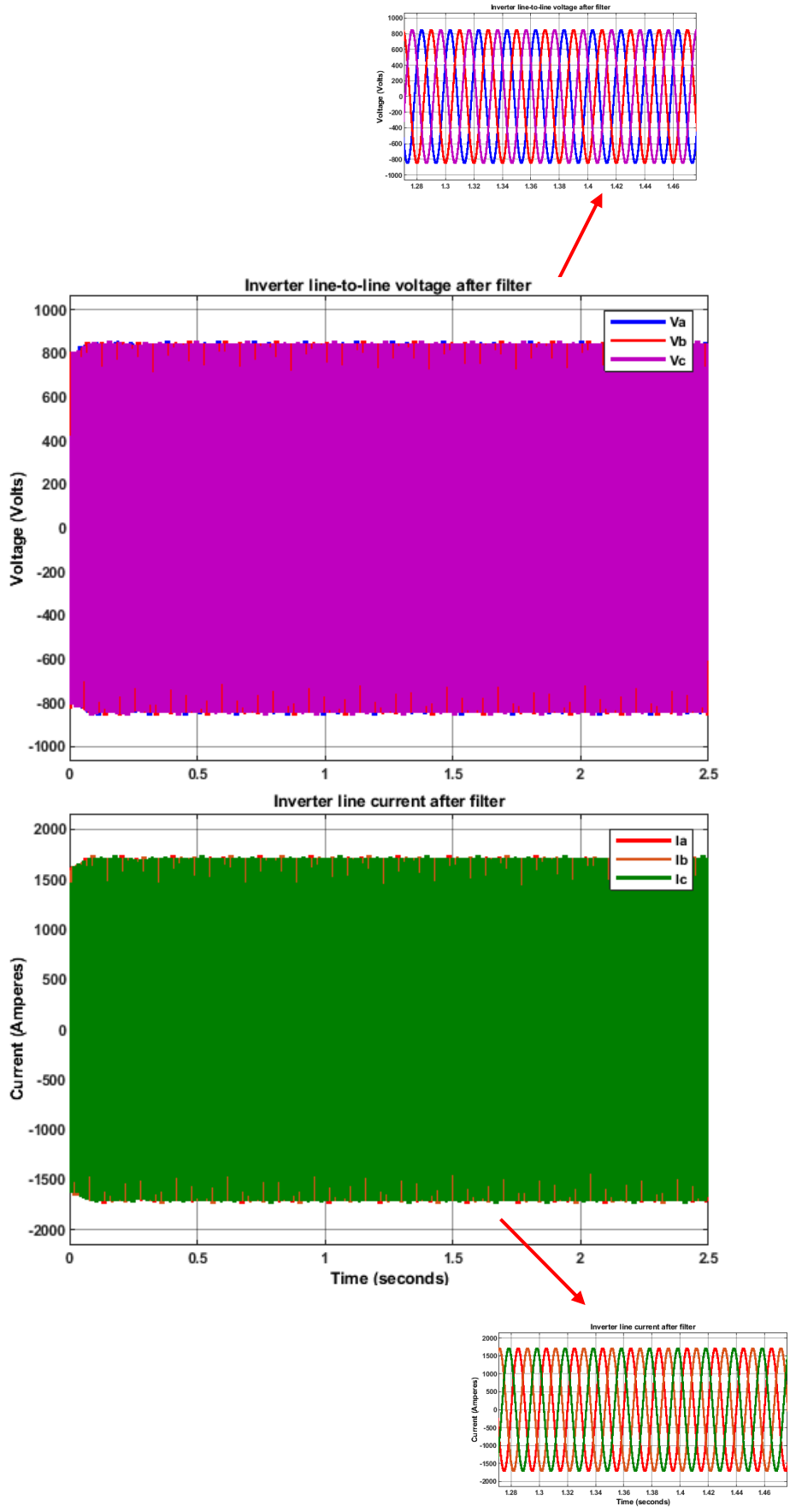

Figure 4. 6: Inverter output voltage and current after the filter.

Similarly, the rise time of the phase current was about 5.819 milliseconds, while the fall time was 5.823 milliseconds. Additionally, the overshoot and undershoot of the voltage at the beginning of the simulation were 1.99 % and 1.99 % respectively.

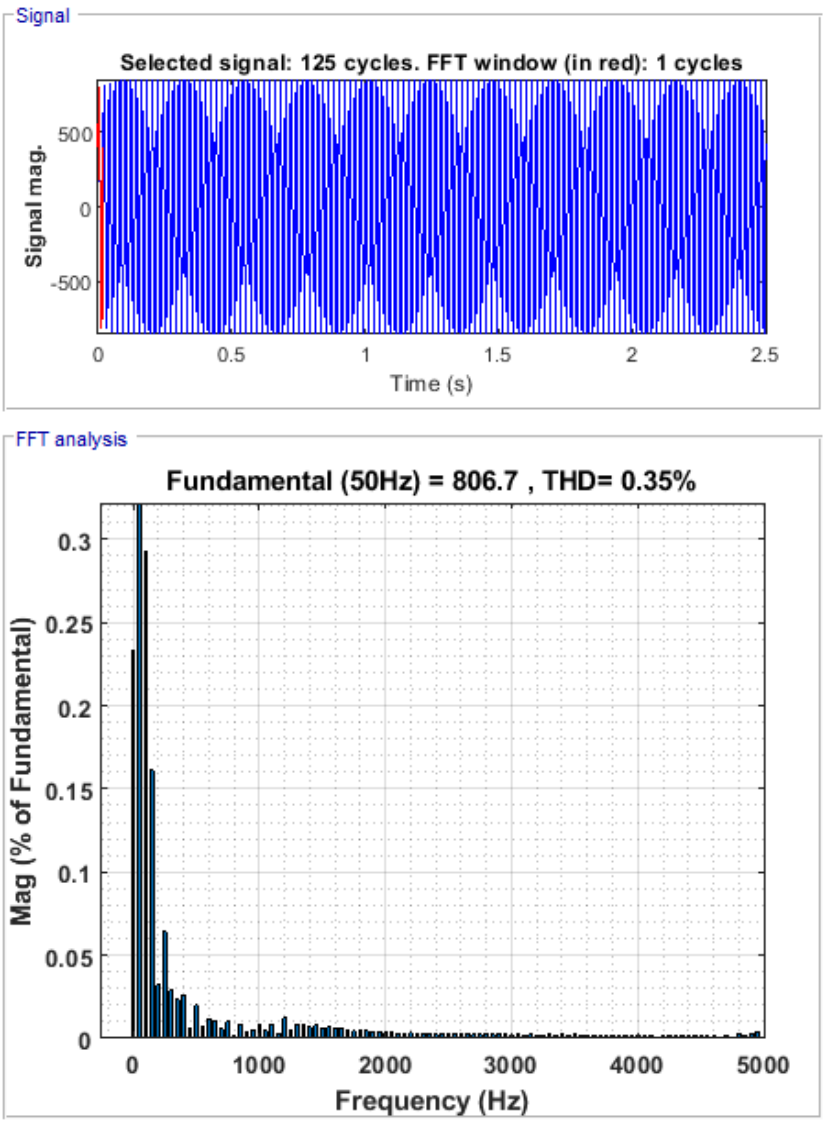

Figure 4. 7: Harmonics voltage after the filter.

Figure 4.7 and Figure 4.8 depict the histograms of voltage total harmonic distortion and current harmonic distortion at the output of the LCL filter respectively. These charts were obtained for a 1.26 MW three-level inverter connected to the grid at 600 V. The time start for both harmonics voltage and current measurement were at zero seconds, and with the designed filter, both harmonics were considerably reduced. The corresponding voltage total harmonic distortion was about 0.35 % whereas the total harmonic distortion of the current was 0.19 %. The obtained values complied with the

IEEE 519-2014 standards which states that the harmonic distortion limit for voltages less than 1 kV is 8 % (Table 4.1). On the other hand, IEEE 519-2014 defines the total demand distortion limit for voltages less than 69 kV and currents greater than 1000 A as equal to 20 %. At a full load, both the total harmonic distortion and the total demand distortion were equal, hence, as the load was simulated at its full value, the corresponding total demand distortion was also equal to 10.67 %. This obtained value conformed to the above-mentioned standards. The comparison of the voltages and currents before and after the LCL filter were as shown in appendices A.8 and A.9.

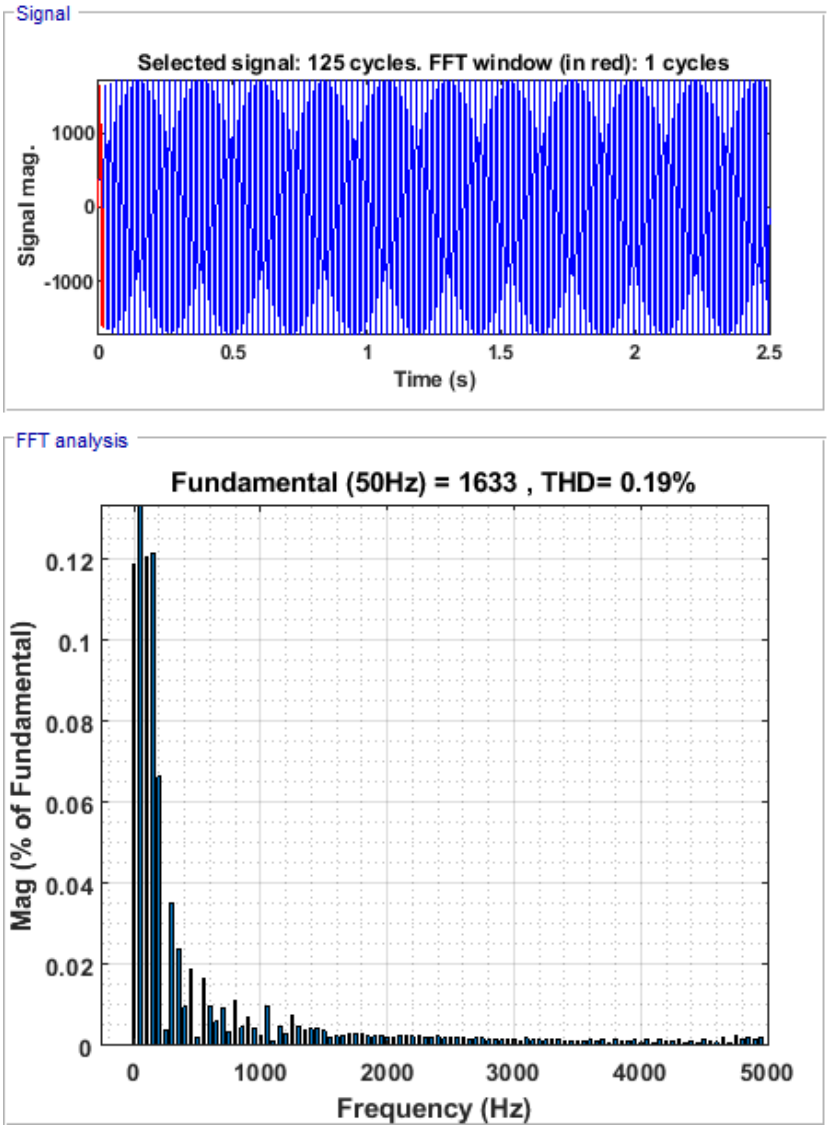

Figure 4. 8:Harmonics current after the filter.

4.4 Inverter control

The three-level inverter control consists of sections such as the PLL, and voltage and current controls. The first step in the control algorithm consisted of transforming the phase voltages and currents into the stationary reference frame. The stationary reference frame voltage components were used by the PLL to evaluate the frequency and provide the phase reference for the inverter. These values were given to the phase regulator which delivered the desired output phase of the inverter. The voltage regulator regulated the desired voltage magnitude of the inverter, while, the PWM generator took the desired voltage magnitude and phase to generate the PWM output signals.

4.4.1 Phase Locked Loop

A typical Phase-Locked Loop (PLL) generates an output signal whose phase is related to the input signal phase. In this case, as stated above, the PLL was used to track the frequency and phase of the sinusoidal three-phase signal with an internal frequency oscillator. The internal oscillator was adjusted by the control system to maintain the phases difference at zero (0). Figure 4.9 shows the frequency of the PLL which is around 50 Hz. This frequency corresponded as well to the grid frequency and may vary slightly around 50 Hz as it could be seen in Figure 4.9.

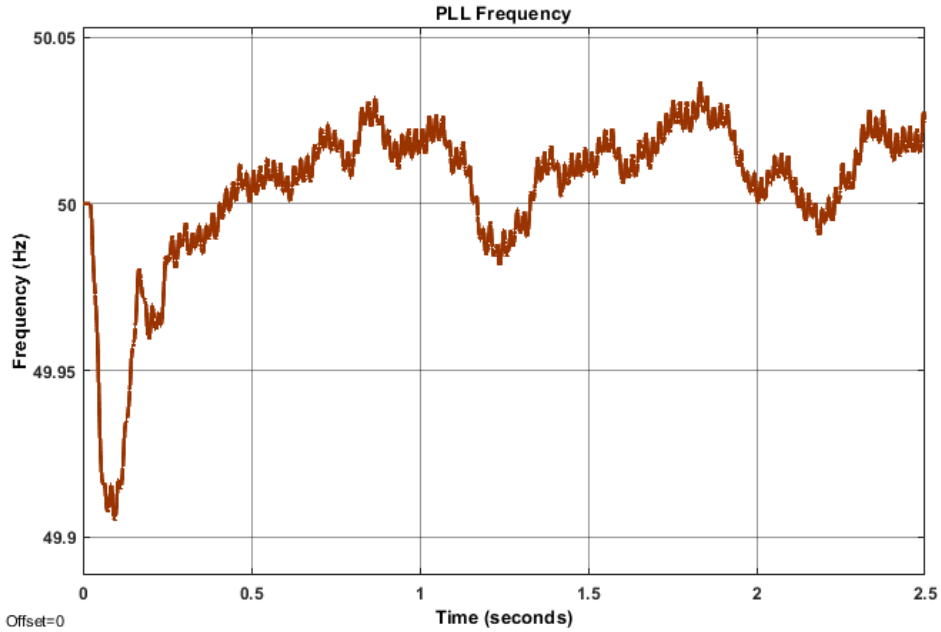

Figure 4. 9: Frequency obtained from the PLL.

Similarly, the phase generated by the PLL is depicted in Figure 4.10, The PLL measured the grid voltage and phase angle used to synchronise the dq frame current control. It can be observed that the PLL produced a proper phase angle to allow the synchronisation of the inverter with respect to the grid.

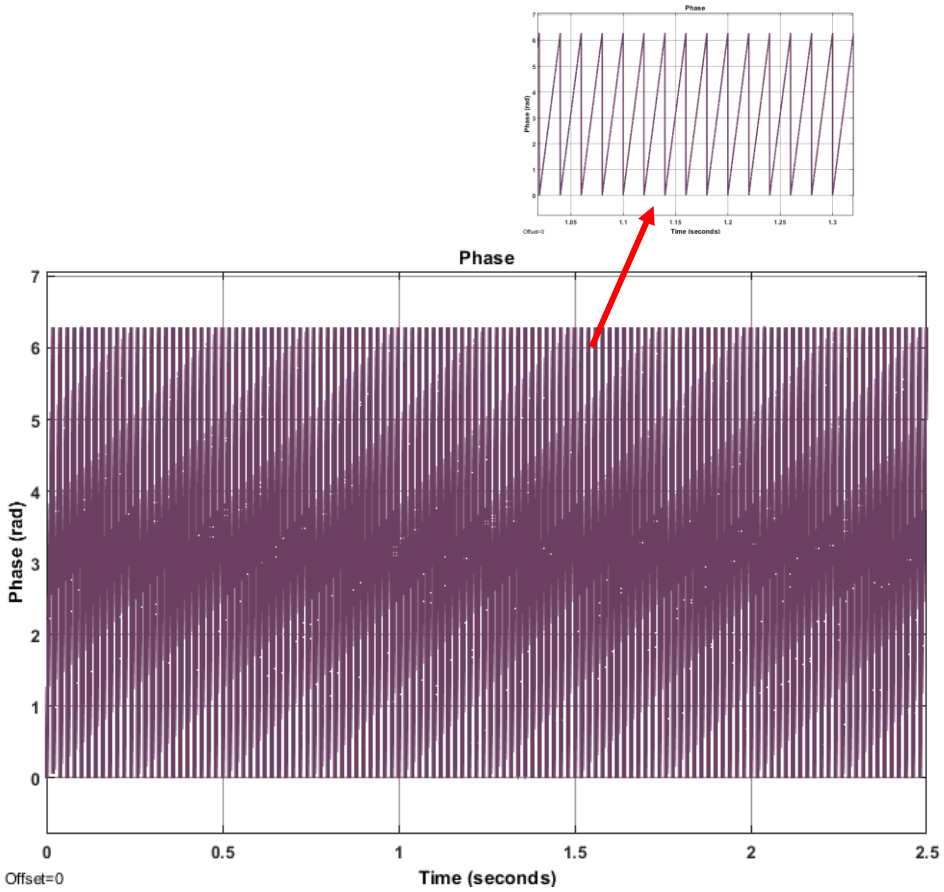

Figure 4. 10: Phase obtained from the PLL.

4.4.2 Voltage control

The voltage control results compared the DC link voltage with the reference voltage set at 1400 V. The error obtained from the comparison of both was used as input to the voltage PI controller to generate the I_d reference. Figure 4.11 shows the actual and the reference voltage of the DC link, the results proved that the control applied to the system had a good response as the error of both voltages was nearly zero. However, an overshoot can be observed at the starting of the simulation, then after, from time t=0.5 second, both voltages had the same values.

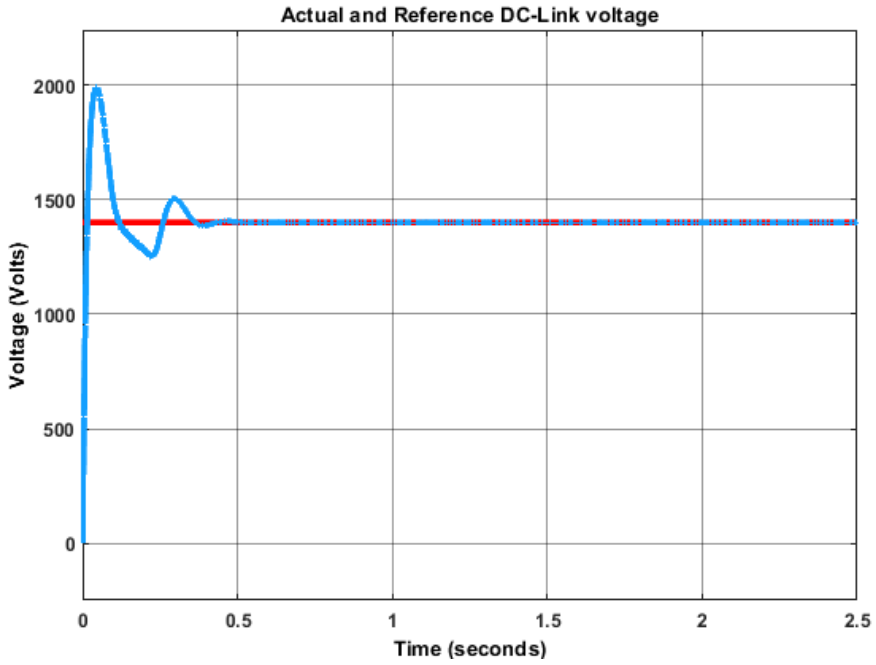

Figure 4. 11: DC link voltage reference and actual values.

Figure 4.12 shows the I_d reference current which was used as the input together with the I_d current obtained from the grid to generate the V_d reference; both I_d and I_d reference were compared (Figure 4.13), and the error obtained was used as the input to the current PI controller in the d-axis for the generation of V_d. As it can be seen in Figure 4.12, the value of I_{d_ref} was about 1766 Amperes. The rise time of this current was about 40.823 milliseconds. Additionally, the overshoot and undershoot of the voltage at the beginning of the simulation were 21.341 % and 1.994 % respectively.

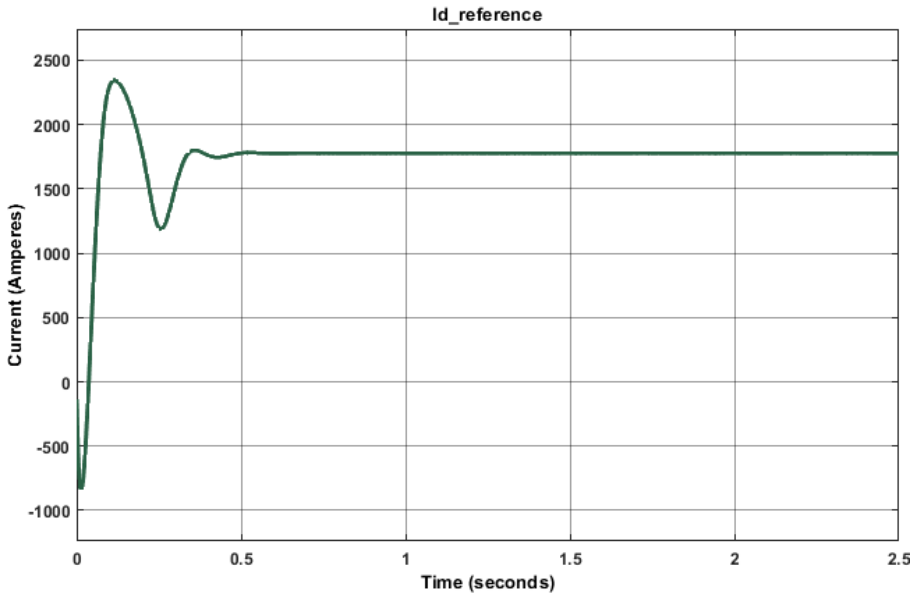

Figure 4. 12: I_d reference.

4.4.3 Current control

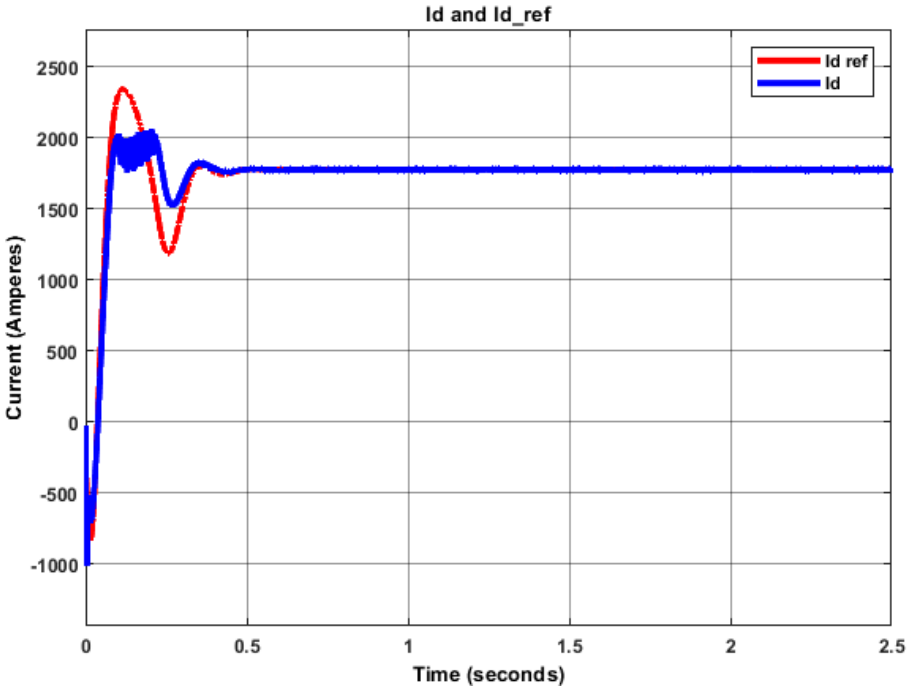

Figure 4. 13: I_d and I_d reference.

Figure 4.14 illustrates the comparison of I_q and I_q reference current and the error obtained between the two currents was used to generate V_q reference through the current PI controller in the q-axis. It can be noted that the value of I_q reference was set to zero.

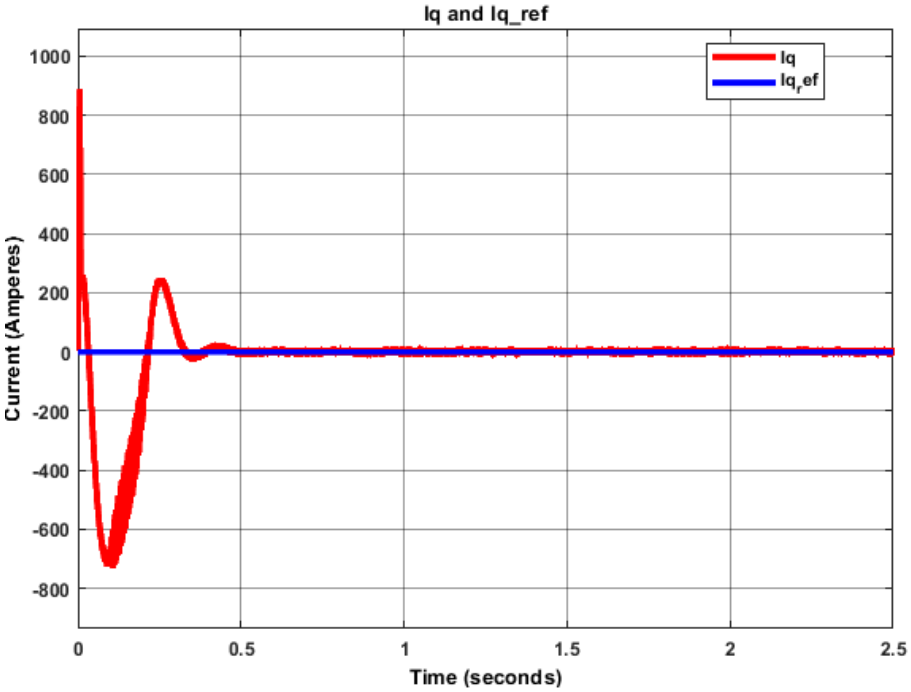

Figure 4. 14: I_q and I_q reference.

Figure 4.15 shows the V_d which was the grid voltage obtained after transformation from the abc to the dq0 frame. The RMS value of this voltage is 490 V; however, the signal is characterised by an overshoot of 13.462% between 0.077 and 0.239 seconds and an undershoot of 2.479% between 0.239 and 0.338 seconds. Its rise time is 43.786 milliseconds. This voltage was required for the generation of U_{d_ref} which is used to obtain m_d.

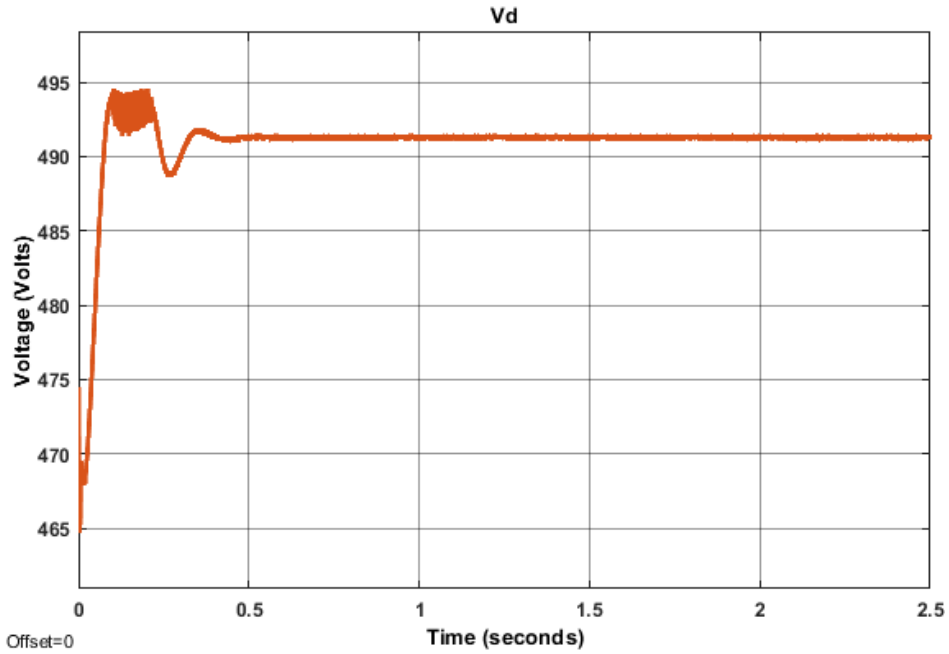

Figure 4. 15: Voltage after transformation in d-axis.

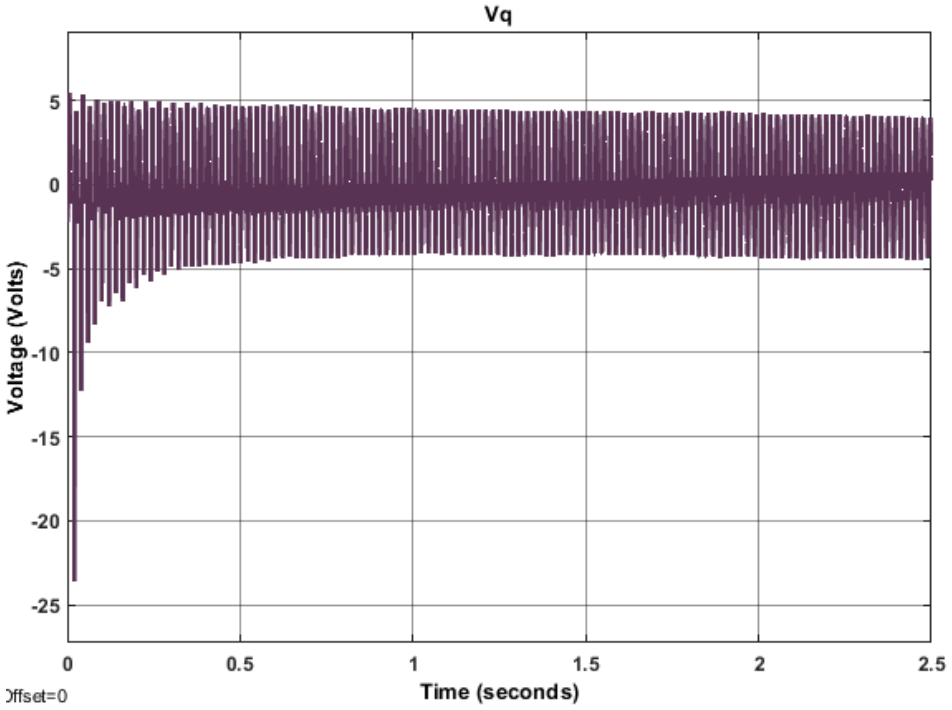

Figure 4. 16: Voltage after transformation in q-axis.

Figure 4.16 displays the voltage V_q obtained from the transformation of the voltage abc from to dq0 frame. This voltage is generally equal to zero since the reactive power from the grid is always controlled. In this case, this voltage is not equal to zero. However, its RMS value is around 2 V which is very close to zero.

U_{d_ref} is the output signals of the current errors used in Equation 3.71, together with current errors in Appendix A.11; as it can be seen in Figure 4.17(a), its RMS value is about 500 V, however, the signal included an overshoot of about 4.578%, while the undershoot was 9.897%, the corresponding rise and fall times were 16.509 milliseconds and 12.463 milliseconds respectively. On the other hand, U_{q_ref} shown in Figure 4.17(b).

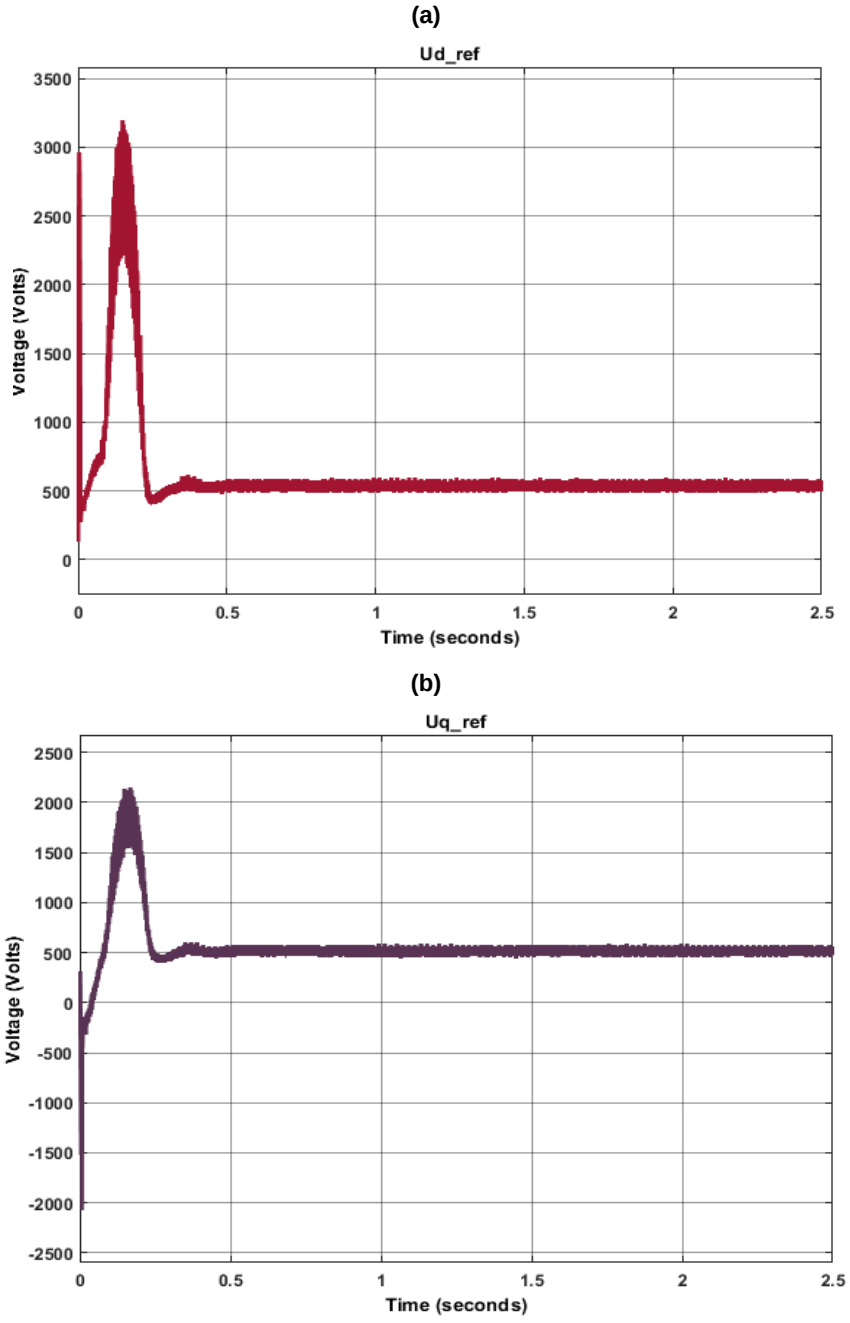

Figure 4. 17: U_d and $U_{q\_reference}$.

Figure 4.18 depicts the modulation signals in the dq0 reference frame, these signals resulted from Equation 3.17 and their values were always between 0 and 1; in this study the obtained values of $m_{\_d}$ (Figure 3.17(a)) and $m_{\_q}$ (Figure 3.17(b)) were 0.7. These modulation signals were transformed into the abc frame then fed into the Pulse Width Generation (PWM) to generate twelve pulses that triggered the three-level inverter. The resulting sinusoidal pulse width modulation signal was as shown in Appendix A.10.

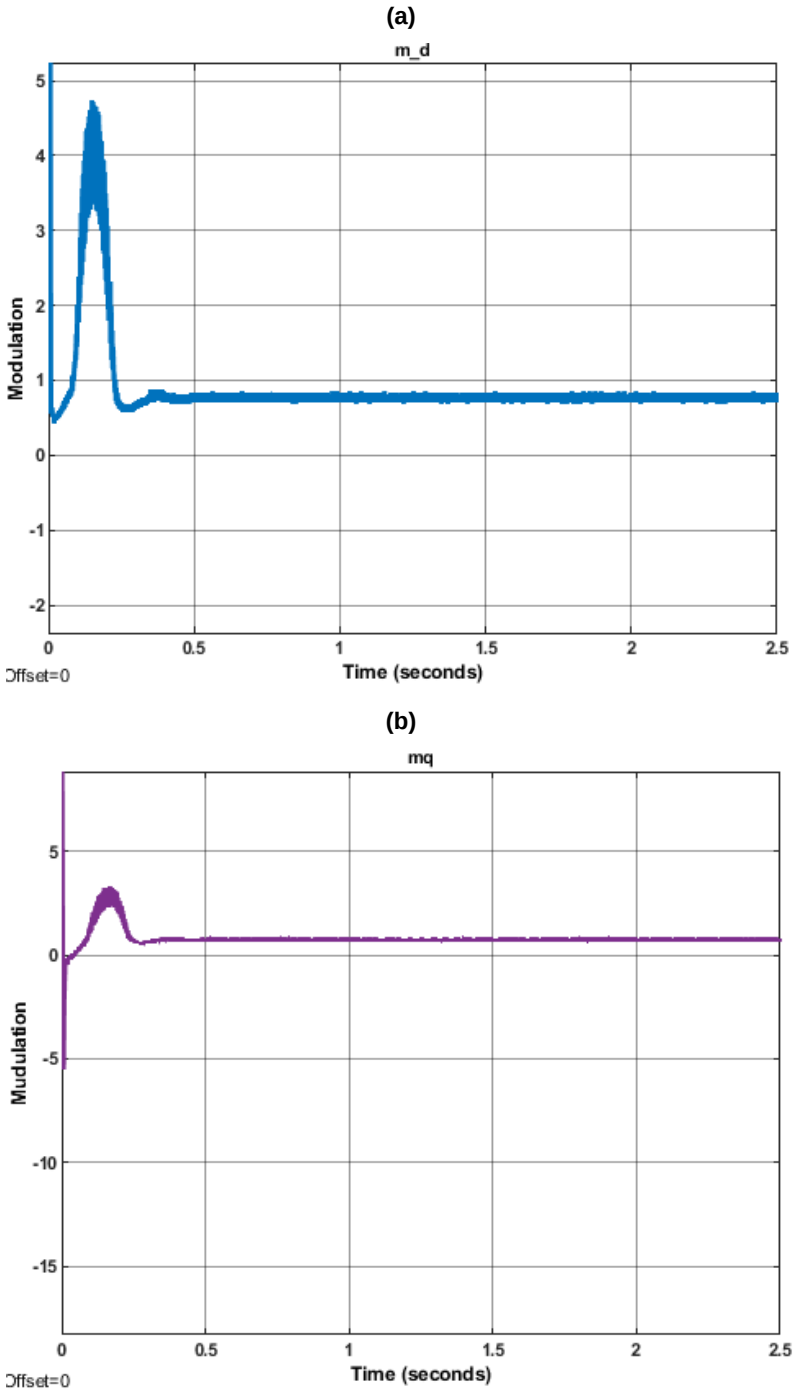

Figure 4. 18: Modulation in dq0 reference frame.

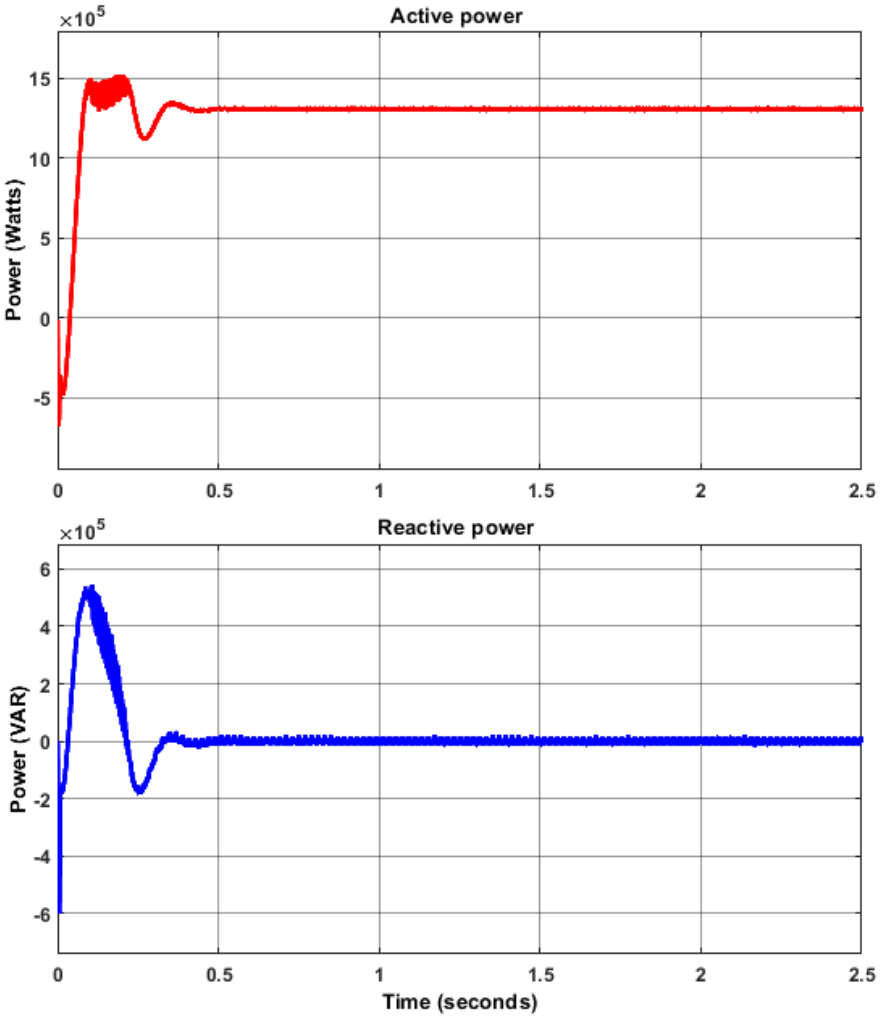

Figure 4. 19: System active and reactive power.

The system active and reactive power were shown in Figure 4.19; the active power was about 1.26 MW (Figure 4.19(a)), while the reactive power varied around zero (2.574e-8 VAR) (Figure 4.19(b)). At the beginning of the simulation, this active power response was characterised by an overshoot of 14.935 % between the time t = 0 and t =0.3 seconds and an undershoot of 2.468 % between t = 0.3 and t = 0.4 seconds, thereafter, this response stabilised to reach the steady state value of 1.26 MW. On the other hand, the reactive power displayed an overshoot of 215.301 %, whereas the undershoot was 2.332 %.

4.5 Case studies

Various case studies based on the loads conditions were considered to evaluate the performance of the system in grid connection as well as in off-grid mode.

4.5.1 Case study 1: 2.5 MW pure resistive load

This scenario considered a purely resistive load of 2.5 MW; the power generated from the megawatt fuel cell was used to supply this load, however, the megawatt fuel cell system required a grid connection operation to allow the grid to support the system in order to provide the deficit power that the fuel cell was not able to meet. The load active and reactive power were as shown in Figure 4.20; the value of the active power resulting from the simulation was about 2.36 MW, while the reactive varied around zero (1.865e-7 VAR). At the beginning of the simulation, this active power response was characterised by an overshoot of 14.557 % between the time t = 0 and t = 0.3 seconds and an undershoot of 1.998 % between t = 0.3 and t = 0.4 seconds, thereafter, this response stabilised to reach the steady state value of 2.36 MW. On the other hand, the reactive power displayed an overshoot of 95.419 % around the time t = 2 seconds, whereas the undershoot was 40.092 %.

The phase to ground voltages V_a, V_b, and V_c and currents I_a, I_b and I_c after the passage of both waveforms into the low-pass LCL filter were as shown in Figure 4.21. As expected, the magnitudes of the phase voltages were around 336 V (Figure 4.21(a)), and the magnitudes of the phase currents were around 2334 A (Figure 4.21(b)). The corresponding rise time of the phase to ground voltage was about 5.853 milliseconds, while the fall time was 5.857 milliseconds. Additionally, the overshoot and undershoot of the voltage at the beginning of the simulation are 0.321 % and 1.984 % respectively.

Similarly, the rise time of the phase current was about 5.855 milliseconds, while the fall time was 5.856 milliseconds. Additionally, the overshoot and undershoot of the voltage at the beginning of the simulation were 0.283 % and 1.99 % respectively.

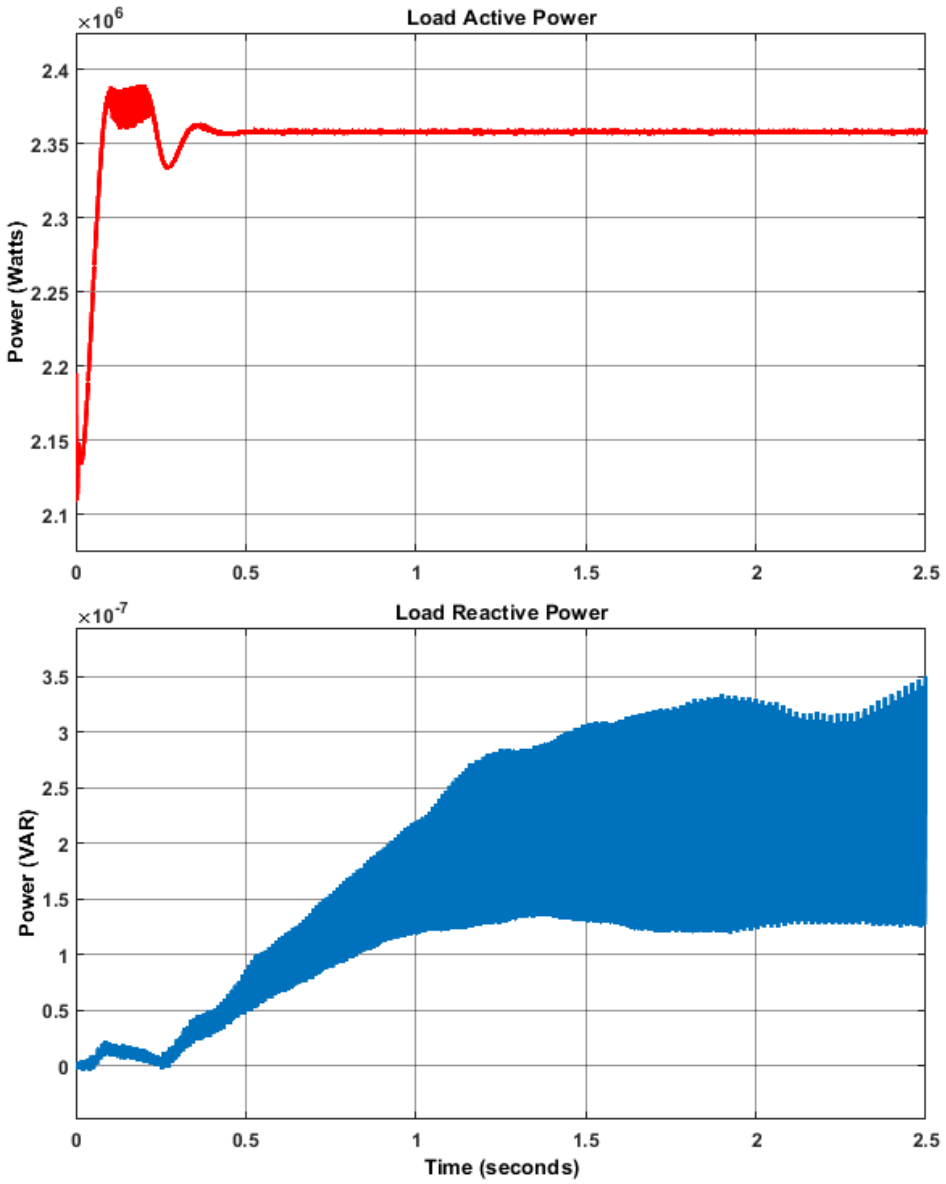

Figure 4. 20: Active and reactive power.

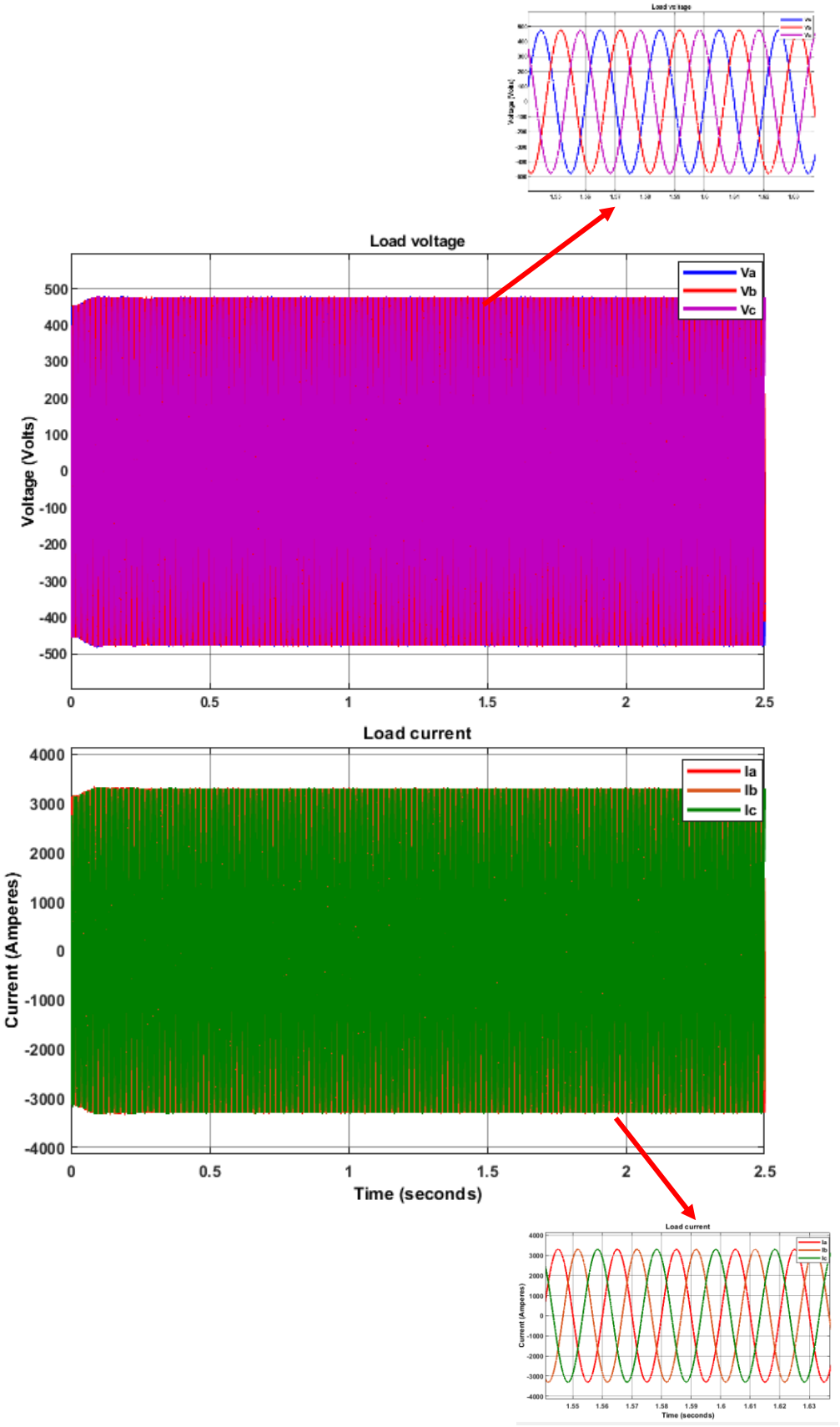

Figure 4. 21: Load voltage and current.

The active and reactive power received from the grid was as shown in Figure 4.22; these powers represented the deficit unable to be provided from the megawatt fuel cell. The grid supplied about 1.638 MW to the load, while the megawatt fuel cell is provided the remaining portion. The reactive power was about 862 kVAR, whereas the active power was 1.7 MW. At the beginning of the simulation, this active power response was characterised by an overshoot 11.932 % between t = 0.1 and t = 0.2 seconds and an undershoot of 7.784 % between t = 0.2 and t = 0.3 seconds, thereafter, this response stabilised to reach the steady state value of 2.36 MW. On the other hand, the reactive power displayed an overshoot of 55.882 % between t = 0.1 and t = 0.2 seconds, whereas the undershoot was 1.985 % between t = 0.2 and t = 0.3 seconds.

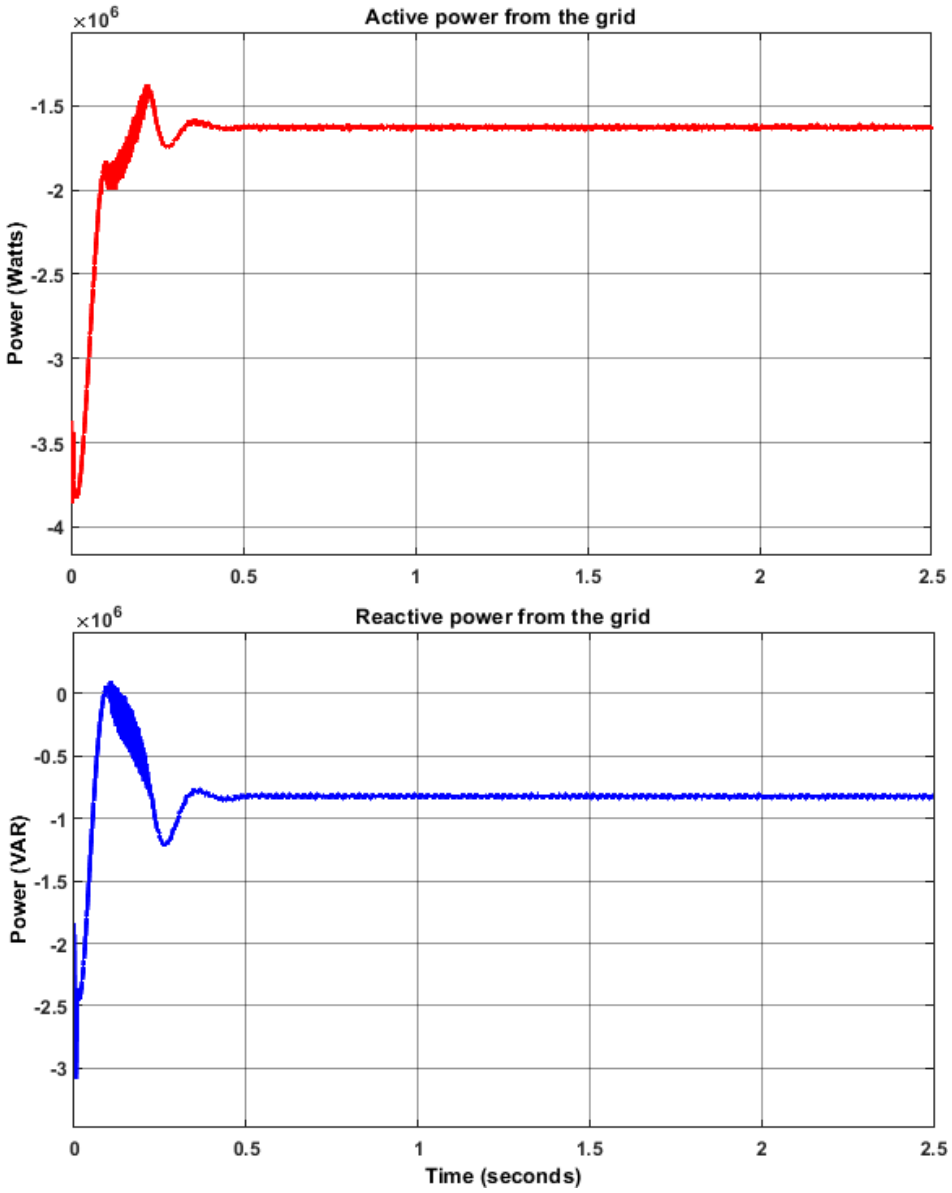

Figure 4. 22: Active and reactive power from the grid.

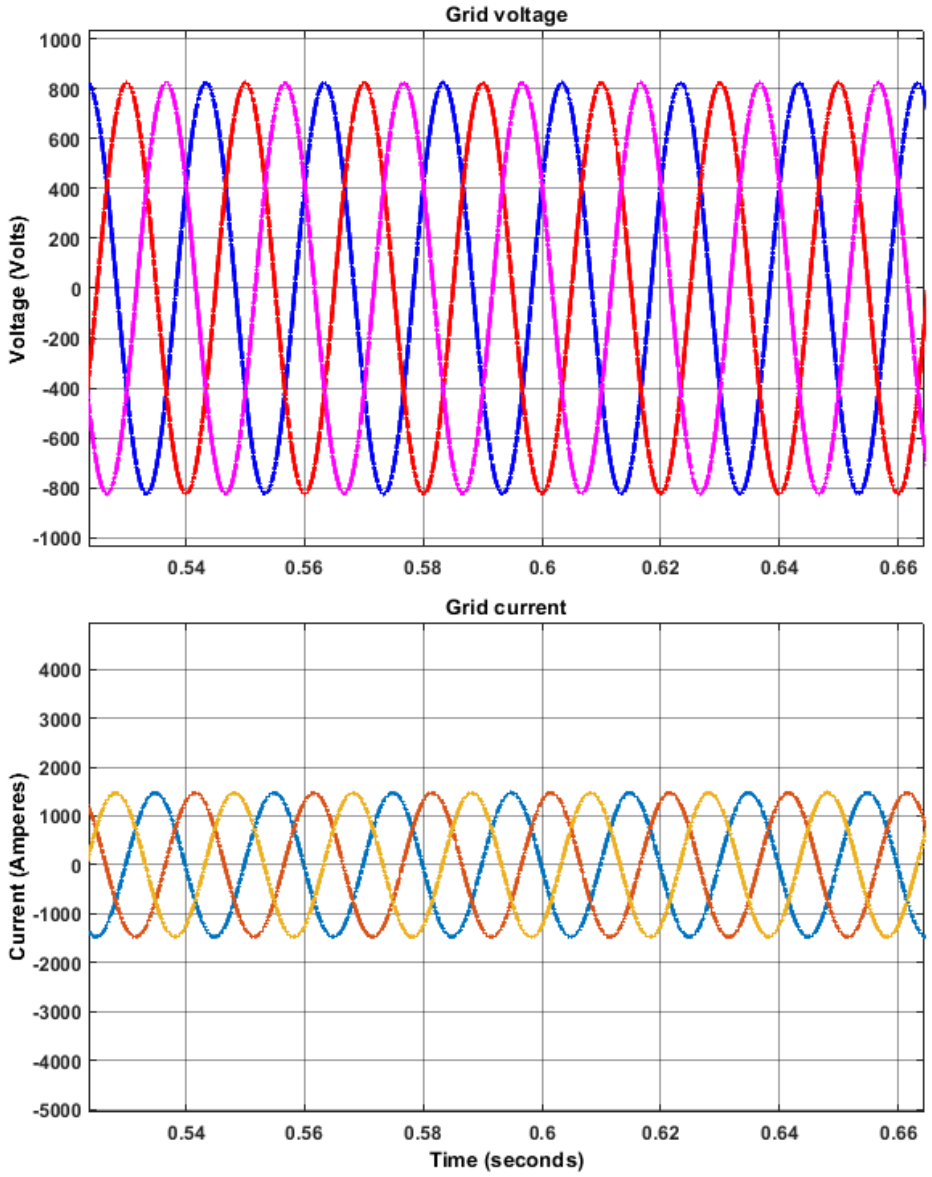

Figure 4. 23: Grid voltage and current.

The grid voltage and current were as depicted in Figure 4.23; their RMS magnitudes were 582 V (Figure 4.23(a)) between phases and 1105 A (Figure 4.23(b)) in a phase for the voltage and the current respectively. The phase to phase voltage response had a rise time of about 5.577 milliseconds, while the fall time was 5.542 milliseconds. Additionally, the overshoot and undershoot of the voltage at the beginning of the simulation were 11.932 % and 2.779 % respectively.

4.5.2 Case study 2: Nonlinear RL load

This case considered a nonlinear RL load of 2.5 MW and 150 kVAR; the megawatt fuel cell system was operated in grid connection mode to allow the grid to support the system in order to provide the deficit power that the fuel cell was not able to meet. The load active and reactive power were as shown in Figure 4.24; the value of the active power resulting from the simulation was about 2.36 MW (Figure 4.24(a)), while the reactive power varied around zero (1.865e-7 VAR) (Figure 4.24(b)). At the beginning of the simulation, this active power response was characterised by an overshoot of 14.557 % between the time t = 0 and t =0.3 seconds and an undershoot of 1.998 % between t = 0.3 and t = 0.4 seconds, thereafter, this response stabilised to reach the steady state value of 2.36 MW. On the other hand, the reactive power displayed an overshoot of 95.419 % around the time t = 2 seconds, whereas the undershoot was 40.092 %.

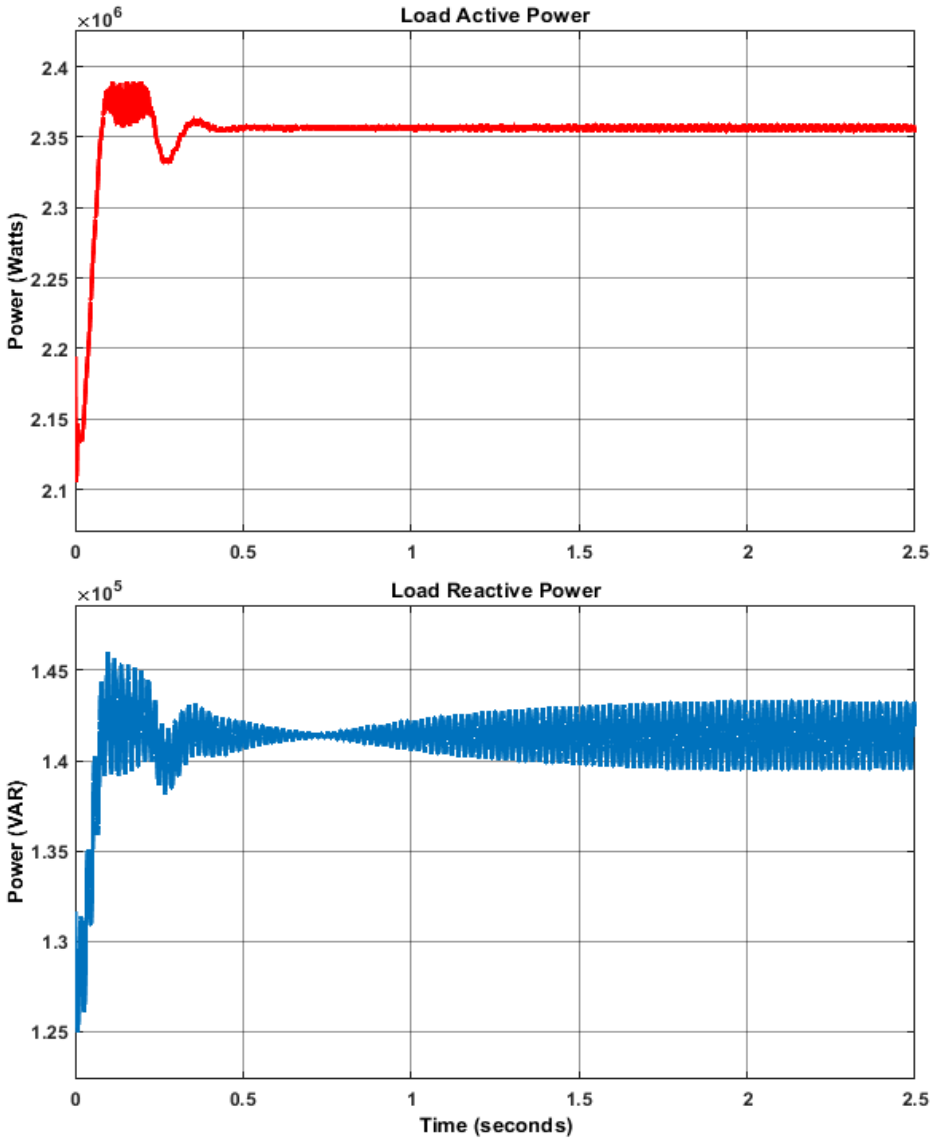

Figure 4. 24: Load active and reactive power.

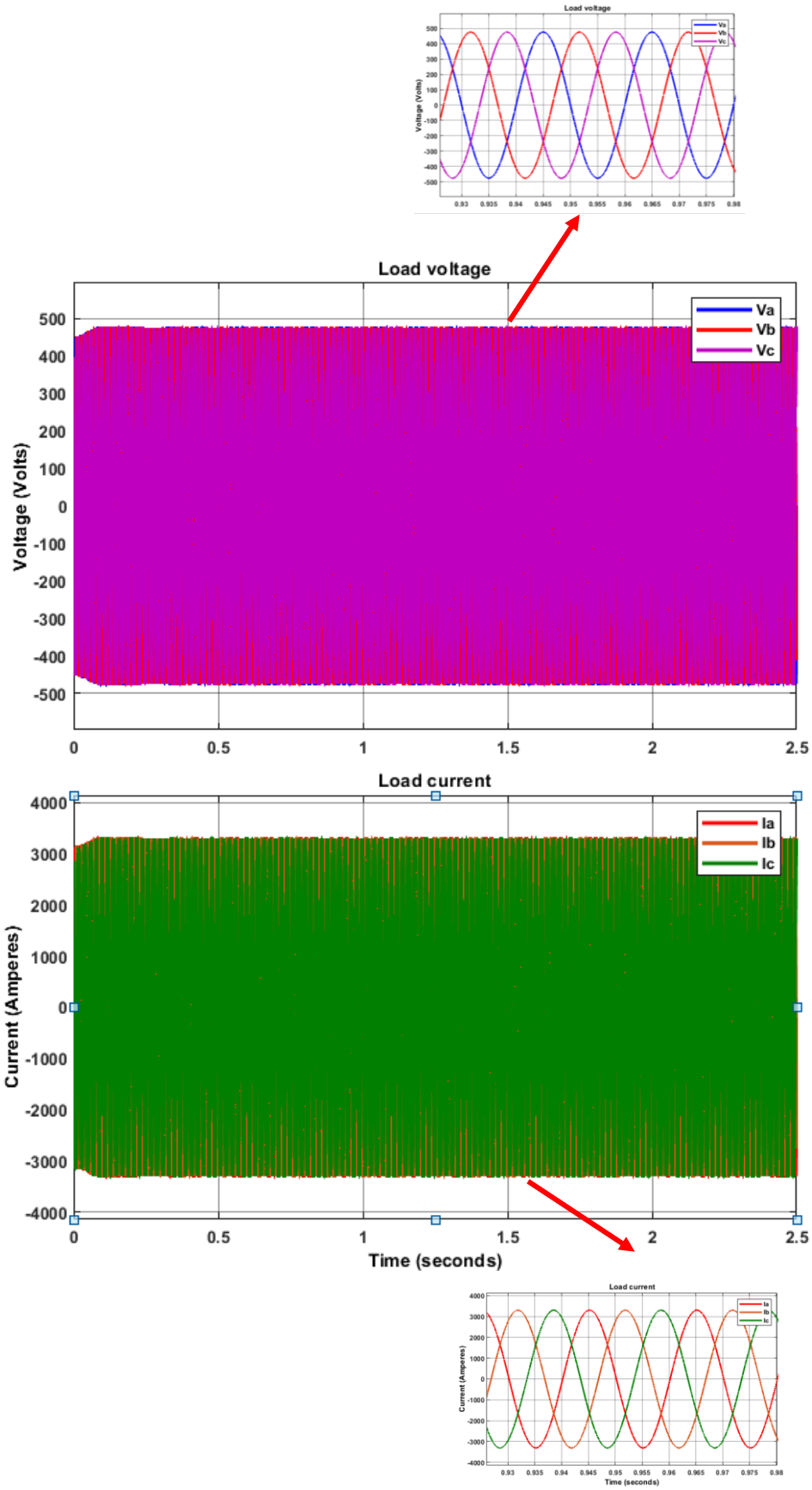

Figure 4. 25: Load voltage and current.

The phase to ground voltages V_a, V_b, and V_c, and the phase currents I_a, I_b and I_c after the filter were as shown in Figure 4.25. The magnitudes of the phase voltages were around 336 V (Figure 4.25(a)), and the magnitudes of the phase currents were around 2334 A (Figure 4.25(b)). The rise time of the phase to ground voltage was about 5.853 milliseconds, while the fall time was 5.857 milliseconds. Additionally, the overshoot and undershoot of this voltage at the beginning of the simulation were 0.321 % and 1.993 % respectively. On the other hand, the rise time of the phase current was about 5.852 milliseconds, while the fall time is 5.855 milliseconds. Additionally, the overshoot and undershoot of this voltage at the beginning of the simulation were 1.987 % and 0.213 % respectively.

The active and reactive power received from the grid were as depicted in Figure 4.26; these powers represented the deficit power unable to be provided from the megawatt fuel cell. The grid supplied about 1.5 MW to the load, while the megawatt fuel cell is provided the remaining portion. The active power response has a rise time of 67.634 milliseconds, the overshoot and undershoot were 11.932 % and 7.983 % respectively.

To compensate for the reactive power consumed by the nonlinear load, the grid provides about 1 MW. The rise time of this power was about 29.532 milliseconds, the overshoot and undershoot were 59 % and 1.999% respectively.

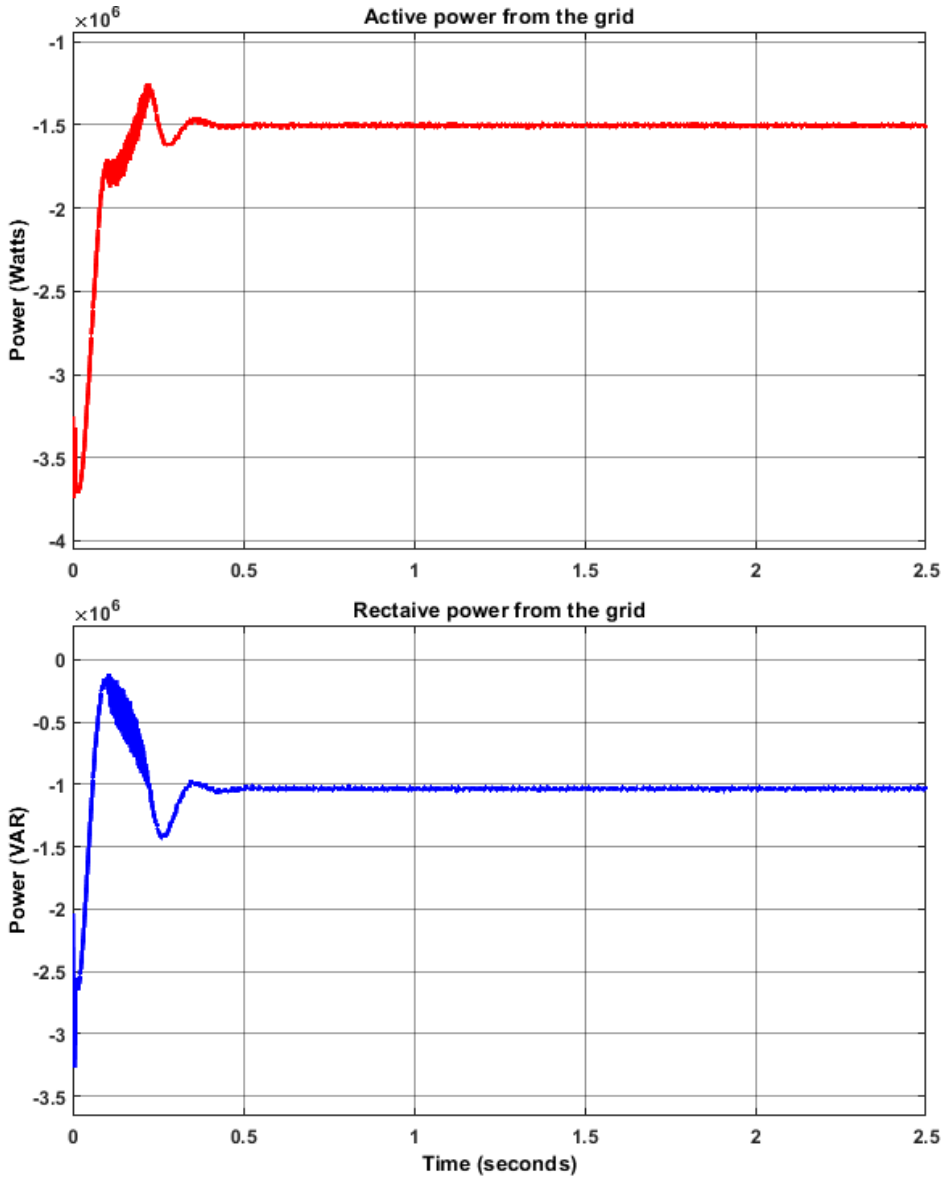

Figure 4. 26: Grid active and reactive power.

The grid voltage and current were as depicted in Figure 4.27; both signals were sine waves and their RMS magnitudes were 582 V between phases (Figure 4.27(a)) and 1105 A in a phase (Figure 4.27(a)) for the voltage and the current respectively. The phase to phase voltage response had a rise time of about 5.577 milliseconds, while the fall time was 5.542 milliseconds. Additionally, the overshoot and undershoot of the voltage at the beginning of the simulation were 11.932 % and 2.779 % respectively.

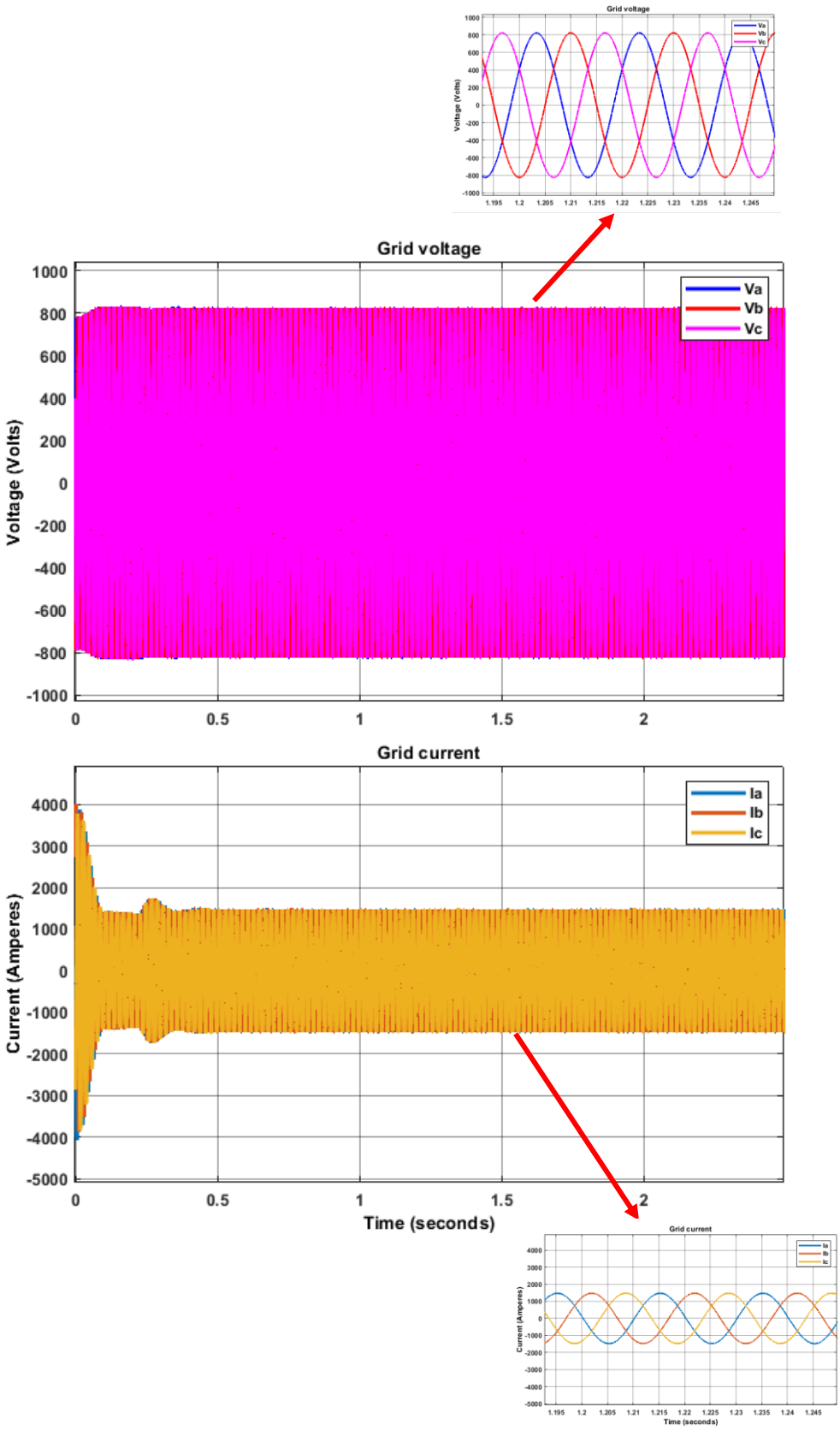

Figure 4. 27: Grid voltage and current.

4.5.3 Case study 3: 900 kW purely resistive load

The load considered in this case study was a purely resistive load of 900 kW; this load is fully met by the megawatt fuel cell and any excess power was conveyed to the grid. The load active and reactive load power were as shown in Figure 4.28; the value of the active power resulting from the simulation was about 917 kW, while the reactive varies between 0 and 287.8 nano VAR. At the beginning of the simulation, this active power response was characterised by overshoot 14.935 % between the time t = 0 and t =0.3 seconds and an undershoot of 2.187 % between t = 0.3 and t = 0.4 seconds, thereafter, this response stabilised to reach the steady state value of 917 kW.

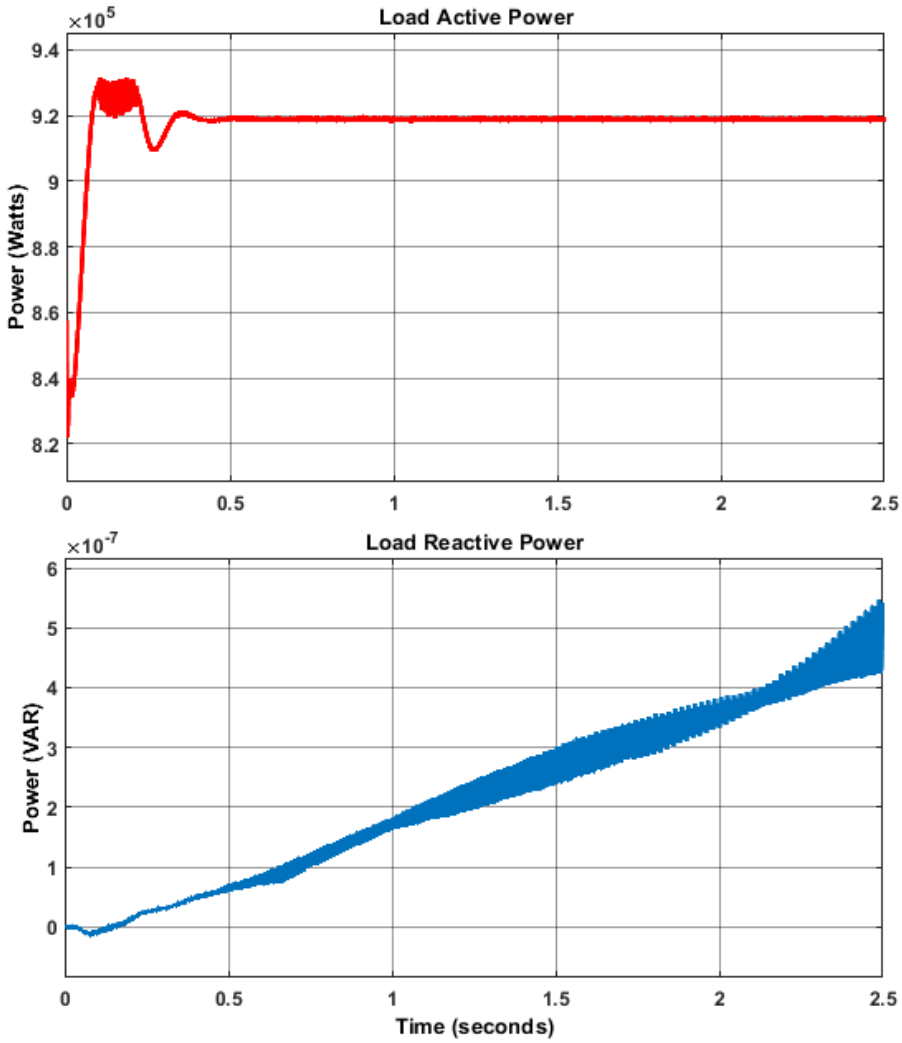

Figure 4. 28: Load active and reactive power.

The phase to ground voltages and the phase currents after the filter were as shown in Figure 4.29; both signals were pure sine waves. The magnitudes of the phase voltages were around 349.8 V (Figure 4.29(a)), and the magnitudes of the phase currents were around 874.7 A (Figure 4.29(b)). The rise time of the phase to ground voltage was

about 5.854 milliseconds, while the fall time was 5.858 milliseconds. Additionally, the overshoot and undershoot of this voltage at the beginning of the simulation were 0.312 % and 1.983 % respectively. On the other hand, the rise time of the phase current was about 5.858 milliseconds, while the fall time was 5.855 milliseconds. Additionally, the overshoot and undershoot of the currents at the beginning of the simulation were 1.984 % and 0.310 % respectively.

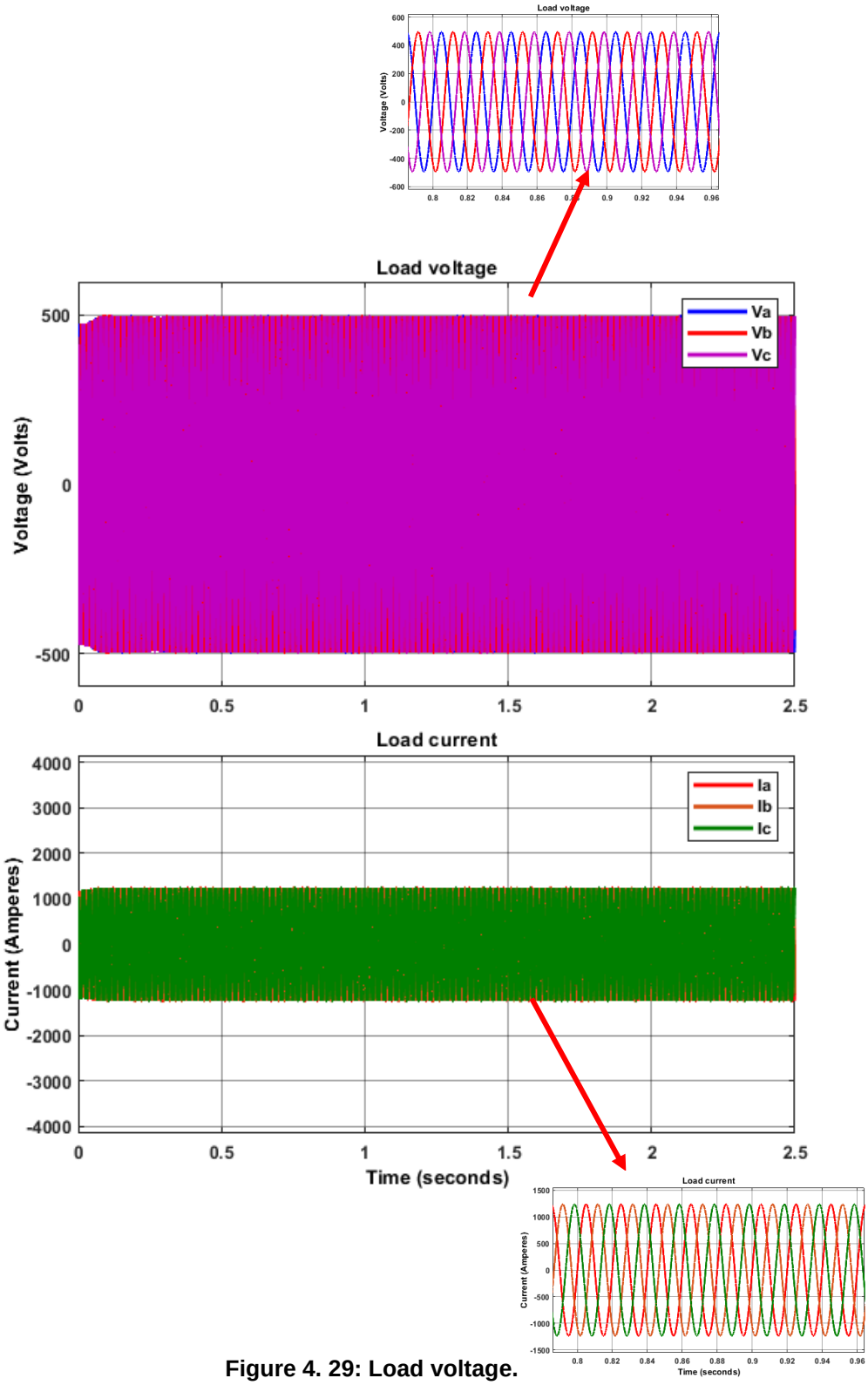

Figure 4. 29: Load voltage.

The active and reactive power supply to the grid were as depicted in Figure 4.30; these powers represented the excess power generated by the megawatt fuel cell. The grid received an active power of about 573.9 kW (Figure 4.30(a)) from the megawatt fuel cell system, while the reactive power received was around 508.4 kVAR (Figure 4.30(b)). The response of the active power had a rise time of 61.950 milliseconds, the overshoot and undershoot were 10.92 % and 8.35 % respectively, while that of the reactive power had a rise time equals to 29.842 milliseconds and an overshoot and undershoot of 55 % and 1.986 % respectively.

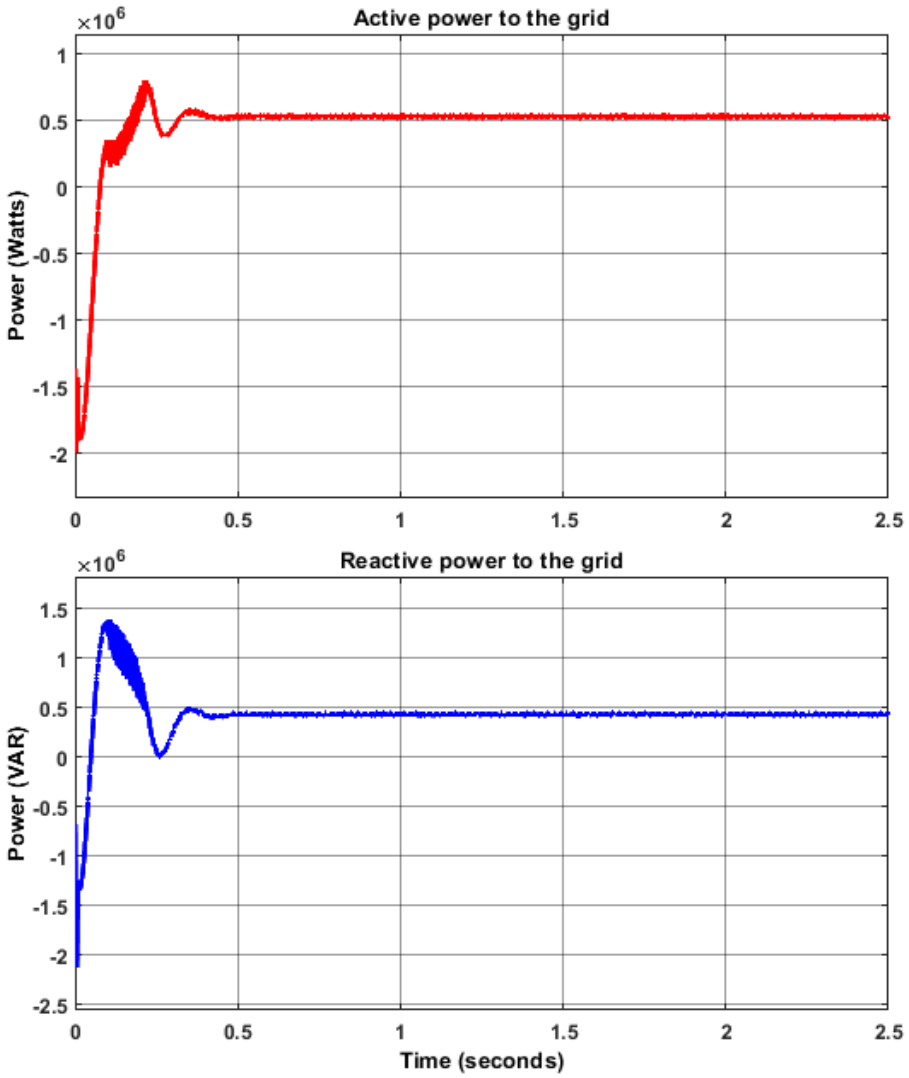

Figure 4. 30: Grid active and reactive power.

The voltage and current of the grid received from the megawatt fuel cell system were as depicted in Figure 4.31. Both these voltages and currents were sine waves; their RMS magnitudes were 605.8 V (Figure 4.31(a)) between phases and 427.1 A (Figure 4.31(b)) in-phase for the voltage and the current respectively. The phase to phase voltage response had a rise time of about 5.867 milliseconds, while the fall time was

5.866 milliseconds. Furthermore, the overshoot and undershoot of the voltage at the beginning of the simulation were 0.211 % and 1.987 % respectively. On the other hand, the current response had a rise time of about 5.459 milliseconds, while the fall time was 5.381 milliseconds. Furthermore, the overshoot and undershoot of the voltage at the beginning of the simulation were 6.19 % and 1.983 % respectively.

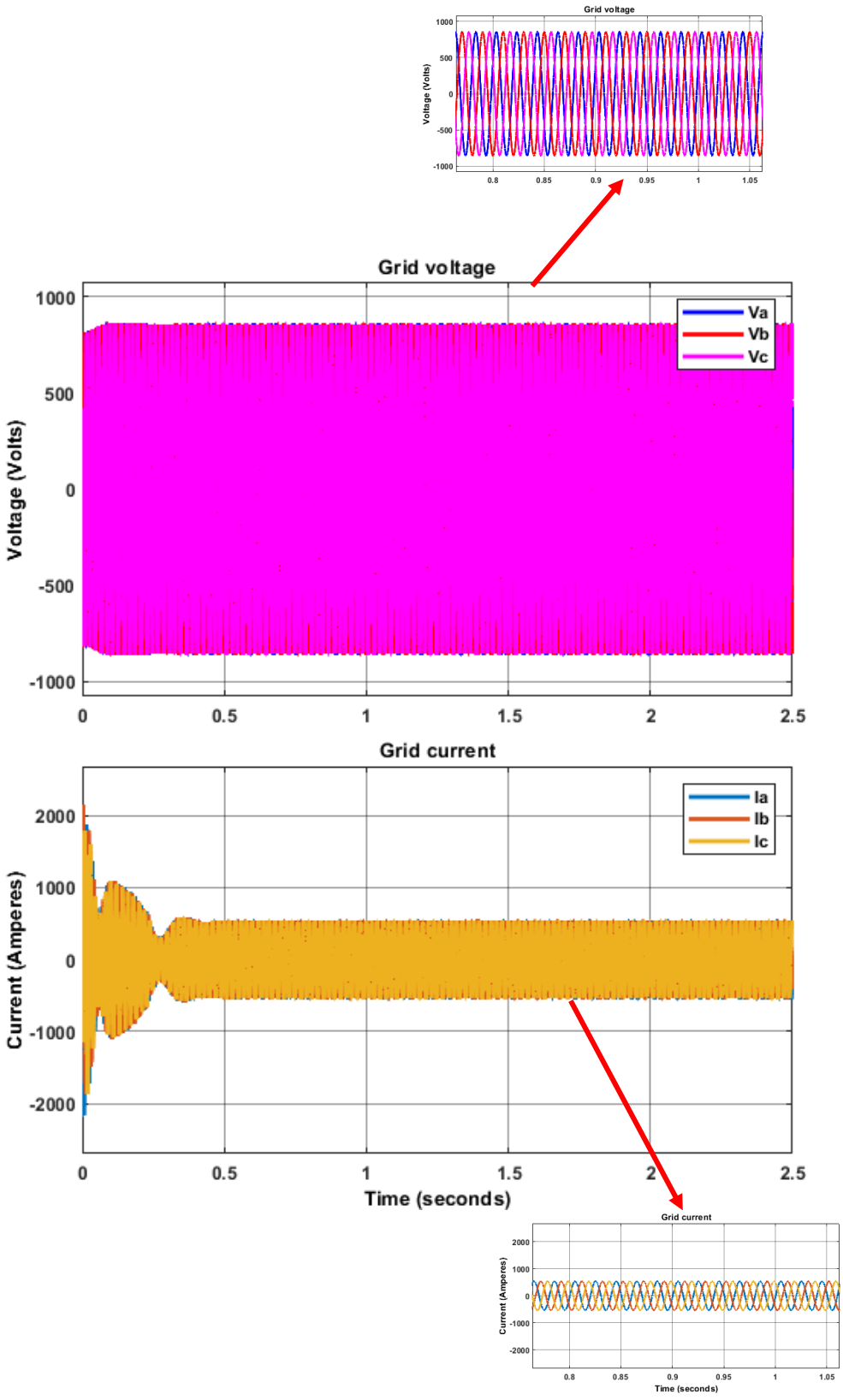

Figure 4. 31: Grid voltage and current.

4.5.4 Case study 4: 1.26 MW purely resistive load

The load considered in this case study was a purely resistive load equal in magnitude to the maximum power of the megawatt fuel cell system (1.26 MW). This load was fully met by the megawatt fuel cell and no excess power was conveyed to the grid. The load active and reactive power were as shown in Figure 4.32; the value of the active power resulting from the simulation was about 1.262 MW (Figure 4.32(a)), while the reactive varied between 0 and 27.4 nano VAR (Figure 4.32(b)). At the beginning of the simulation, this active power response was characterised by overshoot 14.935 % between the time t = 0 and t =0.3 seconds and an undershoot of 2.325 % between t = 0.3 and t = 0.4 seconds, thereafter, this response stabilised to reach the steady state value of 1.262 MW.

The reactive power had a rise time of 846.443 microseconds, a fall time of 806.453 microseconds and overshoot and undershoot of 135.906 % and 3.083 % respectively.

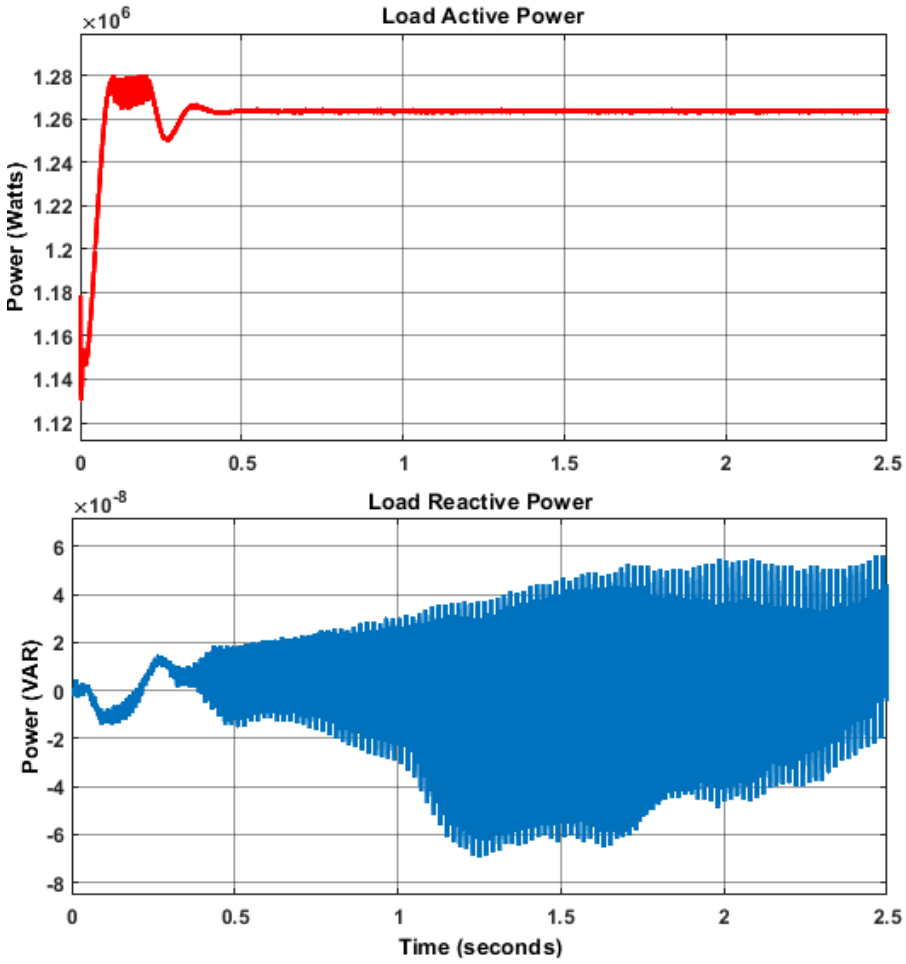

Figure 4. 32: Load active and reactive power.

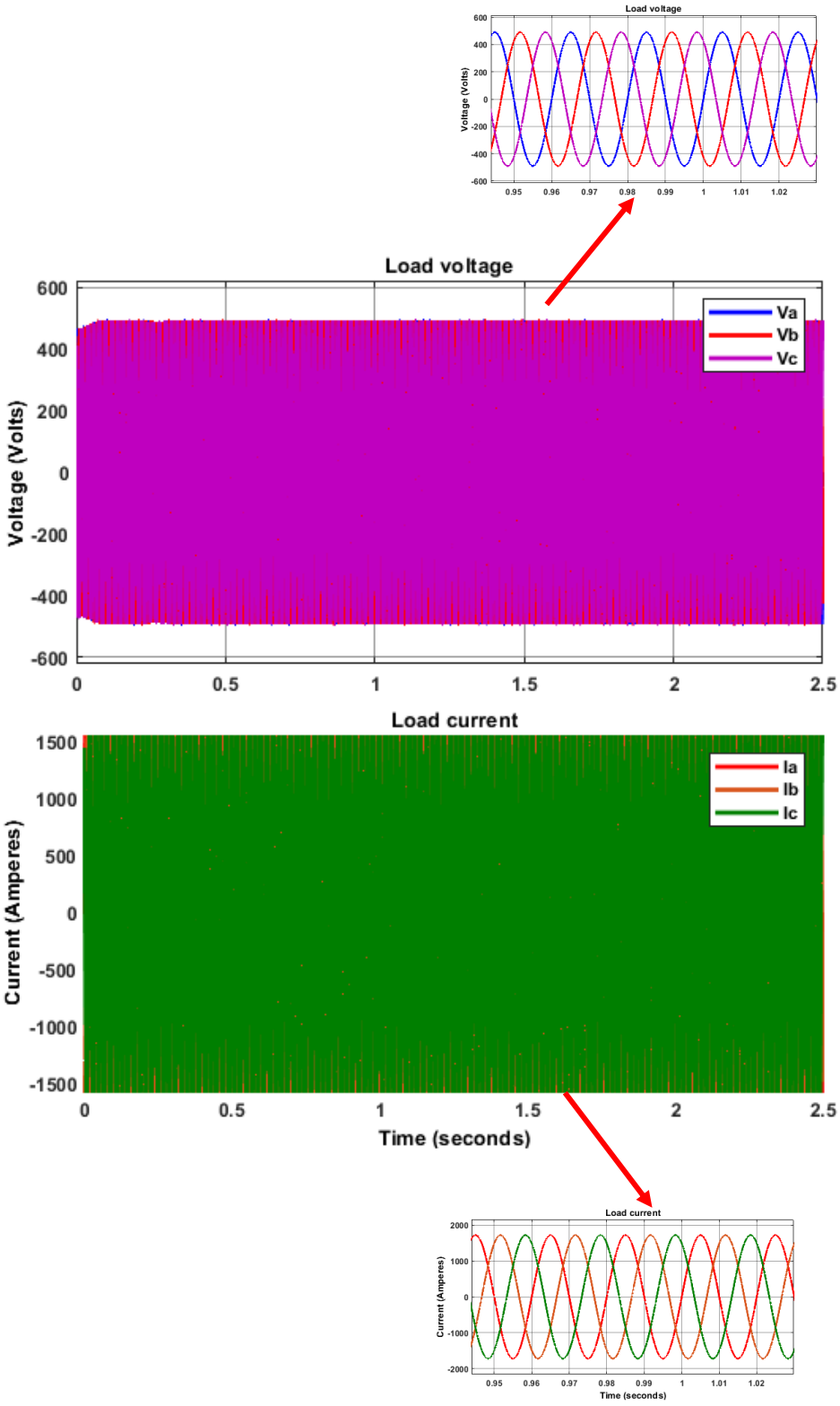

Figure 4. 33: Load voltage and current.

The phase to ground voltages and the phase current sine waves were as shown in Figure 4.33. The magnitudes of the phase voltages were around 346.6 V (Figure 4.33(a)), while those of the phase currents were around 1213 A (Figure 4.33(b)). The

rise time of the phase to ground voltage was about 5.853 milliseconds, while the fall time was 5.857 milliseconds. Additionally, the overshoot and undershoot of this voltage at the beginning of the simulation were 0.323 % and 1.987 % respectively. On the other hand, the rise time of the phase current was about 5.858 milliseconds, while the fall time was 5.856 milliseconds. Additionally, the overshoot and undershoot of the currents at the beginning of the simulation were 1.986 % and 0.306 % respectively.

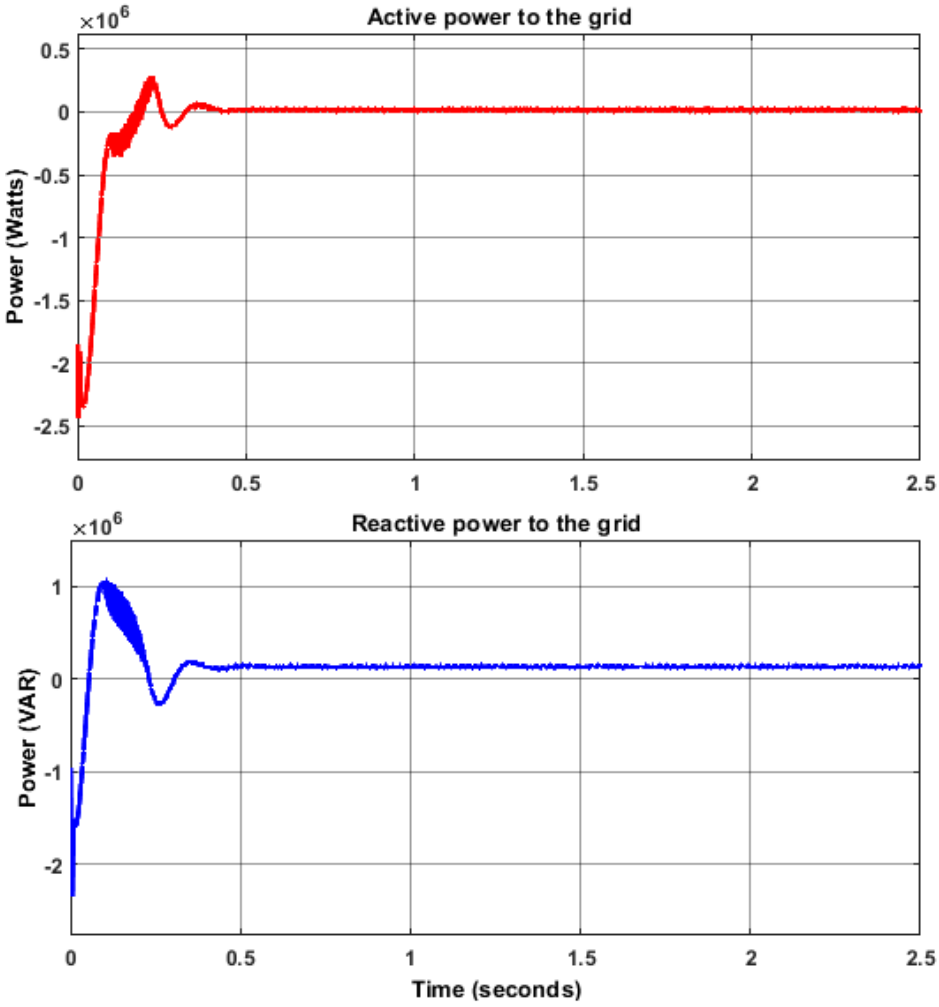

Figure 4. 34: Grid active and reactive power.

The grid active and reactive power were as shown in Figure 4.34; since no power was injected into the grid from the megawatt fuel cell, the active power was around zero (Figure 4.34(a)), while the reactive power received was around 295.1 kVAR (Figure 4.34(b)). The response of the active power had a rise time of 61.902 milliseconds, and an overshoot and undershoot of 10.92 % and 8.621 % respectively. Similarly, the reactive power had a rise time equals to 29.842 milliseconds and an overshoot and undershoot of 55 % and 1.995 % respectively.

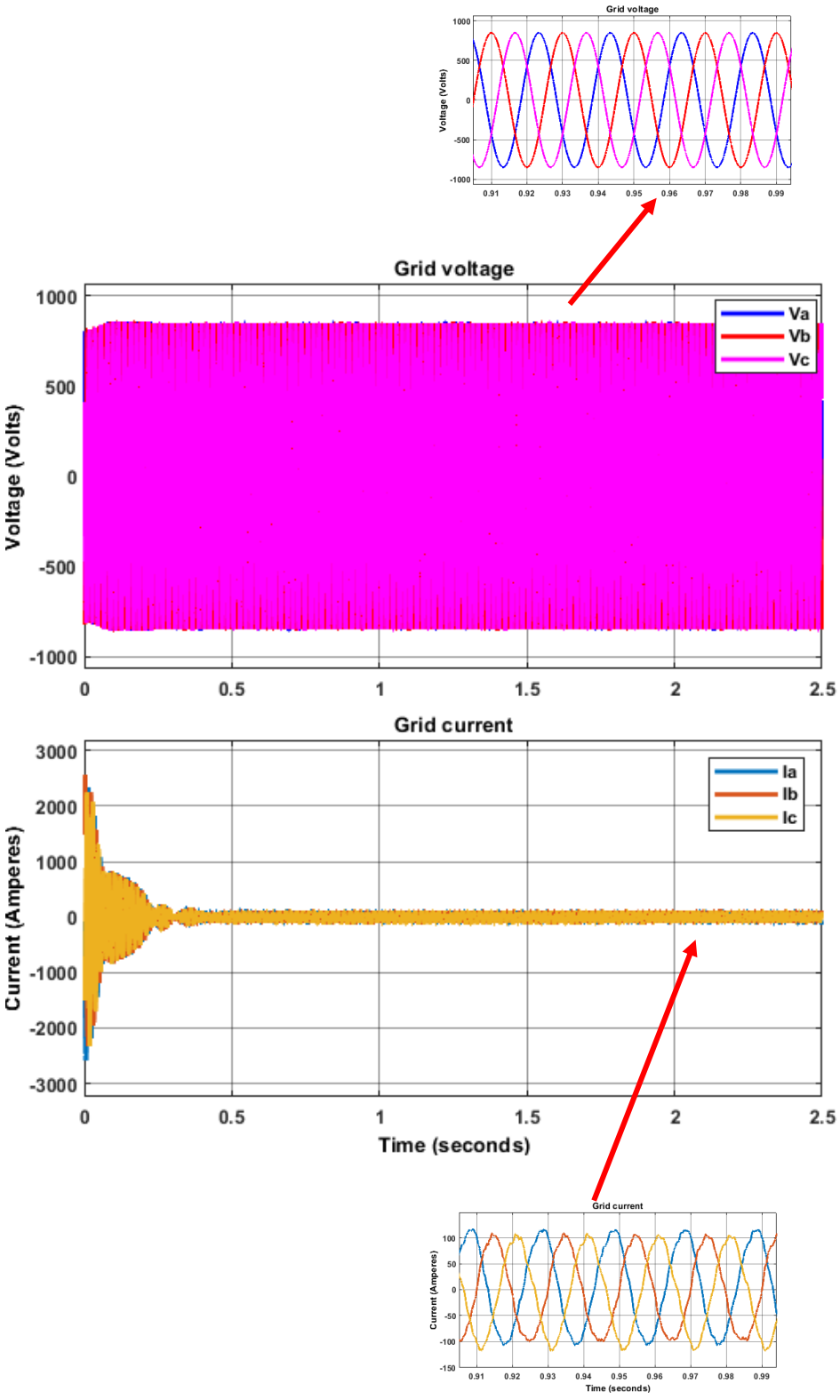

Figure 4. 35: Grid voltage and current.

The voltage and current sine waves of the grid were as depicted in Figure 4.35; their RMS magnitudes were 600.3 V (Figure 4.35(a)) between phases and 241.2 A (Figure 4.35(b)) in-phase for the voltage and the current respectively. The phase to phase voltage response had a rise time of about 5.867 milliseconds, while the fall time was 5.866 milliseconds. Furthermore, the overshoot and undershoot of the voltage at the beginning of the simulation were 0.206 % and 1.986 % respectively. On the other hand, the current response had a rise time of about 0 seconds, and a fall time was 0 seconds as no current was being fed into the grid.

4.5.5 Case study 5: Off-grid operation of the megawatt fuel cell system without the main utility grid

This case study considered the operation of the megawatt fuel cell system in an off-grid mode; without the main utility grid. The system was meant to meet a load requirement of 1.26 MW at 400 V (Figure 4.36(a)) and Figure 4.36(b) gave the reactive power curve which varied between 0 and 27.4 nano VAR.

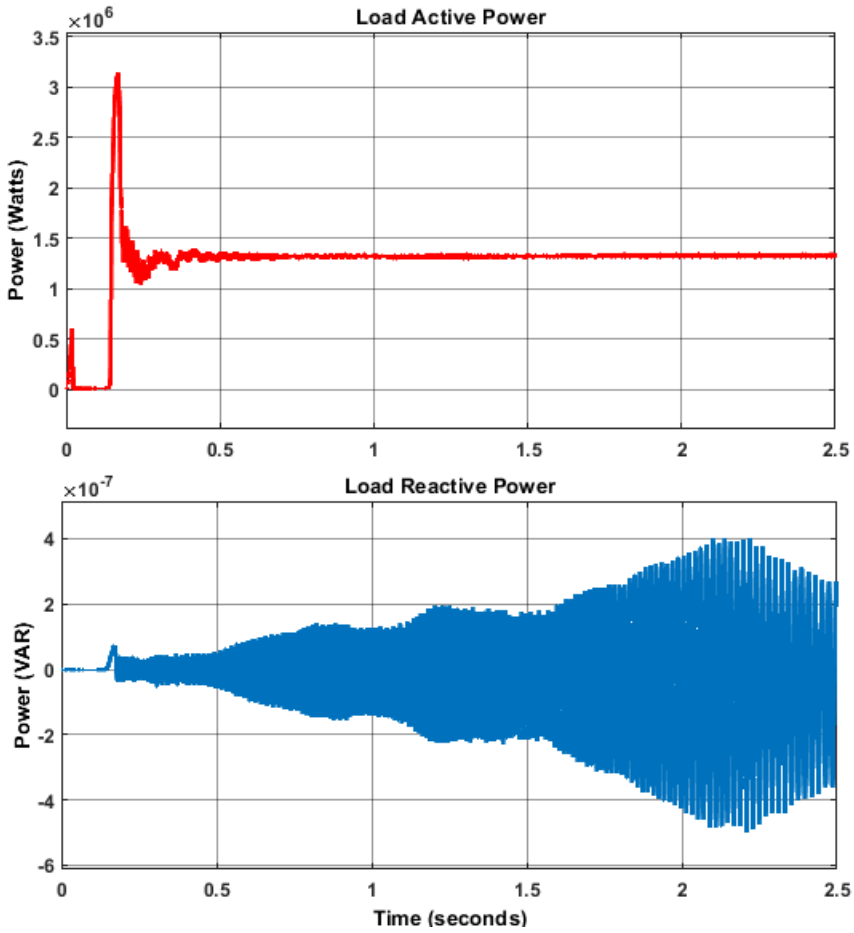

Figure 4. 36: Load active and reactive power.

At the beginning of the simulation, this active power response was characterised by an overshoot 14.935 % between the time t = 0 and t =0.3 seconds and an undershoot of 2.325 % between t = 0.3 and t = 0.4 seconds, thereafter, this response stabilised to reach the steady state value of 1.262 MW.

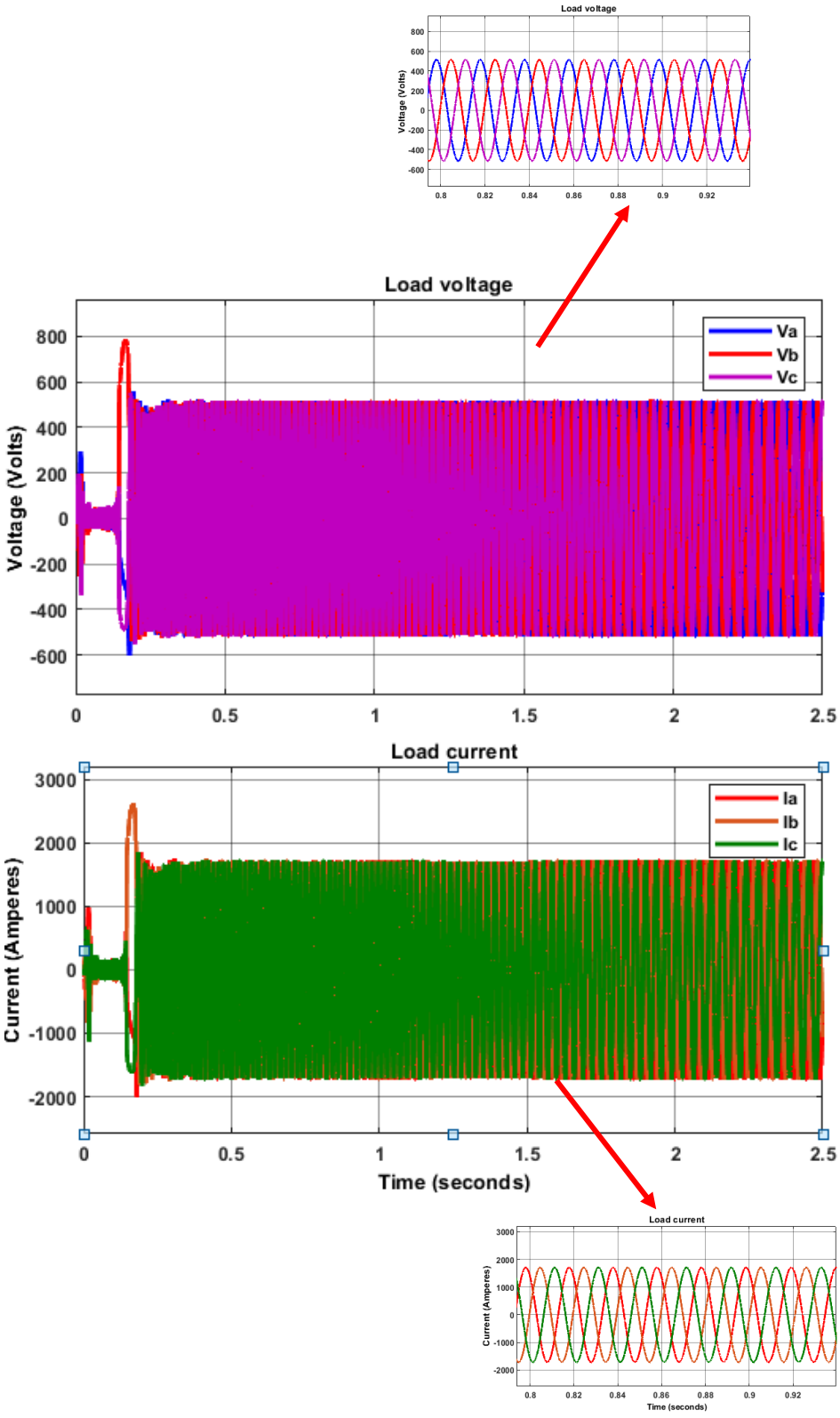

Figure 4. 37: Load current and voltage.

The voltage and current sine waves of the grid were as depicted in Figure 4.37; their RMS magnitudes were 600.3 V (Figure 4.37(a)) between phases and 241.2 A (Figure 4.37(b)) in-phase for the voltage and the current respectively. The phase to phase voltage response had a rise time of about 5.867 milliseconds, while the fall time was 5.866 milliseconds. Furthermore, the overshoot and undershoot of the voltage at the beginning of the simulation were 0.206 % and 1.986 % respectively. On the other hand, the current response had a rise time of about 0 seconds, and a fall time was 0 seconds as no current was being fed into the grid.

4.5.6 Case study 6: Megawatt fuel cell operating in off-grid mode and connected to an RL load

In this case study, the megawatt fuel cell system was operated in off-grid mode connected to a RL load of 1 MW and 663 kVAR. Figure 4.38 gave the active and reactive power curves, both curves were subjected to harmonics due to the presence of an inductive load. In such a case, a redesign of the filter was required in order to mitigate the effect of these harmonics.

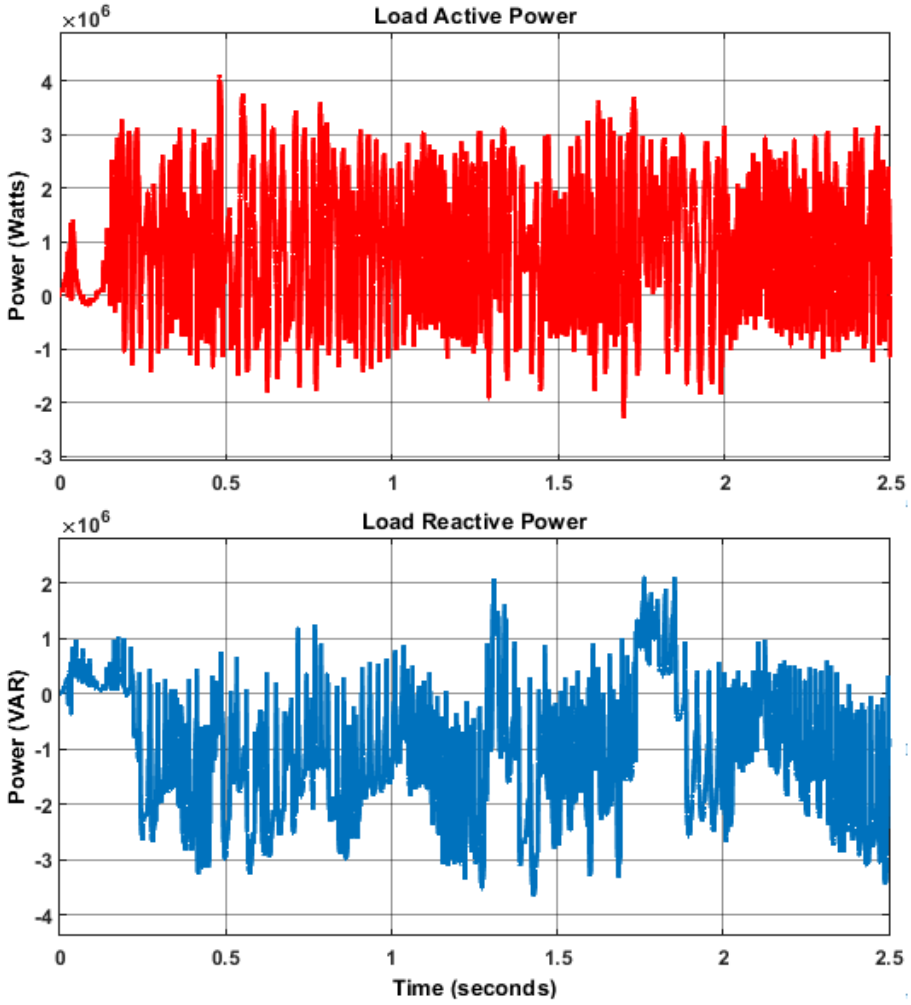

Figure 4. 38: Load active and reactive power.

The voltage and current at the load side were as illustrated in Figure 4.39. The effect of harmonics was as in both signals. The total harmonic distortion of both the voltage and current were 28.93 % and 30.53 % respectively.

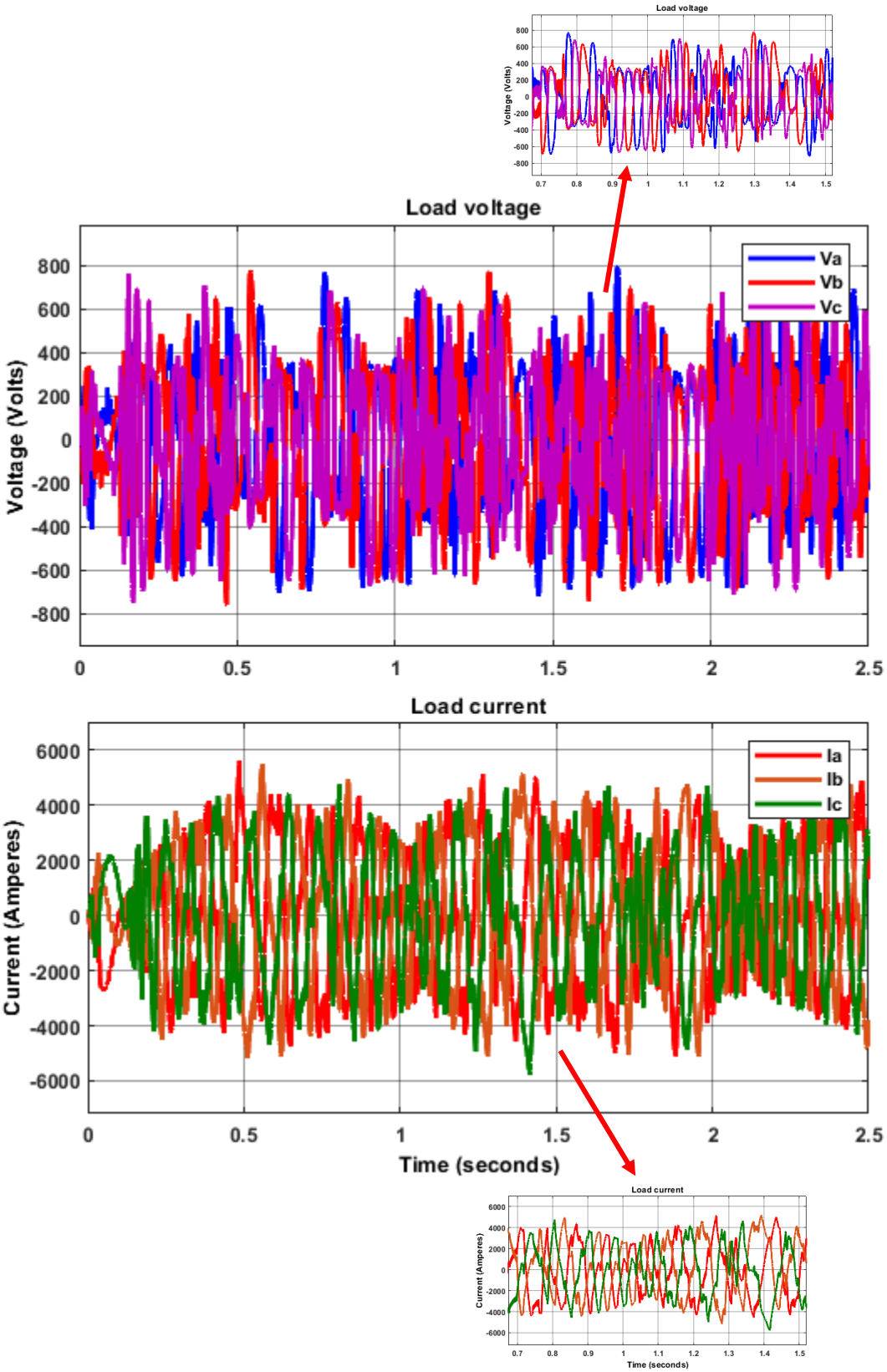

Figure 4. 39: Load voltage and current.

4.6 Summary

A simulation was carried out to evaluate the operation of the system in grid-connected mode, a total of twelve PEMFC stacks were connected in parallel to obtain the megawatt fuel cell stack. It was assumed that during the simulation that the hydrogen and oxygen composition, system temperature, hydrogen and oxygen pressure were unchanged, whereas the hydrogen and oxygen flow rate were depending on Equation 4.1 and Equation 4.2. The results showed a good performance of the developed system with a low total harmonic distortion of about 0.35% for the voltage and 0.19% for the current, therefore the system as designed complied with IEEE and IEC standards. Different case studies were also considered in grid-connected and offered operation modes depending on the load condition. It was observed that in off-grid mode, with a high inductive load, the filter might require redesign to mitigate the effect of harmonics.

CHAPTER FIVE
CONCLUSIONS AND RECOMMENDATIONS FOR FURTHER RESEARCH

5.1 Conclusion

This thesis dealt with the modelling and control of a three-level inverter for a grid-connected megawatt fuel cell stack. With the fast exhaustion of fossil fuels, the expansion of the world energy demand and concerns over global warming, new energy systems dependent on renewable and other sustainable energy are gaining more interests. It is a fact that future development in the energy sector would be founded on the utilisation of renewable and sustainable energy sources to meet the double targets of diminishing greenhouse gas emissions and ensuring reliable and cost-effective energy supply. Fuel cells are one of the advanced clean energy technologies and have demonstrated their ability to be a decent substitute to replace fossil fuel-based power systems. Various types of fuel cells can be found in the market, however, Proton Exchange Membrane Fuel Cell (PEMFC) is the most appealing in view of its low operating temperature, low noise, high efficiency and low pollution.

In general, PEMFC like other fuel cell types produces DC (direct current) power at a low-voltage level. To acquire high-power fuel cell systems, PEMFCs are associated in series and parallel to form multi-stacks fuel cell systems. To operate in grid-tied mode, a power converter is required to condition the generated DC power and converts it to AC with synchronised frequency and phases. This power converter can also permit the control of power quality and power supply. A power converter can be either a DC to DC converter or an inverter or both depending on the loads.

Several ways exist to connect fuel cell systems into an AC utility grid using power converters, the most popular connection topologies include centralised, string and multi-string configurations. The topology adopted in this study is centralised configuration. On the other hand, different types of inverter ranging from low to high level can be used in centralised configuration depending on the power requirement. For low power and low-voltage applications, the two-level inverters are the most used topologies whereas for high power and high-voltage applications, multi-level inverter configurations are more suitable. Applications of multi-level inverters range from medium to high voltage and comprise power distribution, motor drives, etc. For a given application, the choice of appropriate multi-level topology and its control scheme are not defined and depend on various engineering compromises, however, the most developed multi-level inverter topologies include the diode clamped, the flying capacitor and the cascade full bridge inverters.

Amongst the above-mentioned inverter topologies, the diode clamped multilevel inverter is the most accepted topology and the three-level diode clamped inverter is one of the most available inverters in the market.

Furthermore, a common inverter generates harmonics as its output voltage or current is not a pure sine wave. These harmonics impact negatively on sensitive equipment. Standards such each IEEE 519 and IEC 61000-3-6 set the allowable harmonic distortion for both the current and the voltage in a power system based on the current level and the voltage level respectively. Hence, the current injected into the grid should be balanced, sinusoidal, and have a total harmonic distortion lower than 5%. To comply with these requirements, the control of the inverter plays a vital role. In such a case, the objective of the control action is to properly feed the extracted power to the grid.

The goal of this research was to model and control a three-level diode clamped inverter for a grid-connected megawatt fuel cell stack. The considered system included a 1.54 MW/1400 V DC proton exchange membrane fuel cell stack, a 1.3 MW/600 V three-level diode clamped inverter and an LCL filter. The inverter control scheme comprised of voltage and current regulators to provide a good power factor and satisfy synchronisation requirements with the grid. The frequency and phase were synchronised with those of the grid through a phase locked loop. Modelling and simulation was performed using Matlab/Simulink. To achieve the goal, the research was divided in five chapters. Besides the introduction and the conclusion, the rest of the study can be summarised as follows:

Chapter two dealt with the literature survey on alternative power technologies including solar power, wind turbine, geothermal power, hydropower, biomass power and fuel cell. A section dedicated to power quality requirements for the grid connection of these technologies was considered with focus on grid code modifications to allow these alternative energy systems to operate in smart manner when there are connected to the utility grid. Furthermore, a section dealing with power converters for alternative energy systems including the different topologies for various power rating was presented.

Chapter three focused on the description of the grid-connected megawatt fuel cell system and the modelling of components involved on it. The adopted configuration consisted of components such as a 1.54 MW fuel cell stack, a three-level diode clamped inverter to convert the 1400 DC volts of the fuel cell into 600 AC volts between

phases, and an LCL filter to mitigate the effect of voltage and the current harmonics generated by the inverter.

The megawatt fuel cell stack included of several proton exchange membrane fuel cell (PEMFC) stacks connected in series and parallel. The system was developed based on the model of each component and the designed parameters of the fuel cell, inverter, LCL filter were also presented.

The last section of this chapter was oriented on the modelling of the control system for the inverter to properly deliver the generated power from the megawatt fuel cell stack to the grid and local load. It was stated that under nominal grid operation, the control of the feed-in current is important. This control is realised through a dual-loop control. The control of the current can be realised in different reference frames including the dq frame which allow the use of PI controllers. Moreover, the harmonic compensation and the synchronisation were also considered.

Chapter four dealt with the simulation results of the developed system; a total of twelve PEMFC stacks were connected in parallel to obtain the megawatt fuel cell stack. It was assumed that during the simulation that the hydrogen and oxygen composition, system temperature, hydrogen and oxygen pressure were unchanged, whereas the hydrogen and oxygen flow rate were depending on Equation 4.1 and Equation 4.2. The results show good performance of the developed system with a low total harmonic distortion of about 0.35% for the voltage and 0.19% for the current, therefore the system as designed complies with IEEE and IEC standards. Different case studies were also considered in grid-connected and offered operation modes depending on the load condition and it was observed that in off-grid mode, with a high inductive load, the filter might require redesign to mitigate the effect of harmonics.

5.2 Recommendation for further research

Further research should focus on the use:

i. intelligence control approach for the inverter;
ii. five, nine, or eleven level inverter and
iii. other inverter topologies.

REFERENCES

Abd, K. & Wahid, E. 2015. LCL Filter Design With Passive Damping For Photovoltaic Grid Connected Systems. In *6th International Renewable Energy Congress (IREC)*.

Abderezzak, B. 2018. Introduction to Hydrogen Technology. In *Introduction to Transfer Phenomena in PEM Fuel Cell*. Elsevier Ltd: 186.

Aguilar, M, D, B., Colome, D, G., Aguero, E. & Molina, M, G. 2016. Impact of Increased Penetration of Large-Scale PV Generation on Short-Term Stability of Power Systems. In *2016 IEEE 36th Central American and Panama Convention (CONCAPAN XXXVI)*. San Jose, Costa Rica: IEEE.

Al-Shetwi, A.Q., Sujod, M.Z. & Blaabjerg, F. 2018. Low Voltage Ride-Through Capability Control for Single-Stage Inverter-Based Grid-Connected Photovoltaic Power Plant. *Solar Energy*, 159: 665–681. https://doi.org/10.1016/j.solener.2017.11.027.

Al-Shetwi, A.Q., Sujod, M.Z., Blaabjerg, F. & Yang, Y. 2019. Fault Ride-Through Control of grid-connected Photovoltaic Power Plants: A review. *Solar Energy*, 180(November 2018): 340–350. https://doi.org/10.1016/j.solener.2019.01.032.

Alatrash, H., Amarin, R.A. & Lam, C. 2012. Enabling Large-Scale PV Integration into the Grid. In *2012 IEEE Green Technologies Conference*. Tulsa, OK: IEEE.

Albarbar, A. & Alrweq, M. 2018. *Proton Exchange Membrane Fuel Cells: Design, Modelling and Performance Assessment Techniques*. Manchester: Springer.

Ali, D.M. & Salman, S.K. 2006. Investigation into Modelling of A fuel Cell Stack System. In *Proceedings of the 41st International Universities Power Engineering Conference*. Newcastle-upon-Tyne: 137–141.

Ali, Z., Christo, N., Hadjidemetriou, L., Kyriakides, E. & Yang, Y. 2018. Three-phase phase-locked loop synchronization algorithms for grid- connected renewable energy systems : A review. *Renewable and Sustainable Energy Reviews*, 90: 434–452.

Aly, M. & Ramadan, H.A. 2019. Design and Implementation of Adaptive SVPWM Algorithm for Multilevel Inverters in Renewable Energy Applications. *Solar Energy*, 183: 745–754. https://doi.org/10.1016/j.solener.2019.03.069.

Aoki, I.H. 2009. *Information Architecture Design for*. Delft University of Technology MSc Engineering and Policy Analysis Irelia.

Arancibia, A., Strunz, K. & Mancilla-david, F. 2013. A Uni fi ed Single- and Three-Phase Control for Grid Connected Electric Vehicles. *IEEE Transactions on Smart Grid*, 4(4): 1780–1790.

Azani, H., Massoud, A., Benbrahim, L., Holiday, D. & Williams, B. 2016. An active damping approach for PR-based current control of grid-tied VSI with LCL filter. In *8th IET International Conference on Power Electronics, Machines and Drives*. Glasgow.

Bao, C., Ruan, X., Wang, X., Li, W., Pan, D. & Weng, K. 2013. Step-by-Step Controller Design for LCL-Type Grid-Connected Inverter with Capacitor–Current-Feedback Active-

Damping. *IEEE Transactions on Power Electronics*, 29(3): 1239–1253.

Barbir, F., Basile, A. & Veziroğlu, T.N. 2016. *Compendium of Hydrogen Energy : Hydrogen Energy Conversion*. 1st ed. B. Frano, B. Angelo, & V. T.Nejat, eds. Woodhead Publishing Limited.

Basar, M., Ahmad, A., Hasim, N. & Sopian, K. 2011. Introduction to the pico hydro power and the status of implementation in Malaysia. *Proceedings - 2011 IEEE Student Conference on Research and Development, SCOReD 2011*: 283–288.

Bayoumi, E.H. 2015. Three-phase LCL-Filter for Grid-Connected Inverter Using Cooperative Three-phase LCL-filter for Grid-connected Inverter Using Cooperative Bacteria Foraging Optimization. *Wseas Transactions on Systems and Control*, 10(2224–2856): 493–502.

Behera, R.R. & Thakur, A. 2016. An Overview of Various Grid Synchronization Techniques for Single-Phase Grid Integration of Renewable Distributed Power Generation Systems. In *2016 International Conference on Electrical, Electronics, and Optimization Techniques (ICEEOT)*. Chennai: IEEE: 2876–2880.

Behrouzi, F., Nakisa, M., Maimun, A. & Ahmed, Y.M. 2016. Global Renewable Energy and its potential in Malaysia : A review of Hydrokinetic turbine technology. *Renewable and Sustainable Energy Reviews*, 62: 1270–1281. http://dx.doi.org/10.1016/j.rser.2016.05.020.

Benzazah, C., Lazrak, L. & Ait, M. 2015. Design and Performance Analysis of Energy Conversion Chain , from Multilevel Inverter until the Grid. In *2015 27th International Conference on Microelectronics (ICM)*. Casablanca: IEEE: 311–314.

Blaabjerg, F., Teodorescu, R., Liserre, M. & Timbus, A. V. 2006. Overview of Control and Grid Synchronization for Distributed Power Generation Systems. *IEEE Transactions on Industrial Electronics*, 53(5): 1398–1409.

Bouchafaa, F., Beriber, D. & Boucherit, M. 2010. Modeling and control of a gird connected PV generation system. In *18th Mediterranean Conference on Control and Automation, MED'10 - Conference Proceedings*. IEEE: 315–320.

Braun, M., Stetz, T., Bründlinger, R., Mayr, C. & Ogimoto, K. 2011. Is the distribution grid ready to accept large - scale photovoltaic deployment ? State of the art , progress , and future prospects. *Progress in Photovoltaics Research and Applications*, 20(6).

Brown, M. 2019. Concentrated Solar Power: Dubai Reveals Plan for the World's Largest System | Inverse.

Buau, X., Wang, X., Pan, D., Yang, D., Li, W. & Bao, C. 2018. Control Techniques for LCL-Type Grid- Connected Inverters. : 319.

Camm, E.H., Behnke, M.R., Bolado, O., Bollen, M., Bradt, M., Brooks, C., Dilling, W., Edds, M., Hejdak, W.J., Houseman, D., Klein, S., Li, F., Li, J., Maibach, P., Nicolai, T., Patiño, J., Pasupulati, S. V., Samaan, N., Saylors, S., Siebert, T., Smith, T., Starke, M. & Walling, R. 2009. Characteristics of wind turbine generators for wind power plants. *2009*

IEEE Power and Energy Society General Meeting, PES '09: 1–5.

De Castro, C., Mediavilla, M., Miguel, L.J. & Frechoso, F. 2013. Global Solar Electric Potential: A Review of Their Technical and Sustainable Limits. *Renewable and Sustainable Energy Reviews*, 28: 824–835. http://dx.doi.org/10.1016/j.rser.2013.08.040.

Chakraborty, S., Vu, H., Hasan, M.M., Tran, D., Baghdadi, M. El & Hegazy, O. 2019. DC-DC Converter Topologies for Electric Vehicles , Plug-in Hybrid Electric Vehicles and Fast Charging Stations : State of the Art and Future Trends. *energies*, 12(8).

Chatterjee, A. & Mohanty, K.B. 2018. Current Control Strategies for Single Phase Grid Integrated Inverters for Photovoltaic Applications-A review. *Renewable and Sustainable Energy Reviews*, 92: 554–569. https://doi.org/10.1016/j.rser.2018.04.115.

Chaturvedi, P., Shailendra Jain & Pramod Agrawal. 2005. Modeling, Simulation and Analysis of Three-Level Neutral Point Clamped Inverter Using Matlab/Simulink/Power System Blockset. In *2005 International Conference on Electrical Machines and Systems*. Nanjing.

Chen, W., Han, Y., Li, Q., Liu, Z. & Peng, F. 2014. Design of Proton Exchange Membrane Fuel Cell Grid-Connected System Based on Resonant Current Controller. *International Journal of Hydrogen Energy*, 9: 0–8.

Chen, Y. & Liu, Y. 2017. Latest Advances of LLC Converters in High Current , Fast Dynamic Response , and Wide Voltage Range Applications. *Transactions on Power Electronics*, 2(1): 59–67.

Chu, G., Wen, H., Jiang, L., Hu, Y. & Li, X. 2017. Bidirectional Flyback Based Isolated-port Submodule Differential Power Processing Optimizer for Photovoltaic Applications. *Solar Energy*, 158(November): 929–940. http://dx.doi.org/10.1016/j.solener.2017.10.053.

Colak, I., Kabalci, E. & Bayindir, R. 2011. Review of multilevel voltage source inverter topologies and control schemes. *Energy Conversion and Management*, 52(2): 1114–1128.

Corrêa, J.M., Farret, F.A., Canha, L.N. & Simoes, M.G. 2004. An electrochemical-based fuel-cell model suitable for electrical engineering automation approach. *IEEE Transactions on Industrial Electronics*, 51(5): 1103–1112.

Crosson, C.R., Saha, A.K., Ijumba, N.M., Chetty, L., Chikuni, E. & Africa, S. 2011. Stand-Alone and Grid -Connected Operation of Fuel Cell. In *IET Conference on Renewable Power Generation (RPG 2011)*. Edinburgh.

Dai, K., Bergot, A., Liang, C., Xiang, W.N. & Huang, Z. 2015. Environmental issues associated with wind energy - A review. *Renewable Energy*, 75: 911–921. http://dx.doi.org/10.1016/j.renene.2014.10.074.

Dai, Y., Li, W., Zhou, C. & Zhuang, S. 2018. Research on Transformerless Dual-Buck Full-Bridge Grid-Connected Inverter With H5-Type for PV Systems. *IET Power Electronics*, 12(1): 44–50.

Das, M. & Das, N. 2009. BIOMASS: A sustainable source of energy. *Asia-Pacific Power and Energy Engineering Conference, APPEEC*: 1–4.

Daware, K. 2015. Geothermal Energy and Geothermal Power Plants | electricaleasy.com. *Electricaleasy.com*.

Dhar, S. & Dash, P. 2016. Adaptive backstepping sliding mode control of a grid interactive PV-VSC system with LCL filter. *Sustainable Energy, Grids and Networks*, 6: 109–124.

Dicks, L, A. & Rand, J, A, D. 2018. *Fuel Cell Systems Explained*. 3rd ed. Wiley.

Drewry, M.A. & Georgiou, G.A. 2007. A review of NDT techniques for wind turbines. *Insight: Non-Destructive Testing and Condition Monitoring*, 49(3): 137–141.

Energy.gov. 2019. Solar Dish/Engine Power Plant Illustration | Department of Energy.

Erfanmanesh, T. & Dehghani, M. 2013. Adaptive sliding mode controller design for power converters of fuel cell system. In *3rd International Conference on Control, Instrumentation, and Automation (ICCIA 2013*. Tehran: IEEE.

Esmaeilian, H.R., Fadaeinedjad, R. & Moschopoulos, G. 2014. Dynamic Operation and Control of a Stand-Alone PEM Fuel Cell System. In *2014 IEEE Applied Power Electronics Conference and Exposition - APEC 2014*. Fort Worth, TX: IEEE: 3378–3384.

Espinoza, J.R., Jobs, G., Pkrez, M. & T, L.A.M. 2000. Stability Issues in Three-phase PWM Current/Voltage Source Rectifiers in the Regeneration Mode. In *ISIE'2000. Proceedings of the 2000 IEEE International Symposium on Industrial Electronics (Cat. No.00TH8543)*. Cholula, Puebla: IEEE: 453–458.

Felix, M. & Gheewala, S.H. 2011. A Review of Biomass Energy Dependency in Tanzania. *Energy Procedia*, 9: 338–343.

Firdaus, A., Mishra, S. & Bhende, C.N. 2017. Modelling A Droop Controlled Multi PV Inverter System to Study Effects of System Parameters on Oscillatory Modes. In *2017 Asian Conference on Energy, Power and Transportation Electrification, ACEPT 2017*. 1–6.

Frappé, E., De Bernardinis, A., Coquery, G., Bethoux, O. & Marchand, C. 2010. Corrective Action with Power Converter for Faulty Multiple Fuel Cells Generator Used in Transportation. In *2010 IEEE Vehicle Power and Propulsion Conference, VPPC 2010*. Lille.

Freddy, K.S.T., Lee, J., Moon, H. & Lee, K. 2017. Modulation Technique for Single-Phase Transformerless Photovoltaic Inverters With Reactive Power Capability. *IEEE Transactions on Industrial Electronics*, 64(9): 6989–6999.

Gaiceanu, M. 2007. Inverter Control for Three-Phase Grid Connected Fuel Cell Power System. In *2007 Compatibility in Power Electronics*. Gdansk.

Gao, F., Blunier'Benjamin & Miraoui, A. 2012. *Proton Exchange Membrane Fuel Cells Modeling*. Wiley.

Gonzalez, S.A., Verne, S.A. & Valla, M.I. 2013. *Multilevel Converters applIcatIons*. CRC

Press.

Ben Hamad, K., Taha, M.H., Almaktoof, A. & Kahn, M.T.E. 2019. Modelling and analysis of a grid-connected Megawatt Fuel Cell stack. In *2019 International Conference on the Domestic Use of Energy (DUE)*. IEEE: 147–155.

Hamoud, F., Doumbia, M.L. & Cheriti, A. 2016. Power factor improvement in WECS using cascade PI control of passive damping LCL-filter. *2015 International Conference on Sustainable Mobility Applications, Renewables and Technology, SMART 2015*.

Hani, S. El, Mediouni, H. & Echchaachouai, A. 2017. Comparative Analysis on Current Control Methods Grid Energy Quality. In *3rd International Conference on Electrical and Information Technologies ICEIT'2017 Comparativ*.

Hassaine, L., Olias, E., Quintero, J. & Salas, V. 2014. Overview of power inverter topologies and control structures for grid connected photovoltaic systems. *Renewable and Sustainable Energy Reviews*, 30: 796–807. http://dx.doi.org/10.1016/j.rser.2013.11.005.

Hossain, S., Abdalla, A.M., Jamain, S.N.B., Zaini, J.H. & Azad, A.K. 2017. A review on Proton Conducting Electrolytes for Clean Energy and Intermediate Temperature-Solid Oxide Fuel Cells. *Renewable and Sustainable Energy Reviews*, 79: 750–764. http://dx.doi.org/10.1016/j.rser.2017.05.147.

Hu, S., Cui, W., Li, W. & Cao, F. 2014. A High-Efficiency Single-Phase Inverter for Transformerless Photovoltaic Grid-Connection. In *2014 IEEE Energy Conversion Congress and Exposition (ECCE)*. Pittsburgh, PA: IEEE: 4232–4236.

İnci, M. 2019. Design and Modeling of Single Phase Grid Connected Fuel Cell System. In *2019 4th International Conference on Power Electronics and their Applications (ICPEA)*. Hatay: IEEE: 1–6.

Ioannis, N., Andreas, M., Stavros, N., Eleftheria, P. & Argitis, I.M. 2010. Analysis of a PEM Fuel Cell System dynamic response (Operational and Simulation results). In *45th International Universities Power Engineering Conference UPEC2010*. Cardiff: IEEE: 1–5.

IRENA. 2015. *Renewable Energy and Jobs*.

Islam, M. & Mekhilef, S. 2014. An Improved Transformerless Grid Connected Photovoltaic Inverter with Reduced Leakage Current. *Energy Conversion and Management*, 88: 854–862. http://dx.doi.org/10.1016/j.enconman.2014.09.014.

Islam, M., Shabani, B., Rosengarten, G. & Andrews, J. 2015. The potential of using nanofluids in PEM fuel cell cooling systems: A review. *Renewable and Sustainable Energy Reviews*, 48: 523–539.

Jafarian, H., Kim, N. & Parkhideh, B. 2018. Decentralized Control Strategy for AC-Stacked PV Inverter Architecture Under Grid Background Harmonics. *IEEE Journal of Emerging and Selected Topics in Power Electronics*, 6(1): 84–93.

Jeong, H.-G., Lee, K.-B., Choi, S. & Choi, W. 2010. Performance Improvement of LCL -Filter-

Based Grid-Connected Inverters Using PQR Power Transformation. *IEEE Transactions on Power Electronics*, 25(5): 1320–1330.

Jia, J., Li, Q., Wang, Y., Cham, Y. & Han, M. 2009. Modeling and Dynamic Characteristic Simulation of a Proton Exchange Membrane Fuel Cell. *IEEE Transactions on Energy Conversion*, 24(1): 283–291.

Jia, J., Yang, S., Wang, Y. & Cham, Y.T. 2009. Matlab/Simulink based-study on PEM fuel cell and nonlinear control. In *2009 IEEE International Conference on Control and Automation*. Christchurch: IEEE: 1657–1662.

Jian, Z., Xiaodong, Y., Zhe, C., Yong, M., Model, A. & Stack, S. 2014. Generalized Load Modeling with Solid Oxide Fuel Cell (SOFC) Considered. In *2014 International Conference on Power System Technology*. Chengdu: IEEE: 1040–1046.

Jiang, J.N., Tang, C.Y. & Ramakumar, R.G. 2016. *Control and Operation of Grid-Connected Wind Farms*.

Kantar, E., Usluer, S.N. & Hava, A.M. 2014. Design and performance analysis of a grid connected PWM-VSI system. In *2013 8th International Conference on Electrical and Electronics Engineering (ELECO)*. The Chamber of Turkish Electrical Engineers-Bursa: 157–161.

Kazimierczuk, M.K. 2016. *Pulse-Width Modulated DC–DC Power Converters*. 2nd ed. WILEY.

Keawthai, S. & Po-ngam, S. 2015. Simplified Active Power and Reactive Power Control with MPPT and Islanding Detection for Three-Phase Grid-Connected Photovoltaic Inverters. In *2015 12th International Conference on Electrical Engineering/Electronics, Computer, Telecommunications and Information Technology (ECTI-CON)*. Hua Hin: IEEE.

Kerekes, T., Teodorescu, R. & Rodríguez, P. 2011. A new high-efficiency single-phase transformerless PV inverter topology. In *IEEE Transactions on Industrial Electronics ·*. IEEE.

Khiari, B., Jeguirim, M., Limousy, L. & Bennici, S. 2019. Biomass derived chars for energy applications. *Renewable and Sustainable Energy Reviews*, 108: 253–273. https://doi.org/10.1016/j.rser.2019.03.057.

Kobayashi, H. 2012. Fault Ride Through Requirements and Measures of Distributed PV Systems in Japan. In *2012 IEEE Power and Energy Society General Meeting*. San Diego, CA: IEEE: 1–6.

Konara, K., Kolhe, M. & Nishimura, A. 2016. Grid Integration of PEM Fuel Cell with Multiphase Switching for Maximum Power Operation. In *2016 IEEE International Conference on Power System Technology, POWERCON 2016*.

Kumar, L., Hasanuzzaman, M. & Rahim, N.A. 2019. Global Advancement of Solar Thermal Energy Technologies for Industrial Process Heat and its Future Prospects: A review. *Energy Conversion and Management*, 195: 885–908.

https://doi.org/10.1016/j.enconman.2019.05.081.

Kun-qi, L., Bin, Z. & Wei-qi, X. 2017. Current Predictive Control of Three-Phase PWM Rectifier. In *2017 IEEE 2nd Information Technology, Networking, Electronic and Automation Control Conference (ITNEC)*. 1659–1662.

Lacal-arantegui, R. 2019. Globalization in The wind Energy Industry : Contribution and Economic Impact of European Companies. *Renewable Energy*, 134: 612–628.

Lai, J.-S. & Ellis, M.W. 2017. Fuel Cell Power Systems and Applications. *Proceedings of the IEEE*, 105(11): 2166–2190.

Lee, J.M. & Cho, B.H. 2009. A Dynamic Model of a PEM Fuel Cell System. In *2009 Twenty-Fourth Annual IEEE Applied Power Electronics Conference and Exposition*. Seoul: IEEE: 720–724.

Lee, K.-B. & Lee, J.-S. 2017. *Reliability Improvement Technology for Power Converters*. Singapore: Springer.

Lee, K., Huh, S., Yoo, J. & Blaabjerg, F. 2005. Performance Improvement of DTC for Induction Motor-Fed by Three-Level Inverter With an Uncertainty Observer Using RBFN. *IEEE Transactions on Energy Conversion*, 20(2): 276–283.

Li, Y.W. & He, J. 2014. Distribution System Harmonic Compensation Methods: An Overview of DG-Interfacing Inverters. *IEEE Industrial Electronics Magazine*, 8(December): 18–31.

Liu, J., Su, C., Wang, C., Zhu, L. & He, J. 2019. Influence of solid oxide fuel cell on power system transient stability. *The Journal of Engineering*, 2019(16): 1081–1086.

Liu, J., Zhou, L., Yu, X., Li, B. & Zheng, C. 2016. Design and analysis of an LCL circuit-based three-phase grid-connected inverter. *IET Power Electronics*, 10(2): 232–239.

Luna, A., Rocabert, J., Candela, J.I., Hermoso, J.R., Teodorescu, R., Blaabjerg, F. & Rodríguez, P. 2015. Grid Voltage Synchronization for Distributed Generation Systems Under Grid Fault Conditions. *IEEE Transactions on Industry Applications*, 51(4): 3414–3425.

Luta, D.N. & Raji, A.K. 2018. Optimal sizing of hybrid fuel cell-supercapacitor storage system for off-grid renewable applications. *Energy*, 166: 530–540.

Maghami, M.R., Hizam, H., Gomes, C., Radzi, M.A., Rezadad, M.I. & Hajighorbani, S. 2016. Power loss due to soiling on solar panel: A review. *Renewable and Sustainable Energy Reviews*, 59: 1307–1316.

Mahlooji, M.H., Mohammadi, H.R. & Rahimi, M. 2018. A review on Modeling and Control of Grid-Connected Photovoltaic Inverters with LCL Filter. *Renewable and Sustainable Energy Reviews*, 81: 563–578. http://dx.doi.org/10.1016/j.rser.2017.08.002.

Majlan, E., Rohendi, D., Daud, W., Husaini, T. & Haque, M. 2018. Electrode for Proton Exchange Membrane Fuel Cells: A review. *Renewable and Sustainable Energy Reviews*, 89: 117–134. https://doi.org/10.1016/j.rser.2018.03.007.

Mancilla-David, F., Arancibia, A., Riganti-Fulginei, F., Muljadi, E. & Cerroni, M. 2012a. A

maximum power point tracker variable-dc-link three-phase inverter for grid-connected PV panels. In *IEEE PES Innovative Smart Grid Technologies Conference Europe*. IEEE: 1–7.

Mancilla-David, F., Arancibia, A., Riganti-Fulginei, F., Muljadi, E. & Cerroni, M. 2012b. A maximum power point tracker variable-dc-link three-phase inverter for grid-connected PV panels. In *IEEE PES Innovative Smart Grid Technologies Conference Europe*. Berlin: IEEE: 1–7.

Manias, S.N. 2016. *Power Electronics and Motor Drive Systems*. ELSEVIER.

Mann, R.F., Amphlett, J.C., Hooper, M.A.I., Jensen, H.M., Peppley, B.A. & Roberge, P.R. 2000. Development and application of a generalised steady-state electrochemical model for a PEM fuel cell. *Journal of Power Sources*, 86(1–2): 173–180.

Marx, N., Boulon, L., Gustin, F., Hissel, D. & Agbossou, K. 2014. A review of Multi-stack and Modular Fuel Cell Systems: Interests, Application Areas and on-Going Research Activities. *International Journal of Hydrogen Energy*, 39(23): 12101–12111. http://dx.doi.org/10.1016/j.ijhydene.2014.05.187.

Maswood, A.I. & Tafti, H.D. 2019. *Advanced Multilevel Converters and Edited by*. John Wiley.

Mendecka, B. & Lombardi, L. 2019. Life Cycle Environmental Impacts of Wind Energy Technologies : A review of Simplified Models and Harmonization of The results. *Renewable and Sustainable Energy Reviews*, 111: 462–480. https://doi.org/10.1016/j.rser.2019.05.019.

Merai, M., Naouar, M.W. & Slama-belkhodja, I. 2018. An Improved DC-Link Voltage Control Strategy for Grid Connected Converters. *IEEE Transactions on Power Electronics*, 33(4): 3575–3582.

Mirhosseini, M. 2019. Sensitivity Analysis, Adaptability Improvement and Control of Grid-Connected Photovoltaic Power Plants Under Grid Frequency Variations. *Solar Energy*, 184: 260–272. https://doi.org/10.1016/j.solener.2019.03.072.

Murugesan, K. & Senniappan, V. 2013. Investigation of Water Management Dynamics on the Performance of a Ballard-Mark-V Proton Exchange Membrane Fuel Cell Stack System. *International Journal of Electrochemical Science*, 8: 7885–7904.

Nademi, H., Das, A., Burgos, R. & Norum, L.E. 2016. A New Circuit Performance of Modular Multilevel Inverter Suitable for Photovoltaic Conversion Plants. *IEEE Journal of Emerging and Selected Topics in Power Electronics*, 4(2): 393–404.

Naghizadeh, R.A., Jazebi, S. & Vahidi, B. 2012. Modeling hydro power plants and tuning hydro governors as an educational guideline. *International Review on Modelling and Simulations*, 5(4): 1780–1790.

Naik, M.V. & Samuel, P. 2016. Analysis of Ripple Current, Power Losses and High Efficiency of DC-DC Converters for Fuel Cell Power Generating Systems. *Renewable and*

Sustainable Energy Reviews, 59: 1080–1088. http://dx.doi.org/10.1016/j.rser.2016.01.029.

National Energy Technology Laboratory, U.S.D. of E. 2005. *Fuel Cell Handbook*. 7th ed. University Press of the Pacific.

Novak, M., Šunde, V. & Jakopović, Ž. 2015. Model of three level neutral point clamped converter (NPC) for grid connected photovoltaic systems. In *2015 38th International Convention on Information and Communication Technology, Electronics and Microelectronics (MIPRO)*. Opatija: IEEE: 25–29.

Obaid, W., Hamid, A.K. & Ghenai, C. 2018. Hybrid PEM Fuel-Cell-Diesel-Solar Power System Design with Fuzzy Battery Management System and Weather Forecasting for Electric Boats. In *Proceedings of 2018 6th International Renewable and Sustainable Energy Conference, IRSEC 2018*. IEEE: 1–7.

Ouchen, S., Abdeddaim, S., Betka, A. & Menadi, A. 2016. Experimental Validation of Sliding Mode-Predictive Direct Power Control of A grid Connected Photovoltaic System , Feeding A nonlinear Load. *Solar Energy*, 137: 328–336. http://dx.doi.org/10.1016/j.solener.2016.08.031.

Owiro, D., Poquillon, G., Njonjo, S.K. & Odour, C. 2015. *Situational Analysis of Energy Industry , Policy and Strategy for Kenya*.

Patel, P.U. & Pandya, H.D. 2018. Control and Grid Synchronization of Fuel Cell Based Inverter Using Matlab. In *Proceedings of the 2nd International Conference on Electronics, Communication and Aerospace Technology, ICECA 2018*. IEEE: 650–655.

Pereira, I. & Martins, A. 2009. Neutral-Point Voltage Balancing in Three-Phase NPC Converters Using Multicarrier PWM Control. In *2009 International Conference on Power Engineering, Energy and Electrical Drives*. Lisbon: 570–574.

Prasad, B.S., Jain, S. & Agarwal, V. 2008. Universal Single-Stage Grid-Connected Inverter. , 23(1): 128–137.

Ragab, A. s, Saad, N.H. & A.El-sattar, A. 2017. LLC Resonant DC-DC Converter for Grid-Connected PV System. In *2017 12th International Conference on Computer Engineering and Systems*. Cairo: IEEE.

Ramezanizadeh, M., Alhuyi Nazari, M., Hossein Ahmadi, M. & Chen, L. 2019. A review on The Approaches Applied for Cooling Fuel Cells. *International Journal of Heat and Mass Transfer*, 139: 517–525. https://doi.org/10.1016/j.ijheatmasstransfer.2019.05.032.

Reznik, A., Simoes, M.G., Al-Durra, A. & Muyeen, S.M. 2014. LCL Filter Design and Performance Analysis for Grid-Interconnected Systems. *IEEE Transactions on Industry Applications*, 50(2): 1225–1232.

Rosales-Asensio, E., Borge-Diez, D., Blanes-Peiró, J.J., Pérez-Hoyos, A. & Comenar-Santos, A. 2019. Review of Wind Energy Technology and associated Market and Economic Conditions in Spain. *Renewable and Sustainable Energy Reviews*, 101: 415–

427. https://doi.org/10.1016/j.rser.2018.11.029.

Roy, T. & Mahmud, M. 2017. Active Power Control of Three-Phase Grid-Connected Solar PV Systems Using a Robust Nonlinear Adaptive Backstepping Approach. *Solar Energy*, 153: 64–76. http://dx.doi.org/10.1016/j.solener.2017.04.044.

Rslan, H., Ahmed, M., Orabi, M. & Youssef, M. 2010. Development of Grid Connected Power Conditioner System Compatible with Fuel Cell Applications. In *The 2nd International Symposium on Power Electronics for Distributed Generation Systems*. Hefei: IEEE: 935–941.

Saeed, W. & Warkozek, G. 2015. Modeling and Analysis of Renewable PEM Fuel Cell System. *Energy Procedia*, 74: 87–101. http://dx.doi.org/10.1016/j.egypro.2015.07.527.

Sahoo, H.K. & Subudhi, U. 2018. Power System Harmonics Estimation Using Adaptive Filters. In *Compendium of New Techniques in Harmonic Analysis*. Intech Open Access.

Sanjeevarayudu, S., Kanth, D.S.K. & Ramana, B.V. 2017. Enhanced Performance of H6 Full Bridge Inverter in Reducing the Leakage Currents in Transformerless PV system. *International Journal of Electrical and Computer Engineering*, 9(1): 1–10.

Sen, S., Yenduri, K. & Sensarma, P. 2014. Step-by-step Design and Control of LCL filter based Three Phase Grid-connected Inverter. In *2014 IEEE International Conference on Industrial Technology (ICIT)*. Busan: IEEE: 503–508.

Seyezhai, R. & Mathur, B. 2011. Mathematical Modeling of Proton Exchange Membrane Fuel Cell. *International Journal of Computer Applications*, 20(5): 1–6.

Solangi, K., Islam, M., Saidur, R., Rahim, N. & Fayaz, H. 2011. A review on global solar energy policy. *Renewable and Sustainable Energy Reviews*, 15(4): 2149–2163. http://dx.doi.org/10.1016/j.rser.2011.01.007.

SolarPACES. 2018. How CSP Works: Tower, Trough, Fresnel or Dish - SolarPACES.

Spanias, C. & Lestas, I. 2019. A System Reference Frame Approach for Stability Analysis and Control of Power Grids. *IEEE Transactions on Power Systems*, 34(2): 1105–1115.

Suryoatmojo, H., Mardiyanto, R., Riawan, D., Anam, S., Setijadi, E., Ito, S. & Wan, I. 2018. Implementation of High Voltage Gain DC-DC Boost Converter for Fuel Cell Application. In *ICEAST 2018 - 4th International Conference on Engineering, Applied Sciences and Technology: Exploring Innovative Solutions for Smart Society*. 2–5.

Tafti, H.D., Maswood, A.I., Lim, Z., Ooi, G.H.P. & Raj, P.H. 2015. A Review of Active / Reactive Power Control Strategies for PV Power Plants under Unbalanced Grid Faults. In *2015 IEEE Innovative Smart Grid Technologies - Asia (ISGT ASIA)*. Bangkok: IEEE: 1–6.

Tarasantisuk, C., Suyata, T., Tarateeraseth, V. & Witheephanich, K. 2016. Active and Reactive Power Control for Three-Phase Grid Inverters with Proportional Resonant Control Strategies. In *2016 13th International Conference on Electrical Engineering/Electronics, Computer, Telecommunications and Information Technology*

(ECTI-CON). Chiang Mai: IEEE: 1–6.

Teknos. 2018. Coating Solutions for Hydropower Plants - Teknos. https://www.teknos.com/industrial-coatings/industries/industrial-metal/energy/hydropower-plants/ 24 November 2019.

Teodorescu, R., Liserre, M. & Rodríguez, P. 2011. *Grid Converters for Photovoltaic and Wind Power Systems*. Wiley.

The World Bank. Rural population (% of total population) | Data.

Timbus, A., Teodorescu, R., Blaabjerg, F. & Liserre, M. 2005. Synchronization Methods for Three Phase Distributed Power Generation Systems. An Overview and Evaluation. In *Power Electronics Specialists (PESC), Annual IEEE Confrence*. IEEE.

Tuyen, N.D. & Fujita, G. 2015. PV-Active Power Filter Combination Supplies Power to Nonlinear Load and Compensates Utility Current. *IEEE Power and Energy Technology Systems Journal*, 2(1): 32–42.

Viuquezl, N., Almazin, J., Alvarez, J., Aguilat, C. & Arau, J. 1999. Analysis and Experimental Study of the Buck , Boost and Buck-Boost Inverters. In *30th Annual IEEE Power Electronics Specialists Conference.* Charleston, SC: IEEE.

Vu, H.G., Yahoui, H., Chorot, T. & Hammouri, H. 2012. Control active and reactive power of Voltage Source Inverter (VSI). In *2012 2nd International Symposium On Environment Friendly Energies And Applications*. Newcastle upon Tyne: IEEE: 308–311.

Vukosavic, S.N. 2018. *Grid-Side Converters Control and Design Interfacing Between the AC Grid and Renewable Power Sources*. Springer.

Wang, C. 2004. A Novel Single-Stage Full-Bridge Buck-Boost Inverter. *IEEE Transactions on Power Electronics*, 19(1): 150–159.

Wang, J., Ji, B., Zhao, J. & Yu, J. 2012. From H4 , H5 to H6 — Standardization of Full-Bridge Single Phase Photovoltaic Inverter Topologies without Ground Leakage Current Issue. In *2012 IEEE Energy Conversion Congress and Exposition (ECCE)*. IEEE: 2419–2425.

Wang, L., Lam, C. & Wong, M. 2017. Analysis , Control and Design of Hybrid Grid-Connected Inverter for Renewable Energy Generation with Power Quality Conditioning. *IEEE Transactions on Power Electronics*, 33(2).

Wu, B. & Narimani, M. 2017. *High-Power Converters and AC Drives*. 2nd ed. WILEY.

Wu, B., Parkes, M.A., Yufit, V., De Benedetti, L., Veismann, S., Wirsching, C., Vesper, F., Martinez-Botas, R.F., Marquis, A.J., Offer, G.J. & Brandon, N.P. 2014. Design and testing of a 9.5 kWe proton exchange membrane fuel cell-supercapacitor passive hybrid system. *International Journal of Hydrogen Energy*, 39(15): 7885–7896.

Wu, Z., Gao, W., Gao, T., Yan, W., Zhang, H., Yan, S. & Wang, X. 2018. State-of-the-art review on frequency response of wind power plants in power systems. *Journal of Modern Power Systems and Clean Energy*, 6(1): 1–16.

Yang, Y. & Blaabjerg, F. 2015. Overview of Single-Phase Grid-Connected Photovoltaic

Systems. *Electric Power Components and Systems*, 42(12): 11.

Yang, Y., Blaabjerg, F., Wang, H. & Simões, M.G. 2016. Power control flexibilities for grid-connected multi-functional photovoltaic inverters. *IET Renewable Power Generation*, 10(4): 504–513.

Yang, Y., Enjeti, P., Frede, B. & Wang, H. 2015. Wide-Scale Adoption of Photovoltaic Energy: Grid Code Modifications Are Explored in the Distribution Grid. *IEEE Industry Applications Magazine*, 21(5): 21–31.

Yang, Y., Kim, K.A., Blaabjerg, F. & Sangwongwanich, A. 2019. *Advances in Grid-Connected Photovoltaic Power Conversion Systems*. Woodhead Publishing.

Yang, Y., Sangwongwanich, A. & Blaabjerg, F. 2016. Design for Reliability of Power Electronics for Grid-Connected Photovoltaic SystemS. *CPSS Transactions on Power Electronics and Applications*, 1(1).

Yao, W., Yang, Y. & Zhang, X. 2017. Design and Analysis of Robust Active Damping for LCL Filters Using Digital Notch Filters. *IEEE Transactions on Power Electronics*, 32(3): 2360–2375.

Yongli, Z. 2013. Simulation Study of PEM Fuel Cell and its Dynamic Characteristics. In *2013 IEEE Power & Energy Society General Meeting*. Vancouver, BC.

Yu, W., York, B. & Lai, J. 2012. Inductorless Forward-Flyback Soft-Switching Converter with Dual Constant On-time Modulation for Photovoltaic Applications. In *2012 IEEE Energy Conversion Congress and Exposition (ECCE)*. Raleigh: IEEE: 3549–3555.

Yu, X., Starke, M., Tolbert, L. & Ozpineci, B. 2007. Fuel Cell Power Conditioning for Electric Power Applications: A summary. *IET Electric Power Applications*, 1(1): 643–656.

Yuan, Y., Qu, Z., Wang, W., Ren, G. & Hu, B. 2019. Illustrative Case Study on the Performance and Optimization of Proton Exchange Membrane Fuel Cell. *ChemEngineering*, 3(1): 23.

Zhang, L., Sun, K., Xing, Y. & Xing, M. 2014. H6 Transformerless Full-Bridge PV Grid-Tied. *IEEE Transactions on Power Electronics*, 29(3): 1229–1238.

Zhang, X., Chen, P., Yu, C., Li, F. & Do, H.T. 2017. Study of a Current Control Strategy Based on Multisampling for High-Power Grid-Connected Inverters With an LCL filter. *IEEE Transactions on Power Electronics*, 32(7): 5023–5034.

Zhong, Q.-C. & Hornik, T. 2013. *Control of Power Inverters in Renewable Energy and Smart Grid Integration*. WILEY.

Zhou, K., Wang, D., Yang, Y. & Blaabjerg, F. 2017. *Periodic Control of Power Electronic Converters*. The Institution of Engineering and Technology.

Zhu, J., Hu, K., Lu, X., Huang, X., Liu, K. & Wu, X. 2015. A review of geothermal energy resources, development, and applications in China: Current status and prospects. *Energy*, 93: 466–483.

Zou, Y., Qin, J., Zhang, L. & Zhang, Z. 2018. Novel Control Approach for Modular Multilevel

Converter Based on αβ0 Reference Frame Without PLL. In *2018 IEEE Energy Conversion Congress and Exposition (ECCE)*. Portland, OR: 3044–3049.

Zwaan B, V, B., Cameron, L. & Kober, T. 2013. Potential for Renewable Energy Jobs in The Middle East. *Energy Policy*, 60: 296–304. http://dx.doi.org/10.1016/j.enpol.2013.05.014.

APPENDICES

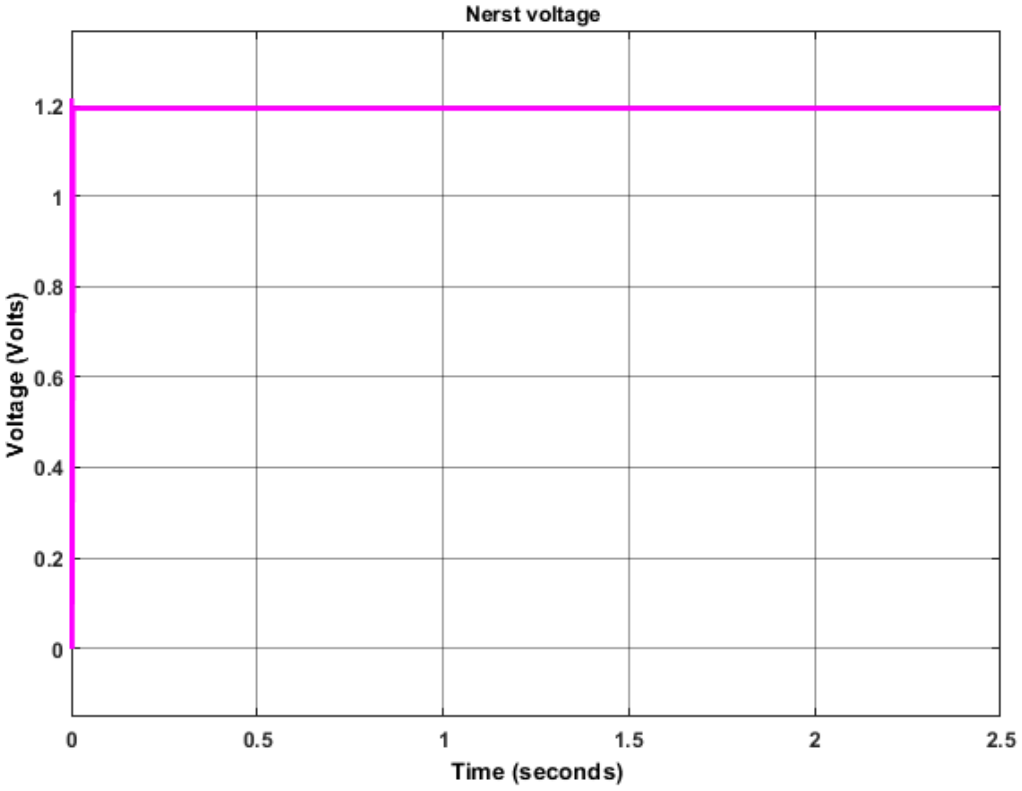

Figure A. 1: Nerst voltage of a cell

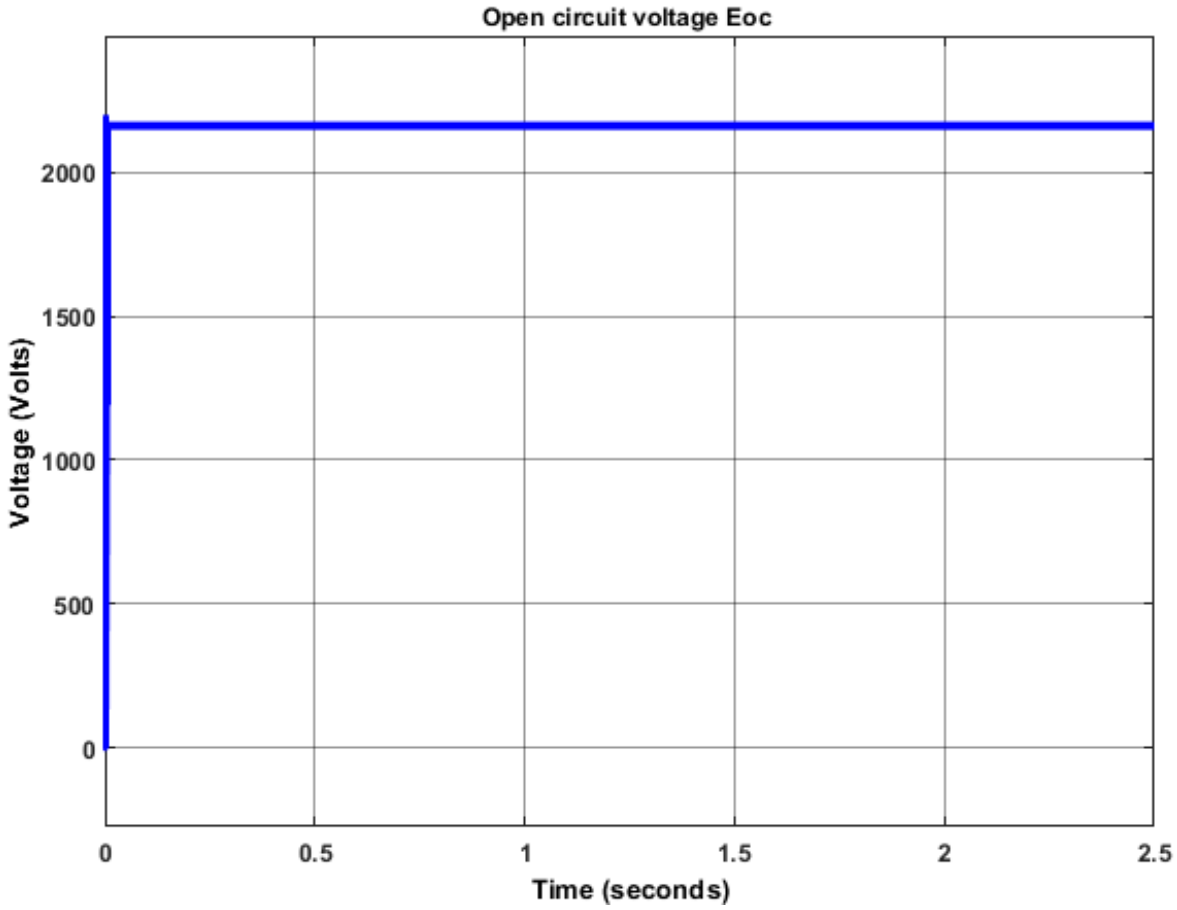

Figure A. 2: Stack open circuit voltage

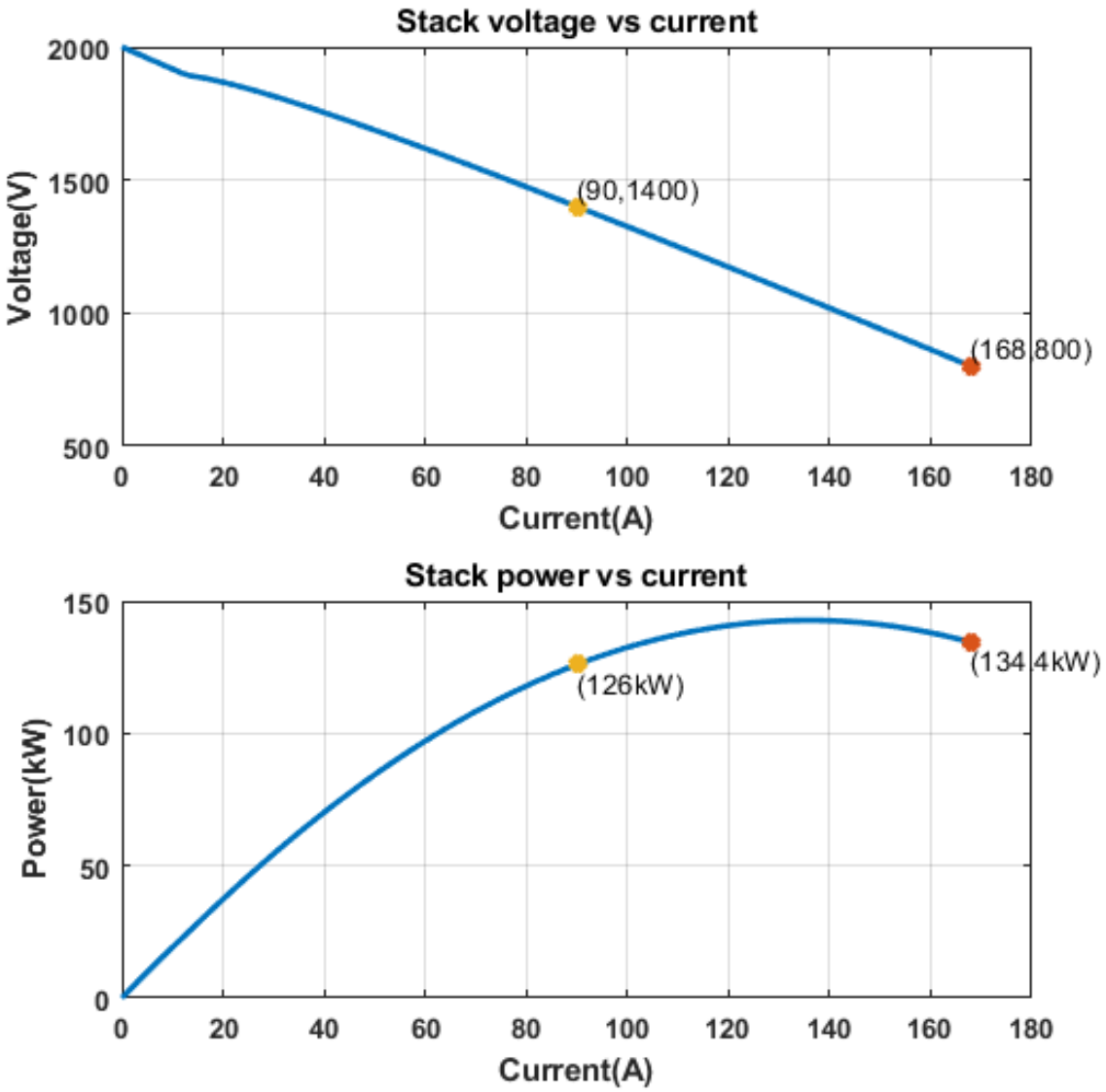

Figure A. 3: Polarisation curves of a single stack

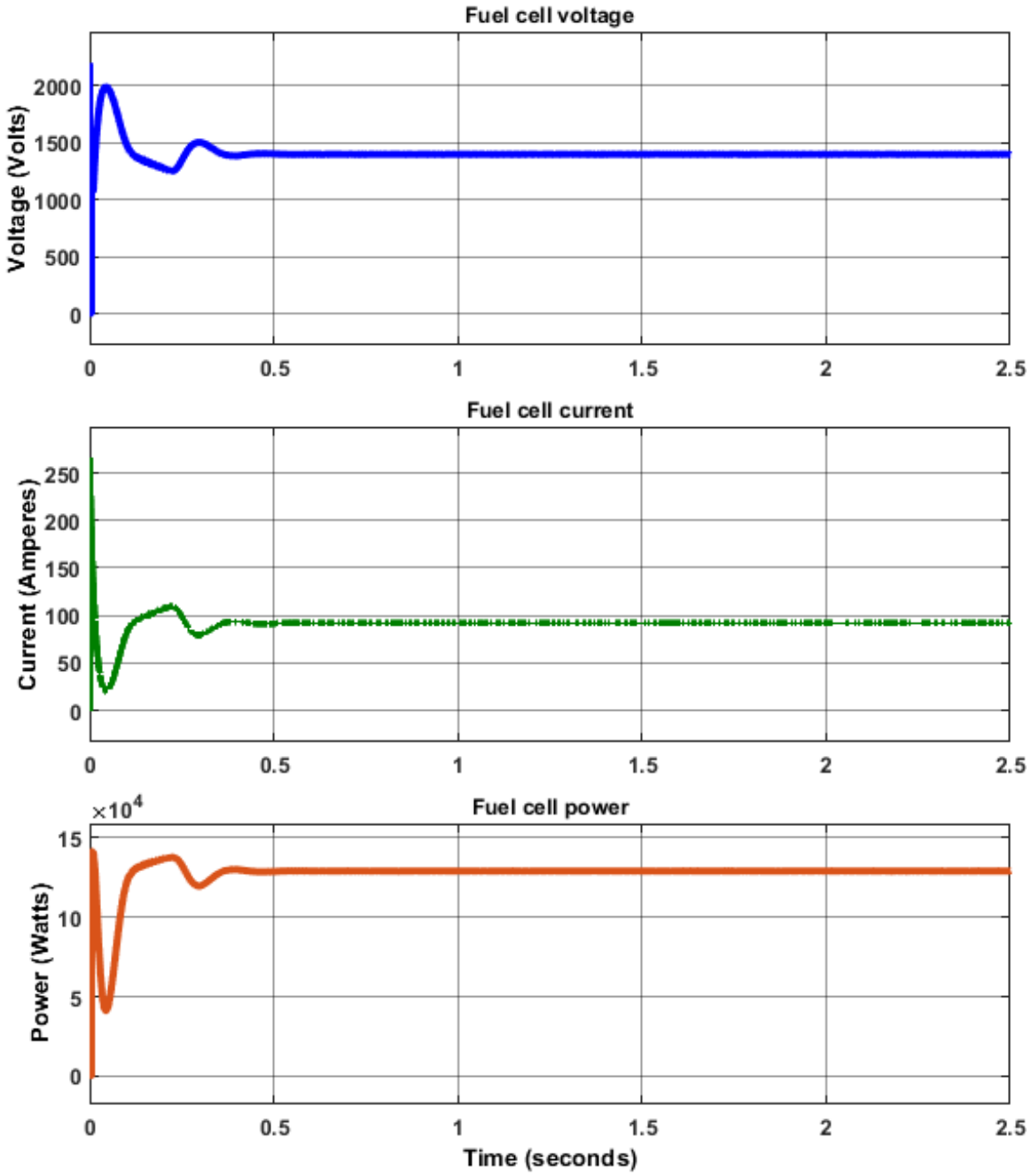

Figure A. 4: Voltage, current and power of a single stack

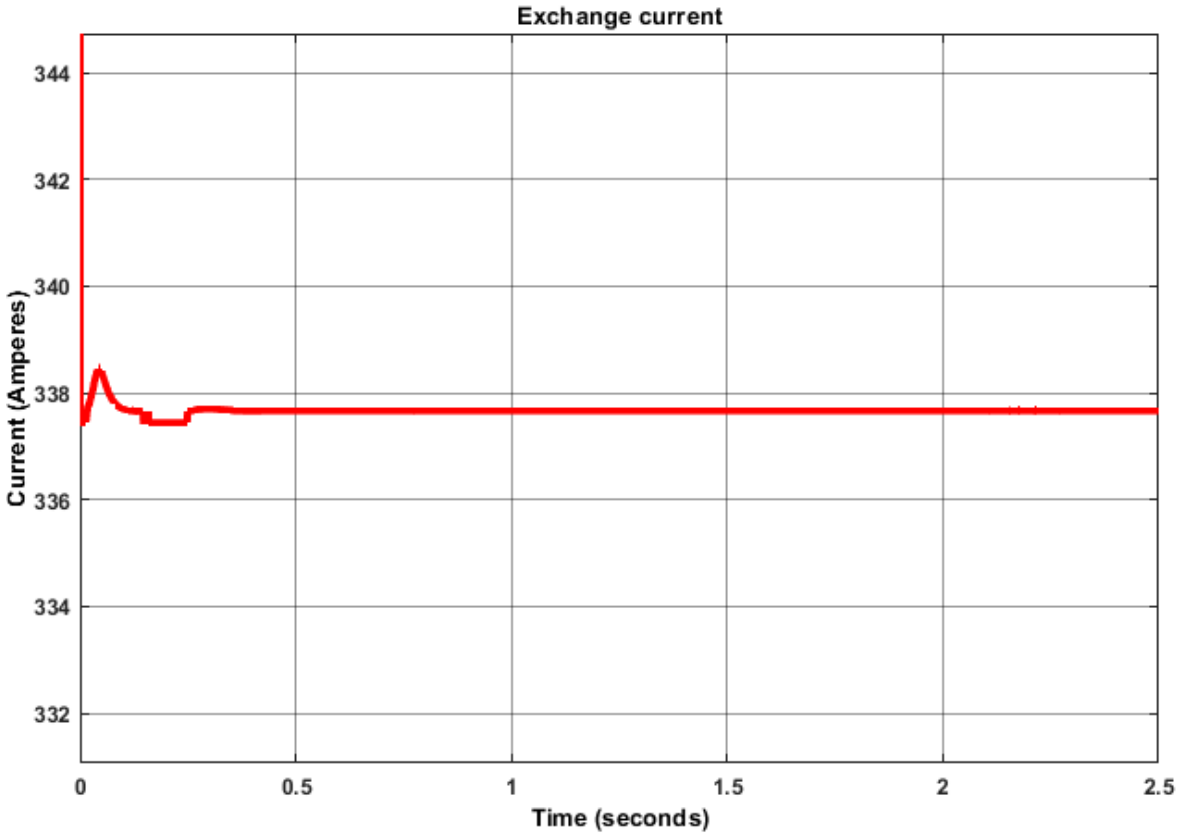

Figure A. 5: Exchange current of a single stack

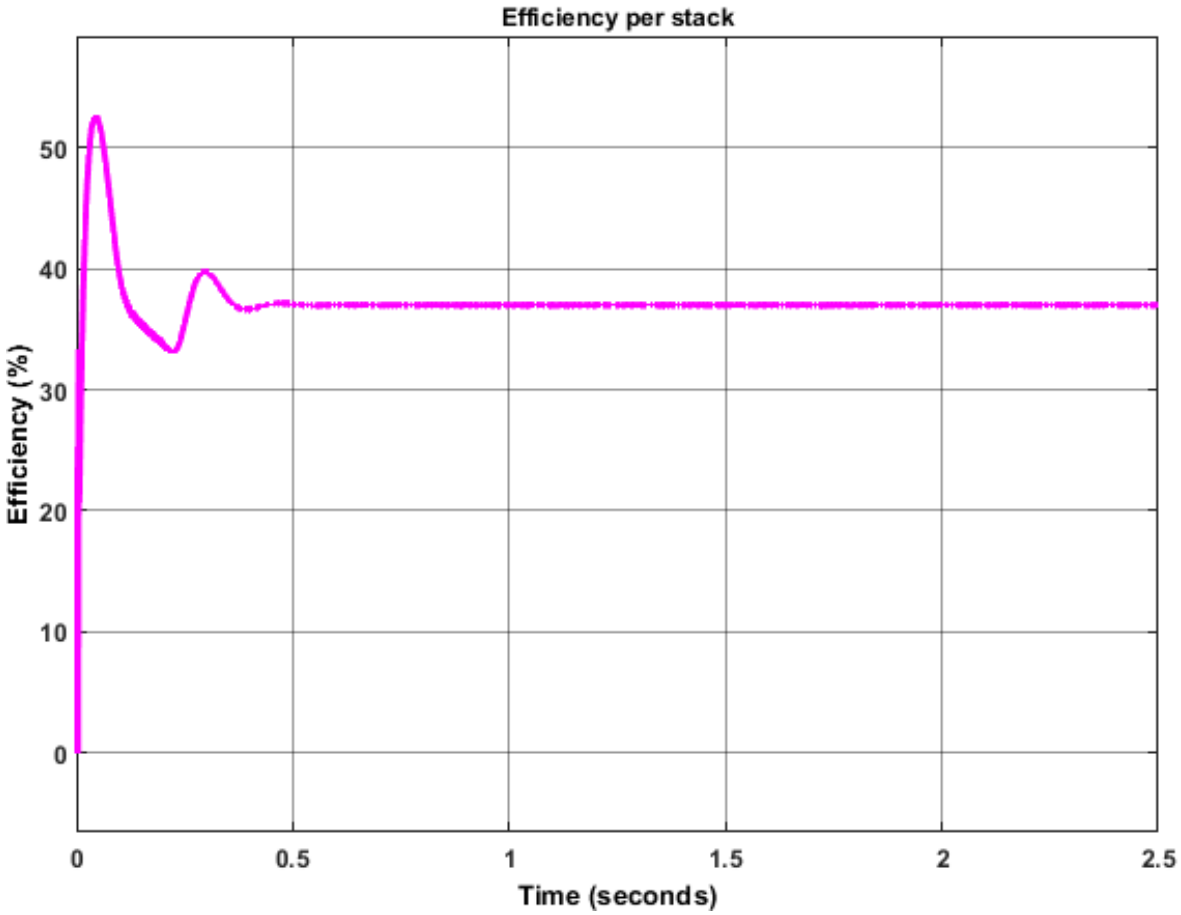

Figure A. 6: Efficiency of each fuel cell stack

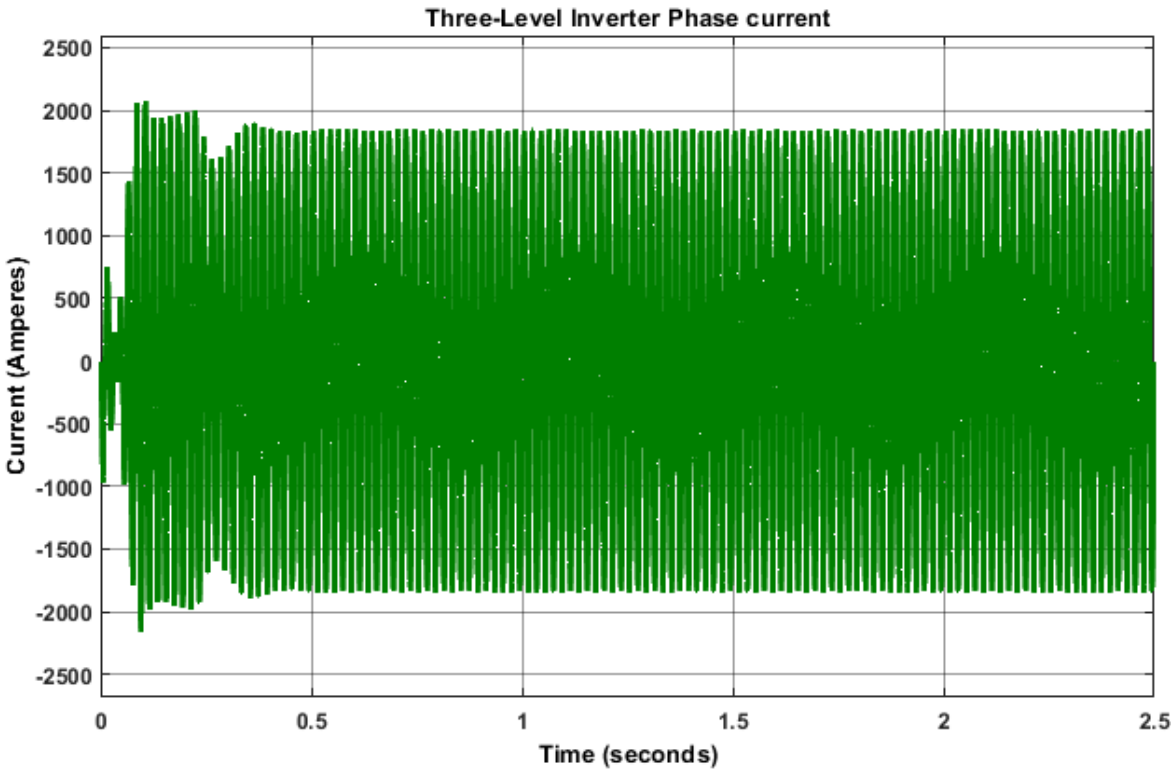

Figure A. 7: Three-level inverter output current before LCL filter

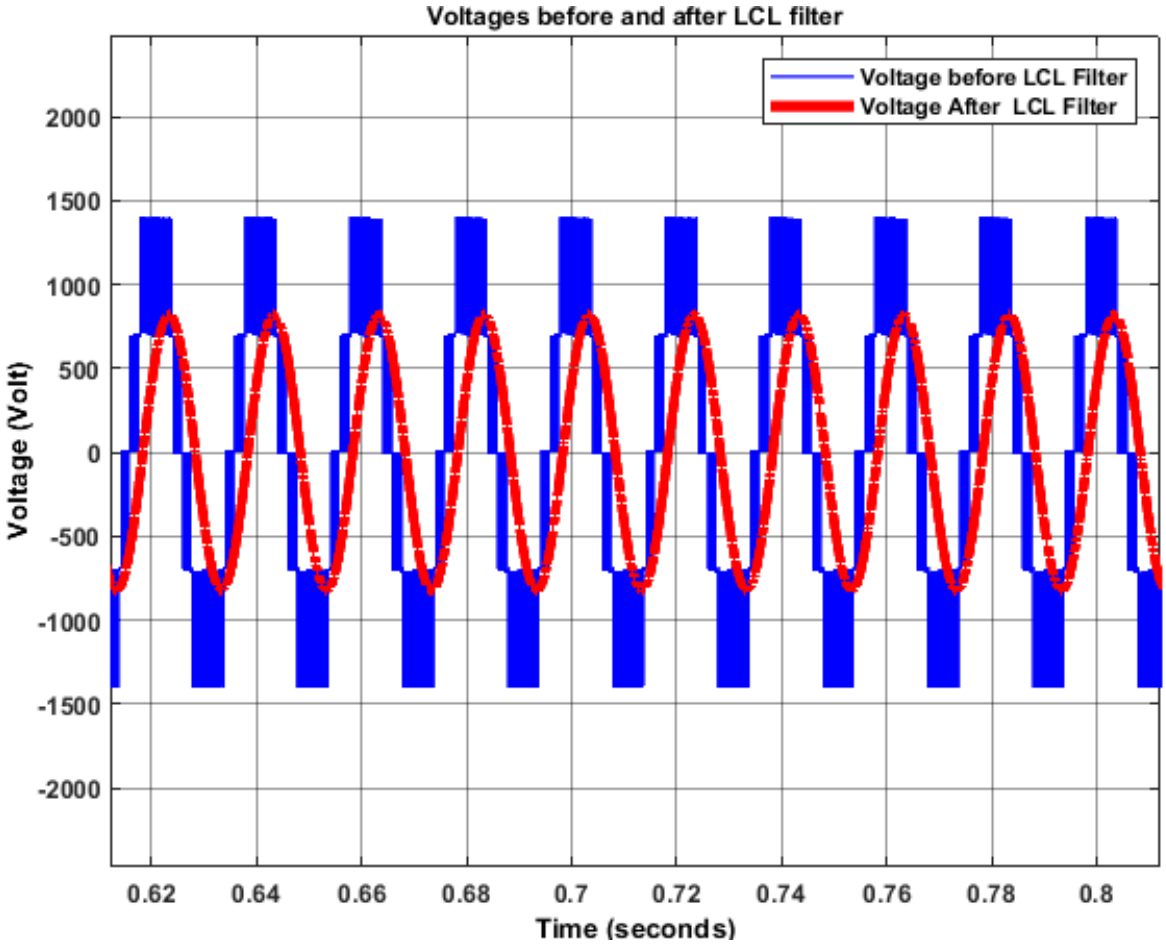

Figure A. 8: Phase to phase voltage before and after LCL filter

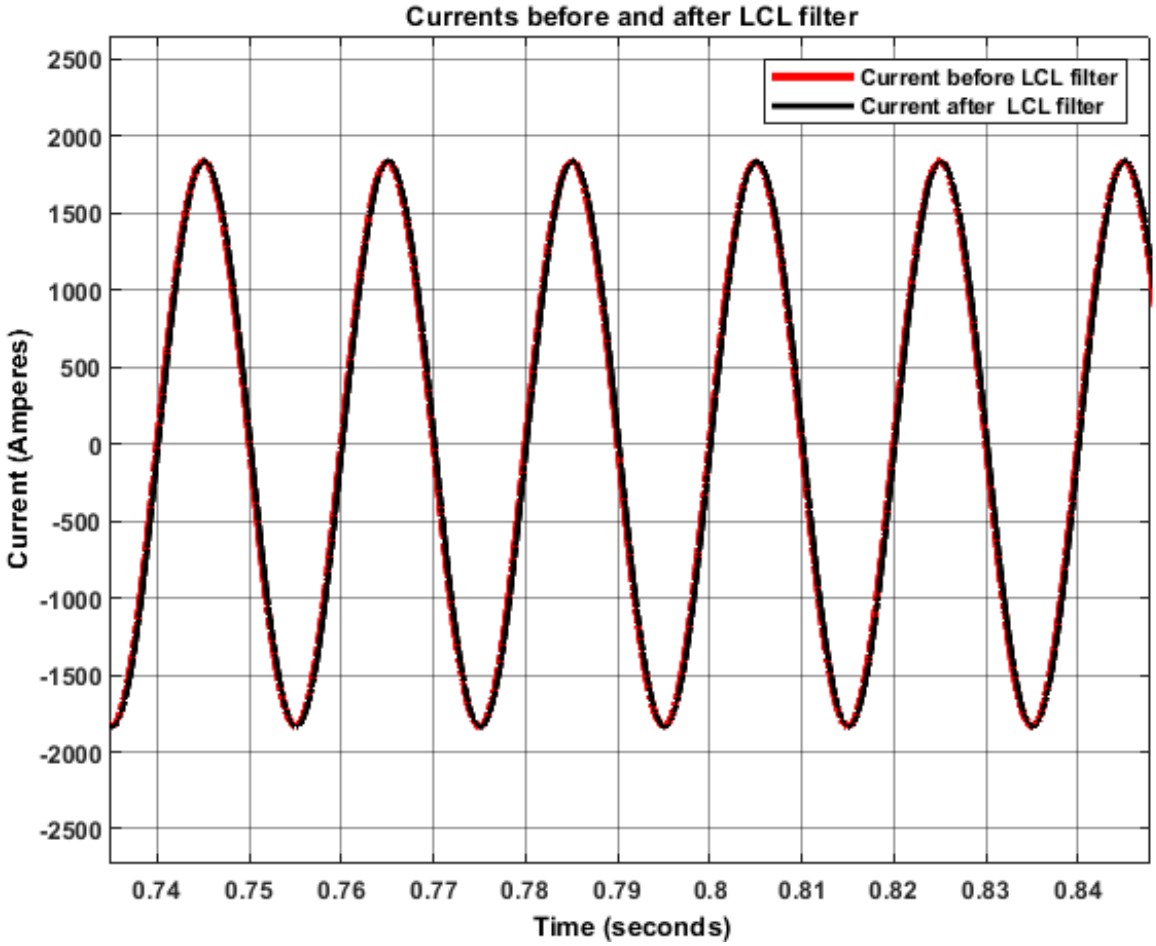

Figure A. 9: Current before and after LCL filter

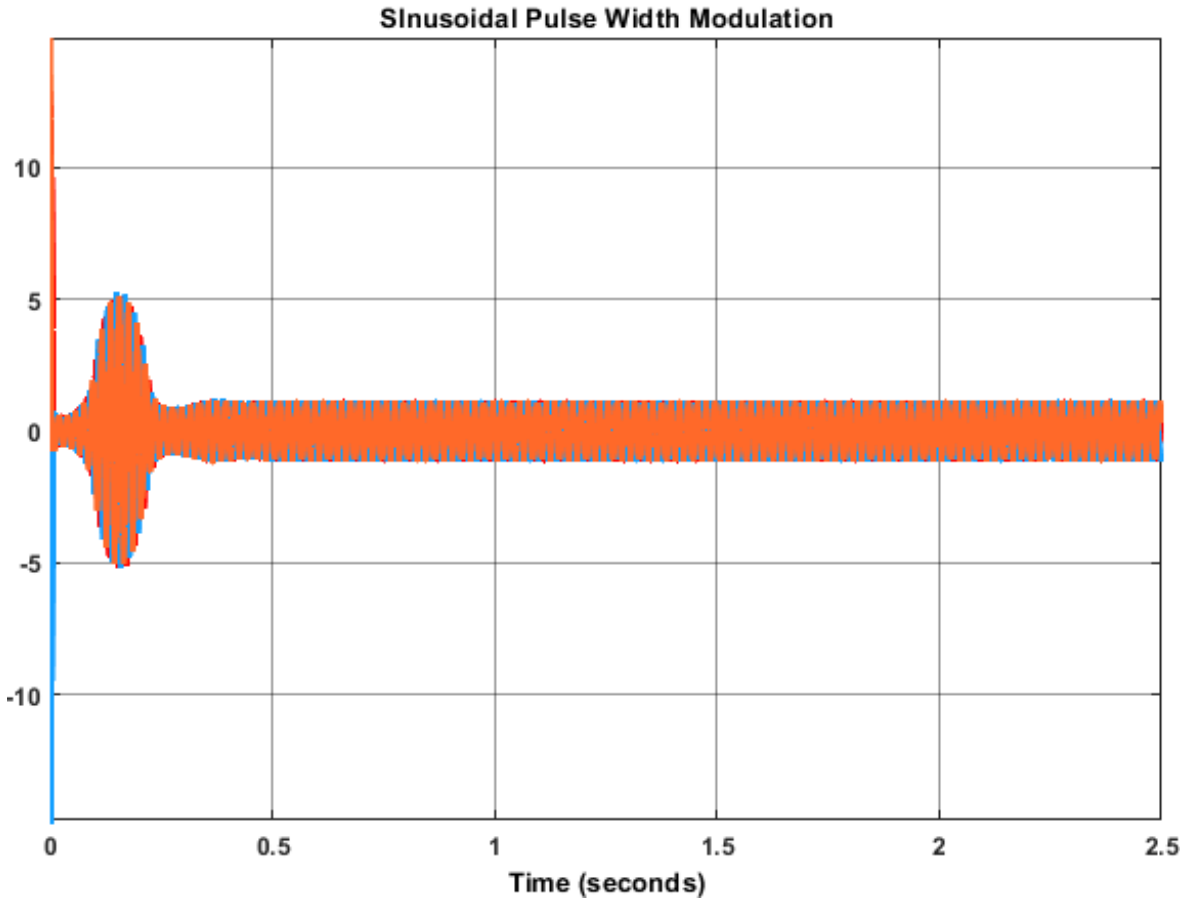

Figure A. 10: Sinusoidal PWM signal

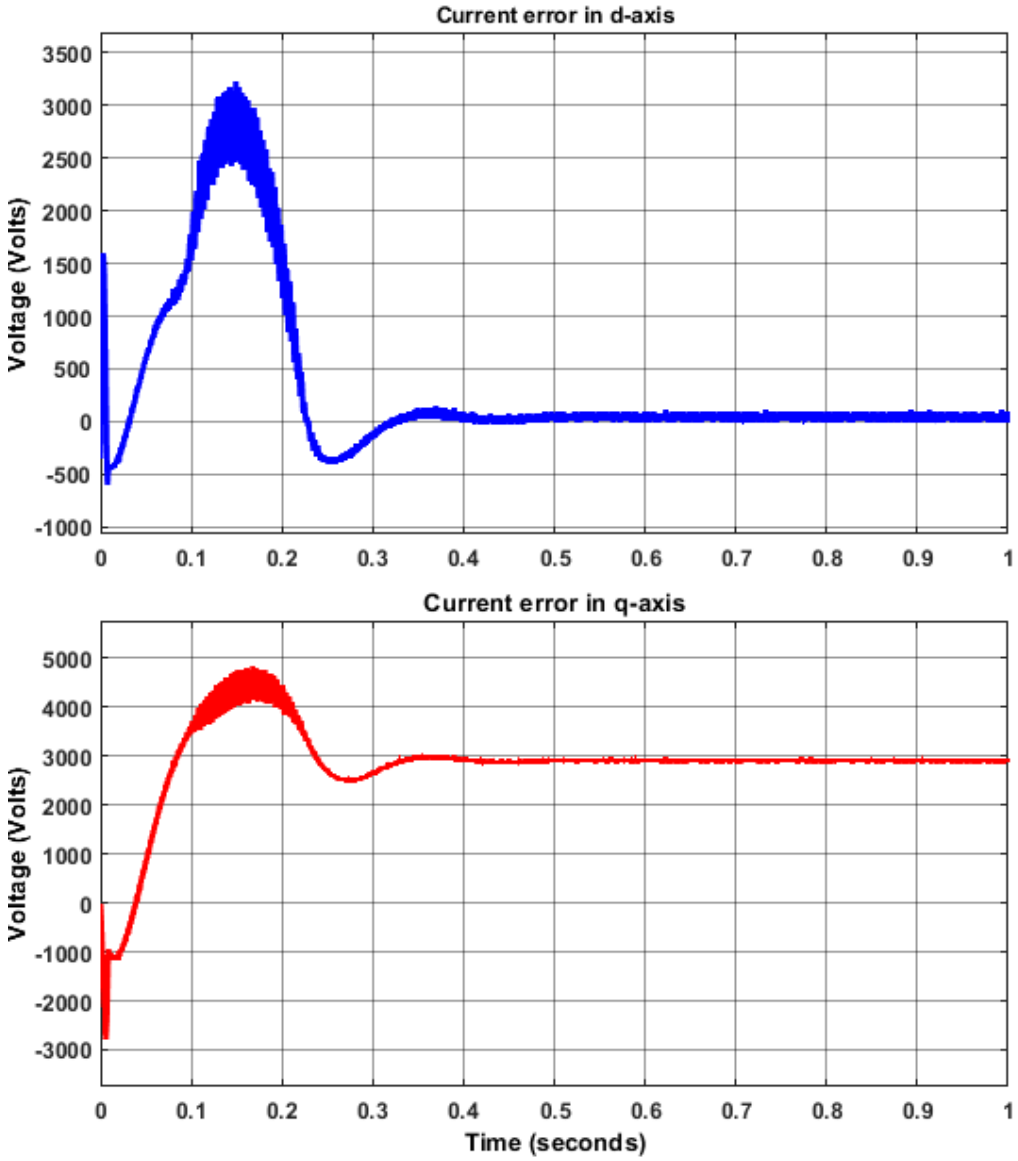

Figure A. 11: Current errors in dq0 reference frame